

APPLICATIONS OF SILVER NANOWIRE NETWORKS  
IN OPTO-ELECTRONIC DEVICES

A THESIS SUBMITTED TO  
THE GRADUATE SCHOOL OF NATURAL AND APPLIED SCIENCES  
OF  
MIDDLE EAST TECHNICAL UNIVERSITY

BY

ŞAHİN COŞKUN

IN PARTIAL FULFILLMENT OF THE REQUIREMENTS  
FOR  
THE DEGREE OF DOCTOR OF PHILOSOPHY  
IN  
METALLURGICAL AND MATERIALS ENGINEERING

JANUARY 2018



Approval of the thesis

**APPLICATIONS OF SILVER NANOWIRE NETWORKS  
IN OPTO-ELECTRONIC DEVICES**

Submitted by ŞAHİN COŞKUN in partial fulfillment of the requirements for the degree of **Doctor of Philosophy in Department of Metallurgical and Materials Engineering, Middle East Technical University** by,

Prof. Dr. Halil Kalıpçılar \_\_\_\_\_  
Dean, Graduate School of **Natural and Applied Sciences, METU**

Prof. Dr. Cemil Hakan Gür \_\_\_\_\_  
Head of Department, **Metallurgical and Mat. Eng. Dept., METU**

Assoc. Prof. Dr. Hüsni Emrah Ünal \_\_\_\_\_  
Supervisor, **Metallurgical and Materials Eng. Dept., METU**

**Examining Committee Members:**

Prof. Dr. Ali Çırpan \_\_\_\_\_  
Chemistry Department, METU

Assoc. Prof. Dr. Hüsni Emrah Ünal \_\_\_\_\_  
Metallurgical and Materials Engineering Dept., METU

Assoc. Prof. Dr. Alpan Bek \_\_\_\_\_  
Physics Department, METU

Assoc. Prof. Dr. Savaş Sönmezoğlu \_\_\_\_\_  
Metallurgical and Materials Engineering Dept., Karamanoğlu  
Mehmetbey University

Assoc. Prof. Dr. Jongee Park \_\_\_\_\_  
Metallurgical and Materials Engineering Dept., Atılım University

**Date:** 30.01.2018

**I hereby declare that all information in this document has been obtained and presented in accordance with academic rules and ethical conduct. I also declare that, as required by these rules and conduct, I have fully cited and referenced all material and results that are not original to this work.**

Name, Last name: Şahin Coşkun

Signature :

## **ABSTRACT**

### **APPLICATIONS OF SILVER NANOWIRE NETWORKS IN OPTO-ELECTRONIC DEVICES**

Coşkun, Şahin

Ph.D., Department of Metallurgical and Materials Engineering

Advisor: Assoc. Prof. Dr. Hüsni Emrah Ünalın

January 2018, 159 pages

The demand for electronic devices such as smart phones, touch screens and flat panel televisions has been increased over the past decade. These devices need transparent conductors and the most widely used transparent conductor as electrode in these devices is indium tin oxide (ITO) due to its high transparency and low sheet resistance. However, ITO thin films have some drawbacks. They are expensive, difficult to deposit, poorly compatible with flexible substrates. Hence, better alternatives for transparent conductors are being studied. Recently, metal nanowires have received a lot of attention due to their unique physical, chemical and optical properties. Due to excellent properties of bulk silver, silver nanowires have been widely investigated. Recently, it was proved that silver nanowire networks provide a suitable path for charge transport and transmit incident visible light. In this thesis, silver nanowires were synthesized in a larger scale via modified polyol process. Afterwards, as synthesized silver nanowires in the form of networks were used to fabricate transparent and conducting electrodes. This was followed by the use of silver nanowire network based transparent and conducting electrodes were used as anodes in organic light emitting diodes (OLEDs). Finally, ambient stability of silver nanowire networks and fabrication of NiO / Ag NWs nanocomposite electrodes were investigated.

**Keywords:** nanowires, transparent conductors, polymer light emitting diodes, silver nanowires.

## ÖZ

### GÜMÜŞ NANOTEL İNCE FİLMLERİN OPTO-ELEKTRONİK CİHAZLARDAKİ UYGULAMALARI

Coşkun, Şahin

Doktora, Metalurji ve Malzeme Mühendisliği

Tez Yöneticisi: Doç. Dr. Hüsnü Emrah Ünalın

Ocak 2018, 159 sayfa

Akıllı telefonlar, dokunmatik ekranlar ve LCD televizyonlar gibi elektronik cihazlara duyulan talep geçtiğimiz on yılda oldukça artmıştır. Bu cihazların ortak özelliği ise hepsinde şeffaf iletken elektrotların kullanılmasıdır. Ticari olarak en çok kullanılan şeffaf iletken elektrot malzemesi ise görünür ışığa karşı yüksek şeffaflığı ve düşük düzlemsel direnci sebebiyle indiyum kalay oksittir (ITO). Ancak indiyum kalay oksitin esnek altlıklara uyumsuzluğu, pahalı olması ve kaplama yönteminin zorluğu sebebiyle alternatif şeffaf iletken malzemeler konusunda araştırmalar yapılmaktadır. Son zamanlarda, metal nanoteller benzersiz fiziksel, kimyasal ve optik özelliklerinden dolayı büyük ilgi görmüştür. Kütle gümüşün mükemmel özellikleri nedeniyle, gümüş nanoteller de büyük ilgi görmüştür. Yakın geçmişte, gümüş nanotel ince filmlerin elektrik yüklerine uygun bir yol sağlarken görünür ışığa karşı da şeffaf olduğu ispatlanmıştır. Bu tezde, öncelikle gümüş nanoteller modifiye polyol prosesi ile daha geniş ölçekte sentezlenmiştir. Daha sonra, sentezlenen gümüş nanoteller şeffaf ve iletken elektrotları üretmek için kullanılmıştır. Bunu takiben, gümüş nanotel ince filmler polimer ışık yayan diyorlarda (PLED) anot malzemesi olarak kullanılmıştır. Son olarak, gümüş nanotel ince filmlerin ortam kararlılığı ve nikel oksit / gümüş nanotel nanokompozit elektrotların üretimi incelenmiştir.

**Anahtar Kelimeler:** nanoteller, Őeffaf elektrotlar, polimer ıŐık yayan diyotlar, gümüş nanoteller.

*To My Family*

## ACKNOWLEDGEMENTS

It has been a long journey leading me to a Ph.D. degree in METU. I have been blessed by the support and kindness of countless people along the way and I am grateful to have a chance to acknowledge their gift. Firstly, I would like to express my deepest gratitude to my advisor Assoc. Prof. Dr. Hüsnu Emrah Ünalın, for his support, guidance and patience throughout the study. It is a great honor to work under his supervision. I also would like to thank my thesis progress committee members, Prof. Dr. Ali Çırpan and Assoc. Prof. Dr. Alpan Bek and for their valuable suggestions, advices and inputs.

This thesis was partially supported by The Scientific and Technological Research Council of Turkey (TÜBİTAK) under grant no 109M487. I would like to thank TÜBİTAK for the funding from International Doctoral Research Fellowship Programme (2214/A) as well. In addition, I would like to thank Prof. Dr. Jiaying Huang for hosting me as visiting research scholar in the Department of Materials Science and Engineering of Northwestern University. I want to thank Prof. Dr. Daniel Bellet from LGMP, France. I also would like to thank METU-ÖYP (Project No:1439) for the funding throughout my graduate studies.

I owe my deepest gratitude to my lab-mates colleagues and dearest friends, Dr. Recep Yüksel, Ayşegül Afal Geniş, Serkan Koylan, Yusuf Tutel, Elif Özlem Güner, Selin Özkul, Mete Batuhan Durukan, Sevim Polat, Doğançan Tigan, Dr. Pantea Aurang, Alptekin Aydınlı, Doğa Doğanay, Ece Alpugan, Onur Türel, İpek Bayraktar, Selen Yüksel, Elif Özlem Güner and Şeyma Koç. I would like to thank Serkan Yılmaz for TEM sessions. In addition, I would like to thank Dr. İbrahim Çam for AFM analysis. I also acknowledge all the great facilities in Metallurgical and Materials Engineering Department. I would like to thank METU Central Laboratory as well.

And finally, I would like to thank my family who always gave me hope during my PhD studies and, my wife, Smevra Doęan Cořkun, thank you for everything, thank you for always being there for me.

## TABLE OF CONTENTS

ABSTRACT .....	v
ÖZ.....	vii
ACKNOWLEDGEMENTS .....	x
TABLE OF CONTENTS .....	xii
LIST OF TABLES .....	xv
LIST OF FIGURES.....	xvi
ABBREVIATION LIST .....	xxvi
CHAPTERS	
1. INTRODUCTION.....	1
DISSERTATION OBJECTIVES.....	6
2. SYNTHESIS OF SILVER NANOWIRES .....	7
2.1. Introduction .....	7
2.2. Templated Methods.....	7
2.3. Template-Free Methods .....	11
2.3.1. Polyol Process .....	11
2.3.2. History and Development of Polyol Process.....	12
2.3.3. Seed-mediated growth approach .....	13
2.3.4. Seedless and surfactantless wet chemical synthesis.....	14
2.3.5. Seedless and surfactant assisted synthesis .....	15
2.3.6. Salt-mediated polyol method .....	18
2.4 Nanowire Characterization Methods.....	20

2.4.1 Scanning Electron Microscopy (SEM) .....	20
2.4.2 Transmission Electron Microscopy (TEM) .....	20
2.4.3 XRD Measurements .....	20
2.5 Experimental Details .....	20
2.5.1 Synthesis of Silver Nanowires .....	21
<b>3. TRANSPARENT AND CONDUCTING SILVER NANOWIRE NETWORKS</b> .....	<b>29</b>
3.1. Introduction .....	29
3.1.1. History of Transparent Conducting Oxides (TCOs) .....	29
3.1.2 Current status of TCCs .....	33
3.1.3 Transparent and Conducting Contact Characteristics .....	34
3.1.4 Types of Transparent and Conducting Contacts .....	39
3.2. Experimental Details .....	63
3.3 Device Characterization Methods .....	65
3.3.1 Scanning Electron Microscopy (SEM) .....	65
3.3.2 Sheet Resistance Measurements .....	65
3.3.3 Transparency Measurements .....	66
3.4. Results .....	67
3.4.1 Effect of Density .....	68
3.4.2 Effect of Annealing Temperature .....	72
3.4.3 Effect of Annealing Time at 200°C .....	74
<b>4. UTILIZATION OF SILVER NANOWIRE NETWORKS AS ANODE IN ORGANIC LIGHT EMITTING DIODES</b> .....	<b>83</b>
4.1. Introduction .....	83
4.2 Characterization Methods .....	87
4.2.1 Atomic Force Microscopy (AFM) .....	87
4.2.2 Current-Voltage Measurements .....	87
4.2.3 Electroluminescence Measurements .....	87
4.3 Fabrication and Characterization of PLEDs .....	87
<b>5. STABILITY OF SILVER NANOWIRES</b> .....	<b>97</b>

5.1. Introduction .....	97
5.2 Corrosion of Bulk Silver .....	98
5.3 Characterization .....	105
5.4 Sample Preparation .....	105
5.5 Results .....	105
<b>6. SOL-GEL COATING OF NiO THIN FILMS ON SILVER NANOWIRE NETWORKS.....</b>	<b>119</b>
6.1. Introduction .....	119
6.2 Characterization .....	121
6.3. Experimental .....	122
6.3.1. Fabrication of Silver Nanowire Network Transparent Electrodes .....	122
6.3.2. Synthesis of Nickel Oxide.....	123
<b>7. CONCLUSIONS AND FUTURE RECOMMENDATIONS .....</b>	<b>135</b>
7.1. Conclusions .....	135
7.2. Future Recommendations.....	136
<b>REFERENCES.....</b>	<b>137</b>
<b>APPENDIX A: PERMISSION LICENSES.....</b>	<b>145</b>
<b>CIRCICULIM VITAE .....</b>	<b>151</b>

## LIST OF TABLES

Table 3. 1 Selected historical TCO references [47].	32
Table 3. 2. The comparison between ITO and other alternative transparent conductors [70].	62
Table 5.1 EDS results of as prepared silver nanowires.	110
Table 5.2 EDS results of corroded silver nanowires kept 6 months in ambient conditions.	111

## LIST OF FIGURES

Figure 2.1 Schematic presentation of Ag NW formation in AAO prepared by electroless deposition and thermal reduction. (a) The AAO membrane was fabricated by a two-step anodization process through pore widening. (b) Ripping the aluminum layer from AAO. (c) AgNO <sub>3</sub> was electroless deposited into the nanochannels of the AAO membrane. (d) The AAO membrane was dissolved by immersing into 0.2M NaOH for 1 h to separate the Ag NWs [33].	8
Figure 2.2 (a) SEM image of the AAO membrane fabricated by a second anodization process using a pore widening process for 2 h (pore size about 50 nm). (b) A cross-sectional image of the AAO membrane (pore size about 50 nm). (c) A cross-sectional image of AAO membrane (pore size about 10 nm) without applying the pore widening process. (d) After four hours of the pore widening process (pore size about 100 nm) [33].	9
Figure 2.3 Top view SEM image of Ag NW arrays grown on the surface of AAO membrane: (a) low magnification image, (b) high magnification image, SEM image of (c) and (d) silver nanowires after eliminating the AAO membrane in a NaOH solution [33].	11
Figure 2.4 TEM image of shape-separated Ag NWs synthesized through seed-mediated approach [40].	14
Figure 2.5 TEM micrographs of Ag NWs synthesized with 3 μL of NaOH added at magnifications of (a) 15 kX and (b) 100 kX [40].	15
Figure 2.6 TEM and SEM images of silver nanorods and nanowires prepared using a,b) 0.8 mM Na <sub>3</sub> C <sub>6</sub> H <sub>5</sub> O <sub>7</sub> and c,d) 1.2 mM Na <sub>3</sub> C <sub>6</sub> H <sub>5</sub> O <sub>7</sub> [41].	16
Figure 2.7 Schematic illustration of the experimental mechanisms to generate spherical, rod and wire-like nanoparticles [41].	17
Figure 2.8 Schematic illustration of the mechanism proposed to account for the growth of silver nanowires with pentagonal cross sections: (a) Evolution of a nanorod from a MTP of silver under the confinement of five twin planes and with the assistance of PVP. The ends of this nanorod are terminated by {111} facets, and the	

side surfaces are bounded by {100} facets. The strong interaction between PVP and the {100} facets is indicated with a dark-gray color, and the weak interaction with the {111} facets is marked by a light-blue color. The red lines on the end surfaces represent the twin boundaries that can serve as active sites for the addition of silver atoms. The plane marked in red shows one of the five twin planes that can serve as the internal confinement for the evolution of nanorods from MTP. (B) Schematic model illustrating the diffusion of silver atoms toward the two ends of a nanorod, with the side surfaces completely passivated by PVP. This drawing shows a projection perpendicular to one of the five side facets of a nanorod, and the arrows represent the diffusion fluxes of silver atoms [42]..... 18

Figure 2.9 Illustration of the proposed mechanism by which twinned decahedron was etched with the existence of O<sub>2</sub>/Cl and Ag NWs were obtained under argon protection [45]..... 19

Figure 2.10 The experimental setup for Ag NW synthesis by modified polyol process..... 22

Figure 2.11 Schematic representation for the formation of Ag NWs in modified polyol process. .... 23

Figure 2.12 Schematic representation of the passivation of (100) planes by PVP and further growth through active (111) planes..... 24

Figure 2.13 Schematic representation of a Ag NWs..... 24

Figure 2.14 Photographs of the synthesis solution showing its color change during the Ag NW synthesis..... 26

Figure 2.15 (a) Low and (b) high resolution SEM images of as synthesized Ag NWs using modified polyol process. .... 27

Figure 2.16 (a) and (b) TEM and (c) and (d) HRTEM images of as synthesized Ag NWs using modified polyol process. .... 27

Figure 2.17 XRD spectrum of Ag NWs (JCPDS Card No. 04-0783) synthesized using modified polyol process. .... 28

Figure 3.1 Different applications of TCCs..... 31

Figure 3.2 Energy consumption vs. year [51]..... 32

Figure 3.3 Electromagnetic spectrum of light [52]..... 34

Figure 3. 4 Representative set-up for 2-probe measurements [48]..... 36

Figure 3.5 Representative set up for 4-probe measurements [48]. .... 37

Figure 3.6 Schematic energy diagram of a metal [48].	38
Figure 3.7 UP-spectrum of Au surface [53].	39
Figure 3.8 (a) Top and (b) cross-sectional FESEM images of FTO thin films. (c) XRD pattern and (d) UV-visible transmission spectra of FTO thin films deposited at 420°C [57].	41
Figure 3.9 AFM phase images of PEDOT:PSS films with various solvent treatments. (a) Pristine PEDOT:PSS (PH1000) ( $\sigma < 1 \text{ S cm}^{-1}$ ). (b) PEDOT:PSS (PH 510) doped with DMSO 5 vol% ( $\sigma = 389 \text{ S cm}^{-1}$ ). (c) PEDOT:PSS (PH 1000) doped with EG 6 vol% ( $\sigma = 634 \text{ S cm}^{-1}$ ). (d) solvent post-treated PEDOT:PSS (PH 1000) doped with EG 6 vol% ( $\sigma = 1330 \text{ S cm}^{-1}$ ) [58].	42
Figure 3.10 (a) An optical image of mechanically exfoliated graphene flake [59]. (b) Schematic illustration of graphene synthesis by CVD method. (c) Graphene synthesized on nickel thin film; arrows indicate thin monolayer regions. (d) Monolayer graphene synthesized on copper foil and transferred onto a SiO <sub>2</sub> /Si substrate [60].	43
Figure 3.11 Sheet resistance vs. thickness graph for Pt films [61].	44
Figure 3.12 Transparency vs. thickness graph for Pt films [61].	45
Figure 3.13 (a) SEM image of as-fabricated metal electrodes. (b) Average transmittance versus sheet resistance of metal grids with a line width of 120 nm. Absolute value of the modeled optical electric field and power flow for light (600 nm wavelength) incident on a freestanding Ag grating (400 nm period, 40 nm line width, 100 nm high) for both (c) transverse magnetic (TM) and (d) transverse electric (TE) polarization. (e) Simulated transmittance versus wavelength for two modes. The AM 1.5 solar irradiance data (black line) are plotted for comparison [62].	46
Figure 3.14 SEM images of SWNT films deposited from 40 mL SWNT solutions of (a) 0.2 mg/L, (b) 1 mg/L and (c) 2 mg/L concentrations. (d) AFM image of the 1 mg/L SWCNT thin films showing a mixture of bundled and individual SWNTs [63].	47
Figure 3.15 Transmittance of films at three SWCNT concentrations [0.2 mg/L (a), 1 mg/L (b), and 2 mg/L (c)] and six different filtrate volumes. (d) Correlation between film transparency (represented by the transmittance at 550 nm) and sheet resistance. The continuous line is for visual aid. The arrow indicates the approximate position of the percolation threshold of the metallic tubes [63].	48

Figure 3. 16 Fabrication and characterization of Cu nanofibers. (a) Schematic of materials preparation method. Left column: Schematic of an electrospinning setup, shown without a syringe pump. Right column: the fabrication process of Cu nanofibers. In the first step, CuAc2/PVA composite fibers were prepared by electrospinning. In step 2, the fibers were calcinated in air to get CuO nanofibers. In step 3, the CuO nanofibers were reduced to Cu nanofibers by annealing in an H<sub>2</sub> atmosphere. (b) SEM image of Cu nanofibers synthesized by electrospinning. Scale bar is 10 μm. (c) SEM image showing the continuous structure of a Cu nanofiber, indicating a length that can easily exceed 100 μm. Scale bar) 20 μm. (d) Schematic of junctions between solution-processed Ag nanowires (upper) and electropsun Cu nanofibers (down). (e) AFM image of a junction between two nanofibers. The curved lines show the heights of two nanofibers and the cross junction, respectively. (f) Schematic of modified electrospinning setup, oriented nanofibers can be collected on the gaps between two parallel electrodes. (g, h) SEM images of Cu nanofibers with controlled orientations: (g) uniaxially aligned arrays, (h) patterned grids. Scale bar 20 μm [69]...... 49

Figure 3. 17 (a) Structure of the Cu mesh hybrid electrode. (b) and (c) AFM topography images of Cu thin films on polyimide substrates fabricated using a polycrystalline Cu target and a single-crystal Cu target, respectively. (d) and (e) AFM topography images of Cu mesh electrodes fabricated with wet etching using the two types of Cu thin films in (b) and (c), respectively. (f) Illustration and HRTEM image of the crosssectional structure of a Cu mesh hybrid electrode with Al-doped ZnO as the capping layer and polyimide as the polymer substrate [70].... 50

Figure 3.18 Schematics showing how 1D structures can provide suitable paths for charge transport..... 54

Figure 3.19 Graph of the sheet resistance versus volume of Ag NW solution. The onset of conduction across the sample occurs for V<sub>c</sub> = 0.2 mL. The power fit of the data indicated value of critical exponent α = 1.42. The inset shows the logarithmic plot of the data with a linear fit [73]. ..... 56

Figure 3. 20 (a) Photograph of Ag NW ink in ethanol. (b) Meyer rod coating setup for scalable Ag NW coating onto plastic substrates. (c) Finished Ag NW film coating on PET substrate. The Ag NW coating looks uniform over the entire substrate shown

in the figure. (d) A SEM image of Ag NW coating shown in panel (c). The sheet resistance was 50 $\Omega$ /sq [75].	57
Figure 3.21 SEM images of Ag NW films with different densities. The different densities of Ag NW films lead to different sheet resistances: (a) 100, (b and c) 50, and (d) 15 $\Omega$ /sq. The diameters of the Ag NWs are in the range of 40-100 nm [75].	58
Figure 3.22 Optical transmittance of Ag NW network electrodes compared to a commercial ITO thin film [75].	58
Figure 3.23 (a) Schematic representation of the transfer process. (b) Photograph of an Ag NW film transferred onto PET. (c) Photograph of a nanowire film on glass substrate. (d) Photograph of a nanowire film on PET showing the flexibility of film. (e) Photograph showing the results of adhesion tests. Nanowires remain adhered to the PET substrate when sticky tape was peeled off from the area shown by dotted lines. SEM images of the different regions of the film shown in Fig. 1(b), demonstrating uniformity of the film across the entire area [73].	59
Figure 3.24 Patterned transfer of Ag NW film. (a) Schematic diagram of the patterned PDMS stamp in contact with the nanowire film. (b) Photograph of patterned nanowire film transferred to the PET substrate. The size of each pixel is 1 mm $\times$ 1 mm. (c) SEM image showing the nanowire network in one pixel [73].	60
Figure 3.25 (a) Plot of sheet resistance versus transmittance at a wavelength of 550 nm of Ag NW networks. Black dots represent resistance values for films without annealing and red dots represent resistance values after annealing the film samples at 200 $^{\circ}$ C for 20 min in air. Inset shows the transmittance spectra of nanowire networks with different thicknesses. (b) SEM image of an annealed nanowire sample showing melting of nanowires at the ends and subsequent joining with neighboring nanowires. (c) Variation of sheet resistance with the annealing time for nanowire networks of different densities. Sheet resistance decreased initially on annealing and subsequently increased with further annealing. (d) SEM images of nanowire networks prepared using various amounts of nanowire solution. Nanowire density increases with increased volume of the solution [73].	61
Figure 3.26 Flow chart showing the nanowire purification and deposition of Ag NWs onto substrates [48].	63

Figure 3.27 Representative SEM image of Ag NW network and possible path for charge transport.....	64
Figure 3.28 Schematic of the two probe measurement set-up used for obtaining the sheet resistance values of Ag NW networks [48]. .....	66
Figure 3. 29 UV-VIS spectroscopy set-up for transparency measurements of Ag NW networks [48]. .....	67
Figure 3.30 SEM images of top view (a) and 35° inclined view (b) of Ag NW networks fabricated in this work. (c) Photograph of Ag NW networks on a glass substrate. (d) Length distribution of Ag NWs used for the fabrication of networks [76]......	68
Figure 3.31 SEM images of Ag NWs networks with different densities of (a) 0.28, (b) 0.34, (c) 0.44, (d) 0.50, (e) 0.59, (f) 0.70, (g) 0.82, (h) 0.98, (i) 1.35 and (j) 1.62 NW/ $\mu\text{m}^2$ . .....	70
Figure 3.32 Transmittance spectra of Ag NW networks with different densities [76]. Transmittance spectrum for a commercial ITO thin film is also provided for comparison. ....	71
Figure 3.33 Absorption spectra of Ag NW networks, SWCNT thin films and commercial ITO. ....	71
Figure 3.34 Change in transmittance of Ag NW networks at different nanowire densities. ....	72
Figure 3.35 SEM images of (a) as deposited, (b) 100, (c) 200, (d) 300°C annealed Ag NW networks (30 minutes) [76]. All scales are the same. ....	73
Figure 3.36 SEM images of Ag NW networks annealed at (a) 400 and (b) 500°C for 30 minutes [76]. Both scales are the same. ....	74
Figure 3.37 Sheet resistance versus transparency of as deposited and annealed (200 °C for 20 min.) Ag NWs networks [76]. ....	75
Figure 3.38 Sheet resistance versus transmittance of annealed Ag NW networks in comparison to various transparent electrodes reported in literature, modified from Ref. 77. ....	76
Figure 3.39 A literature comparison showing lowest sheet resistances versus transmittance at 550 nm of Ag NW networks reported by other groups [76]. ....	76
Figure 3.40 SEM images of Ag NW networks annealed at 200°C with different durations of (a) 30, (b) 60, (c) 120, (d) 180, (e) 240 and (f) 300 minutes [76]. ....	78

Figure 3.41 Change in sheet resistance of Ag NW networks annealed at 200°C with time [76].	79
Figure 3.42 Change in sheet resistance of an Ag NW network measured at 25 different spots on the sample [76].	80
Figure 3.43 Current stability of ITO and Ag NW networks [76].	81
Figure 4.1 Schematic of a typical MEH-PPV based PLED.	84
Figure 4.2 $I - V - L$ curves of PLEDs having a sandwich structure of AgNWs (or ITO) anode/PEDOT:PSS/SY-PPV/CsF/Al (a) and the luminous efficacy and current density graph of the fabricated devices (b) [79].	86
Figure 4.3 Top and cross-sectional SEM images of Ag NW networks on Si wafer. Both scales are the same [76].	88
Figure 4.4 AFM phase images of Ag NW networks that are (a) as coated, (b) pressed during annealing, (c) PEDOT:PSS/IPA spin coated at 2500 rpm, (d) 1500 rpm (e) 1000 rpm, (f) PEDOT:PSS spin coated at 2500 rpm, (g) 1500 rpm, (h) 1000 rpm, respectively [76].	90
Figure 4.5 AFM 3D images of Ag NW networks that are (a) as deposited, (b) pressed during annealing, (c) PEDOT:PSS/IPA spin coated at 2500 rpm, (d) 1500 rpm (e) 1000 rpm, (f) PEDOT:PSS spin coated at 2500 rpm, (g) 1500 rpm, (h) 1000 rpm, respectively [76].	91
Figure 4.6 RMS roughness change of different Ag NW network samples [76].	92
Figure 4.7 Schematic structure of PLED in which Ag NW networks were used as anode.	93
Figure 4.8 Corresponding band diagram of the fabricated PLED devices with both ITO and Ag NW network anodes.	93
Figure 4.9 Current-voltage (I-V) characteristics of the PLED devices fabricated in this work [76].	94
Figure 4.10 Electroluminescence characteristics of PLED device with ITO anode [76]. Inset shows a photo of emission.	95
Figure 4.11 Electroluminescence characteristics of PLED device with Ag NWs networks anode [76]. Inset shows a photo of emission.	96
Figure 5.1 Growth rates of Ag <sub>2</sub> S when exposed to various ambient sulfur-containing gases such as H <sub>2</sub> S, OCS, SO <sub>2</sub> and CS <sub>2</sub> [86].	98

Figure 5.2 Cross-sectional STEM and EDS mapping images of oxidized sample. (a–d) STEM images of a single Ag NW and stacked Ag NWs. EDS mapping images in (b) and (e) correspond to Ag atoms and those in (c) and (f) for O atoms. Dashed lines are guides for the eyes of pentagonal Ag NWs [87].....	99
Figure 5.3 TEM images of the same sample at different times after exposure to air under ambient conditions. (a) Sample just after synthesis. (b and c) TEM images of the sample after 3 weeks. TEM Images after (d) 4, (e) 5 (f) and 24 weeks [88]. ....	100
Figure 5.4 XPS spectra of sulfurized Ag NWs. (a) C 1s spectrum. (b) N 1s spectrum. (c) O 1s spectrum. (d) Ag 3d <sub>5/2</sub> and Ag 3d <sub>3/2</sub> spectra. (e) S 2p <sub>3/2</sub> and S 2p <sub>1/2</sub> spectra [88].....	101
Figure 5.5 Sheet resistance of the Ag NW electrodes as functions of the (a) thermal treatment temperature and (b) UV/O <sub>3</sub> treatment time [89].....	103
Figure 5.6 SEM images of the (a) pristine Ag NWs, (b) 30 minutes UV/O <sub>3</sub> -treated Ag NWs, (c) 60 minutes UV/O <sub>3</sub> -treated Ag NWs, and the Ag NWs thermally treated at (d) 160, (e) 190, and (f) 210 °C for 10 minutes [89].....	104
Figure 5.7 SEM images of Ag NW networks that are (a) as-prepared and kept in ambient conditions for 6 months (b), (c) and (d). ....	106
Figure 5.8 SEM image of Ag NW networks spin coated with PEDOT:PSS and kept under protective atmosphere for 1 month. ....	107
Figure 5.9 TEM images of various corroded Ag NWs with as formed nanoparticles on their lateral surfaces (a), (b), (c) and (d). ....	108
Figure 5.10 HRTEM images of (a) as-prepared and (b), (c) and (d) various corroded Ag NWs with as formed nanoparticles on their lateral surfaces.....	109
Figure 5.11 EDS analysis of a Ag NW in as-prepared condition. ....	110
Figure 5.12 EDS analysis of an Ag NW with nanoparticles on its lateral surfaces. ....	111
Figure 5.13 XRD spectrum of corroded Ag NWs. (JCPDS card no 04-0783 for pure Ag, 76-1393 for Ag <sub>2</sub> O and 65-2356 for Ag <sub>2</sub> S) .....	112
Figure 5.14 XPS survey spectrum of corroded Ag NWs.....	113
Figure 5.15 High-resolution XPS spectrum of Ag 3d.....	114
Figure 5.16 High-resolution XPS spectrum of C 1s. ....	114
Figure 5.17 High resolution XPS spectrum of O 1s. ....	115
Figure 5.18 High resolution XPS spectrum of S 2p.....	115

Figure 5.19 SEM images of Ag NWs kept in (a) DI water, (b) ethanol, (c) IPA and (d) chloroform at 4°C for 2 years. All scales are the same.....	116
Figure 5.20 SEM images of failed Ag NW networks under high current.....	117
Figure 5.21 Resistance change in Ag NW nanowire networks with increasing temperature. Inset show photograph of the measurement setup. ....	118
Figure 6.1 Schematic representation of the preparation of IZO / Ag NW nano composite [91].....	120
Figure 6.2 Tilted cross-sectional SEM image of transferred Ag NWs (a), a composite Ag NW/IZO film (b). ....	120
Figure 6.3 Image of spray deposition set-up for silver nanowire coating.....	122
Figure 6.4 (a) – (d) SEM images of silver nanowire based transparent conductors.	123
Figure 6.5 Flowchart showing sol preparation and spin coating procedure of NiO thin films [99]......	124
Figure 6.6 XRD pattern of a NiO thin film annealed at 500° C (JCPDS card no 47-1049) [99]......	124
Figure 6.7 (a) Top-view, (b) – (d) cross-sectional SEM images of NiO thin films on silicon substrates [99]......	125
Figure 6.8 SEM images of NiO thin films on silicon substrates annealed at different temperatures of (a) 400, (b) 450 and (c) 500 °C [99]......	126
Figure 6.9 Top-view SEM images of (a) bare Ag NWs networks, (b) 5, (c) 10 and (d) 15 times spin coated NiO thin films.....	127
Figure 6. 10 Cross-sectional SEM images of NiO coated Ag NWs from 2 different spots.....	127
Figure 6.11 SEM images of NiO / Ag NWs thin films on silicon substrates annealed at 500 °C in air atmosphere (a) 5x, (b) 10x and (c) 15x.....	128
Figure 6.12 SEM images of NiO/Ag NW nano composite films on Si substrates annealed at different temperatures with different coating cycles (a) 5 times, (b) 10 times, (c) 15 times at 400 °C , (d) 5 times, (e) 10 times, (f) 15 times 450 °C, (g) 5 times, (h) 10X times and (I) 15 times 500 °C under argon atmosphere.....	129
Figure 6. 13 SEM images of (a) 5, (b) 10 and (c) 15 times NiO deposited Ag NW networks after 4 months. Under ambient conditions. All scales are the same. ....	130
Figure 6. 14 Change in sheet resistance for NiO / Ag NW nano composites with the number of NiO deposition cycles.....	130

Figure 6.15 Change in sheet resistance for NiO / Ag NW nano composites with time. .....	131
Figure 6.16 Percent transmittance of NiO / Ag NW nano composites. ....	132
Figure 6.17 Percent absorbance of NiO / Ag NW nano composites.....	132
Figure 6.18 SEM images of (a) and (b) 5X (60 m) NiO deposited Ag NW networks after 18 months storage under ambient conditions. ....	133
Figure 6.19 SEM images of (a) (b) 10 times and NiO deposited Ag NW networks after 18 months under ambient conditions. ....	133
Figure 6.20 SEM images of (a) and (b) 15 times NiO deposited Ag NW networks after 18 months under ambient conditions. ....	134

## ABBREVIATION LIST

0D Zero dimensional  
1D One dimensional  
2D Two dimensional  
3D Three dimensional  
AAO Anodic aluminum oxide  
AFM Atomic force microscopy  
AgBr Silver bromide  
Ag NW Silver nanowire  
AgNO<sub>3</sub> Silver Nitrate  
AgS<sub>2</sub> Silver sulfate  
AOT Sodium bis(2-ethylhexyl) sulfosuccinate  
AZO Aluminum doped zinc oxide  
C<sub>6</sub>H<sub>8</sub>O<sub>6</sub> Ascorbic acid  
CNT Carbon Nanotube  
CO<sub>2</sub> Carbon dioxide  
CPD Contact Potential Difference  
CTAB Cetyl trimethylammonium bromide  
CuCl Copper (I) chloride  
CuCl<sub>2</sub> Copper (II) chloride  
CVD Chemical vapour deposition  
DC Direct current  
DI Deionized  
DNA Deoxyribonucleic acid  
EDS Energy dispersive X-ray spectroscopy  
EG Ethylene glycol  
EL Emissive layer

FCC Face centered cubic  
Fe(NO<sub>3</sub>) Iron nitrate  
FE-SEM Field emission scanning electron microscopy  
FTO Fluorine doped indium tin oxide  
GZO Gallium doped zinc oxide  
H<sub>2</sub>S Hydrogen sulfide  
HIL Hole Injection layer  
HRTEM High-resolution transmission electron microscopy  
HTL Hole transport layer  
HOMO Highest occupied molecular orbital  
In<sub>2</sub>O<sub>3</sub> Indium (III) oxide  
IR Infrared  
IPA 2-propanol  
ITO Indium tin oxide  
IZO Indium doped zinc oxide  
KP Kelvin probe  
LCD Liquid crystal display  
LED Light emitting diode  
MEA Monoethanolamine  
MEH-PVV Poly[2-methoxy-5-(2-ethylhexyloxy)-1,4-phenylenevinylene]  
MTP Multiple twin particle  
MWCNT Multi-walled carbon nanotubes  
Na<sub>3</sub>C<sub>6</sub>H<sub>5</sub>O<sub>7</sub> trisodium citrate  
NaCl Sodium Chloride  
NaOH Sodium hydroxide  
NiO Nickel oxide  
Ni(CH<sub>3</sub>COO)<sub>2</sub>·4H<sub>2</sub>O Nickel acetate  
NP Nanoparticle  
OCS carbonyl sulfide  
OLED Organic light emitting diodes  
OPV Organic photovoltaic  
PET polyethylene terephthalate  
PEDOT:PSS Poly(3,4-ethylenedioxythiophene) poly(styrenesulfonate)

PDMS Polydimethylsiloxane  
PLED Polymer light emitting diode  
PVA Poly(vinyl acetate)  
PVP Poly(vinylpyrrolidone)  
RPM Root mean square  
SEM Scanning electron microscopy  
SDSN sodium dodecylsulfonate  
SnO<sub>2</sub> Tin (IV) oxide  
STEM Scanning transmission electron microscopy  
SWCNT Single-walled carbon nanotube  
TE Transverse electric  
TEM Transmission electron microscopy  
TCC Transparent and conducting contact  
TCO Transparent and conducting oxide  
THz Terahertz  
TM Transverse magnetic  
UV Ultraviolet  
UV-VIS Ultraviolet–visible spectroscopy  
UPS Ultraviolet photoelectron spectroscopy  
VLS Vapor-liquid-solid technique  
XRD X-ray diffraction  
XPS X-ray photoelectron spectroscopy

# **CHAPTER 1**

## **INTRODUCTION**

Recently, population of the world in conjunction with accessibility of the people to technology and electronic devices showed a considerable increase. In parallel the diversity and the use of these electronic devices gradually increased the world's energy demand gradually. However, the current and major fossil based energy sources are limited. In addition, pollution of earth by the waste of fossil based energy sources is another problem. Many research projects focus on new, clean and renewable energy sources such as wind, wave and solar. When one looks at the new renewable energy sources, solar cell technology stands out as the most promising one due to its ability to directly convert sunlight into electricity. Moreover, solar cells do not require complex or moving parts unlike wind turbines. In addition to new clean energy sources as stated above, there are also developments in decreasing the energy consumption of the existing devices. Organic light emitting diodes (OLEDs) and smart windows are the two common examples for energy efficient devices. Currently, OLEDs are used in televisions, monitors, cell phones and even in buildings for lighting purposes. OLEDs convert almost all of the supplied electricity into light, while for halogen lamps this conversion is only around 5%, remainder is emitted as heat. Smart windows decrease the use of air conditioners by blocking infrared (IR) portion of sunlight, which corresponds to nearly half of the energy provided by the sunlight.

These new technologies would take place in our life only when they are produced abundantly and economically. In order to produce these devices abundantly, each component that form the device should be cheap. One of the most widely used

components in thin film and third generation solar cells, OLEDs and smart windows is transparent and conducting contacts (TCCs) or alternatively transparent conducting oxides (TCOs). A TCC takes place on top of a solar cell and used for charge collection. Since it is transparent, it does not prevent sunlight reaching the photoactive layer of the solar cell and since it is conducting, it can effectively collect charges. The most widely used and commercial TCC is indium tin oxide (ITO). ITO based TCCs have been widely used not only in solar cells and OLEDs, but also in touch screens and smart windows. New device architectures increase the demand on TCCs and require even higher performance and especially mechanical flexibility. Moreover, due to its crystalline structure ITO's flexibility is very limited. It seems that ITO will not be able to meet the flexibility requirements of flexible electronics. At this point, ITO starts to fail. Moreover, indium sources are limited and therefore its price is gradually increasing. Its price in the market almost tripled in the last five years. In addition, in order to deposit ITO thin films with high transparency and low sheet resistance, vacuum processes and complex fabrication set-ups such as radio frequency-sputtering (RF) are required.

Due to the reasons listed above, scientist started to develop new TCCs that possibly replace ITO. Primary requirement is that they should be produced in large scale. Firstly, other metal-based doped oxides were investigated. Aluminum doped zinc oxide (AZO), fluorine doped tin oxide (FTO) are a few examples of such systems. However, they showed similar properties with ITO and so suffered from discussed issues. Single-walled carbon nanotube (SWCNT) thin films were then introduced as alternatives to TCCs. However, due to very high tube-to-tube contact resistance of SWCNTs, the electrical properties of SWCNT thin films were found to be inferior that of ITO. Moreover, since SWCNT thin films contain metallic and semiconducting tubes as a mixture, the semiconducting ones create Schottky junctions and deteriorate conduction. Recently, graphene started to be investigated as another alternative and showed promising results, especially in sheet resistance values. However, its electrical properties must be further enhanced for current driven devices, such as solar cells. Besides these alternatives, random networks of metallic nanowires are also realized as TCCs. Random networks of silver nanowires (Ag

NWs), in particular, showed optical and electrical properties that are comparable to that of commercially available ITO.

Nanotechnology made it possible to produce materials at nano-scale. Interestingly, materials at nano-scale showed unprecedented properties different than their bulk counterparts. These new properties enabled nanomaterials to find new application areas. A material can be formed into a nanostructure by two different approaches. The first one is the “top-down” approach. In this technique, one starts with a bulk material and reduces its size to reach below the “nano” size. Top-down approach results in nanomaterials with artifacts and poor surface quality. The second approach is the “bottom-up approach”. This approach is based on the assembly of atoms one-by-one to form the nanostructured material. Nanostructured materials are divided into four groups according to their dimensionality. These are zero dimensional (0-D) quantum dots, one dimensional (1-D) nanowires, two dimensional (2-D) nano sheets and three dimensional (3D) nanoparticles. Nanowires are 1-D nanomaterials and their diameter is generally lower than 100 nm. They have micron scale lengths; therefore, their aspect ratio is very high. Ag NWs have received much attention especially in the last decade due to the unique properties of bulk silver, such as the highest electrical conductivity among other metals and highest thermal conductivity among all types of materials. Nanowire form of Ag possesses unique electrical and optical properties besides its inherited properties from the bulk.

So far, many different techniques have been developed for the synthesis of Ag NWs. For instance, Vapor-Liquid-Solid (VLS) growth technique can be used for their synthesis. VLS technique was widely used to grow metallic and semiconducting nanowires or nanotubes due to its ability to synthesize highly pure and crystalline nanostructures. However, catalyst contamination and high cost equipment limit the scope of this method [1]. Alternative Ag NW synthesis techniques can be divided into template-directed and template-free subgroups. Template-directed synthesis of nanowires involves chemical or electrochemical deposition of silver metal within the channels of nanoporous membranes [2]. Various templates made of both hard and soft materials were investigated for the synthesis of nanowires. Investigated hard templates include porous anodic alumina [3] or track-etched polycarbonate [4], pores

within zeolite [5] or mesoporous silica [6], CNTs [7] and steps or edges supported on solid substrates [8]. Although these templates were effective in fabricating nanowires with uniform and controllable dimensions, most of them needed to be selectively etched under harsh conditions in order to obtain nanowires. Alternatively, soft templates can be used. Soft templates used in literature include poly vinyl alcohol (PVA) [9], deoxyribonucleic acid chains (DNA) [10], self-assembled copolymers [11], cetyl trimethylammonium bromide (CTAB) [12], sodium bis(2-ethylhexyl) sulfosuccinate (AOT) /p-xylene/water [13] arrays of calix (4)hydroquinone nanotubes [14]. In general, limitation of the nanowire diameter by the pore size of the template, limited amount of pores and usually high cost of the template are the disadvantages of these template based methods. Several direct chemical or electrochemical template-free synthesis techniques of Ag NWs were developed as alternatives. With the help of a developer by reducing silver nitrate ( $\text{AgNO}_3$ ) and using silver bromide (AgBr) nanocrystals, Ag NWs were synthesized (24). Ultraviolet (UV) irradiation or electroreduction in aqueous solution are other template free methods. However, low yield, irregular morphology, polycrystallinity and low aspect ratio of the obtained nanowires are the main disadvantages of these template free methods.

On the other hand, so called Polyol process, which deprived all these disadvantages, stands as an alternative method for the synthesis of Ag NWs. Polyol process seems to be the most suitable and feasible method for the mass production of Ag NWs. It is also convenient and highly efficient when compared to other techniques discussed above. Polyol process is based on the reduction of metallic salts by polyols at elevated temperatures and controlled nucleation followed by 1D growth of metallic nanowires with the help of a surfactant. This solution based synthesis method was first introduced by Fievet and co-workers for the synthesis of colloidal particles of metals and alloys such as silver (Ag), gold (Au), copper (Cu), cobalt (Co), palladium (Pd), iridium (Ir), platinum (Pt), ruthenium (Ru), cobalt nickel alloy (CoNi) and iron nickel alloy (FeNi) [15]. Basically, this process starts with the reduction of an inorganic salt by a solvent at an elevated temperature. Then, continued addition of a stabilizer polymer prevents the agglomeration of the colloidal particles. Since the polyols can dissolve many inorganic salts and that they have highly temperature

dependent reducing ability, they become very popular for the synthesis of metal colloidal particles [16]. Later on, Xia and co-workers developed a suitable polyol process for the shape controlled synthesis of Ag nanostructures [17]. In this method, ethylene glycol (EG) was used both as a solvent and reducing agent, poly(vinylpyrrolidone) (PVP) was used as a stabilizing agent and  $\text{AgNO}_3$  was used as the Ag source. Following the synthesis, Ag NWs are purified via centrifugation. Optical polarizers [18], photonic crystals [19], catalysts [20], surface enhanced Raman spectroscopy [21] are only a few application areas of Ag NWs. Recently, a new application of Ag NWs has also been demonstrated, in which the nanowires are used to fabricate TCCs. Since Ag NWs are long, they can percolate and provide a suitable path for charge transport and their small enough diameter makes these networks transparent in the visible portion of the electromagnetic spectrum (wavelengths between 400nm and 700 nm). In this thesis, firstly (Chapter 2) classical polyol process was modified in order to obtain silver nanowires in a larger scale. Then, Fabrication of TCEs using as synthesized Ag NWs was investigated (Chapter 3). Effect of Ag NWs density, annealing temperature and time were investigated on opto-electronic properties of Ag NWs based transparent conductors with optimum visible transparency and sheet resistance combination. In the following part of the thesis, (Chapter 4), in order to investigate the performance of fabricated transparent and conducting Ag NW networks they are used as anode to fabricate a PLED. In the fifth chapter (Chapter 5), stability of Ag NWs was investigated. Effect of ambient conditions, solvent type and direct current (DC) on morphology and structure of Ag Nws. In the final part of the thesis (Chapter 6) effect of sol-gel coated nickel oxide thin films on opto-electronic properties of Ag NWs networks were investigated.

## **DISSERTATION OBJECTIVES**

The limitations of ITO have motivated a search to find a flexible and low cost alternative that can be deposited via simple, solution based deposition methods. According to recent studies, Ag NWs based transparent conductors show comparable transmittance and sheet resistance behavior to that of ITO. On the other hand, there are no systematic studies on the parameters affecting opto-electronic properties of Ag NWs based transparent conductors. The aim of this dissertation is to investigate opto-electronic properties of Ag NWs based transparent conductors and their demonstration in polymer light emitting diode (PLED) devices as anode. In addition, stability of Ag NWs based transparent conductors and compatibility with NiO thin films were also investigated.

Six specific chapters address these questions with the following objectives:

1. To synthesize Ag NWs in large scale via modified polyol process (Chapter 2),
2. To fabricate transparent and conducting Ag NW network based electrodes (Chapter 3),
3. To investigate effect of parameters on the opto-electronic properties of Ag NW based transparent electrodes (Chapter 3),
4. To utilize Ag NW network based transparent electrodes in PLEDs as anode (Chapter 4),
5. To investigate ambient stability of Ag NW networks (Chapter 5 ),
6. To investigate opto-electronic behaviors of sol-gel coated nickel oxide (NiO) thin films on Ag NW networks (Chapter 6).

## CHAPTER 2

### SYNTHESIS OF SILVER NANOWIRES

#### 2.1. Introduction

Metallic nanowires can be synthesized via various techniques that are demonstrated in literature. Vapor-Liquid-Solid (VLS) based methods are one of the first approaches to fabricate nanowires. VLS technique was widely used to grow metallic and semiconducting nanowires due to its ability to synthesize highly pure and crystalline nanostructures. However, catalyst contamination and high cost equipment limit the scope of this method. Then, chemical based methods were offered. Synthesis of metallic nanowires via chemical reduction of precursors can be classified mainly two groups as templated and template-free routes. Firstly, templated methods were applied for the fabrication of metallic nanowires. Templated fabrication of metallic nanowires is based on the electrochemical reduction of the metal ions inside the nano-pore channels of an insulating membrane which is fabricated via self-assembly methods. On the other hand, template-free methods for the synthesis of metallic nanowires are based on reduction of silver ions in well-designed conditions and obtaining anisotropic growth with the help of a suitable capping agent.

#### 2.2. Templated Methods

So far, via utilization of template-based routes, Ag NWs were fabricated successfully using porous hard templates such as nanoporous materials [22-24], polymeric templates [25-28], biomolecules [29-31], or carbon nanotubes [32]. This type of approach provides one of the most straightforward methods of guiding the growth of

silver nanocrystals into nanowires either in cylindrical nanochannels or in a tubular one dimensional objects. Although nanowires of silver and other metals can be fabricated with the assistance of templates listed above, the preparation and removal of templates are costly and the quality of the resulting metallic nanowires, in terms of crystallinity and surface smoothness make them not suitable to be used in optoelectronic applications. In addition, the low yields of Ag NWs with an irregular morphology and low aspect ratio have limited their large-scale production with this method. Furthermore, to obtain the nanowires, the templates need to be fabricated before the synthesis of nanowires and removed selectively (by chemical etching or calcination) in a post-synthesis process to obtain the nanowires. Purification of nanowires is a time-consuming and high-cost process since the templates can only be used once in these nanowire fabrication methods.

Kim et al. showed fabrication of Ag NWs within the nano cylindrical channels of anodic aluminum oxide (AAO) [33]. Figure 2.1 shows schematic diagrams of Ag NWs formation in the AAO membrane via the electroless and thermal reduction process. Figure 2.1 (c) shows the steps of electroless deposition performed by dropping an aqueous solution of 0.1M silver nitrate ( $\text{AgNO}_3$ ) into nanochannels and thermally reduced by increasing the temperature to  $350^\circ\text{C}$ , and silver nanowires were separated by immersing the sample in a sodium hydroxide ( $\text{NaOH}$ ) solution.

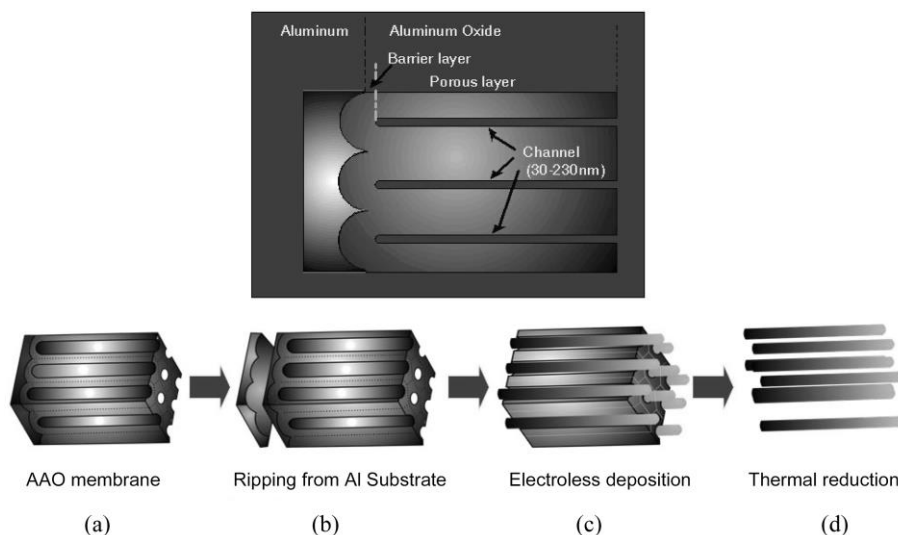


**Figure 2.1** Schematic presentation of Ag NW formation in AAO prepared by electroless deposition and thermal reduction. (a) The AAO membrane was fabricated by a two-step anodization process through pore widening. (b) Ripping the aluminum

layer from AAO. (c)  $\text{AgNO}_3$  was electroless deposited into the nanochannels of the AAO membrane. (d) The AAO membrane was dissolved by immersing into 0.2M NaOH for 1 h to separate the Ag NWs [33].

Figure 2.2 shows scanning electron microscopy (SEM) images of the surface of the AAO membrane after the second anodization process. The thickness and pore size of the AAO can be controlled by changing the concentration of electrolytes, the time of anodic oxidation, time of pore widening, and other conditions. A self-ordered AAO membrane has around 50 nm pores as shown in Figure 2.2(a). The nanopores exhibit almost perfect two-dimensional arrays with a hexagonal pattern. Hexagonal patterns are more apparent if the pore size is larger than 80 nm. In this image, it could be confirmed that around 50 nm nanopores can be prepared by immersing the sample in a 0.1 M phosphoric acid solution at  $60^\circ\text{C}$  for 2 hours. Figure 2.2 (b) shows that the nanochannels can be comparatively homogeneous without distorting the structure, resulting in them being highly oriented in one direction with a large aspect ratio. Figure 2.2 (c) shows a cross-sectional image of a sample prior to the pore widening process. In the sample, the distance among the pores is around 100 nm with a pore size of 10 nm. Figure 2.2 (d) shows the pore sizes around of 100 nm following the widening process for 4 hours is provided.

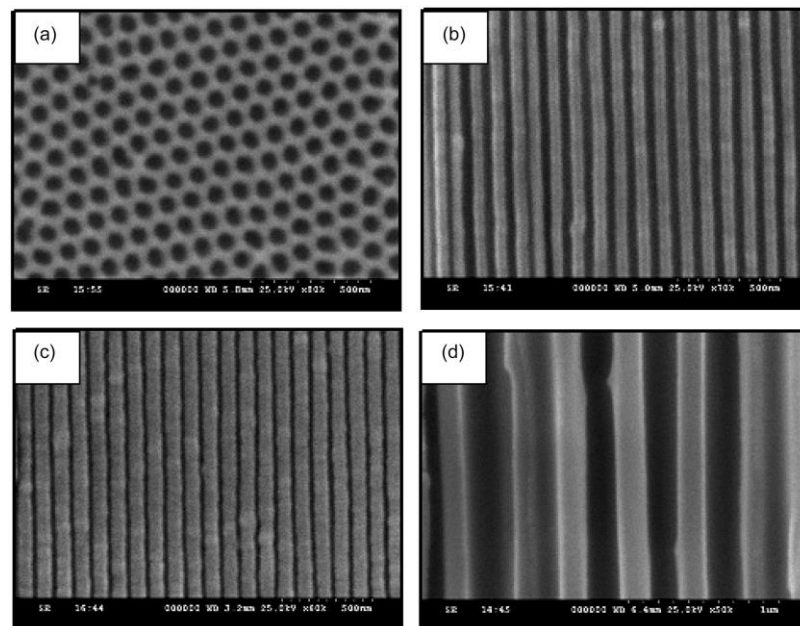


**Figure 2.2** (a) SEM image of the AAO membrane fabricated by a second anodization process using a pore widening process for 2 h (pore size about 50 nm).

(b) A cross-sectional image of the AAO membrane (pore size about 50 nm). (c) A cross-sectional image of AAO membrane (pore size about 10 nm) without applying the pore widening process. (d) After four hours of the pore widening process (pore size about 100 nm) [33].

Figure 2.3 shows SEM images of Ag NWs on the AAO membrane. In electroless deposition, 0.1 M AgNO<sub>3</sub> solution was directly dropped into the AAO membrane. The nanopores have a strong capillary force when the Ag solution is deposited onto the surface resulting in spontaneous ion movement into the nanochannels. When Ag<sup>+</sup> ions were dissolved in the aqueous solution, the surface tension of this solution is smaller than that of pure water droplets. Consequently, the Ag<sup>+</sup> solution has a smaller wetting angle than the water itself. Even though the nanochannels have a strong capillary force, the intermolecular interactions between the alumina surface and Ag<sup>+</sup> solution are of an immiscible phase resulting in strong surface tensions. Generally, the oxide surfaces show hydrophobic properties and repel water droplets minimizing the surface tension. To improve the final density of the Ag NWs, the AAO membrane was immersed in a 0.1 M AgNO<sub>3</sub> solution under ultrasonic agitation for 1 min to eradicate the air bubbles in the nanopores. This step is quite significant for the fabrication of high quality nanowires. Figure 3 (a-b) shows the SEM images of an AAO membrane surface after thermal reduction at 350°C for 1 h. It seems that Ag NWs were coalesced on the surface of AAO because the gravity of the metal silver is 10.5. The Ag NWs are sufficiently small after being thermally reduced and can be easily melted because their high surface area, even though the melting point of silver is 961°C.

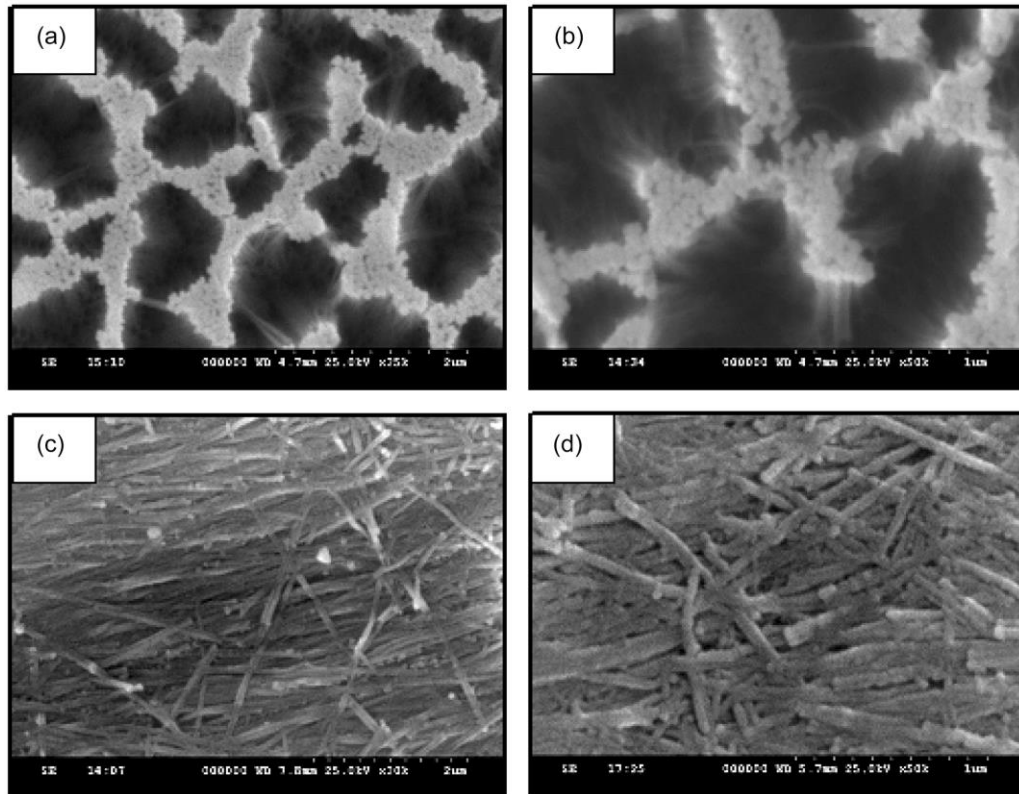


**Figure 2.3** Top view SEM image of Ag NW arrays grown on the surface of AAO membrane: (a) low magnification image, (b) high magnification image, SEM image of (c) and (d) silver nanowires after eliminating the AAO membrane in a NaOH solution [33].

### 2.3. Template-Free Methods

Basically, the template-free methods are simpler and less expensive compared to template-based methods, since they do not require hard or soft templates or any post treatment processes for the template removal. Instead, nanostructures grow from nanoparticles that were either homogeneously or inhomogeneously nucleated.

#### 2.3.1. Polyol Process

In the one-pot reduction route, silver precursors are added slowly to reaction systems generally using syringe pumps. At the initial stage of the reaction, the Ag atoms are

generated and condense into nuclei with the appropriate crystalline structures to serve as seeds for the further deposition of Ag atoms in a continuous reaction. This leads to the growth of Ag NWs. On the other hand, with the anisotropic growth directed by a surfactant using polyol both as a reductant and solvent, nanoparticles were generated by the reduction of precursors. With this method, many types of Ag precursors can be used to synthesize Ag NWs. The polyol method is the most popular method for preparation of Ag NWs with a uniform size and morphology. For example, Sun et al. reported the polyol reduction of  $\text{AgNO}_3$  with the assistance of polymeric surfactants, such as poly(vinylpyrrolidone) (PVP) in the presence of Pt seeds, which is one of the most successful fabrication routes for the synthesis of high quality Ag NWs in large quantities [34]. According to this method, ethylene glycol (EG) was used as a reduction agent and solvent to fabricate AG NWs with a well-controlled morphology and uniform size in the presence of PVP. In addition, exterior Pt nanoparticles serve as crystal seeds for the crystallization of silver atoms at the initial stage. The characteristic results of the Ag NWs grown through the polyol process suggests that each nanowire is grown from a decahedral seed with the assistance of PVP. Silvert et al. proposed the following mechanism for this method: each Ag decahedral particle with five-fold multiple twinned structures has fivefold symmetry with its surfaces bounded by ten facets [35].

Among all synthesis methods of 1D silver nanostructures, solution based polyol process is the most effective one in terms of its cost and simplicity. In addition, polyol process is also the most promising method for the large-scale synthesis of Ag NWs. Moreover, commercially available Ag NWs were also synthesized via polyol process (Cambrios, Bluenano etc.).

### **2.3.2. History and Development of Polyol Process**

As it was discussed in previous chapter, polyol process was first introduced by Fievet and co-workers the synthesis of colloidal particles of various metals and alloys [36]. This approach is based on reduction of an inorganic salt by a solvent at an elevated temperature. Then, continued addition of a stabilizer polymer prevents the

agglomeration of the colloidal particles. Since the polyols can dissolve many inorganic salts and have a highly temperature dependent reducing ability, they become very popular for the synthesis of colloidal metal particles [37]. In particular, the temperature dependent reducibility of this process makes it suitable over a broad range of size and shape. In polyol process, one can easily control the nucleation and growth stages via temperature. In addition, some more reactive and less reducible metals such as Ni, Cd, Co, Pb and Bi can be reduced by high boiling point solvents [38]. In 2002, Xia and co-workers developed a suitable polyol process for the shape controlled synthesis of Ag nanostructures [39].

Although polyol synthesis of Ag NWs seems to be very clear and straightforward, several modifications were investigated. Manipulation of process parameters or addition of different reagents resulted in the synthesis Ag NWs with different sizes and morphologies.

### **2.3.3. Seed-mediated growth approach**

Murphy et al. firstly reported the synthesis of Ag NWs with uniform diameter by seed-mediated growth approach in a rod-like micellar media [40]. Two steps were needed in order to achieve the formation of Ag NWs. Firstly, silver nanoseeds with an average diameter of 4 nm were prepared by chemical reduction of  $\text{AgNO}_3$  by sodium borohydride ( $\text{NaBH}_4$ ) in the presence of trisodium citrate ( $\text{Na}_3\text{C}_6\text{H}_5\text{O}_7$ ). Then  $\text{AgNO}_3$  was reduced by ascorbic acid ( $\text{C}_6\text{H}_8\text{O}_6$ ) in the presence of silver seeds obtained in the first step. Then micellar template cetyltrimethylammonium bromide (CTAB), and NaOH were used in order to synthesize the nanorods and nanowires with various aspect ratios. This seed-mediated growth approach is capable of synthesizing Ag NWs with different aspect ratios. However, it was always a great challenge to achieve precise control over the length and width of Ag nanorods and nanowires. At the same time, silver nanorods and nanowires with pentagonal cross-sections have been proposed to initiate from the evolvment of decahedra. Figure 2.4 shows TEM image of Ag NWs synthesized by seed-mediated polyol process.



**Figure 2.4** TEM image of shape-separated Ag NWs synthesized through seed-mediated approach [40].

#### **2.3.4. Seedless and surfactantless wet chemical synthesis**

Most of the Ag NW synthesis procedures use surfactants or stabilizing polymers. Then, multiple washing or centrifuging steps are needed for the removal of these agents from the surfaces of the nanowires. In some applications, for example sensing, the surface-bound residuals, which remain from the synthesis, increases the difficulty of modification of surface chemistry. Murphy and co-workers reported a method to synthesize crystalline Ag NWs in water without adding seed crystallites. Furthermore, they did not use any surfactant or polymer to direct the nanoparticle growth. [40]. They reduced  $\text{AgNO}_3$  to metallic silver at 100 °C by sodium citrate in

the presence of NaOH. In this process, hydroxide ion concentration was an important factor in determining the morphology of the final product. As synthesized Ag NWs were up to 12  $\mu\text{m}$  in length. The citrate has multiple tasks in this process. It not only strongly form complexes with the silver ions but also responsible for the reduction to metallic silver and acts as a capping agent to the silver metal. Although only small amount of hydroxide exists in the reaction solution and hydroxides usually form weak complexes with the silver ions, it is enough to interfere with the capping ability of citrate and lead to the formation of Ag NWs. Figure 2.5 shows TEM images of Ag NWs synthesized using seedless and surfactantless method. However, due to absence of surfactant and agglomeration problem is a deficiency of this approach.

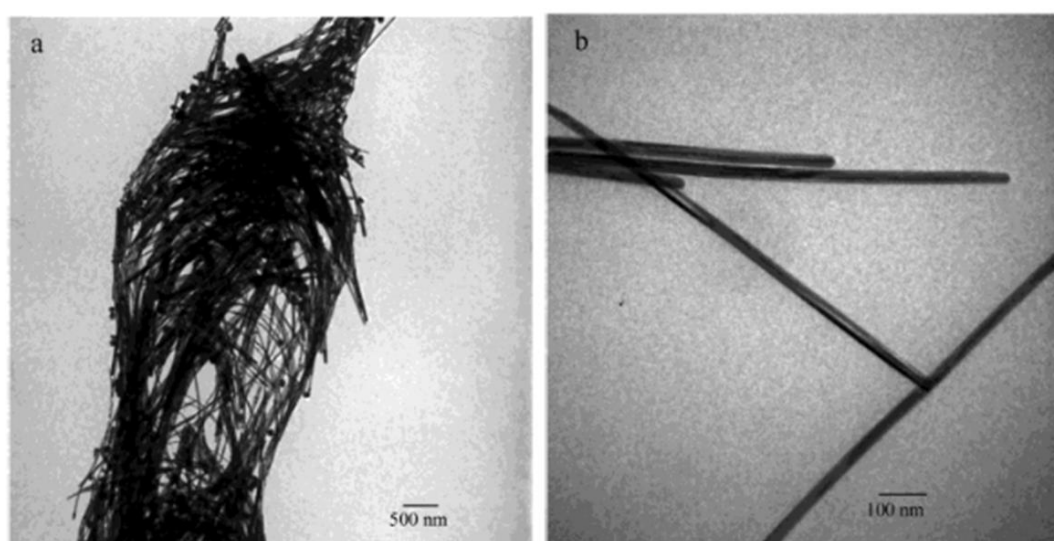
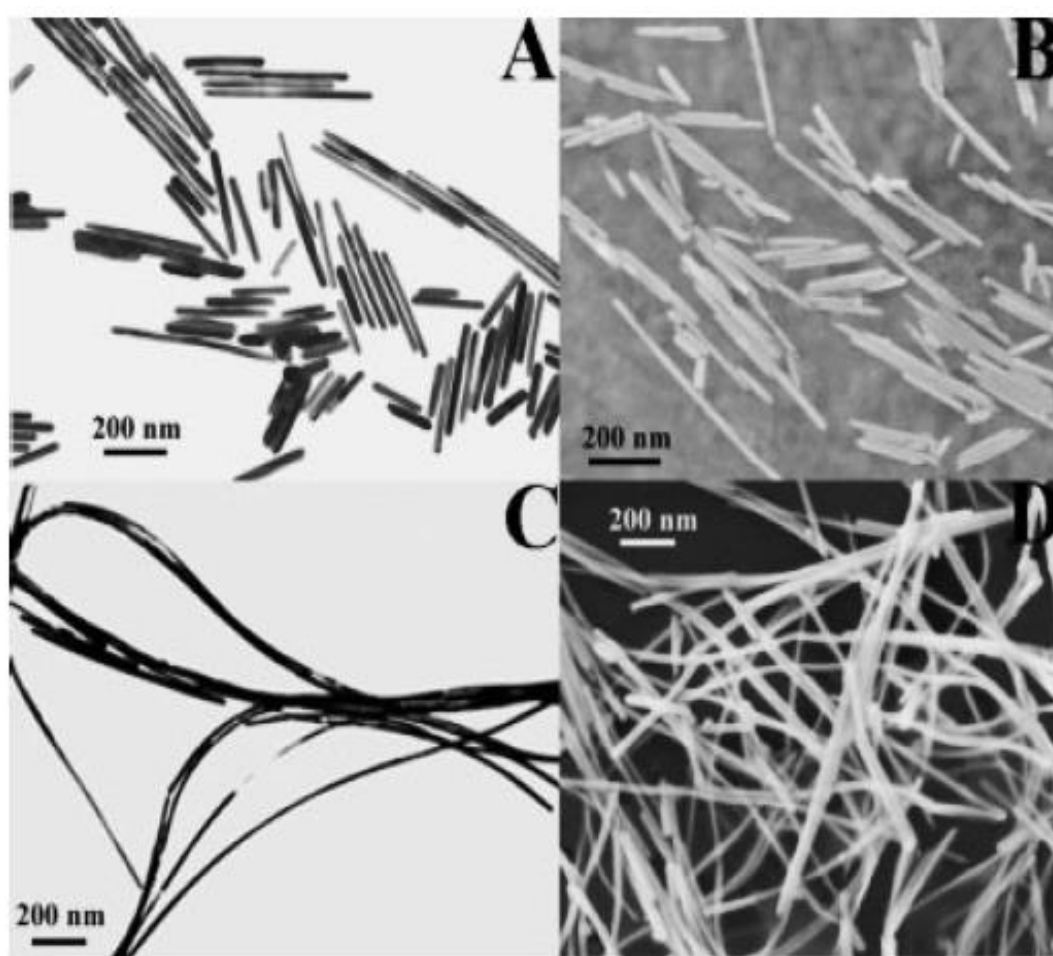


**Figure 2.5** TEM micrographs of Ag NWs synthesized with 3  $\mu\text{L}$  of NaOH added at magnifications of (a) 15 kX and (b) 100 kX [40].

### 2.3.5. Seedless and surfactant assisted synthesis

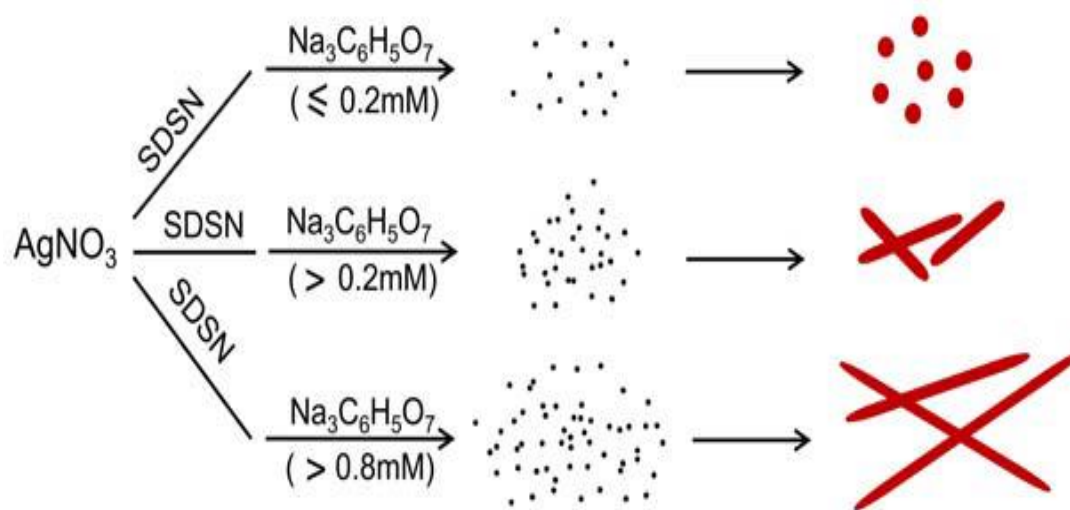
Moreover, due to limitations of surfactantless approach such as inability to precisely control the dimensions and morphologies of the product, this method was not preferred. Tian et al. demonstrated a seedless surfactant assistant process to synthesize high-quality Ag nanorods and nanowires in large quantities [41]. In this method,  $\text{AgNO}_3$  is reduced by trisodium citrate ( $\text{Na}_3\text{C}_6\text{H}_5\text{O}_7$ ) in the presence of sodium dodecylsulfonate (SDSN). Tri-sodium citrate plays an important role, and SDSN only has an assisting role as a capping agent in the formation of Ag NWs. The actual concentration of SDSN used in the experiment was only 1 mM, which was far

lower than the critical concentration for the formation of spherical micelles (9.7 mM, 40 °C). Especially, the critical concentration of the micelle formation for SDSN increases with temperature. So there are no SDSN micelles formed to serve as a soft template during the entire nanostructure forming process. The diameters and aspect ratios of Ag NWs or nanorods can be controlled by changing the concentration of trisodium citrate. However, it does not mean that SDSN is unnecessary for the formation of nanorods or nanowires. Ag NWs cannot be formed under too low or too high concentrations of SDSN. The key to form Ag NWs is to precisely control the trisodium citrate concentration for a fixed SDSN concentration.



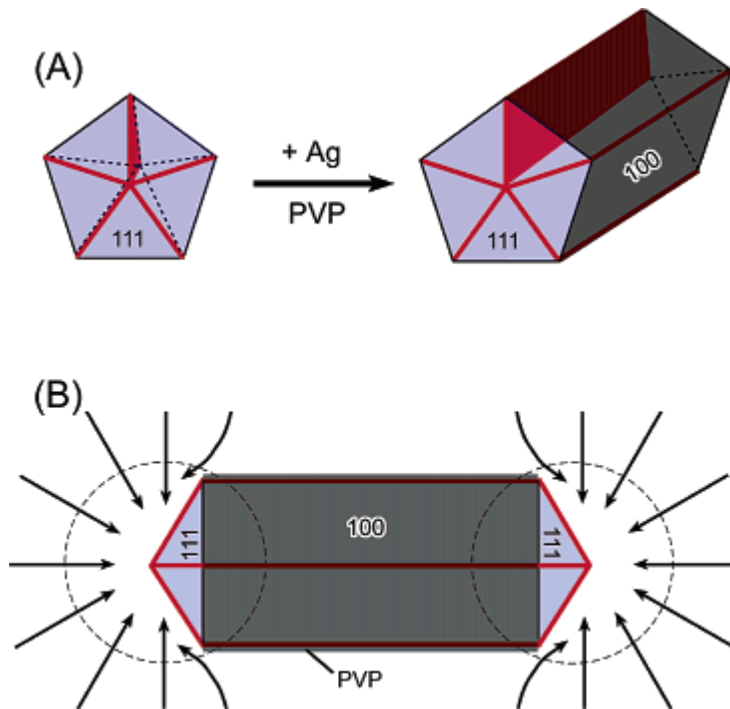
**Figure 2.6** TEM and SEM images of silver nanorods and nanowires prepared using a,b) 0.8 mM  $\text{Na}_3\text{C}_6\text{H}_5\text{O}_7$  and c,d) 1.2 mM  $\text{Na}_3\text{C}_6\text{H}_5\text{O}_7$  [41].

Figure 2.7 shows the proposed schematic for the growth of Ag nanorods and nanowires. At a lower concentration of tri-sodium citrate below 0.2 mM, Ag monomer concentration favors the formation of nanospheres according to Ostwald ripening and small particles dissolve into the solution and deposit onto large particles. At a higher concentration of tri-sodium citrate beyond 0.2 mM, large quantity of monomers is produced in the solution and the growth mode is diffusion-controlled. It is well documented that the activation energy of the (110) facet is lower than that of (100) and (111) owing to the relatively high surface free energies of a face centered cubic (FCC) structured metal particle. Therefore, monomer particles grow up along  $\langle 110 \rangle$  directions owing to the strong bonding abilities and chemical reactivities of (110) facet. Thus, nanorods are obtained. At higher concentration tri-sodium citrate ( $>0.8$  mM), nanowires with smaller diameter and higher aspect ratio can be formed because of the higher Ag monomer concentration and high velocity of crystal growth.



**Figure 2.7** Schematic illustration of the experimental mechanisms to generate spherical, rod and wire-like nanoparticles [41].

Figure 2.8 (a) shows a schematic illustration for the evolution of Ag NWs from multiple twin particles (MTPs). Since PVP molecules cover and passivate (100) surfaces of Ag MTPs, newly reduced Ag atoms are added into active (111) planes. Figure 2.8 (s) shows how Ag atoms diffuse into (111) planes of the Ag NWs.



**Figure 2.8** Schematic illustration of the mechanism proposed to account for the growth of silver nanowires with pentagonal cross sections: (a) Evolution of a nanorod from a MTP of silver under the confinement of five twin planes and with the assistance of PVP. The ends of this nanorod are terminated by  $\{111\}$  facets, and the side surfaces are bounded by  $\{100\}$  facets. The strong interaction between PVP and the  $\{100\}$  facets is indicated with a dark-gray color, and the weak interaction with the  $\{111\}$  facets is marked by a light-blue color. The red lines on the end surfaces represent the twin boundaries that can serve as active sites for the addition of silver atoms. The plane marked in red shows one of the five twin planes that can serve as the internal confinement for the evolution of nanorods from MTP. (B) Schematic model illustrating the diffusion of silver atoms toward the two ends of a nanorod, with the side surfaces completely passivated by PVP. This drawing shows a projection perpendicular to one of the five side facets of a nanorod, and the arrows represent the diffusion fluxes of silver atoms [42].

### 2.3.6. Salt-mediated polyol method

Based on the PVP-assisted polyol method, Xia and co-workers also developed a salt mediated polyol process to synthesize Ag NWs [43,44]. The addition of a trace

amount of salt, such as sodium chloride (NaCl), iron nitrate ( $\text{Fe}(\text{NO}_3)_3$ ), copper (II) chloride ( $\text{CuCl}_2$ ) and copper (I) chloride ( $\text{CuCl}$ ) has been shown to influence the morphology of the final products. Usually salt-mediated synthesis strategy is a simple and effective method for the large scale synthesis of the Ag NWs. For example, they synthesized Ag NWs with high yields by reducing  $\text{AgNO}_3$  with EG heated at  $148^\circ\text{C}$  in the presence of PVP and a trace amount of NaCl. It was found that oxygen must be removed from the reaction solution in the presence of  $\text{Cl}^-$  anions in order to obtain Ag NWs. Figure 2.9 shows the proposed mechanism of oxidative etching and growth of MTPs. Five-twinned decahedral particles were proposed to be seeds of Ag NWs. The defects among single-crystal tetrahedron subunits of decahedral particles provide high-energy sites for atomic addition, leading to one dimensional Ag products via anisotropic growth along the  $\langle 110 \rangle$  direction. The addition of chloride causes enhanced oxidation and preferential etching of twinned particles, leaving only single-crystal particles (or seeds) to grow. Under similar conditions, Xia's experiment has been carried out within argon atmosphere, which supplied an anoxic (non-oxidative) condition and the twinned particles that formed in the early stage of the reaction could grow into uniform nanowires [45].

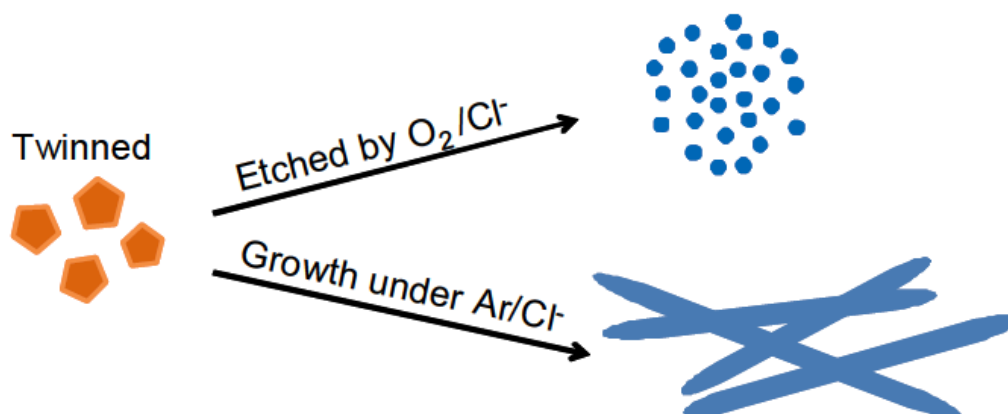


**Figure 2.9** Illustration of the proposed mechanism by which twinned decahedron was etched with the existence of  $\text{O}_2/\text{Cl}^-$  and Ag NWs were obtained under argon protection [45].

## **2.4 Nanowire Characterization Methods**

### **2.4.1 Scanning Electron Microscopy (SEM)**

Products of the polyol process were analyzed by Field Emission Scanning Electron Microscopy (FE-SEM) (Nova NanoSEM 430) operated at 10 kV voltage. For the preparation of SEM samples, ethanolic solution of nanowires were simply sprinkled onto silicon wafer and allowed to dry. They were then placed onto SEM stubs with carbon tapes. No gold or carbon coating was utilized.

### **2.4.2 Transmission Electron Microscopy (TEM)**

Transmission Electron Microscope (TEM) was used to observe the surface morphology in atomic scale. For the preparation of TEM samples Ag NWs suspended in ethanol were simply drop casted on holey carbon coated 400 mesh copper grids. A JEOL 2010 high-resolution transmission electron microscopy (HRTEM) operated at 200 kV was used for characterization.

### **2.4.3 XRD Measurements**

X-ray diffraction (XRD) analyses were performed for phase identification of the products. The crystal structure of the Ag NWs was investigated by XRD on a Rigaku D/Max-2000 pc diffractometer with Cu K $\alpha$  radiation operating at 40 kV range of 30-60° at a scanning rate of 1°/min.

## **2.5 Experimental Details**

All glassware (Erlenmayer bulbs, beakers) used in the experiments were cleaned using detergent (Alconox), deionized water, basic solution (pH: 11), acidic solution (pH: 2), acetone (99.8%), isopropyl alcohol (99.8%) and finally deionized water (18.3 M $\Omega$ ) through 5 minutes sonication for each. All chemicals were purchased from Sigma-Aldrich and used without further purification.

### 2.5.1 Synthesis of Silver Nanowires

In a previous work, an extensive parametric study was conducted on the polyol synthesis of Ag NWs [21]. Parameters such as temperature, injection rate, PVP:AgNO<sub>3</sub> ratio, NaCl amount and stirring rate were investigated. Although the optimized parameters were quite successful in order to obtain Ag NWs with high yield and narrow size distribution, the amount of obtained Ag NWs was very limited (~50 mg/experiment). Since Ag NWs will be needed in large quantities, classical polyol process need to be modified, so then larger scale synthesis of nanowires became possible [46]. In the modified version of synthesis experiments, temperature was used to simply control the reducing power of EG. Hence, the precursor can be safely added into reaction bath in larger volumes. A typical experiment starts with the preparation of an 80 ml and 0.45 M EG solution of PVP (monomer-based calculation MW= 55000) and a 1 mM NaCl (99.5%) in an erlenmeyer bulb. Ingredients dissolved in ethylene glycol at 100°C and then the solution was cooled down to the room temperature. In the meantime, a 0.12 M AgNO<sub>3</sub> (99.5%) solution in 40 ml EG was prepared at room temperature. After that, the AgNO<sub>3</sub> / EG solution was heated to 120 °C in a silicon oil bath on a hot-plate. Also a reflux unit was used to eliminate concentration changes due to heating. Then, PVP/EG solution was added into AgNO<sub>3</sub> /EG solution within 10 minutes. Then, the temperature of the oil bath was set to 160 °C. When the oil bath reached the desired temperature, the solution was annealed for an additional 90 minutes. Moreover, the solution was stirred at a rate of 1000 rpm through a magnetic stirrer during the whole process. Figure 2.10 shows experimental setup for the large scale synthesis of Ag NWs.

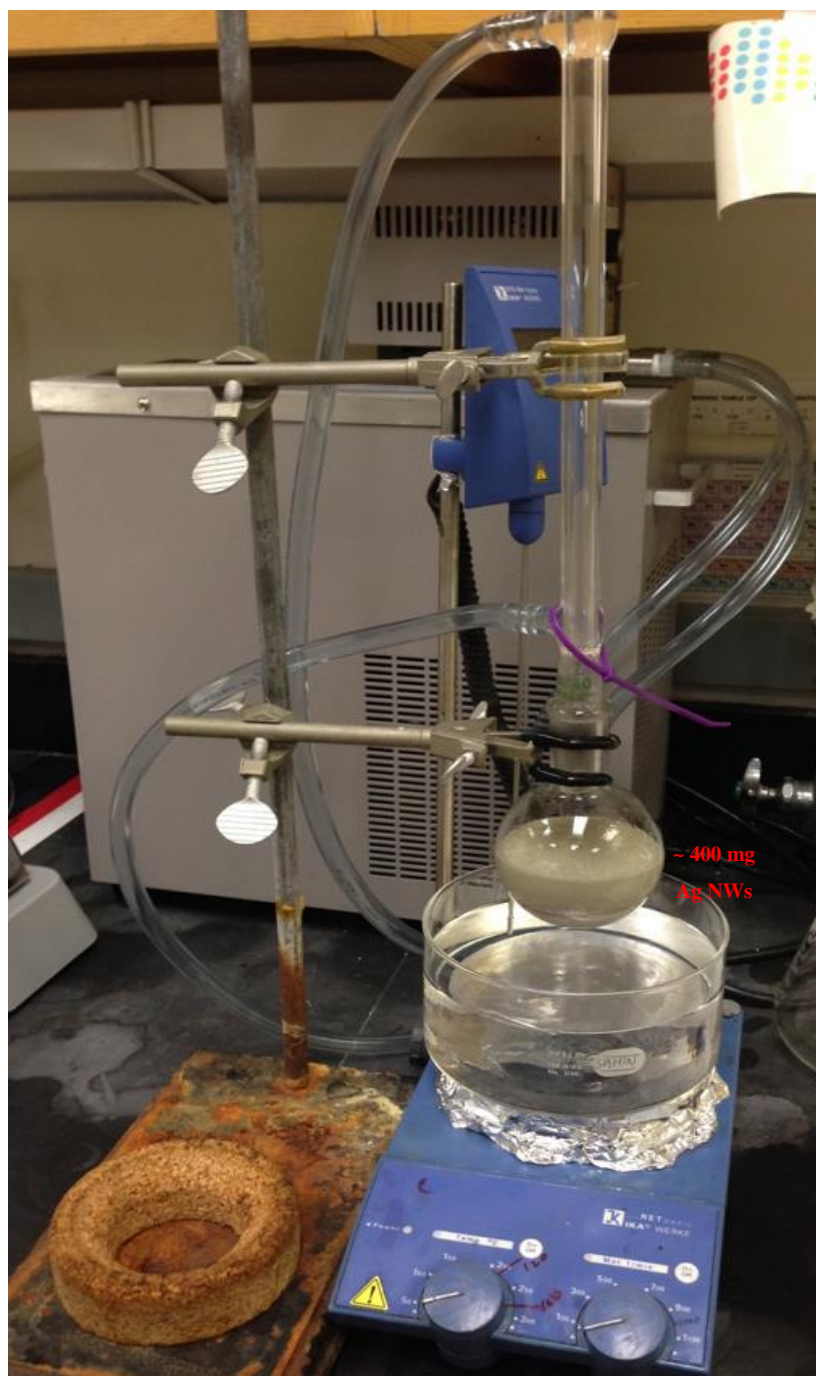


**Figure 2.10** The experimental setup for Ag NW synthesis by modified polyol process.

During the nanowire synthesis as the temperature starts to increase, reducing power of the EG increases. Hence, reduction of  $\text{Ag}^+$  ions in the solution starts according to the reaction shown in Figure 2.11. As a result, Ag nanoparticles start to form via homogeneous nucleation with various shapes. Among these nanoparticles,

pentagonal shape MTPs are unique in terms of their morphology and stability in that reaction conditions.

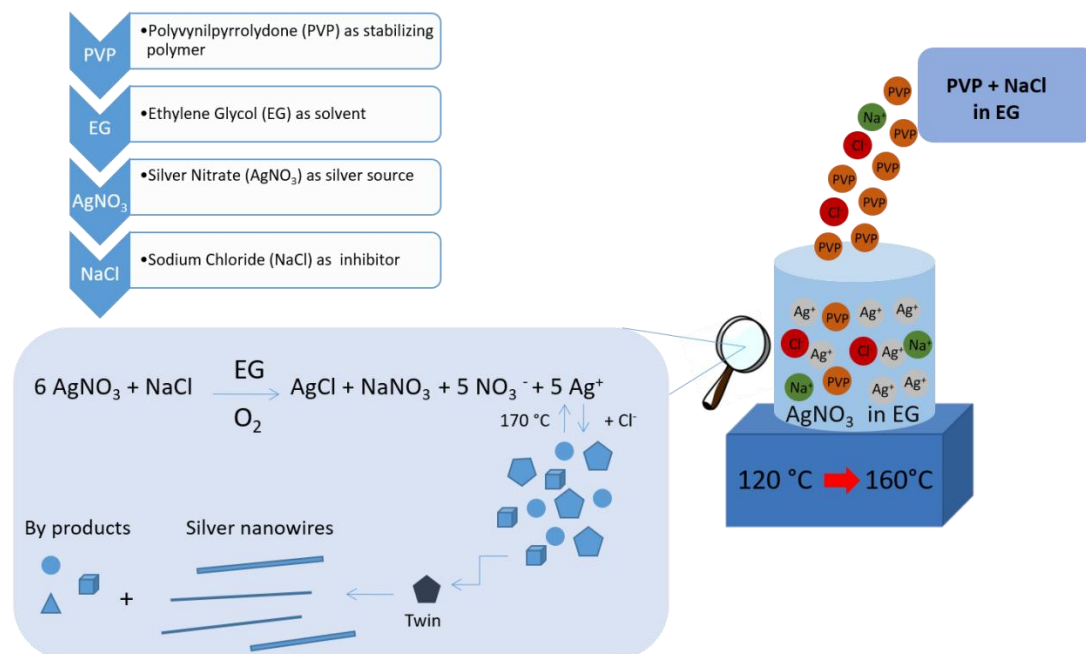


**Figure 2.11** Schematic representation for the formation of Ag NWs in modified polyol process.

As-formed Ag nanoparticles are prevented from aggregation with the help of PVP molecules. Chemical adsorption of PVP molecules onto the surfaces of as-formed Ag nanoparticles is the reason for them to remain at nanoscale [47]. As the process continues, some of the Ag nanoparticles start to dissolve and grow as larger nanoparticles via the mechanism known as Oswald ripening [38]. With the passivation of particular facets of these particles by PVP, some nanoparticles can grow into MTPs. PVP is believed to passivate (100) faces of these multi-twin particles and have (111) planes active for anisotropic growth at [110] direction. Figure 2.12 shows how PVP molecules selectively adsorb on multi-twin particles and ensures other surfaces remain active to obtain anisotropic growth. As the addition of Ag<sup>+</sup> ions continue, MTPs grow into Ag NWs. Figure 2.13 shows an illustration of the growth of Ag NWs.

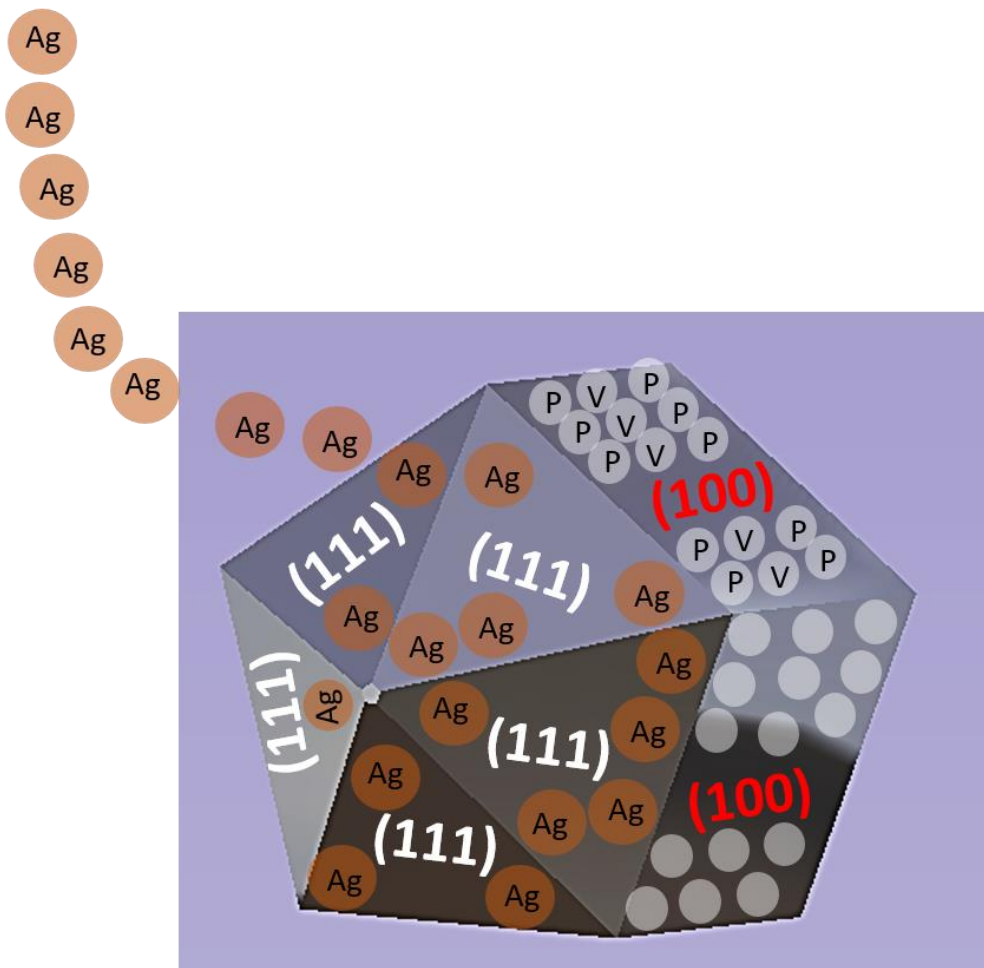


**Figure 2.12** Schematic representation of the passivation of (100) planes by PVP and further growth through active (111) planes.

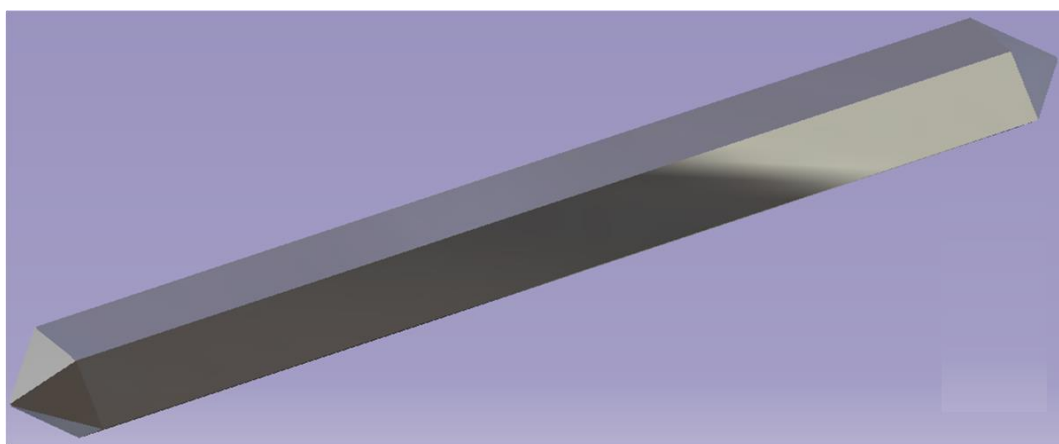


**Figure 2.13** Schematic representation of an Ag NWs.

Figure 2.14 shows photographs of Ag NW synthesis solution throughout the process. Following the introduction of PVP/EG solution and starting to increase the temperature of the oil bath, reduction of silver ions and formation of silver nanoparticles causes a series of color change in the solution. Initial color change shows the reduction of silver ions into metallic silver and thus the formation of silver nanoparticles. As the morphology, size and the fraction of the nanoparticles changes, the color of the reaction solution changes. Final color indicates the presence of nanowires.

Following synthesis, purification of Ag NWs was done by centrifuging process. In order to separate PVP and EG from the Ag NWs, the solution was diluted with acetone (in a ratio of 1:10) and centrifuged two times at 6000 rpm for 20 minutes. After that, the nanowires were dispersed in ethanol and again centrifuged at 6000 rpm for another 20 minutes. The final product was dispersed in ethanol for further characterization or directly coated onto carbon tapes for SEM analysis.

SEM images of the obtained Ag NWs following purification process are shown in Figure 2.15. SEM images show Ag NWs have an average diameter of 50 nm. Figure 2.16 shows TEM and HRTEM images of as-synthesized Ag NWs using modified polyol process. Ag NWs have smooth surface and perfect crystallinity. In addition, as it can be seen from the HRTEM images (Figure 16 (b) and (c)) even after purification a residual layer of PVP still remains on lateral surfaces of Ag NWs (2-3 nm). Figure 2.17 shows XRD spectra of Ag NWs. All diffraction peaks belong to pure face centered cubic (FCC) silver (JCPDS Card No. 04-0783).

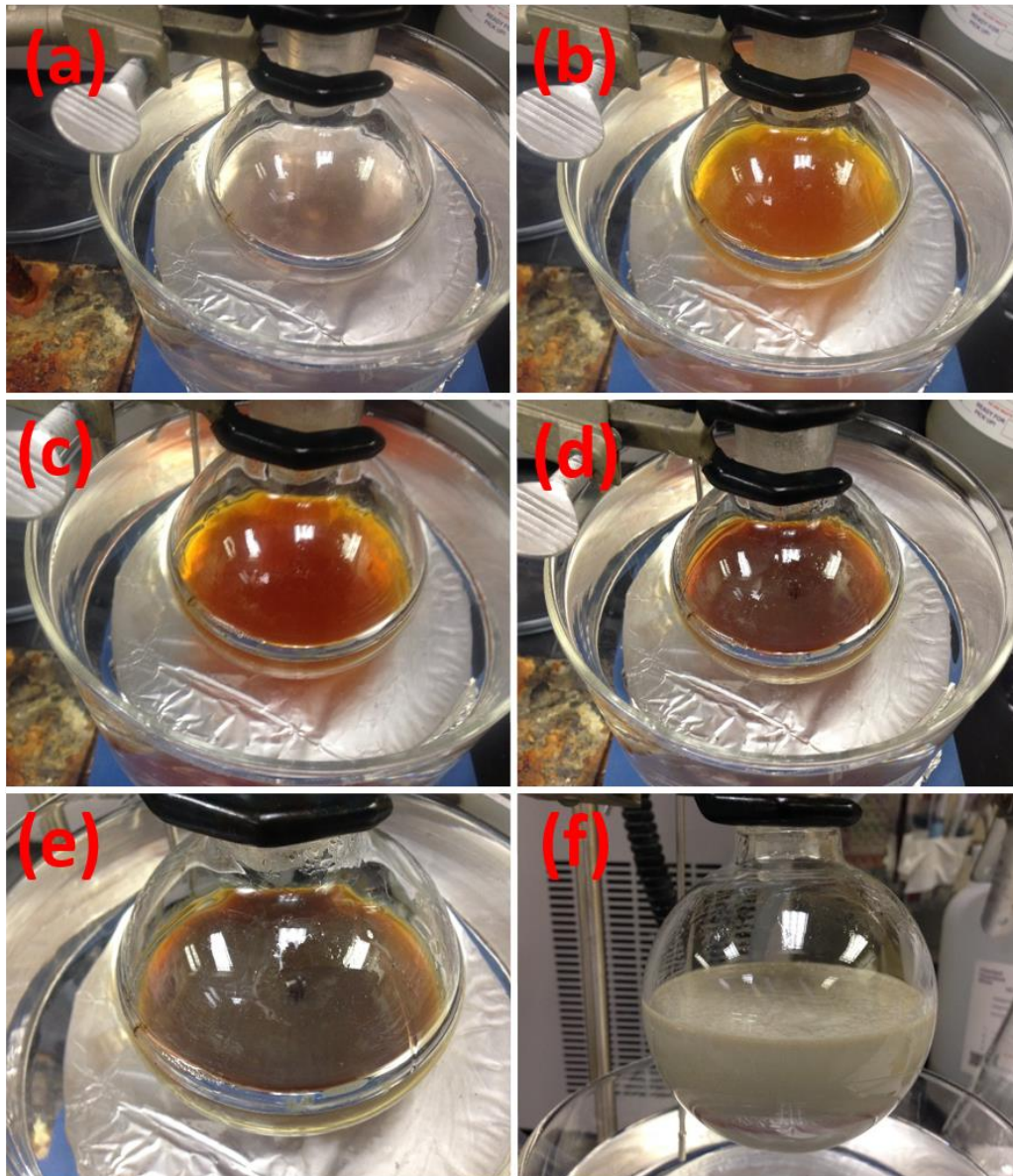


**Figure 2.14** Photographs of the synthesis solution showing its color change during the Ag NW synthesis.

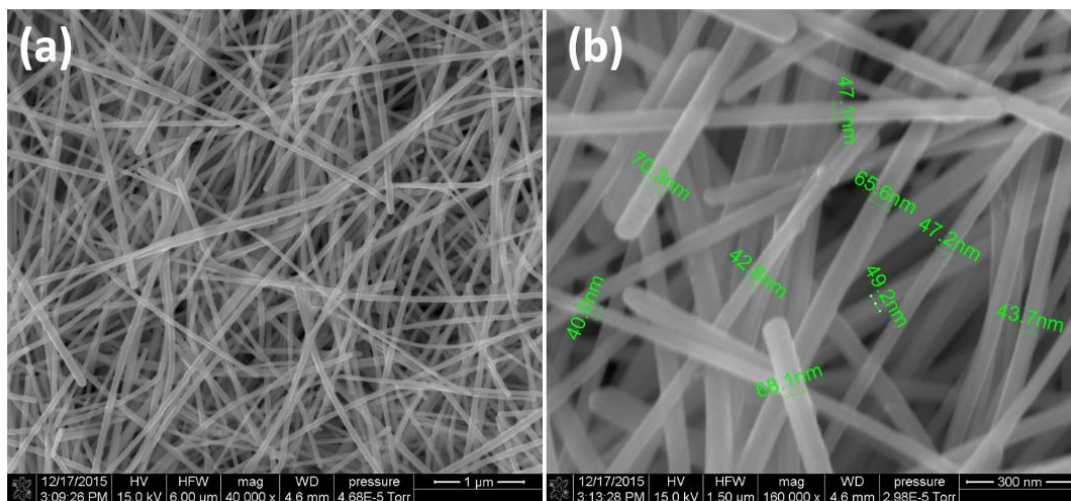


**Figure 2.15** (a) Low and (b) high resolution SEM images of as synthesized Ag NWs using modified polyol process.

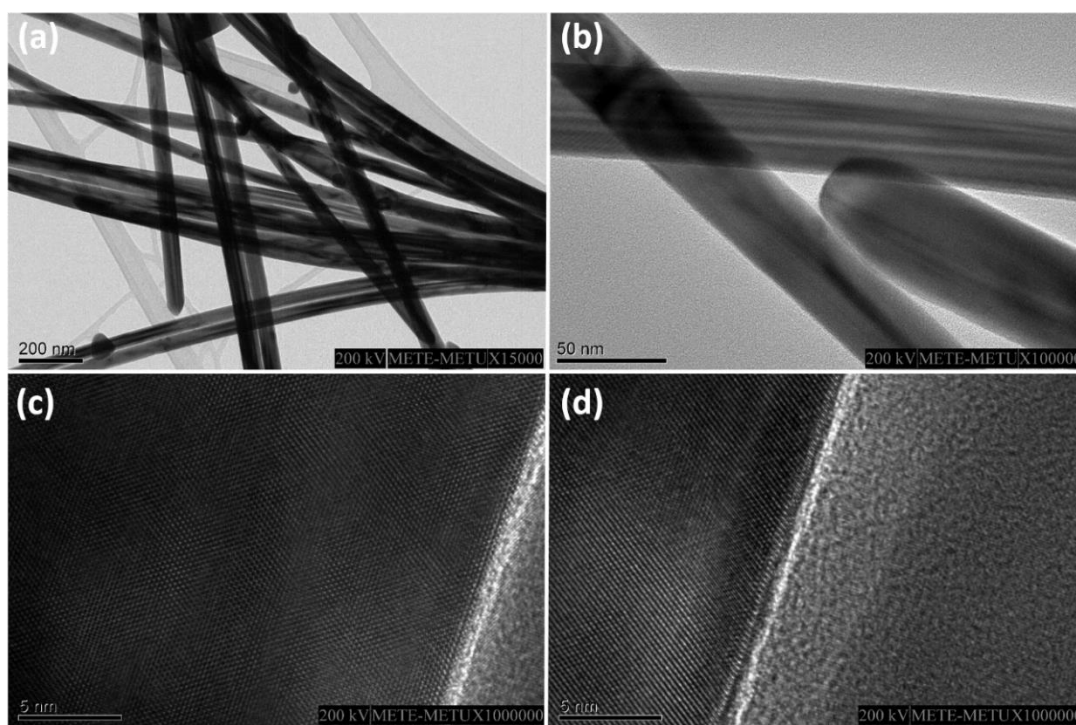


**Figure 2.16** (a) and (b) TEM and (c) and (d) HRTEM images of as synthesized Ag NWs using modified polyol process.

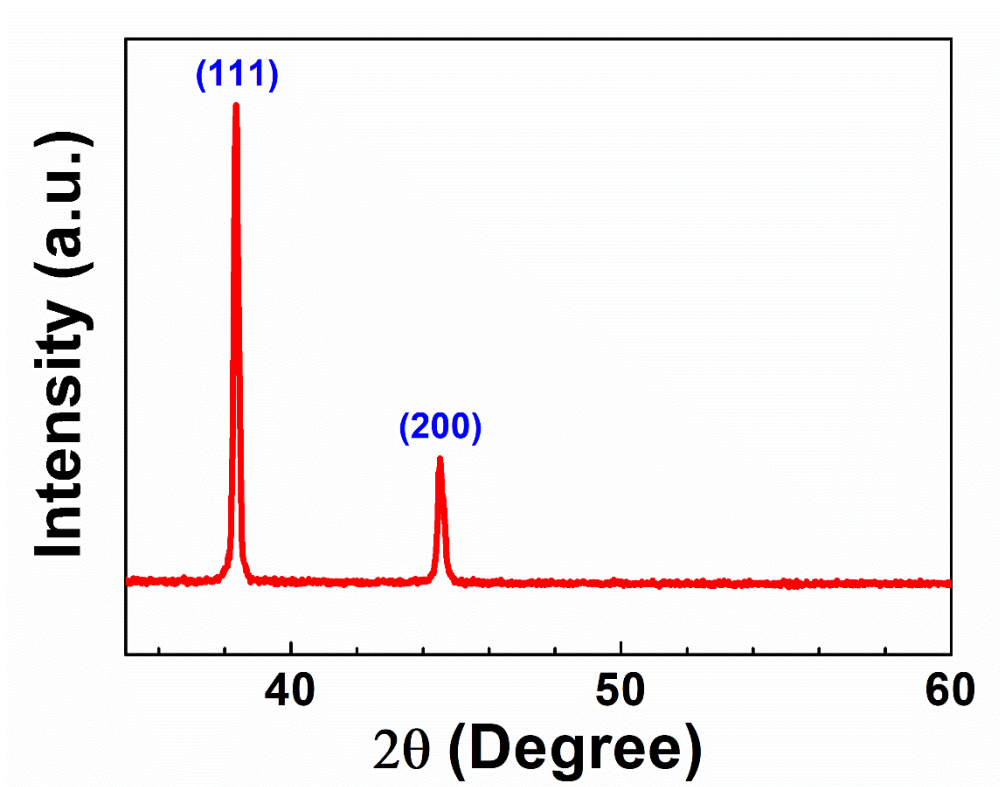


**Figure 2.17** XRD spectrum of Ag NWs (JCPDS Card No. 04-0783) synthesized using modified polyol process.

## CHAPTER 3

### TRANSPARENT AND CONDUCTING SILVER NANOWIRE NETWORKS

#### 3.1. Introduction

Materials with visible transparency and electrical conductivity at the same time are utilized as transparent conducting contacts (TCCs). These materials are widely used in flat panel televisions, touch-screens, smart phones, photovoltaics, low-emissivity (low-e) windows, flexible electronics, organic light emitting diodes (OLEDs) and electromagnetic interference shielding materials. Figure 3.1 shows several current applications of TCCs. Moreover, the requirements in transparent and conducting contact market are now beyond the simple combination of high visible transparency and low sheet resistance. For instance, suitable work function, processing ease and patterning, morphology, stability, low cost, elemental abundance and compatibility with flexible substrates are becoming the main requirements that need to be addressed. Main transparent and conducting contacts are transparent conducting metal oxides (TCOs). So far, fluorine doped tin oxide (FTO), aluminum doped zinc oxide (AZO) and tin doped indium oxide (ITO) underwent a detailed investigation in research and industry. Since these commercially available transparent conductors could not meet all the requirements listed above, new alternatives are being investigated by many research groups [48]. However, it can be said that history of TCCs starts with TCOs [49].

##### 3.1.1. History of Transparent Conducting Oxides (TCOs)

Table 3.1 shows wide diversity of current TCO materials. Although the first studies about TCOs started in the beginning of last century, an enormous increase was

observed after 1995. This is due to global drivers for the development of improved TCOs for new alternative energy and less energy consuming devices. For instance, Figure 3.2 shows energy consumption of the world and makes very clear how it increased rapidly worldwide [50]. Moreover, as our daily life become more technological and new electronic devices are introduced, this energy demand will certainly continue to increase [48].



**Figure 3.1** Different applications of TCCs.

**Table 3.1** Selected historical TCO references [49].

Material	Year	Process	Reference
<i>Cd-O</i>			
CdO	1907	Thermally Oxidation	K. Badeker, Ann. Phys. (Leipzig) 22, 749 (1907)
Cd-O	1952	Sputtering	G. Helwig, Z. Physik, 132, 621 (1952)
<i>Sn-O</i>			
SnO <sub>2</sub> :Cl	1947	Spray pyrolysis	H.A. McMaster, U.S. Patent 2,429,420
SnO <sub>2</sub> :Sb	1947	Spray pyrolysis	J.M. Mochel, U.S. Patent 2,564,706
SnO <sub>2</sub> :F	1951	Spray pyrolysis	W.O. Lytle and A.E. Junge
SnO <sub>2</sub> :Sb	1967	CVD	H.F. Dates and J.K. Davis, USP 3,331,702
<i>Zn-O</i>			
ZnO:Al	1971		T. Hada, Thin Solid Films 7, 135 (1971)
<i>In-O</i>			
In <sub>2</sub> O <sub>3</sub> :Sn	1947		M.J. Zunick, U.S. Patent 2,516,663
In <sub>2</sub> O <sub>3</sub> :Sn	1951	Spray pyrolysis	J.M. Mochel, U.S. Patent 2,564,707 (1951)
In <sub>2</sub> O <sub>3</sub> :Sn	1955	Sputtering	L. Holland and G. Siddall, Vacuum III
In <sub>2</sub> O <sub>3</sub> :Sn	1966	Spray	R. Groth, Phys. Stat. Sol. 14, 69 (1969)
<i>Ti-O</i>			
TiO <sub>2</sub> :Nb	2005	PLD	Furubayashi et al., Appl. Phys. Lett. 86, 252101 (2005)
<i>Zn-Sn-O</i>			
Zn <sub>2</sub> SnO <sub>4</sub>	1992	Sputtering	Enoki et al., Phys. Stat. Solid A 129, 181 (1992)
ZnSnO <sub>3</sub>	1994	Sputtering	Minami et al., Jap. J. Appl. Phys. 2, 33, L1693 (1994)
a-ZnSnO	2004	Sputtering	Moriga et al., J. Vac. Sci. & Tech. A 22, 1705 (2004)
<i>Cd-Sn-O</i>			
Cd <sub>2</sub> SnO <sub>4</sub>	1974	Sputtering	A.J. Nozik, Phys. Rev. B, 6, 453 (1972)
a-CdSnO	1981	Sputtering	F.T.J. Smith and S.L. Lyu, J. Electrochem. Soc. 128, 1083 (1981)
<i>In-Zn-O</i>			
Zn <sub>2</sub> In <sub>2</sub> O <sub>5</sub>	1995	Sputtering	Minami et al., Jap. J. Appl. Phys. P2 34, L971 (1995)
<i>a-InZnO</i>			
<i>In-Ga-Zn-O</i>			
InGaZnO <sub>4</sub>	1995	Sintering	Orita et al., Jap. J. Appl. Phys. P2. 34, 1550 (1995)
a-InGaZnO	2001	PLD	Orita et al., Phil. Mag. B 81, 501 (2001)

CVD chemical vapor deposition; PLD pulsed laser deposition

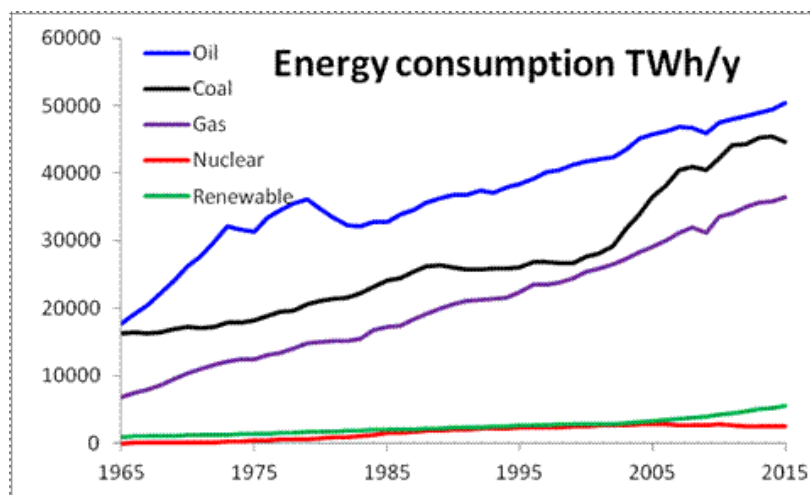


**Figure 3.2** Energy consumption vs. year [51].

Global warming gradually increases due to wastes of traditional energy sources and carbon dioxide (CO<sub>2</sub>) emissions. As a result, in order to bring a valid solution to this problem the world has to develop a fully sustainable life style. For this purpose, sustainability must be a consideration in all aspects of technology including design, processing, delivery, application, service life and recycling. So how can TCCs enter this big scenario? In particular, they are used in alternative energy sources such as solar cells and energy efficient devices like OLEDs for indoor lightning and smart windows. In order to supply these technologies with less environmental impact and lower cost, constituents of these devices should also obey these prerequisites [48].

### **3.1.2 Current status of TCCs**

Today the most widely used TCC is indium tin oxide (ITO) or tin doped indium oxide. Moreover, it is commercially available on different substrates such as glass or polyethylene terephthalate (PET). Its high transparency and conductivity recombination and its availability as a robust film made ITO very useful for various applications. Solar collector panels, photovoltaic cells, low-e residential and commercial windows, liquid crystal displays (LCDs) and low pressure sodium lamps are a few applications where ITO films are used. In addition, due to ITO's high infrared reflectivity, it is used in hot mirrors. However, besides these superior properties and wide applicability of ITO, it has some crucial drawbacks. For example, since indium sources are limited, its price increases gradually. Price of metallic indium has changed from \$150 to \$500 from 1993 to 2008. Moreover, ITO's fragility due to its crystalline ceramic nature and lack of flexibility limit its use in novel flexible electronic devices. In addition, for the production of ITO films with high transparency and low conductivity, high cost vacuum processes such as sputtering is needed. Hence, new alternative materials are being investigated for the replacement of ITO. Aluminum doped zinc oxide (AZO), gallium doped zinc oxide (GZO) and indium doped zinc oxide (IZO) are other oxide based transparent and conducting materials. Moreover, carbon nanotube thin films and graphene sheets are carbon-based alternative TCCs. Recently, random networks of metallic nanowires were also presented as promising candidates for the replacement of ITO [48].

### 3.1.3 Transparent and Conducting Contact Characteristics

#### 3.1.3.1 Transparency

When a material is subjected to light, incident light can be reflected, absorbed or transmitted. The ratio of the transmitted light to incident one is defined as the transmittance of that material and it is generally stated as a percentage. This behavior may vary according to the wavelength of the incident light. For a transparent conductor, in order to be used in display applications, it must transmit light freely across the visible spectrum, which is approximately between 400 and 700 nm. Optical properties strongly depend on carrier density and mobility. Generally, for a material to be transparent in visible range of solar spectrum, its band gap must be larger than 3 eV ( $\lambda \approx 400$  nm). Resistivity of a transparent conductor decreases when its free charge carrier density decreases. This also shifts infrared (IR) absorption edge to shorter wavelengths, as a result, transmission window gets narrower. Transparency measurements are generally made using a UV-Vis spectrometer [48].

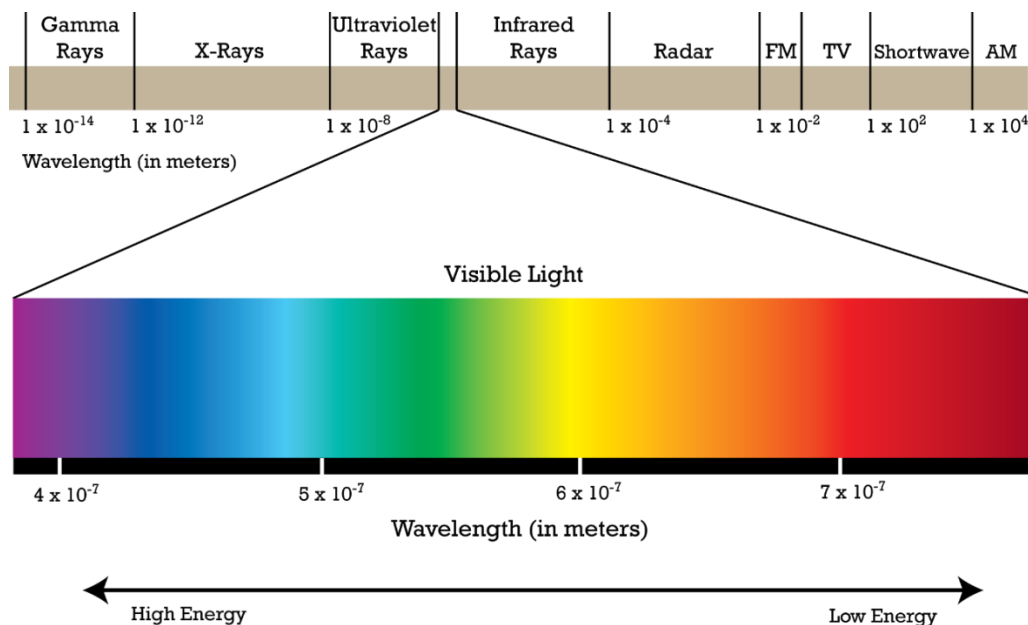


**Figure 3.3** Electromagnetic spectrum of light [52].

### 3.1.3.2 Sheet Resistance

One of the basic properties of materials is resistivity. It is represented by  $\rho$  with the units of  $\Omega \cdot \text{cm}$ . Resistance, which is a geometry dependent property of a material can be related to resistivity through:

$$R=(L/Wt), \quad (3.1)$$

,where  $L$  is the length of the material that the electrical current passes through, and  $W$  is the width and  $t$  is the thickness of it. Since the thicknesses of films are often difficult to measure, sheet resistance is defined to represent resistance per square area of a thin film with the units  $\Omega/\text{sq}$  (ohms per square) and is given by

$$R_s=\rho t \quad (3.2)$$

So,

$$R=R_sLW \quad (3.3)$$

Thus, the total resistance of a film is proportional to the number of squares that can be drawn on the conducting surface area.

#### 3.1.3.2.1 Two Probe Measurements

Ohm's Law ( $V=IR$ ) is used in order to determine the resistance: known current is sourced and it flows through the unknown resistance. One measures the voltage that develops across the resistance by dividing the measured voltage to the sourced current. A problem that occurs when using a 2-wire setup is that the voltage is measured not only across the resistance in question, but also includes the resistance of the leads and contacts. When using an ohmmeter to measure resistances above a few ohms, this added resistance is usually not creating a problem. However, when measuring low resistances or when contact resistances are high, obtaining accurate results with a two probe measurement can be difficult. A representative set up for 2 probe measurement of sheet resistance of a conducting film is provided in Figure 3.4 [48].

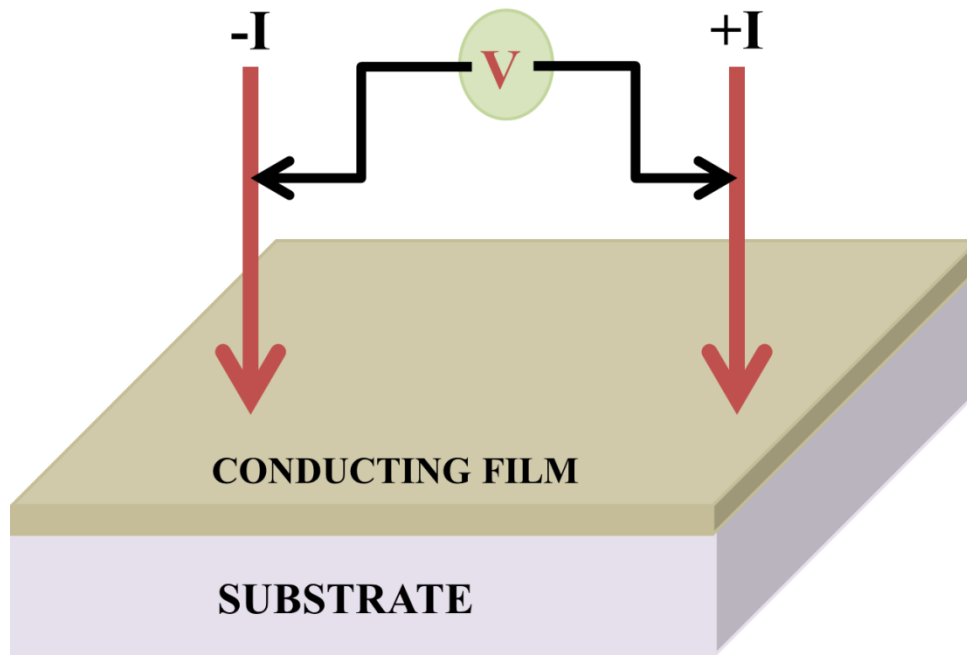


**Figure 3.4** Representative set-up for 2-probe measurements [48].

### 3.1.3.2.2 Four Probe Measurements

A solution to the problem of 2-probe measurements in which the lead and contact resistance is measured along with that of the device under test is the 4-probe measurement. Because a second set of probes is used for sensing and since negligible current flows in these probes, only the voltage drop across the device under test is measured as a result. Thus, the resistance measurement is more accurate. A representative set up for 4-probe measurement of sheet resistance of a conducting film is shown in Figure 3.5 [48]. However, 2-probe measurements generally give reliable results for low sheet resistance systems.

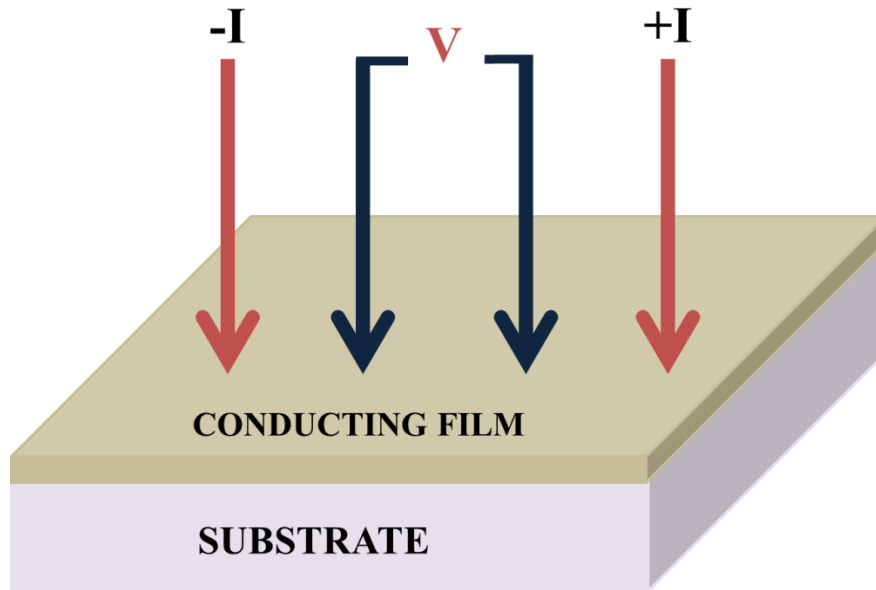


**Figure 3.5** Representative set up for 4-probe measurements [48].

### 3.1.3.3 Work Function Measurements

Figure 3.6 shows a schematic energy diagram of a metal. The valence bands are filled with electrons up to the Fermi level ( $E_F$ ). The energy difference between Fermi level and vacuum level corresponds to the work function ( $\Phi$ ). The work function corresponds to the minimum amount of energy needed to remove an electron from the metal so that it can go to vacuum level with zero energy. In metals, work function and ionization energy are the same [48].

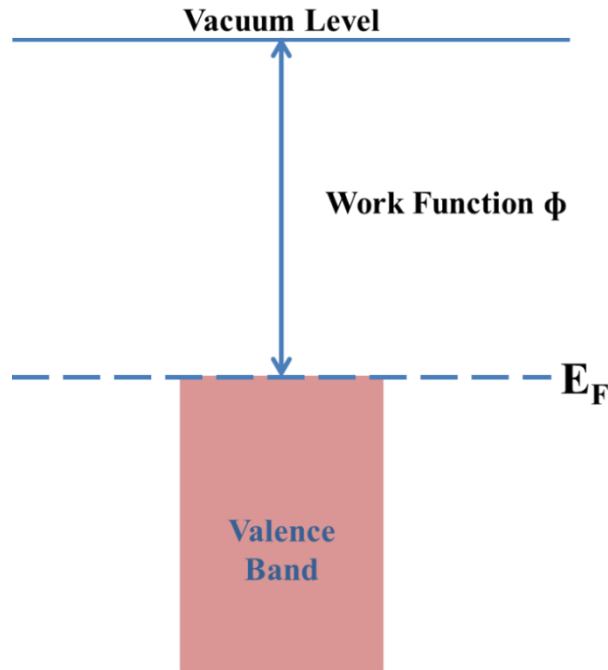


**Figure 3.6** Schematic energy diagram of a metal [48].

The work function of a material can be measured by two alternative methods. These are ultraviolet photoelectron spectroscopy (UPS) and Kelvin probe (KP). While PES allows the measurement of the absolute work function, KP only gives the contact potential difference (CPD) between the actual probe and the sample surface. Calibration with UPS allows turning KP results into absolute values [48]. Figure 3.7 shows a typical UPS spectrum of a gold sample. Since the binding energy of the electrons right at the secondary edge are known the work function can be determined, which is just the difference between the energy of the UV photons (21.21 eV for He Irradiation) and the binding energy of the secondary edge (15.9 eV in the case of Au). From Figure 3.7, it follows that the investigated Au surface has a work function of,

$$\Phi_{\text{Au}} = 21.21 \text{ eV} - 15.9 \text{ eV} = 5.3 \text{ eV}.$$

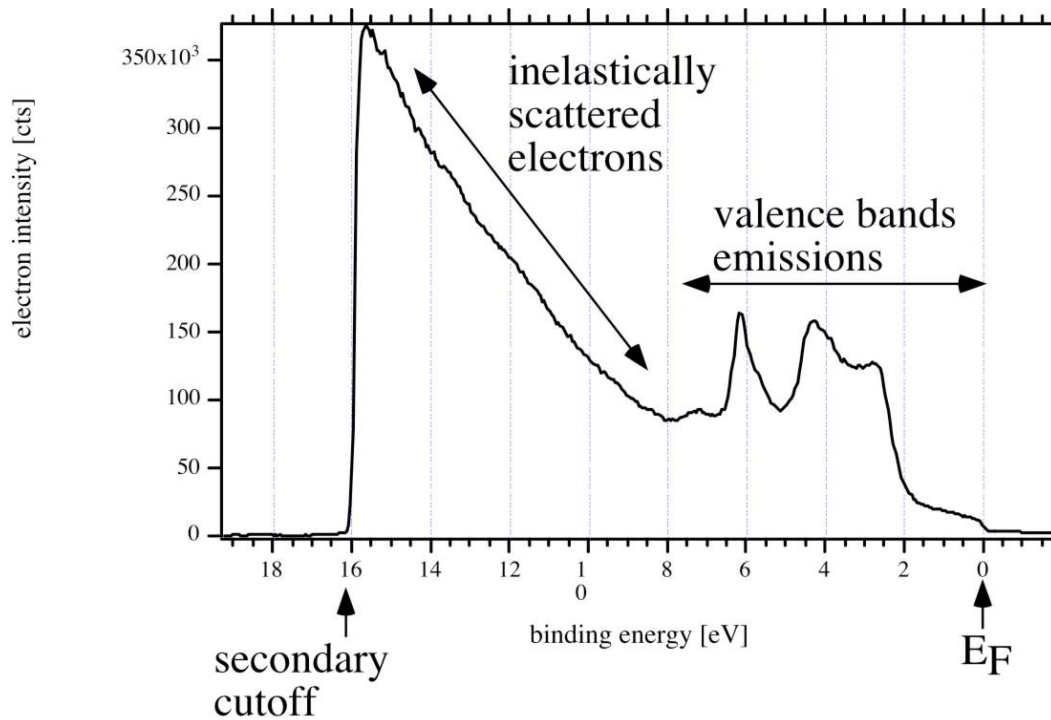


**Figure 3.7** UP-spectrum of Au surface [53].

### 3.1.4 Types of Transparent and Conducting Contacts

#### 3.1.4.1 Indium Tin Oxide (ITO)

Indium tin oxide (ITO or tin-doped indium oxide) is a mixture of indium (III) oxide ( $\text{In}_2\text{O}_3$ ) and tin (IV) (Sn), typically 90%  $\text{In}_2\text{O}_3$ , 10%  $\text{SnO}_2$  by weight. In powder form it has a yellow-green color; however, when it is deposited as a thin film with a thickness in the range of 100 to 300 nm it is transparent and colorless. Moreover, due to the presence of charge carriers, it is also conductive. Hence, it is widely used in the devices in which both transparency and conductivity are needed. ITO is generally deposited through RF-sputtering [54] onto transparent substrates such as glass, which necessitates in-situ annealing or a post annealing step is necessary for crystallization. As a result, sheet resistance, ( $R_{sh}$ ), about  $10 \Omega/\text{sq}$  at a transparency of 90% in visible spectrum is observed for ITO [50]. ITO is an n-type semiconductor with a work function between 4.3 - 4.7 eV. ITO is a commercial standard in many electronic devices such as solar cells, organic light emitting diodes (OLEDs) and

electrochromic windows. However, despite its superior transparent and conducting characteristics, ITO cannot meet all the market demands. Firstly, ITO requires annealing at relatively high temperatures ( $>200^{\circ}\text{C}$ ) [55] in order to attain low resistivity values. However, polymer based substrates such as PET cannot withstand this treatment. Thus, ITO films on polymer substrates usually have amorphous structure and exhibit considerably higher  $R_{\text{sh}}$  (60-300  $\Omega/\text{sq}$ ) values [56]. The increased usage of liquid crystal displays and plasma screens is another issue raised with the use of ITO. Increased use of ITO increased the demand of the world to this material. Hence, the price of indium per kilogram, which is the main constituent of ITO has raised from \$100 in 2002 to \$1000 in 2005. Now it is around with prices around \$500 [56]. In addition, due to its oxide structure, ITO suffers from flexibility. Moreover, most of the high performance ITO films are deposited through sputtering. Sputtering processes are generally inefficient [56] because only a small percentage of sputtered material covers the substrate. In addition, recycling processes for sputtering methods are expensive and yield of this process is very low considering day by day enlarging flat panel dimensions. Therefore, new alternatives to ITO have been considered. These include conducting polymers, graphene sheets, metal thin films, metallic nanogrids, single walled carbon nanotube (SWCNT) thin films and random networks of metallic nanowires, Ag NWs in particular. These alternative materials are explained in detail below [48].

#### **3.1.4.2 Fluorine Doped Tin Oxide (FTO)**

Another metal oxide based transparent conducting contact is fluorine doped tin oxide (FTO). FTO exhibits higher thermal, chemical and mechanical stability and are made of cheaper elements compared to that of ITO. FTO thin films can be fabricated alternatively via spray pyrolysis method. Figure 3.8 (a) and (b) show top and cross-sectional SEM images of an FTO thin film, respectively. It is clear that the film has textured columnar grain structure. FTO films are deposited at  $420^{\circ}\text{C}$  and XRD analysis shows polycrystalline tetragonal cassiterite structure of  $\text{SnO}_2$ . Although FTO thin films do not have constant transmittance in the visible range, a total transmittance over 70% and a sheet resistance around 13  $\text{ohm}/\text{sq}$  was obtained [57].

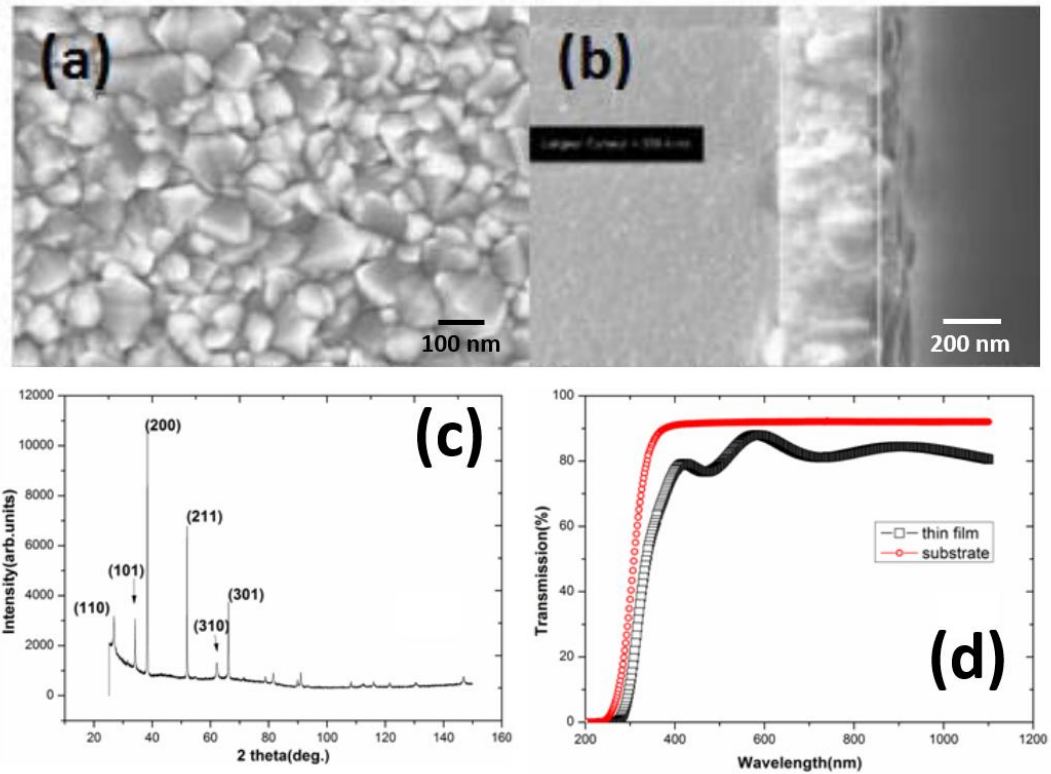


**Figure 3.8** (a) Top and (b) cross-sectional FESEM images of FTO thin films. (c) XRD pattern and (d) UV-visible transmission spectra of FTO thin films deposited at 420°C [57].

### 3.1.4.3 Conducting Polymers (PEDOT:PSS)

Poly(3,4-ethylenedioxythiophene) (PEDOT) is a polymer that is conductive (conductivity ( $\sigma$ ) of  $10^2$  S/cm) and transparent in thin film form. It has been generally used as a hole injection layer in OLEDs. Due to its insolubility in most of the solvents it is dispersed in water using poly (styrene sulfonate) (PSS). Although it is useful in OLEDs as hole injection layer due to its high work function and hole affinity, solely PEDOT:PSS cannot be used in solar cells as an electrode due to its low conductivity. An exception has been reported by Kim et al. [58]. In their work it has been showed that the conductivity of PEDOT:PSS films can be increased by solvent-post treatment method and then it can by itself be used as the electrode material. Figure 3.9 shows AFM phase images of PEDOT:PSS films with different solvent treatments. In these images, bright zones show PEDOT-rich grains and dark

zones correspond to PSS-rich grains. Solvent-post treatment process transforms the shape of the PEDOT-rich grains from short curved domains to long stretched network. As a result, larger contacts are formed between better oriented PEDOT-rich grains and conductivity was increased. They claimed that increasing the number of layers of PEDOT:PSS films result in low sheet resistance ( $< 65 \Omega/\text{sq}^{-1}$ ) with a visible transparency around 80% [48].

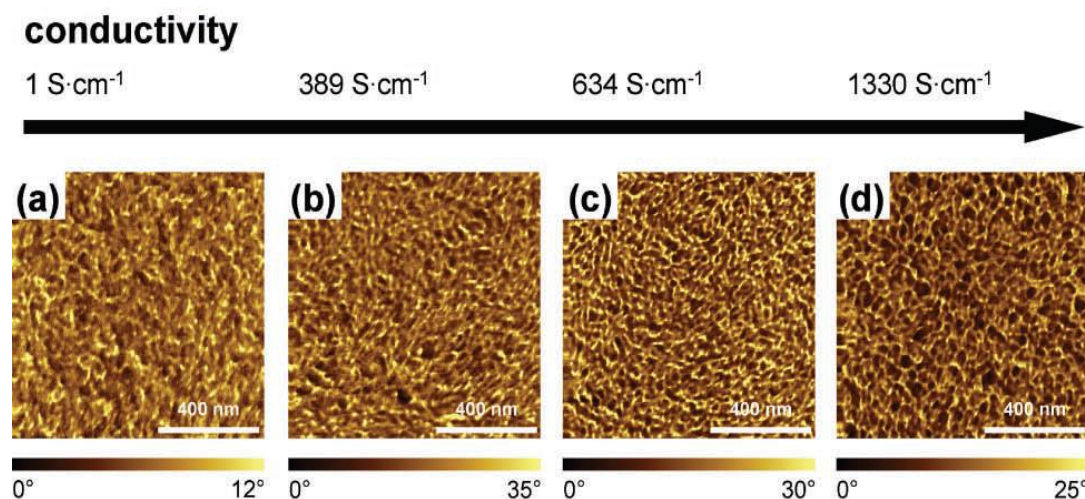


**Figure 3. 9** AFM phase images of PEDOT:PSS films with various solvent treatments. (a) Pristine PEDOT:PSS (PH1000) ( $\sigma < 1 \text{ S cm}^{-1}$ ). (b) PEDOT:PSS (PH 510) doped with DMSO 5 vol% ( $\sigma = 389 \text{ S cm}^{-1}$ ). (c) PEDOT:PSS (PH 1000) doped with EG 6 vol% ( $\sigma = 634 \text{ S cm}^{-1}$ ). (d) solvent post-treated PEDOT:PSS (PH 1000) doped with EG 6 vol% ( $\sigma = 1330 \text{ S cm}^{-1}$ ) [58].

### 3.1.4.4 Graphene

Graphene is one atom thick planar sheet of  $\text{sp}^2$ -bonded carbon atoms packed in a “honeycomb” crystal lattice. It is one layer of stacked graphite. Graphene was firstly isolated from graphite flakes in 2004 via scotch-tape method [59]. Figure 3.10 (a) shows an optical image of an exfoliated graphene sheet. However, size of the graphene flakes obtained from this method is limited to a few hundred microns. Hence, scotch-tape approach is not suitable for the use of graphene in opto-electronic devices. Researchers then developed a chemical vapor deposition (CVD) based approach for the synthesis of monolayer graphene sheets. CVD method results

in the formation of scalable and large area monolayer graphene sheets. As fabricated graphene sheets have visible absorption around 2.3 % per layer and a few hundred ohms/sq sheet resistance. Figure 3.10 (b) shows a CVD set up schematically demonstrating graphene synthesis on copper foils. Utilization of complex equipment, limitation of substrate dimensions and multilayer graphene are the main disadvantages of graphene synthesis via CVD method.

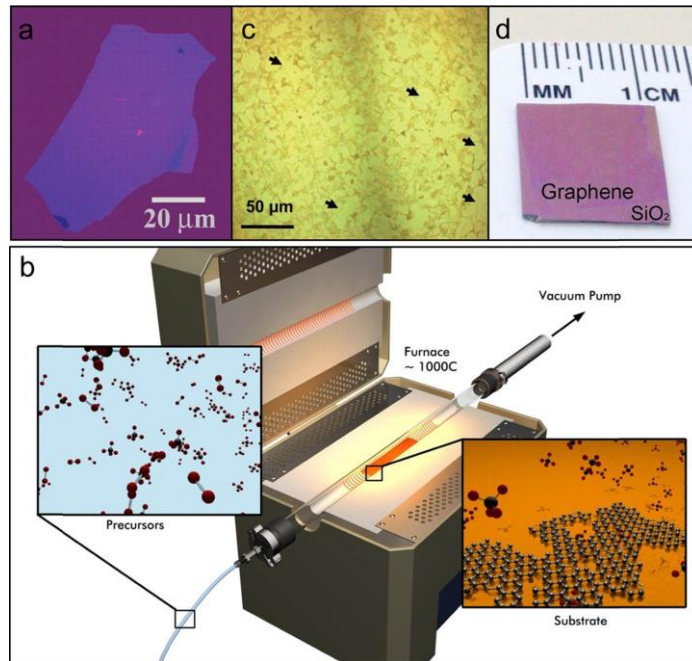


**Figure 3.10** (a) An optical image of mechanically exfoliated graphene flake [59]. (b) Schematic illustration of graphene synthesis by CVD method. (c) Graphene synthesized on nickel thin film; arrows indicate thin monolayer regions. (d) Monolayer graphene synthesized on copper foil and transferred onto a SiO<sub>2</sub>/Si substrate [60].

### 3.1.4.5 Thin Metal Films

Metals are malleable and can be deposited onto substrates using straightforward methods. They are intrinsically conductive and keep this property even when they are deposited as very thin films. Moreover, metals show visible transparency in thin film form. Generally, under a certain thickness the transparency of a metal film increases with decreasing thickness; however, their sheet resistance increases rapidly under

these circumstances. Suitable metal film thickness is between 10-20 nm for considerable transparency and sheet resistance combination [48]. Avrech et al. showed the use of filtered vacuum arc plasma deposited of platinum (Pt) thin films as transparent and conducting contacts [61]. Figure 3.11 shows how sheet resistance of Pt films change with film thickness. Typically, a transmittance of 60% was obtained from these thin films at a sheet resistance of 300ohm/sq. Figure 3.12 show how visible transparency changes with increasing thickness of Pt films. Pt thin films were not transparent at all over a thick film of 250 nm thickness.

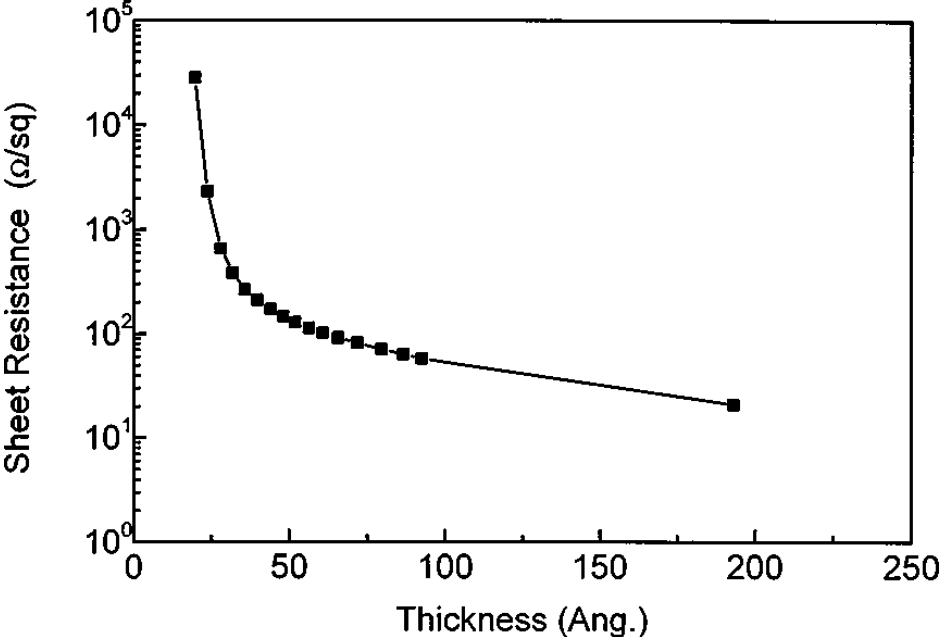
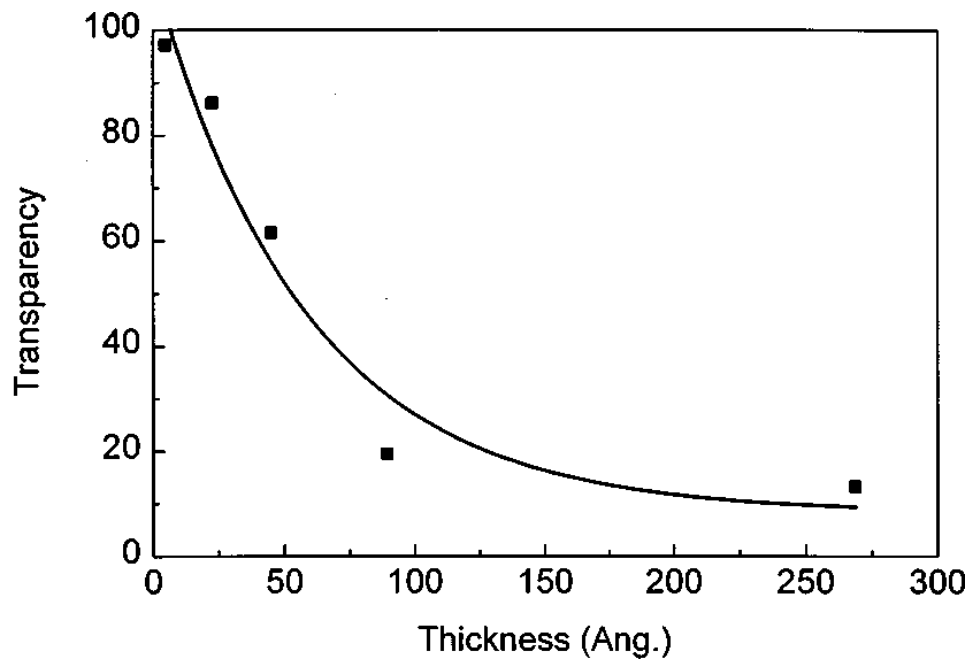


Figure 3.11 Sheet resistance vs. thickness graph for Pt films [61].



**Figure 3.12** Transparency vs. thickness graph for Pt films [61].

#### 3.1.4.6 Metal Nanogrids

Another metal based TCCs are metal nanogrids. One model structure is a metal nanogrid with periodic metal lines. Such nanostructures provide opportunities to manipulate photons and electrons to achieve unique properties that are not possible with flat ITO electrodes. One major advantage of these metal grids is that their conductivity is close to that of the bulk counterparts. This is because the thickness of the metal lines is much larger than that of metal films, electron scattering due to the substrate roughness and the strain boundaries decreases. Light scattering and coupling in such nanogrids also provides additional benefits for device applications, particularly for solar cells where light scattering enhances the absorption within the active layer [48]. Guo et al. [62] stated that two design considerations must be taken into account for nanogrid-based transparent electrodes: (1) the line width of the metal mesh should be subwavelength to provide sufficient transparency; (2) the period of the mesh should be submicrometer to ensure the uniformity of the current across the active layer. In addition, optical electrical field and power flow of silver nanogrids

were calculated (Figure 3.13 (a) and (b) ). Then, in Figure 3.13 (c), (d) and (e) finite-element modeling technique was used to calculate the transmittance of those metal nanogrids.

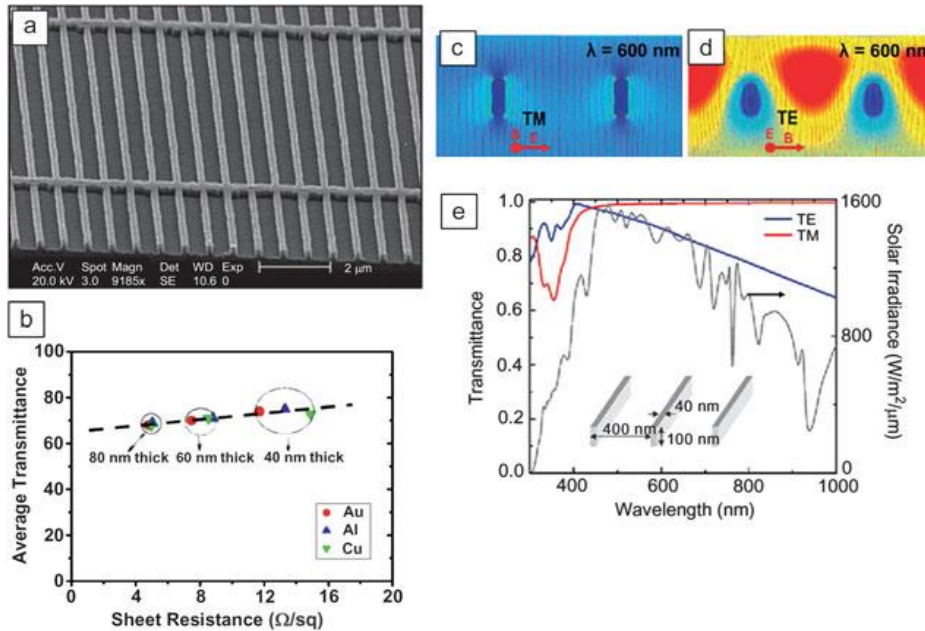


**Figure 3.13** (a) SEM image of as-fabricated metal electrodes. (b) Average transmittance versus sheet resistance of metal grids with a line width of 120 nm. Absolute value of the modeled optical electric field and power flow for light (600 nm wavelength) incident on a freestanding Ag grating (400 nm period, 40 nm line width, 100 nm high) for both (c) transverse magnetic (TM) and (d) transverse electric (TE) polarization. (e) Simulated transmittance versus wavelength for two modes. The AM 1.5 solar irradiance data (black line) are plotted for comparison [62].

### 3.1.4.6 Single Walled Carbon Nanotube Thin Films (SWCNT)

Unique electrical and mechanical properties of single-wall carbon nanotubes (SWCNTs) opened many different application areas for these 1D nanostructures. When SWCNTs are coated homogeneously onto surfaces and are thin enough, visible light can transmit through this coating. Due to their metallic or semiconducting characteristics, their random networks also provide conductivity. Unalan et al. used vacuum filtration process for the fabrication of SWCNT thin films.

According to their procedure, first a dilute solution containing, SWCNTs and surfactant is prepared. Then, it is filtered on a membrane. As a result, a homogeneous film is formed on the surface of the membrane. Afterwards, surfactant is washed using deionized water. Then, the membrane is dissolved in a solvent. Finally, SWCNT thin film is transferred onto the desired substrates.

Figure 3.14 (a), (b) and (c) shows SEM and (d) AFM images of SWCNT thin films deposited using different solution concentrations. Two dimensional (2D) surface coverage increase with the SWCNT concentration. In addition, some bundles of SWCNT are also observable in SEM images. Bundling may occur during vacuum filtration process. Figure 3.15 shows the optical transmittance and corresponding sheet resistance values at different SWCNT thin film densities [63].

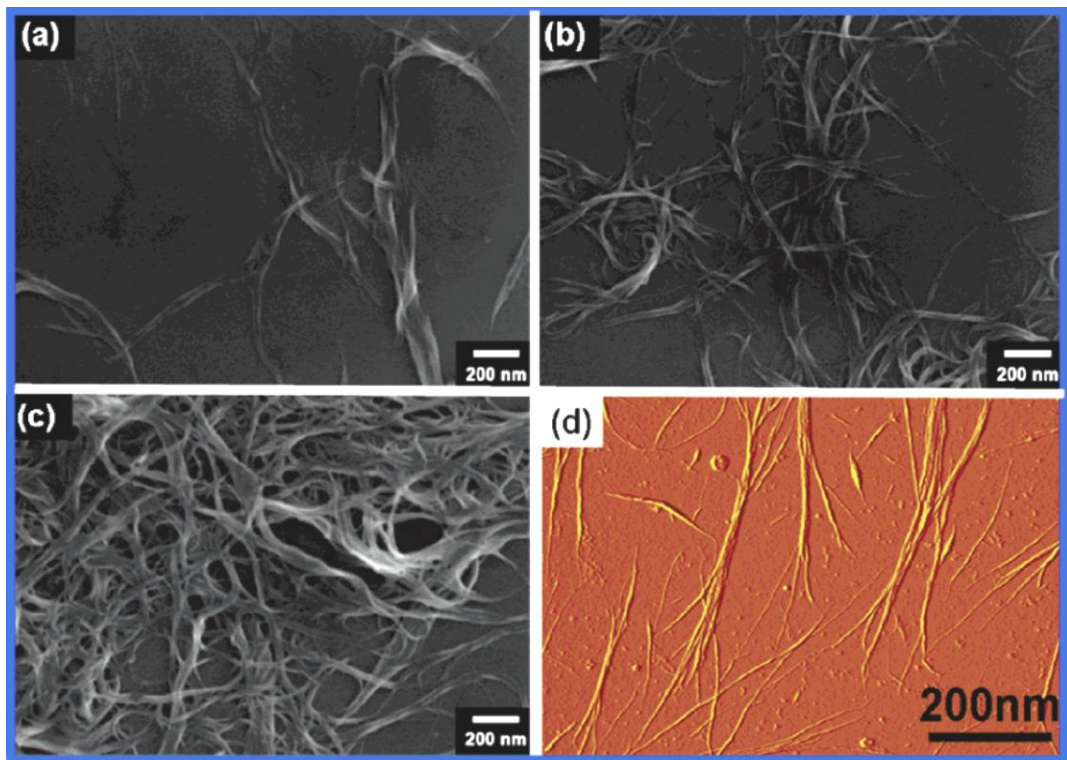


**Figure 3.14** SEM images of SWCNT films deposited from 40 mL SWCNT solutions of (a) 0.2 mg/L, (b) 1 mg/L and (c) 2 mg/L concentrations. (d) AFM image of the 1 mg/L SWCNT thin films showing a mixture of bundled and individual SWNTs [63].

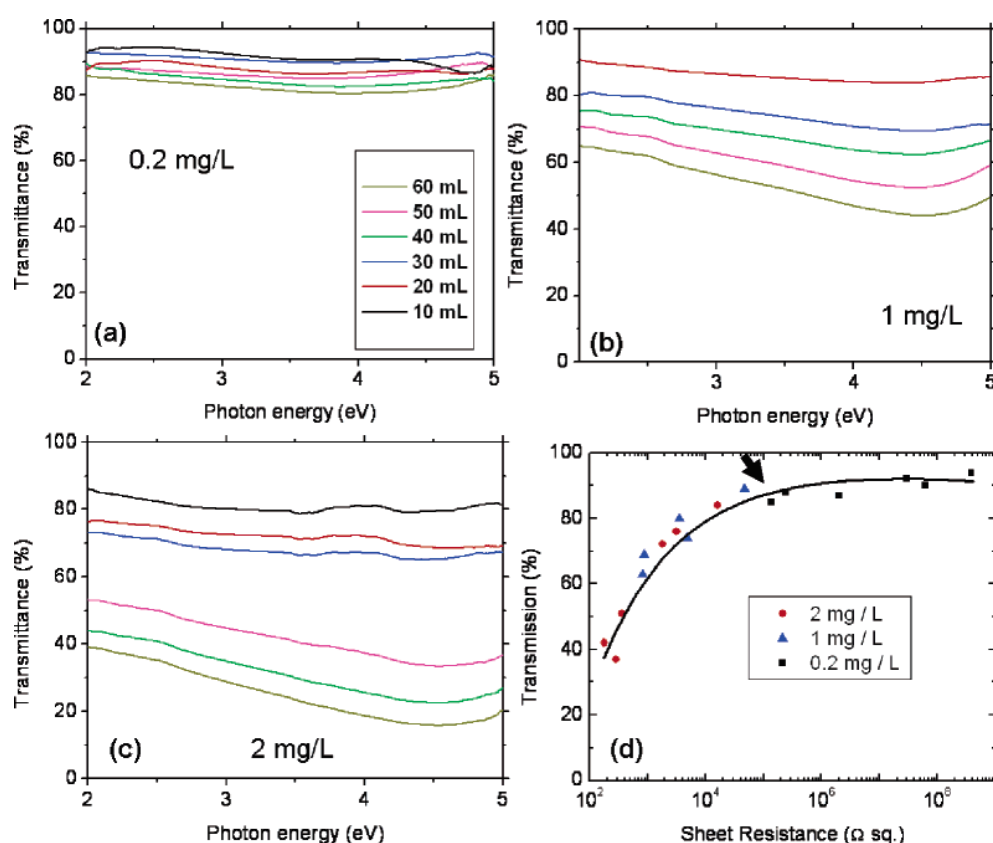


**Figure 3.15** Transmittance of films at three SWCNT concentrations [0.2 mg/L (a), 1 mg/L (b), and 2 mg/L (c)] and six different filtrate volumes. (d) Correlation between film transparency (represented by the transmittance at 550 nm) and sheet resistance. The continuous line is for visual aid. The arrow indicates the approximate position of the percolation threshold of the metallic tubes [63].

### 3.1.4.7 Metal Nano-Fibers

Electrospinning is a versatile technique to fabricate ultra-long fibers in micro and nano-scale. Electrospinning technique is based on the application of a strong electric field in order to draw very thin fibers from a liquid source. Figure 3.16 (a) shows schematic representation of electrospinning method. Electrospinning has been explored as a fast and efficient process to fabricate continuous one-dimensional (1D) nanomaterials composed by polymers, oxides, carbon and more recently, metals [64-68]. Wu et al. [69] dissolved copper acetate in poly(vinyl acetate) (PVA) and it was

electrospun on a glass substrate. The fibers have diameters around 200 nm. Then, a two hours heat treatment at 500 °C was applied for the removal of the polymeric content. In addition, since this heat treatment was applied in ambient atmosphere, the nanofibers were transformed into CuO. Another heat treatment in hydrogen (H<sub>2</sub>) atmosphere at 300°C for one hour to reduce CuO to Cu nanofibers was applied. Figure 3.16 (b) and (c) show SEM images of as fabricated Cu nanofibers. It is also possible to align Cu nanofibers during electrospinning process as it can be seen in Figure 3.16 (g) and (h). When those Cu nanofibers were utilized for the fabrication of transparent conductors, authors obtained a sheet resistance 12 ohm/sq at a visible transparency of 80 %. In addition, due to very high aspect ratio (10000) of those Cu nanofibers, they are found to be highly compatible with flexible substrates.

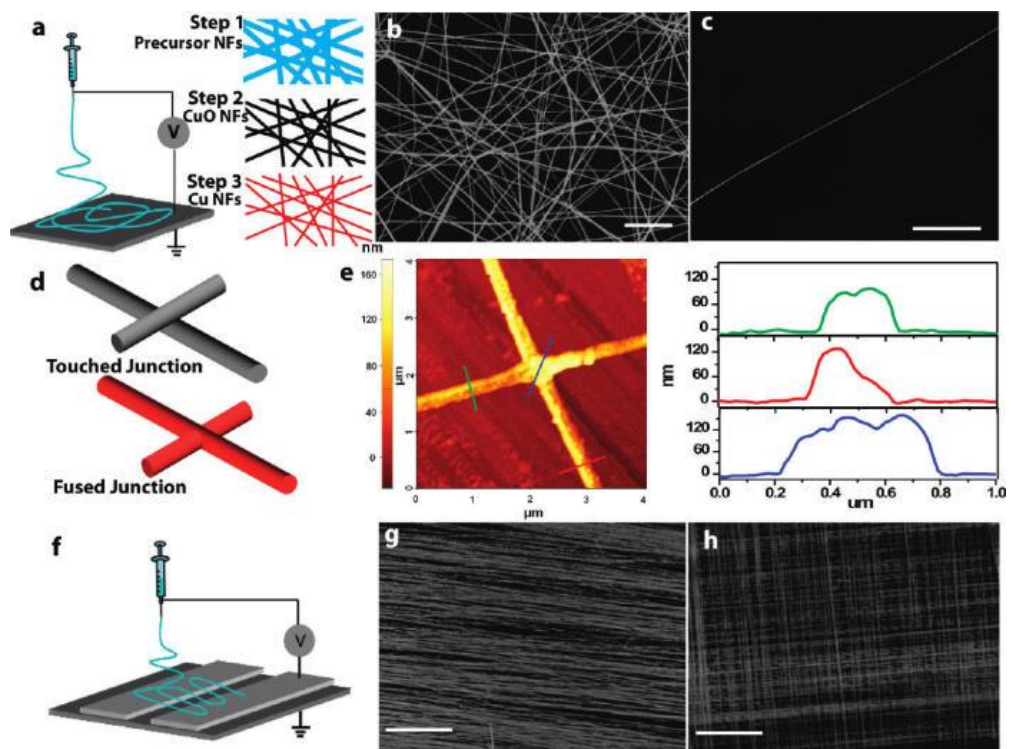


**Figure 3. 16** Fabrication and characterization of Cu nanofibers. (a) Schematic of materials preparation method. Left column: Schematic of an electrospinning setup, shown without a syringe pump. Right column: the fabrication process of Cu nanofibers. In the first step, CuAc<sub>2</sub>/PVA composite fibers were prepared by electrospinning. In step 2, the fibers were calcinated in air to get CuO nanofibers. In

step 3, the CuO nanofibers were reduced to Cu nanofibers by annealing in an H<sub>2</sub> atmosphere. (b) SEM image of Cu nanofibers synthesized by electrospinning. Scale bar is 10 μm. (c) SEM image showing the continuous structure of a Cu nanofiber, indicating a length that can easily exceed 100 μm. Scale bar) 20 μm. (d) Schematic of junctions between solution-processed Ag nanowires (upper) and electrospun Cu nanofibers (down). (e) AFM image of a junction between two nanofibers. The curved lines show the heights of two nanofibers and the cross junction, respectively. (f) Schematic of modified electrospinning setup, oriented nanofibers can be collected on the gaps between two parallel electrodes. (g, h) SEM images of Cu nanofibers with controlled orientations: (g) uniaxially aligned arrays, (h) patterned grids. Scale bar 20 μm [69].

### 3.1.4.8. Sputtered Metal Mesh Electrodes

It is possible to obtain metal mesh structures with the help of a suitable mask. Kim et al. [70] demonstrated fabrication of Cu nano mesh electrodes. The mask with honeycomb network structure was fabricated via ultraviolet (UV) lithography and wet etching method. Then, polycrystalline and single-crystal Cu targets were used in the sputtering. Figure 3.17 (b) and (c) show AFM topography images of Cu thin films on polyimide substrates fabricated using polycrystalline and single-crystalline targets, respectively. Figure 3.17 (d) and (e) show AFM topographical images of honeycomb Cu mesh films fabricated with wet etching technique.

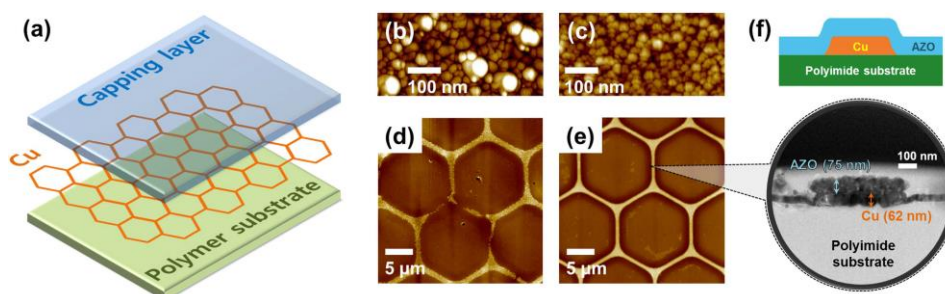


**Figure 3. 17** (a) Structure of the Cu mesh hybrid electrode. (b) and (c) AFM topography images of Cu thin films on polyimide substrates fabricated using a polycrystalline Cu target and a single-crystal Cu target, respectively. (d) and (e)

AFM topography images of Cu mesh electrodes fabricated with wet etching using the two types of Cu thin films in (b) and (c), respectively. (f) Illustration and HRTEM image of the crosssectional structure of a Cu mesh hybrid electrode with Al-doped ZnO as the capping layer and polyimide as the polymer substrate [70].

In order to increase the oxidation resistance of Cu, a capping layer of ZnO or Al doped ZnO was also added to the structure. A sheet resistance of 6.2 ohm/sq was obtained at a visible transmittance of 90%.

### **3.1.4.9. Percolation Theory of One Dimensional Conductors**

#### **3.1.4.9.1. Electrical transport in Metals**

The electrical resistivity of metals has two main components which are namely the residual resistivity ( $\rho_0$ ) and the temperature dependent resistivity  $\rho(T)$ . The intrinsic defects in the metals such as grain boundaries, impurities and vacancies are responsible for the residual resistivity. In addition, the finite diameter contributes to the residual resistivity of the metallic nanowires. On the other hand, the temperature dependent part  $\rho(T)$  of the resistivity may arise from electron-phonon interaction, electron localization and electron-magnon interaction. The electron-phonon interaction ( $\rho_L$ ) which is described by the Bloch-Grüneisen formula is the main reason for temperature dependence of resistivity of non-magnetic metals. However, the electron-magnon interactions are the reason for an additional temperature dependent magnetic contribution ( $\rho_M$ ) to the resistivity of magnetic metals. Hence, the overall electrical resistivity of a metal is given by Eq. 3.1.

$$\rho = \rho_0 + \rho(T) \quad (3.4)$$

$$\rho = \rho_0 + \rho_L + \rho_M \quad (3.5)$$

The electrical, optical and mechanical properties of a random network of 1D nanomaterials are determined by three parameters that (1) the nanomaterial

composition, (2) the nanomaterial geometry, and (3) the morphology of nanomaterials within the random network.

#### **3.1.4.9.2 Electrical transport in 1-D nanostructures**

The dimensionality of nanostructures is determined by the characteristic lengths. Structurally if a nanostructure is confined in two dimensions and free in the third dimension, then it can be called as 1D nanostructured material. For instance, if the physical characteristic lengths get constrained in two dimensions, then the physical/chemical properties are bound to the changes due to finite size statistical mechanical effects/quantum mechanical effects. Depending on the definition, unless there is some or the other forms of quantum mechanical confinement, such systems are termed as quasi one dimensional in nature. Ballistic and diffusive transport mechanisms are two main mechanism to categorize electronic transport of low-dimensional materials systems.

#### **3.1.4.10. Electrical properties of random networks**

Conductive 1D nanostructures may form a percolating network for charge transport. This network may exhibit very high conductivity at low thicknesses. Each individual nanostructure act as a metaphorical “highway” to efficiently transport charge along a confined pathway, which subsequently combine to form a web of conducting channels that enable volumetric flow of charge. These channels may be straight nanostructures such as Ag NWs or nanostructures with high degrees of curvature such as SWCNTs. The low thickness and high porosity of the conductive network promotes other additional beneficial features that are challenging to achieve with solid thin-films, such as high flexibility and high total transmittance.

### 3.1.4.11 Optical properties of random networks

In conjunction with a high conductivity, random networks of 1D nanostructures may exhibit decent optical properties. Ag NWs in particular are widely demonstrated to form random networks that exhibit high total transmittance and simultaneously a low sheet resistance. However, a unique optical problem associated to these networks is the diffuse light scattering or transmission haze. The length and diameter of individual Ag NWs affect their extinction coefficient and thus dictate their scattering interactions. But any understanding of the transmission haze through a random network of Ag NWs or its impact on device functionality is limited. In order to understand how nanowire networks, form a conductive pathway a 2D percolation model can be used. In this particular case, the percolating system is the nanowire network and the open paths are the connections through which electrons can travel. A percolation model is a collection of points distributed in space, certain points of which are said to be adjacent or linked [71]. The band percolation theory deals with conduction processes in electronic devices. The theory is used to describe the connection dependent, insulator to conductor transition in networks of conductive fillers on insulating substrates [72]. The conductivity is provided in 1D network density. For example, up to a certain value of density of nanowires, conductivity cannot be provided and network behaves like an insulator. Percolation threshold defines critical density of conductive fillers that insulator to conductor transition takes place. Figure 3.18 shows representative image of how 1D structures are distributed on a 2D surface randomly. As the number of 1D structures increases (Figure 3.18 (a) to (d)) the possibility of the sticks to touch each other increases. Hence, over a certain density those 1D structures can become conductive.

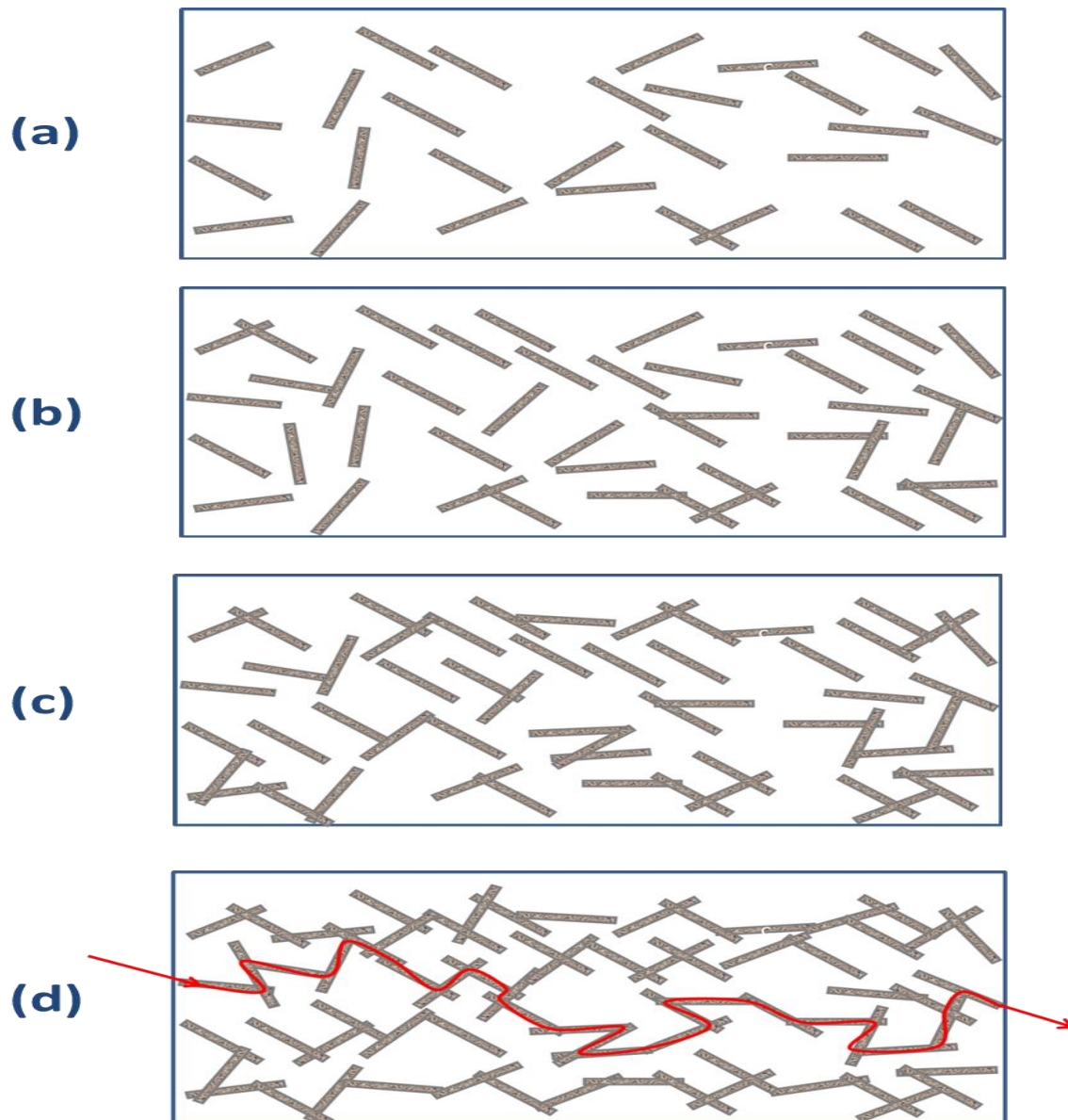


**Figure 3.18** Schematics showing how 1D structures can provide suitable paths for charge transport.

The following three conditions must be satisfied in order to obtain a random nanowire network. These conditions follow the definition of a random network promoted by Kallmes and Corte (1961) [73]:

1. Random distribution of the nanowires on a 2D surface is crucial.
2. Orientation of the nanowires on 2D surface must be uniform and random. In addition, equal probability of falling at any angle is required.

3. Deposition of the nanowires should be independently of one another.

According to the standard percolation theory, the density dependent conductivity behavior of 1D structures is given by

$$\sigma \propto (N - N_c)^\alpha \quad (3.5)$$

, where  $\sigma$  is the conductivity in three dimensions, or sheet conductance in two dimensions,  $N_c$  is the critical nanowire density required for the onset of electrical conduction in a random network, and  $\alpha$  is a critical exponent which depends on the dimensionality of the space involved. The theoretical values of  $\alpha$  are 1.33 for a 2-D percolation network and 1.94 for a 3-D percolation network [73]. For a 2-D network, the sheet resistance ( $R_{sh}$ ) is given by  $R_{sh} = 1/\text{sheet conductance}$ , and the relation between  $R_{sh}$  and volume ( $V$ ) of the nanowire solution can be given the equation provided above as follows:

$$R_{sh} \propto (V - V_c)^{-\alpha} \quad (3.6)$$

For instance, Figure 3.19 shows the variation of sheet resistance with the volume of Ag NW solution used by Madaria et al. [73], and the solid line represent the fitted curve obtained using the given equation. In order to obtain the fitting curve, the value of  $V_c$  has been taken 0.20 mL as this was the minimum volume required to achieve a conducting film. Theoretically, for a model involving random distribution of nanowires [73],  $N_c$  for nanowires with length  $l$  is given by

$$l\sqrt{\pi}N_c = 4.236 \quad (3.7)$$

Substituting the length of Ag NWs (12.5  $\mu\text{m}$ ) in the above equation, the critical density for the networks are calculated to be 0.03657  $\mu\text{m}^{-2}$ . As the critical density is substituted in in equation, the resulting theoretical critical volume  $V_c$  is found as 0.18 mL, which is very close to the experimentally observed critical volume of 0.20 mL. It was noticed that the value of the critical volume obtained experimentally is a little higher than the theoretical value, which can be attributed to the formation of multilayer stacking of nanowires in some regions rather than an ideal monolayer [73].

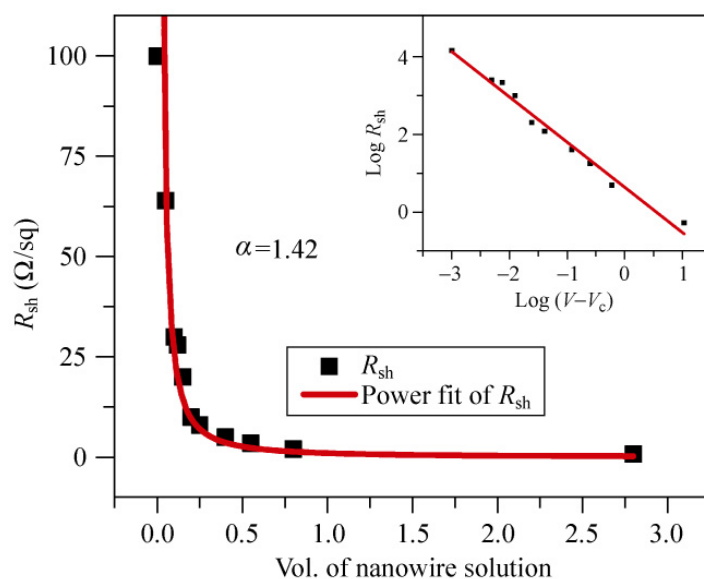


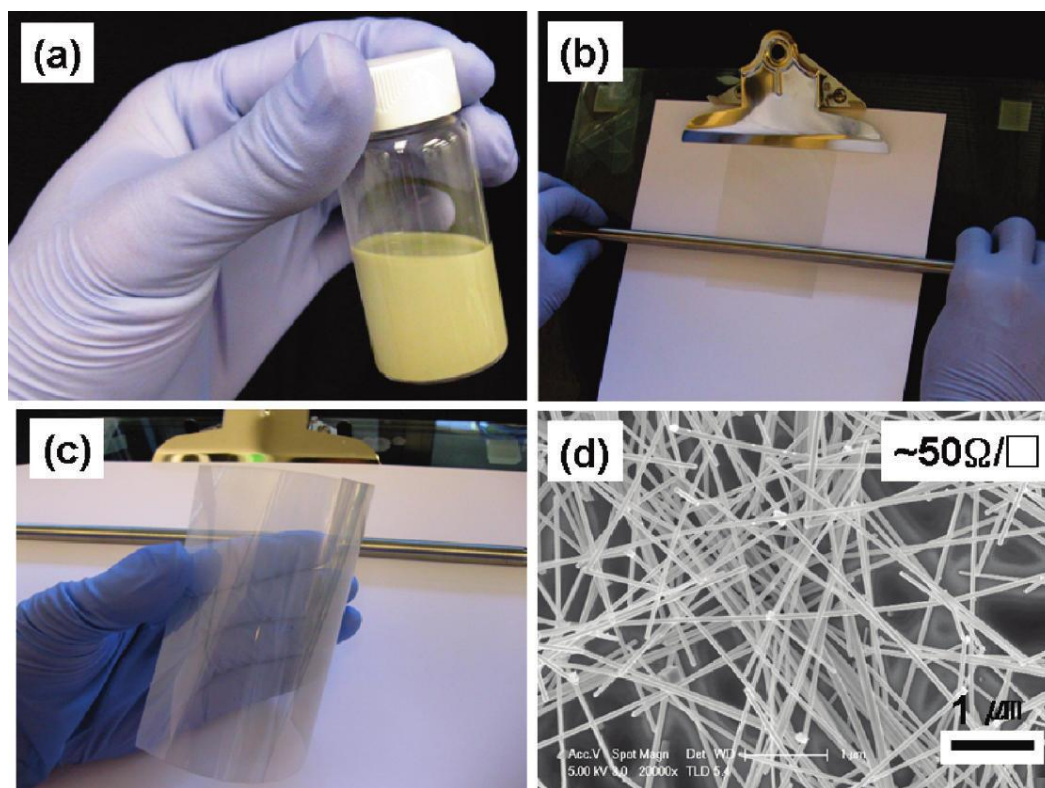
**Figure 3.19** Graph of the sheet resistance versus volume of Ag NW solution. The onset of conduction across the sample occurs for  $V_c = 0.2$  mL. The power fit of the data indicated value of critical exponent  $\alpha = 1.42$ . The inset shows the logarithmic plot of the data with a linear fit [73].

The best fit of equation in Fig. 3.19 is obtained by using  $\alpha = 1.42$ , which is quite close to the value predicted for the 2-D theoretical model. The discrepancy between experimental and theoretical values may indicate that the nanowire film is not a perfect 2-D film, and actually has an intermediate character between 2-D and 3-D. As a result, the experimental value is between that for 2-D ( $\alpha = 1.33$ ) and 3-D ( $\alpha = 1.94$ ). The inset shows the logarithmic fit of the above equation, resulting in a linear plot with good agreement between the experimental and predicted values [74].

### 3.1.4.6. Transparent and Conducting Silver Nanowire Networks

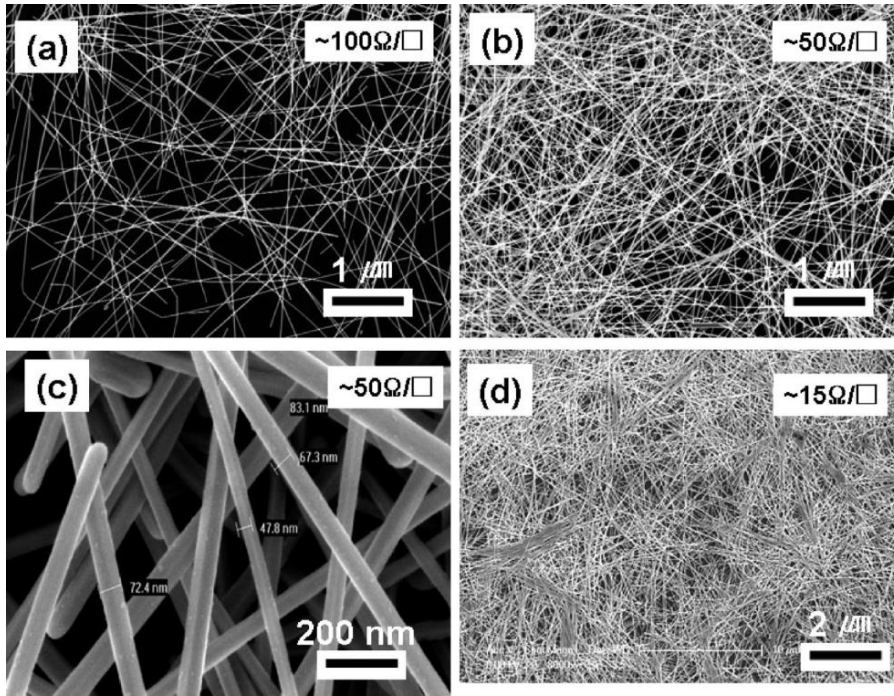
After demonstration of SWCNT thin film transparent electrodes, scientist looked for new 1D alternatives. Surely, conductive 1D nanostructures are needed for transparent conductors. Hence, metals were first candidates especially the ones with high conductivity such as gold, silver and copper. Among these metals, Ag can be synthesized in nanowire form using relatively simple and economical methods. In 2010, first comprehensive study of transparent and conducting Ag NW networks has been published. Hu et al. produced Ag NWs via seed-mediated method and deposited

them onto substrates [75]. Ag NWs were purified and then redispersed in ethanol. Figure 3.20. (a) shows photograph of Ag NW ink solution. Meyer Rod technique was used for the deposition of Ag NWs onto glass and PET substrates.



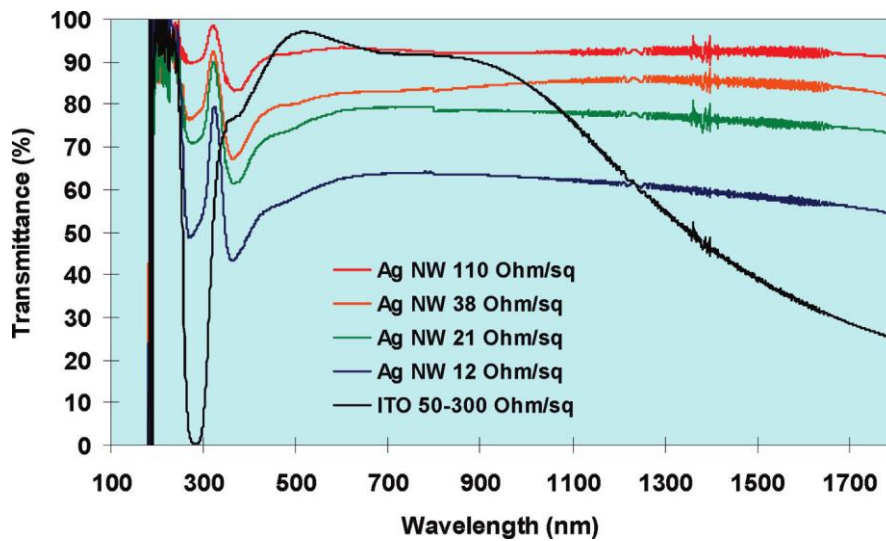
**Figure 3. 20** (a) Photograph of Ag NW ink in ethanol. (b) Meyer rod coating setup for scalable Ag NW coating onto plastic substrates. (c) Finished Ag NW film coating on PET substrate. The Ag NW coating looks uniform over the entire substrate shown in the figure. (d) A SEM image of Ag NW coating shown in panel (c). The sheet resistance was  $50 \Omega/\text{sq}$  [75].

Figure 3.21 shows the SEM images of Ag NW networks with different densities and thus, different sheet resistance values. As the density of Ag NWs increases in the networks, sheet resistance decreases.



**Figure 3.21** SEM images of Ag NW films with different densities. The different densities of Ag NW films lead to different sheet resistances: (a) 100, (b and c) 50, and (d) 15  $\Omega$ /sq. The diameters of the Ag NWs are in the range of 40-100 nm [75].

In Figure 3.22, transparency values of Ag NW networks are compared to a commercially available ITO thin film. The best reported transparency and sheet resistance values for these networks were 80% and 38 ohm/sq, respectively.



**Figure 3.22** Optical transmittance of Ag NW network electrodes compared to a commercial ITO thin film [75].

After the first demonstration of Ag NW networks, different research groups have paid attention on this topic. Hence, different approaches have been offered for the production of Ag NW networks. In fact, some companies started to offer Ag NW dispersions such as Seashell Technologies and Blue Nano. Madaria et al. obtained Ag NW suspensions from Seashell Technologies [73]. Polydimethylsiloxane (PDMS) stamping method was used for the production of Ag NW networks, schematics of which are provided in Figure 3.23 (a). In this method, briefly, Ag NW suspension is filtered through anodic aluminum oxide (AAO) filters. Then a PDMS stamp is pressed onto AAO membrane. Hence, Ag NWs are transferred onto the PDMS stamp. After that, this PDMS stamp is pressed onto glass or PET substrates and peeled off. As a result, Ag NWs are successfully transferred onto these desired substrates in the form of a network. By controlling volume of solution which is filtered through AAO membrane, density of Ag NW networks can be adjusted. Images of Ag NWs/PET electrodes are provided in figure 3.23 (b) to (e). In addition, SEM images of Ag NW networks with different densities can be seen in Figures 3.23 (f) to (i).

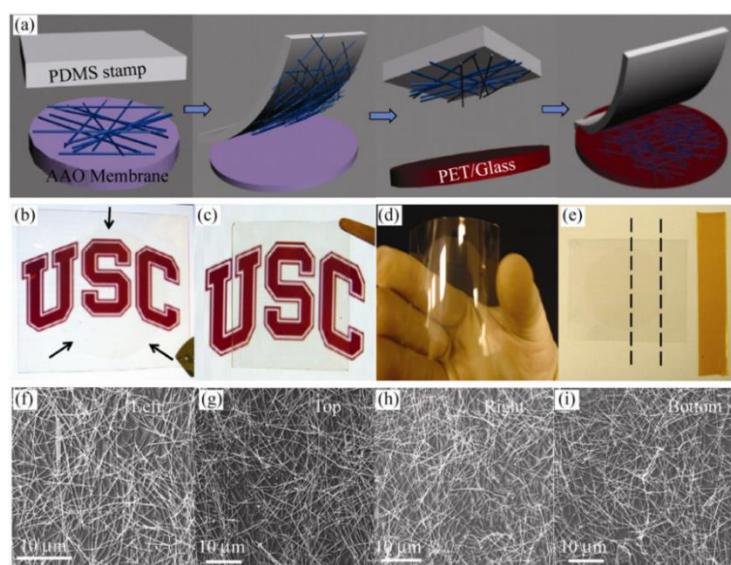


**Figure 3.23** (a) Schematic representation of the transfer process. (b) Photograph of an Ag NW film transferred onto PET. (c) Photograph of a nanowire film on glass substrate. (d) Photograph of a nanowire film on PET showing the flexibility of film. (e) Photograph showing the results of adhesion tests. Nanowires remain adhered to the PET substrate when sticky tape was peeled off from the area shown by dotted

lines. SEM images of the different regions of the film shown in Fig. 1(b), demonstrating uniformity of the film across the entire area [73].

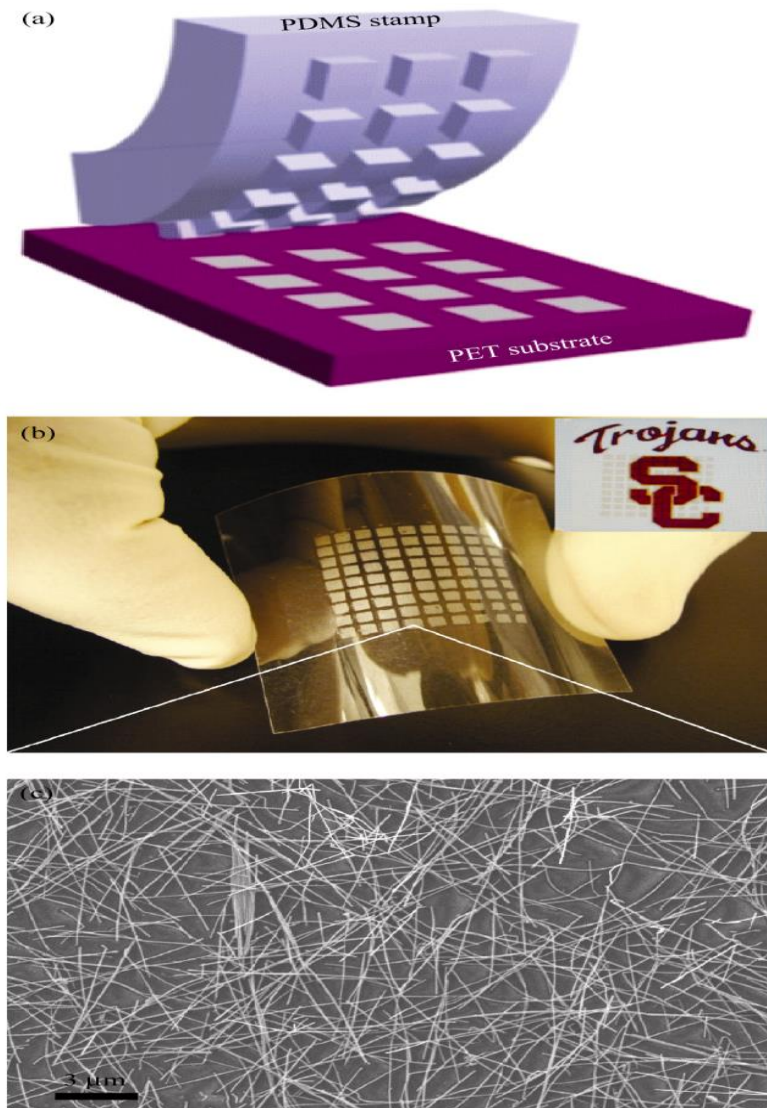


**Figure 3.24** Patterned transfer of Ag NW film. (a) Schematic diagram of the patterned PDMS stamp in contact with the nanowire film. (b) Photograph of patterned nanowire film transferred to the PET substrate. The size of each pixel is 1 mm  $\times$  1 mm. (c) SEM image showing the nanowire network in one pixel [73].

Since PDMS can be fabricated in a patterned form, Ag NW networks can also be patterned. Figure 3.24 (a) shows schematic illustration of patterned PDMS stamp. Same procedure is applied for the patterned PDMS stamp for deposition. As a result,

patterned Ag NW networks can be obtained. Figure 3.24 (b) and (c) show a photograph and SEM image of patterned Ag NW networks, respectively.

Figure 3.25 (a) shows sheet resistance vs. transmittance graph of Ag NW networks. Even after purification processes, there is still a thin PVP layer on lateral surfaces of Ag NWs. This thin polymer layer increases the contact resistance of Ag NWs. A simple annealing process eliminates this problem. Figure 3.25 (c) shows how sheet resistance of Ag NW networks changes with the annealing process. Annealing causes fusion of Ag NWs at contact points. Hence, contact resistance and sheet resistance of the networks decrease. Figure 3.25 (b) shows how Ag NWs are fused at junction points after annealing. Ag NWs networks with different nanowire densities are provided in Figure 5.25 (d).

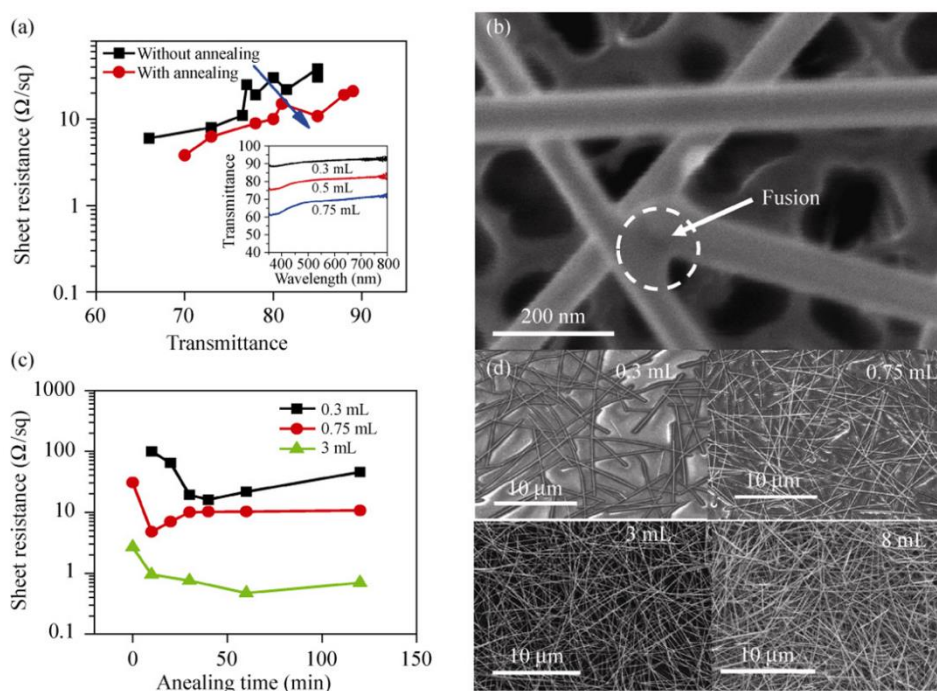


**Figure 3.25** (a) Plot of sheet resistance versus transmittance at a wavelength of 550 nm of Ag NW networks. Black dots represent resistance values for films without annealing and red dots represent resistance values after annealing the film samples at 200 °C for 20 min in air. Inset shows the transmittance spectra of nanowire networks with different thicknesses. (b) SEM image of an annealed nanowire sample showing melting of nanowires at the ends and subsequent joining with neighboring nanowires.

(c) Variation of sheet resistance with the annealing time for nanowire networks of different densities. Sheet resistance decreased initially on annealing and subsequently increased with further annealing. (d) SEM images of nanowire networks prepared using various amounts of nanowire solution. Nanowire density increases with increased volume of the solution [73].

Properties of ITO and its alternative TCCs are compared in Table 3.2. Comparison parameters cover traditional TCC characteristics and recent demand in market. Among the alternative TCCs to ITO, Ag NW networks seem to be the most promising candidate due to their similar if not better properties compared to commercially available ITO.

**Table 3.2** The comparison between ITO and other alternative transparent conductors [73].

	ITO	CNT	Graphene	PEDOT:PSS	Silver grid	AgNWs film
Scalable Fabrication	PVD	Spray Printing	Spray Printing	Spray Printing	Printing	Spray Printing
Optoelectronic performance (highest value of $\sigma_{DC}/\sigma_{Op}$ )	Excellent 330	Median 35	Median 11	Median	Excellent	Excellent 450
High NIR transparency	No	Yes	Yes	No	Yes	Yes
Flexibility	No	Yes	Yes	Yes	Yes	Yes
Abrasion resistance	Yes	Yes	Yes	No	Yes	Yes
Work Function (eV)	4.7	4.7-5.1	4.6-4.7	5.0	4.26	4.26-5.1 <sup>a</sup>
Surface roughness	Excellent	Median	Excellent	Excellent	Poor	Excellent
Thermal stability	Excellent	Excellent	Excellent	Median	Excellent	Excellent
Chemical stability	Excellent	Excellent	Excellent	Median	Median	Median

### 3.2. Experimental Details

Figure 3.26 shows the flowchart for the fabrication of Ag NW networks that has been used for this work. As synthesized nanowire solution is a mixture of Ag NWs, Ag nanoparticles (NPs), PVP and EG. So, a purification process is needed in order to obtain pure Ag NWs. Purification process starts with centrifugation process. In the first step of centrifuge process, solution is diluted with acetone in a ratio of 1/10 ratio and then centrifuged at 8000 rpm for 20 min. This process is repeated twice. Hence, PVP, EG and some Ag NPs are separated from Ag NWs. Following second centrifuge process, remaining Ag nanostructures are dispersed in ethanol. A third centrifuge process is then applied with the same parameters. Purified Ag NWs are re-dispersed in ethanol and used for the characterization and network fabrication.

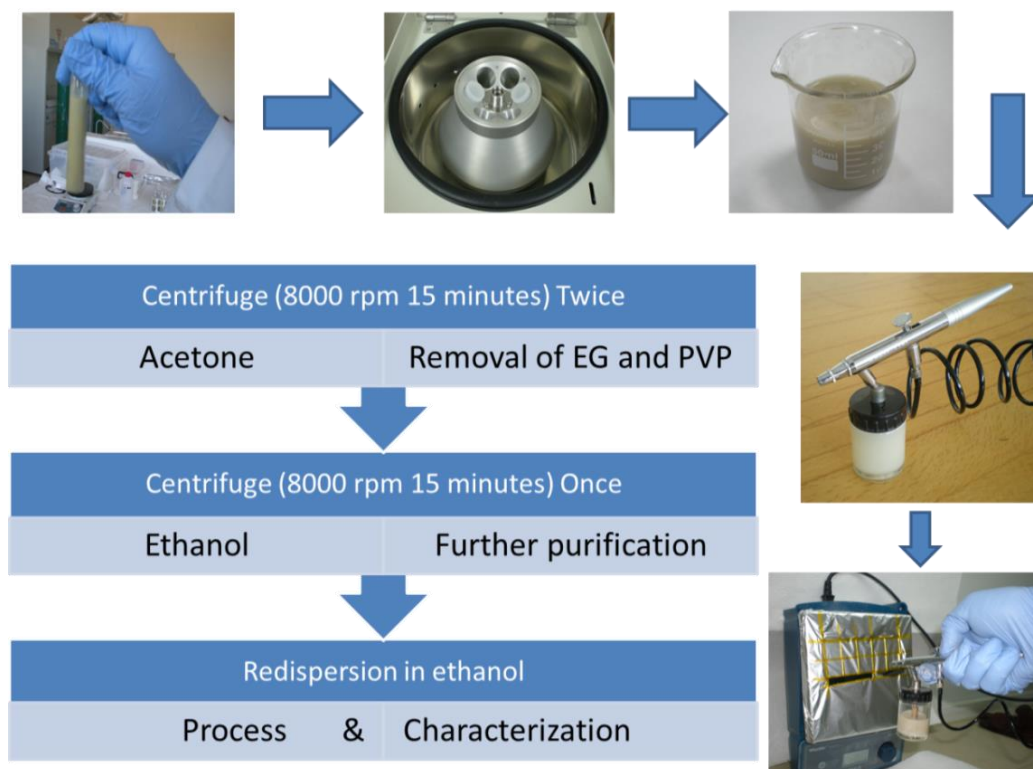


**Figure 3.26** Flow chart showing the nanowire purification and deposition of Ag NWs onto substrates [48].

Produced ethanolic Ag NW suspension is then used for the fabrication of Ag NW networks. An air brush feeded with nitrogen and a hot plate is used for the deposition process. Firstly, substrates to be coated with Ag NWs, such as glass or PET, undergo

a cleaning procedure. Using bath sonication, they are cleaned in acetone, 2-propanol and deionized water (DI water) for each at least for 5 minutes. Right after, they are dried with nitrogen gas. Then they are mounted onto a hot plate using a heat resistant tape. As it is seen from Figure 3.26, a slice of silicon wafer is also mounted for SEM analysis. Then hot plate is heated to 150°C. This temperature is needed for the instant evaporation of ethanol. So then the agglomeration of Ag NWs can be prevented. Using a nitrogen fed air brush, Ag NW/ethanol suspension is spray coated onto the substrates. Pressure of air brush and the distance between air brush and hot plate effect the coating process. So, these parameters must be kept constant for reproducibility. In our experiments, air brush pressure was set to 2 atm and the distance was kept at 10 cm. Density of Ag NWs on substrates can be simply adjusted by controlled by the number of spraying coating cycles.

Figure 3.27 shows a representative SEM image of Ag NW network fabricated through spray coating. It is clear that, the density of Ag NWs is enough to provide percolation. Red line shows one of these possible percolating paths for charge transport.

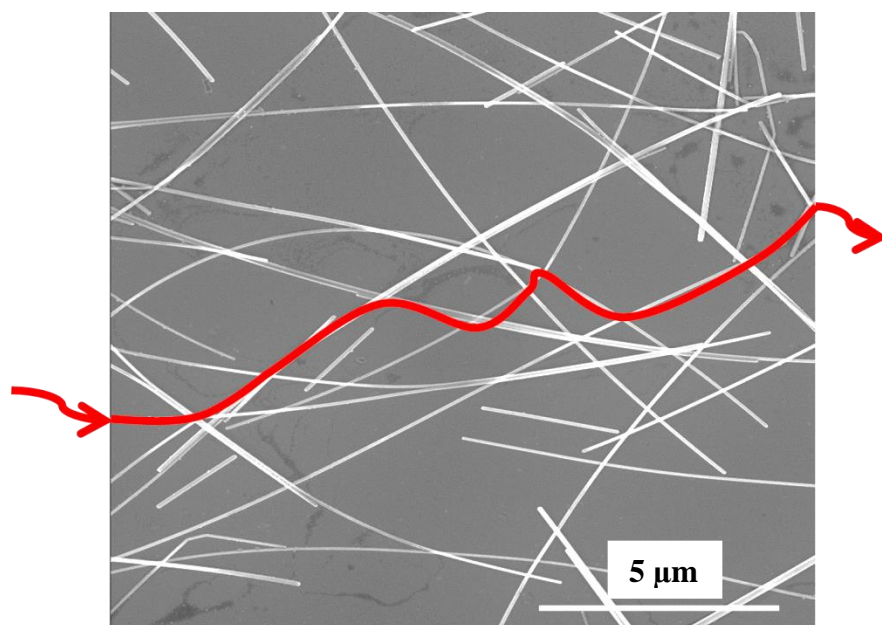


**Figure 3.27** Representative SEM image of Ag NW network and possible path for charge transport.

### 3.3 Device Characterization Methods

#### 3.3.1 Scanning Electron Microscopy (SEM)

Transparent and conducting Ag NW networks were analyzed by FE-SEM (Nova NanoSEM 430) under 10 kV. No conductive coating was used for SEM analysis.

#### 3.3.2 Sheet Resistance Measurements

Sheet resistance measurement was done using Keithley 2400 sourcemeter. In order to measure sheet resistance values of Ag NW networks precisely, a two probe measurement setup was prepared. Figure 3.27 shows two probe sheet resistance measurement set up that was used for the measurements. Gallium-indium eutectic alloy (GaIn) is used for measuring sheet resistance of Ag NW networks. This was necessary because Ag NW networks are not forming a continuous film. In addition, two probe sheet resistance measurement approach can give reliable results for low sheet resistance systems. As read resistance value was used in the given formula and the sheet resistance (ohm/sq) of the networks was obtained. The sheet resistance measurements were performed by doing a +/-1V I-V scan at 100 mV/s between two gallium contacts of diameter  $D = 1.5$  mm and separated by a distance  $L = 3$  mm. The formula used to calculate surface resistance was,

$$r = (V/L) / (IS/D) \quad (3.8)$$

, where  $V$  is the voltage and  $IS$  is the current across the measured area [48].

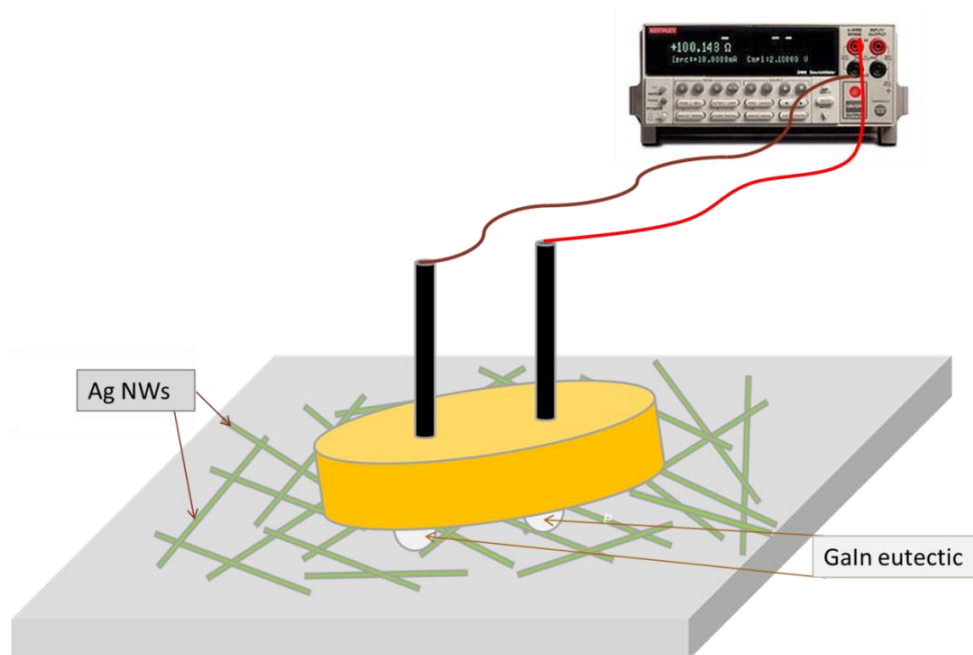


**Figure 3.28** Schematic of the two probe measurement set-up used for obtaining the sheet resistance values of Ag NW networks [48].

### 3.3.3 Transparency Measurements

The optical analyses of the Ag NW networks were performed by UV-VIS spectroscopy (using with Varian-Cary100 Bio) within the wavelength range of 300 - 800 nm at room temperature in the normal incident mode. In UV-VIS analysis, clean glass substrates were used for the baseline correction. Figure 3.29 shows representative set-up for transparency measurements of Ag NW networks [48].

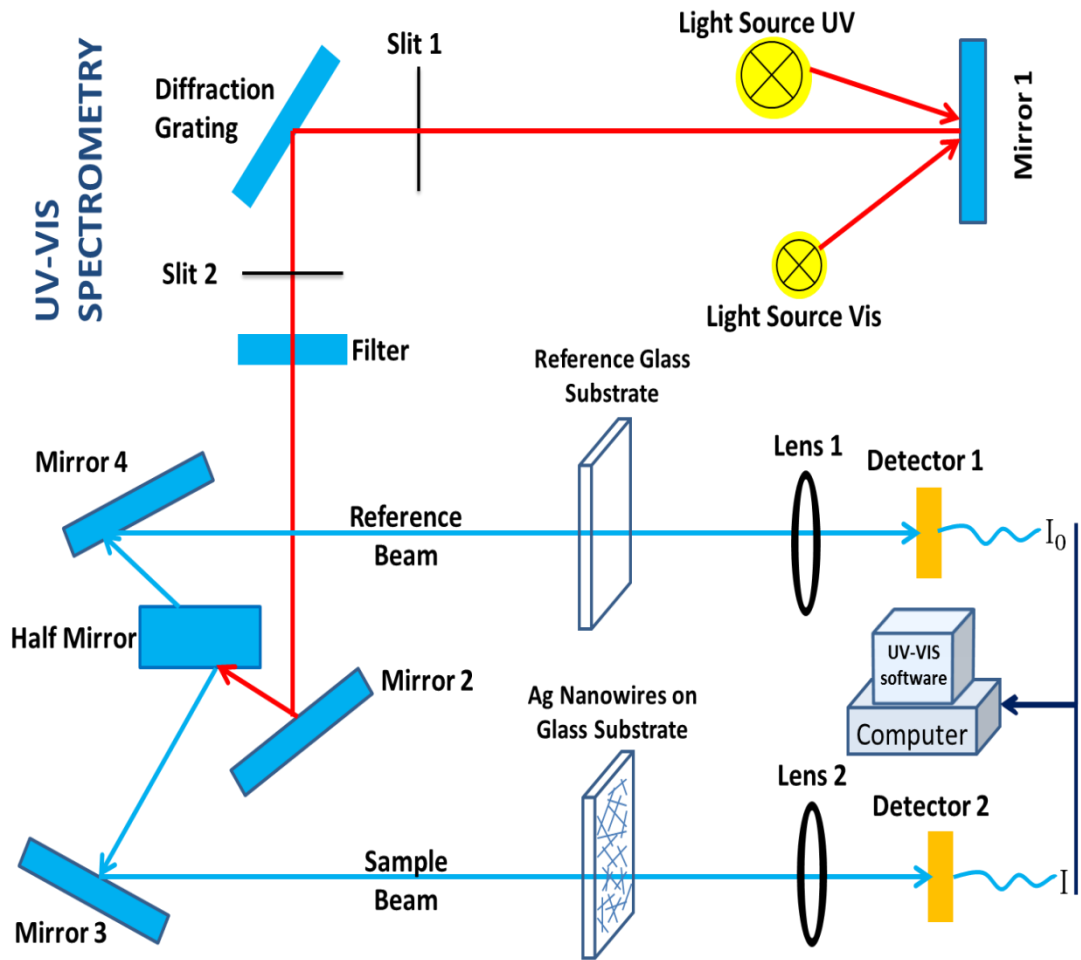


**Figure 3. 29** UV-VIS spectroscopy set-up for transparency measurements of Ag NW networks [48].

### 3.4. Results

Top and 35° inclined SEM images of spray coated Ag NW networks are shown in Figure 3.30 (a) and (b), respectively. A photograph of the Ag NW networks on a glass substrate is shown in Figure 3.30 (c), where the METU logo behind the substrate is clearly apparent revealing the transparency of the networks. Figure 3.30 (d) shows the length distribution of Ag NWs. Average length of the nanowires is measured to be 8  $\mu\text{m}$ .

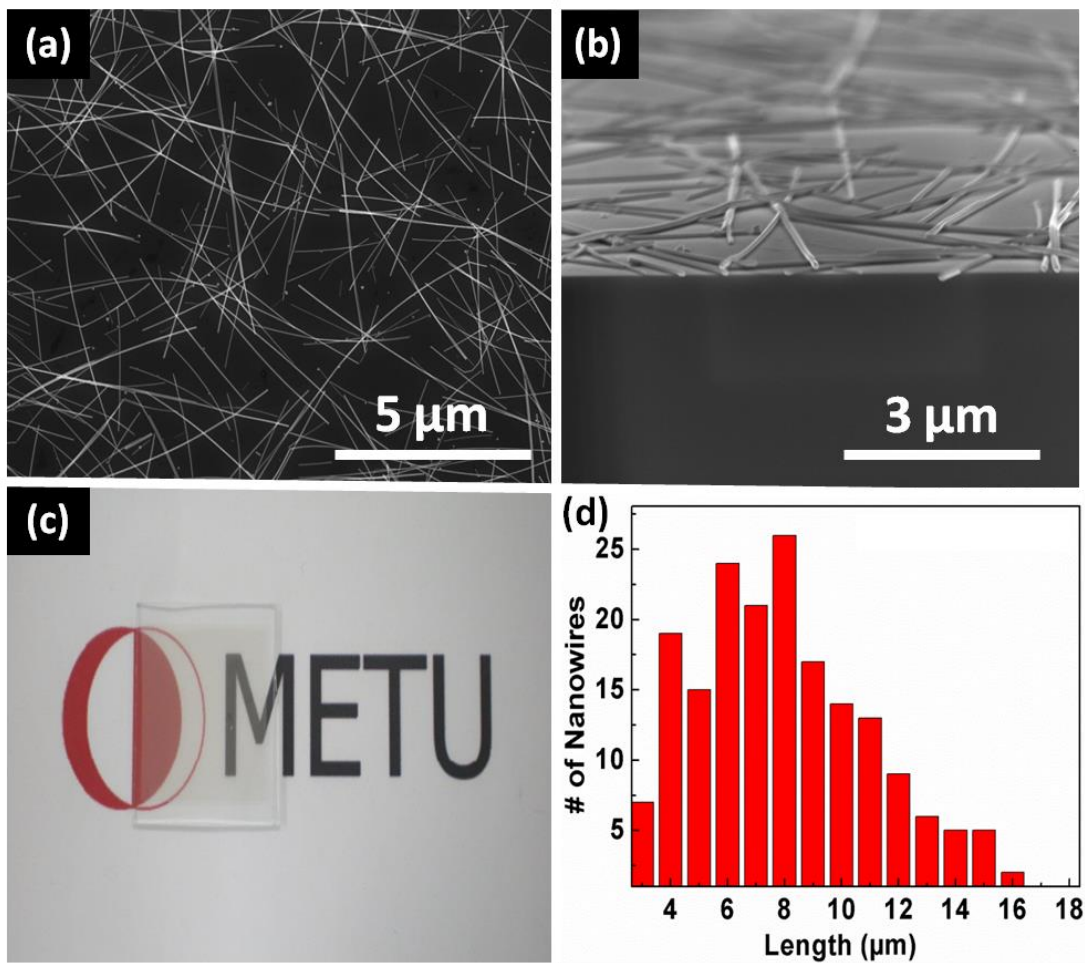


**Figure 3.30** SEM images of top view (a) and 35° inclined view (b) of Ag NW networks fabricated in this work. (c) Photograph of Ag NW networks on a glass substrate. (d) Length distribution of Ag NWs used for the fabrication of networks [76].

### 3.4.1 Effect of Density

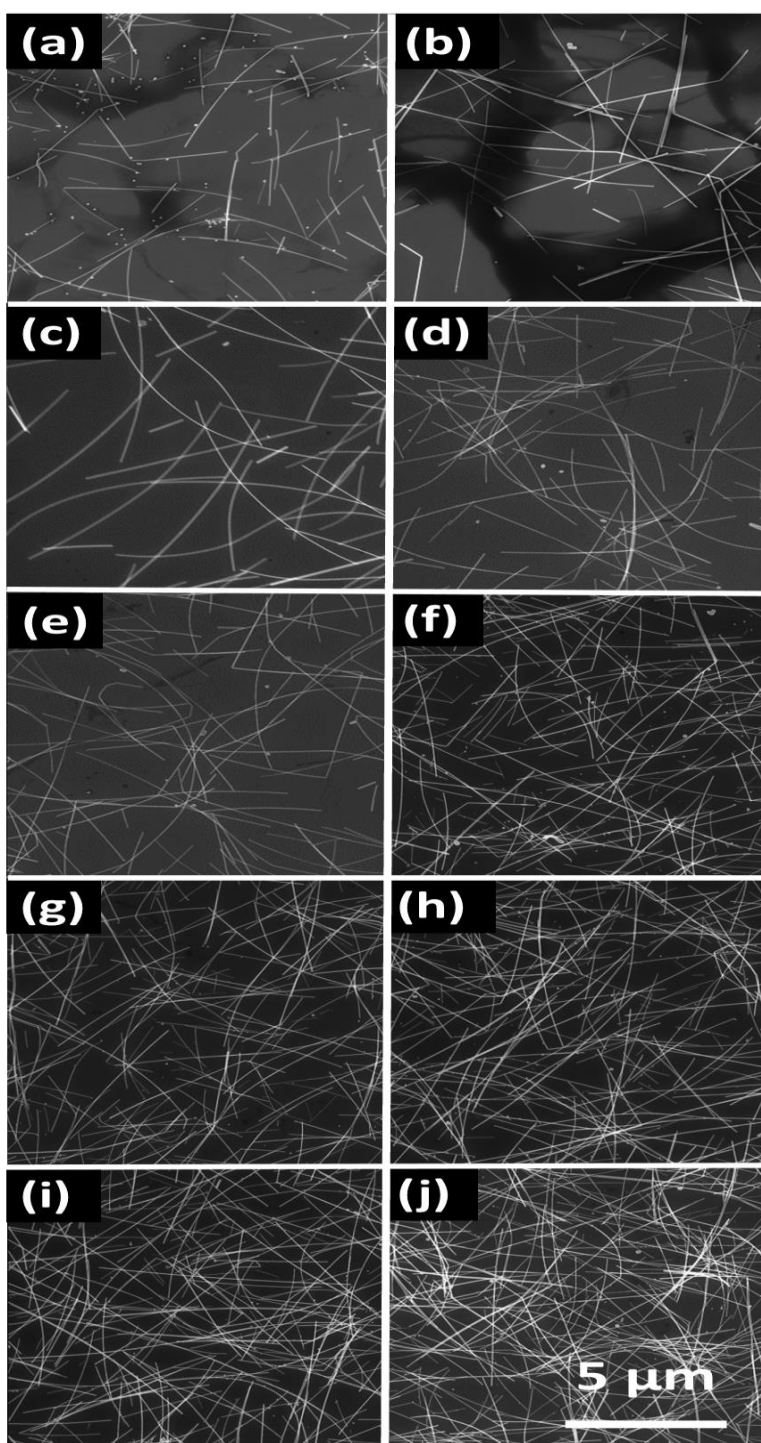
Figure 3.31 shows SEM images of Ag NW networks with different densities. Densities of these Ag NW networks are calculated using a freeware called Image J. Firstly, many different SEM images of the samples are taken. Then, the area covered by nanowires was calculated. Also, area of a single nanowire was calculated using average diameter and the length value. Hence, the density of nanowires on substrates

were obtained. As it is seen from SEM images, with the nanowire density on substrate, the area covered

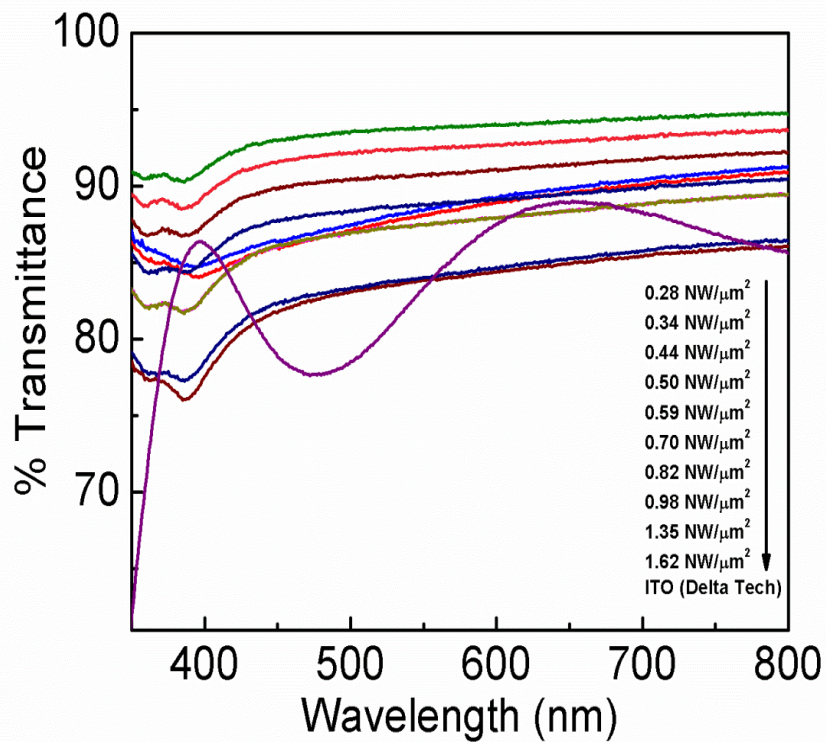
by nanowires increases. In addition, more possible paths are provided for the transport of electrical charges.

Figure 3.32 shows transmittance spectra of Ag NW networks with different nanowire densities. As it is seen from the figure, as the density of nanowires increases transparency decreases. However, increasing nanowire density also decreases sheet resistance of the networks. As described before, controlling nanowire density via spray coating is quite straight forward. Hence, one can easily produce Ag NW networks with desired sheet resistance and transparency values. Transmittance spectrum for a commercially available ITO coated glass substrate is also provided for comparison. Although Ag NW networks have quite smooth transmittance in visible range, commercial ITO gives a wave-like behavior.

Figure 3.33 shows absorption behavior of Ag NW networks, SWCNT thin films and commercial ITO starting from visible spectrum to near infrared (NIR) region. Although commercial ITO film has an increased absorption over a wavelength of 1000 nm, Ag NW networks keep constant absorption behavior in visible and NIR region as well. For Ag NW based transparent conductors, nanowires' junction regions are responsible for any absorption in the visible wavelength range, since the diameters of Ag NWs are less than 100 nm. As the nanowire density increases on a transparent substrate the size of those junction points increases (not linearly) so that the visible transparency decreases. Figure 3.34 shows how transparency changes with respect to the nanowire density. As it can be seen, the graph has different slopes at different nanowire densities. Although the change in visible transmittance is very high at low nanowire densities, it is very low when the nanowire density is over  $1.4 \text{ NW}/\mu\text{m}^2$ .



**Figure 3.31** SEM images of Ag NWs networks with different densities of (a) 0.28, (b) 0.34, (c) 0.44, (d) 0.50, (e) 0.59, (f) 0.70, (g) 0.82, (h) 0.98, (i) 1.35 and (j) 1.62  $\text{NW}/\mu\text{m}^2$ .



**Figure 3.32** Transmittance spectra of Ag NW networks with different densities [76]. Transmittance spectrum for a commercial ITO thin film is also provided for comparison.

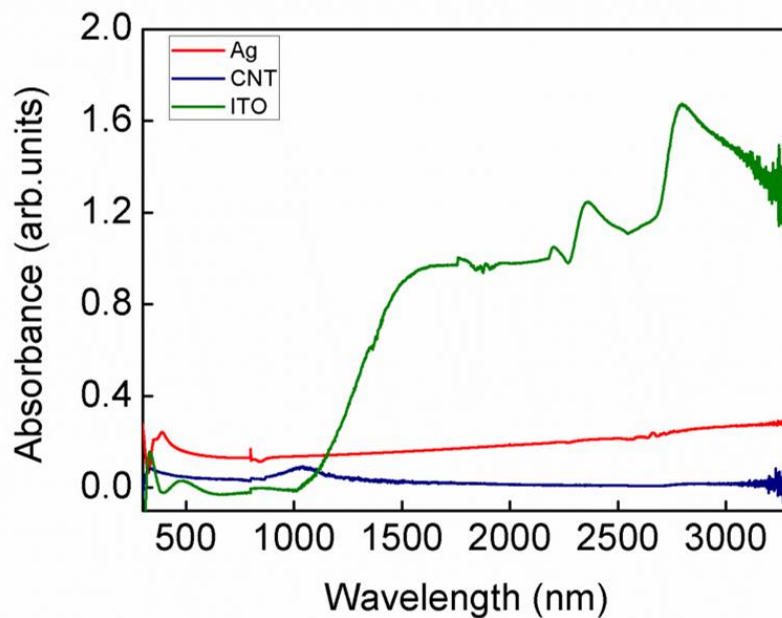


**Figure 3.33** Absorption spectra of Ag NW networks, SWCNT thin films and commercial ITO.

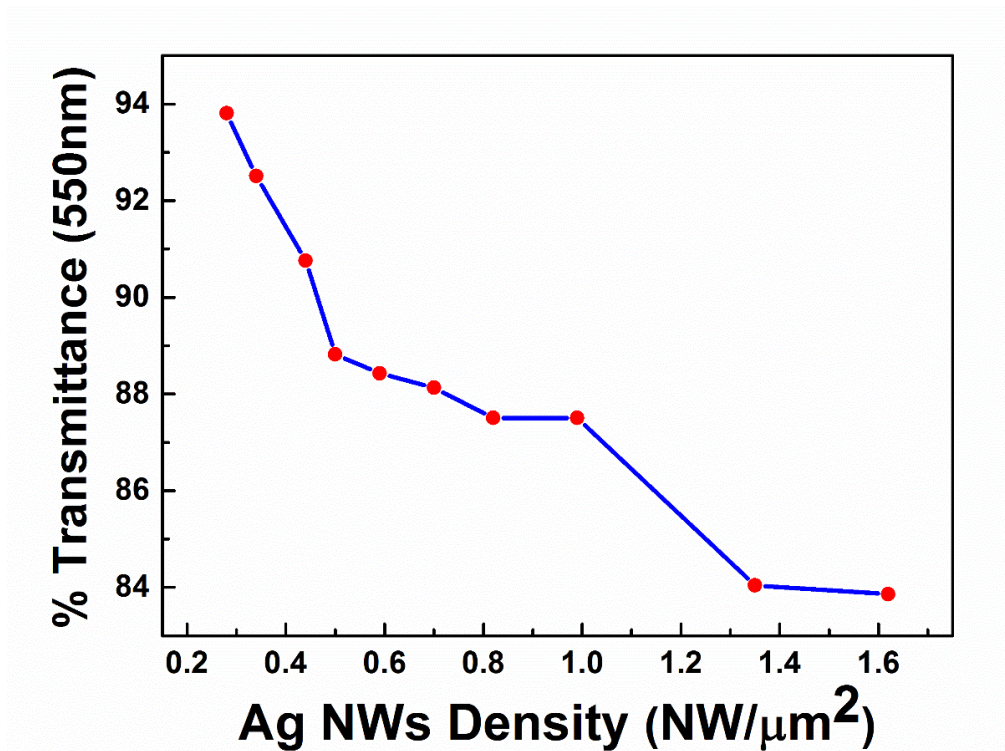


**Figure 3.34** Change in transmittance of Ag NW networks at different nanowire densities.

### 3.4.2 Effect of Annealing Temperature

Ag NW networks were subjected to annealing at different temperatures. All annealing processes were conducted for 30 minutes and corresponding SEM images for the samples annealed at 100, 200, 300, 400 and 500°C are shown in Figure 3.35 (b) - (f), respectively. For comparison, SEM image of the as-deposited sample is also provided in Figure 3.35 (a). Residual PVP layer can be clearly seen for the as-deposited sample. Annealing at 100°C was found to be insufficient for the complete removal of PVP from the lateral surfaces of Ag NWs, as shown in Figure 3.35 (b). Evidenced by the removal of PVP layer and conservation of the nanowire morphology, annealing at 200°C was found to be suitable. Further increase in temperature to 300°C caused Ag NWs to break up, as shown in Figure 3.35 (d) leading to a decrease in the number of nanowire-nanowire junctions and current transport paths. This has also been confirmed by the sheet resistance measurements.

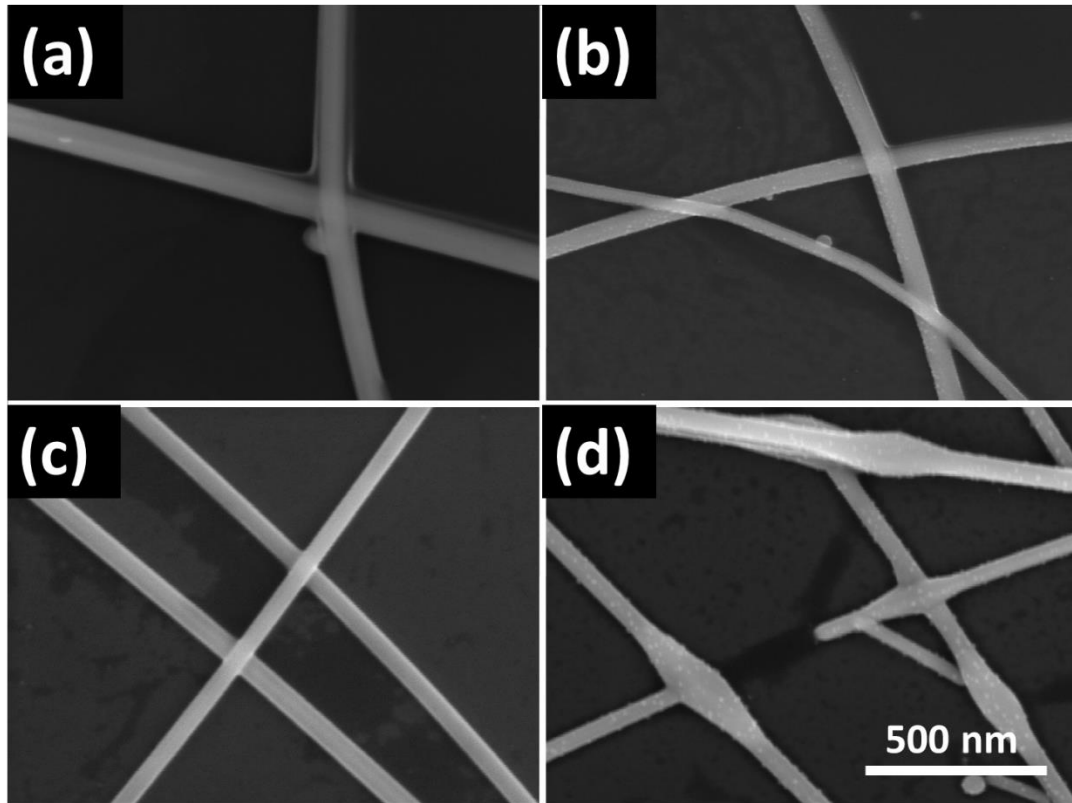


**Figure 3.35** SEM images of (a) as deposited, (b) 100, (c) 200, (d) 300°C annealed Ag NE networks (30 minutes) [76]. All scales are the same.

As it was discussed in Chapter 1, nanomaterials exhibit different physical and chemical properties than their bulk counterparts. Extremely high surface area makes nanowires very sensitive to chemical and physical environment. Although melting temperature of bulk Ag is about 1000°C, Ag NWs were seen to form droplets during annealing below 400°C in air. Such a thermal energy is enough for the Ag NWs to shrink and transform into spherical droplets. Figure 3.36 shows SEM images of Ag NWs annealed at (a) 400 and (b) 500°C. Ag NW networks annealed at 400°C and excess were found to be totally destroyed, leading to the formation of Ag droplets on the substrate surface.

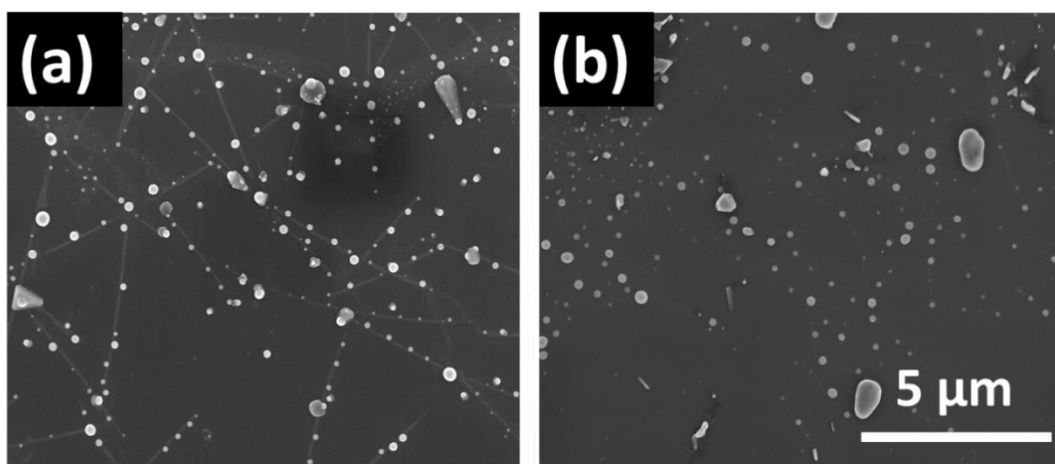
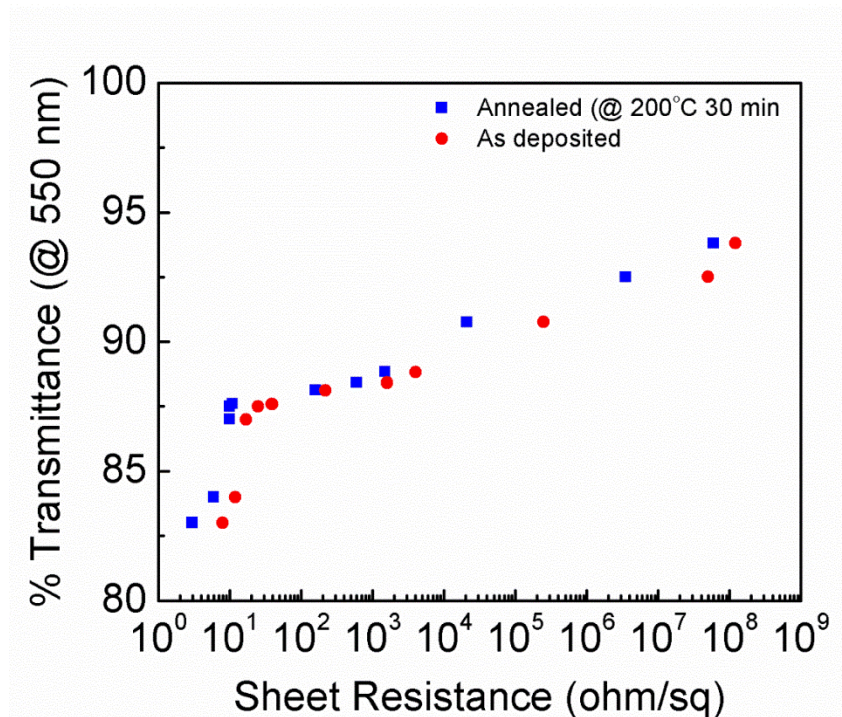


**Figure 3.36** SEM images of Ag NW networks annealed at (a) 400 and (b) 500°C for 30 minutes [76]. Both scales are the same.

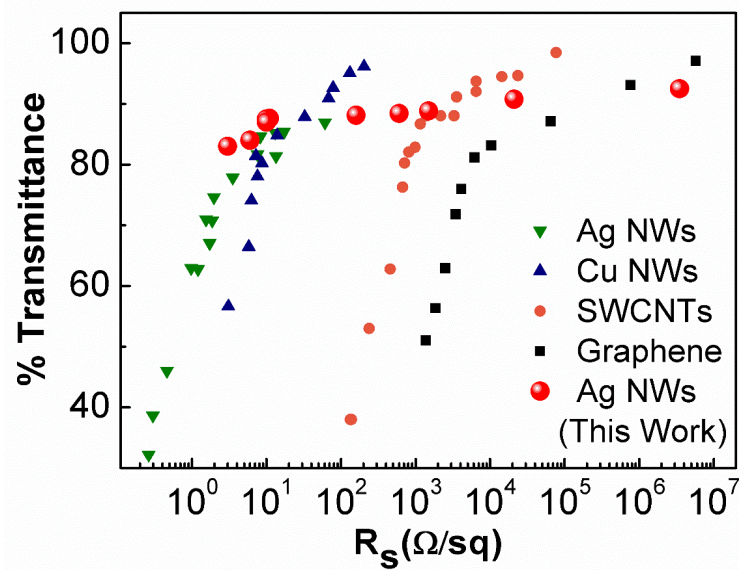
### 3.4.3 Effect of Annealing Time at 200°C

Figure 3.37 shows sheet resistance versus transmittance graph for Ag NW networks fabricated in this work. Since purification processes was not enough for the complete removal of PVP, the contacts resistance of Ag NWs were relatively high. Therefore, as deposited networks lack good contact between the Ag NWs. In order to decrease the contact resistance between Ag NWs, these networks were annealed. Annealing was found to decrease sheet resistance under constant transmittance. 30 minutes of annealing conducted at 200°C was found to be enough for the removal of thin polymer layer, which then provided a good contact between nanowires. Figure 3.37 also shows the effects of annealing process on the sheet resistance of Ag NW networks. In order to put the results of this study in context with reports in the literature, obtained data of transmittance (at 550 nm) versus sheet resistance were compared with several other studies in Figure 3.38. While a set of data points have been used for Bergin et al. [Ref. 26] that are provided for NWs of similar dimensions, individual data points have been taken from other reports. These results clearly demonstrate that the optoelectronic properties of Ag NW networks fabricated within this work are comparable to those in literature and in fact reporting one of the most competitive results obtained with spray coating.

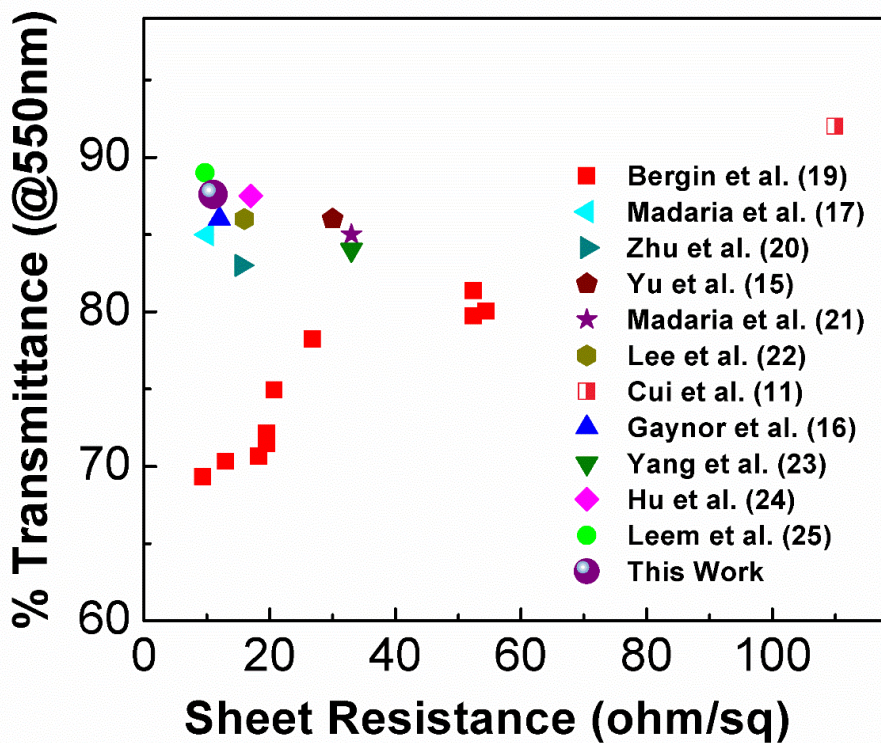
The transmittance and sheet resistance values of various nanostructured ITO alternatives are summarized in Figure 3.39, including the best result obtained in this work. Optoelectronic properties of the Ag NW networks are clearly revealing their potential to be used as nanostructured transparent conducting electrodes that can be deposited through vacuum-less methods.



**Figure 3.37** Sheet resistance versus transparency of as deposited and annealed (200 °C for 20 min.) Ag NWs networks [76].

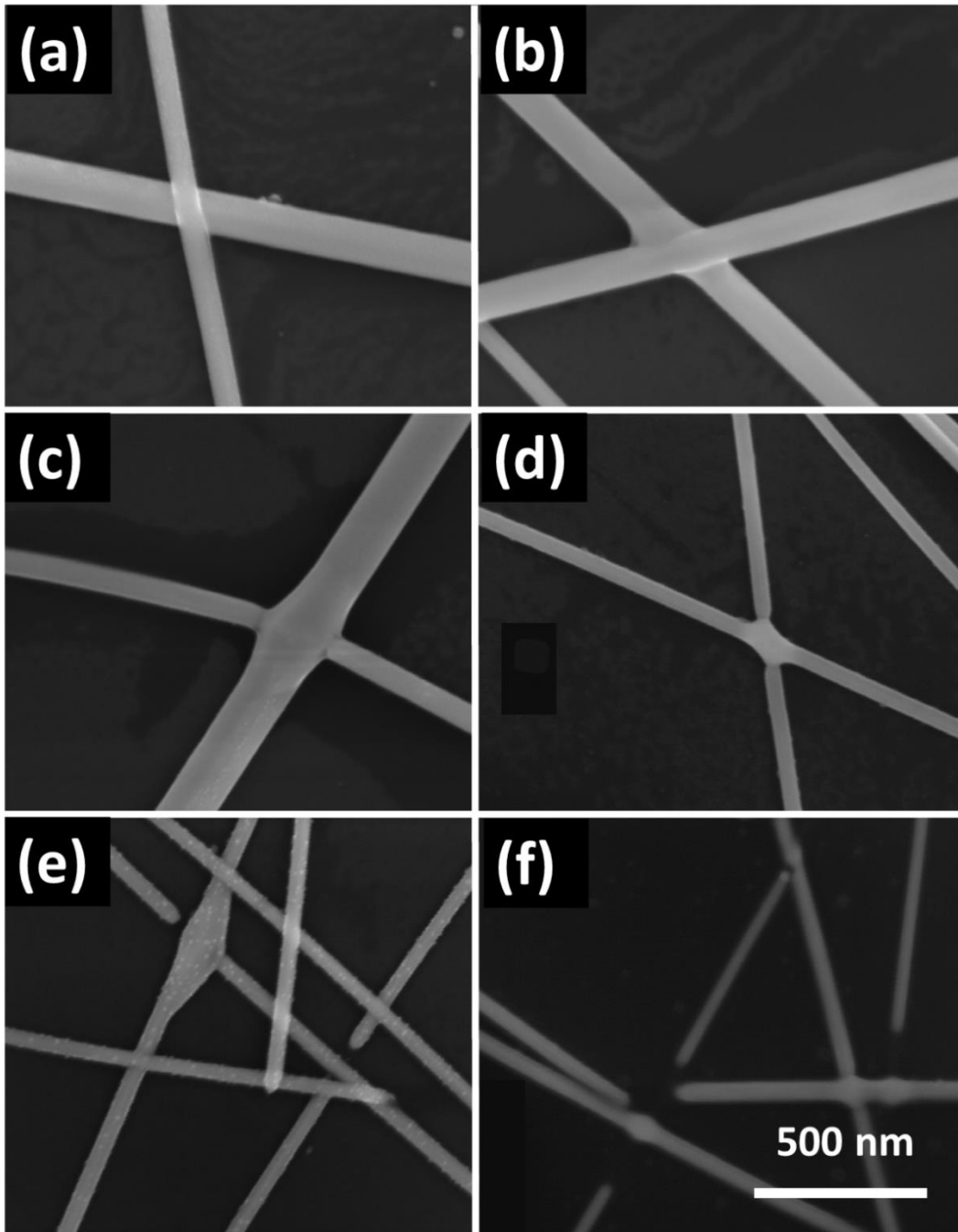


**Figure 3.38** Sheet resistance versus transmittance of annealed Ag NW networks in comparison to various transparent electrodes reported in literature, modified from Ref. 77.

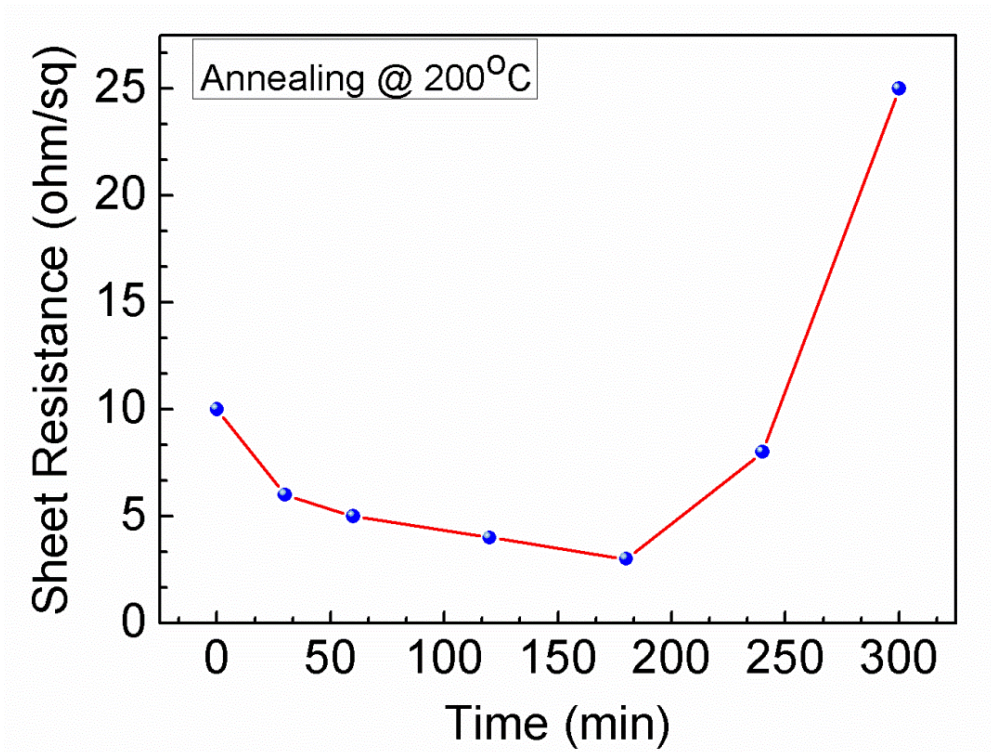


**Figure 3.39** A literature comparison showing lowest sheet resistances versus transmittance at 550 nm of Ag NW networks reported by other groups [76].

SEM images of Ag NW networks subjected to annealing at 200°C for different durations are shown in Figure 3.40 (a) - (f). Corresponding sheet resistance values are plotted with respect to annealing time in Figure 3.41. As it is seen from Figure 3.40 (a), 30 minutes annealing removes the residual PVP layer and decreases the sheet resistance. 60 minutes annealing leads to the fusion of nanowires. After complete fusion, if annealing processes is continued, one of the Ag NWs gets thicker at the expense of the other, as shown in Figure 3.40 (d). Beyond this point, annealing causes breaking of Ag NWs at junctions as shown in Figure 3.40 (e) and (f), which could be due to plasmonic welding or via Rayleigh instability as suggested by Garnett et al. [27]. A similar effect was observed by Lee et al. for longer annealing times [23]. As it can be seen from Figure 3.41, sheet resistance of Ag NW networks decreases with annealing duration up to 180 minutes while further annealing increases the sheet resistance. An optimum annealing time of three hours was found to obtain the lowest sheet resistance.

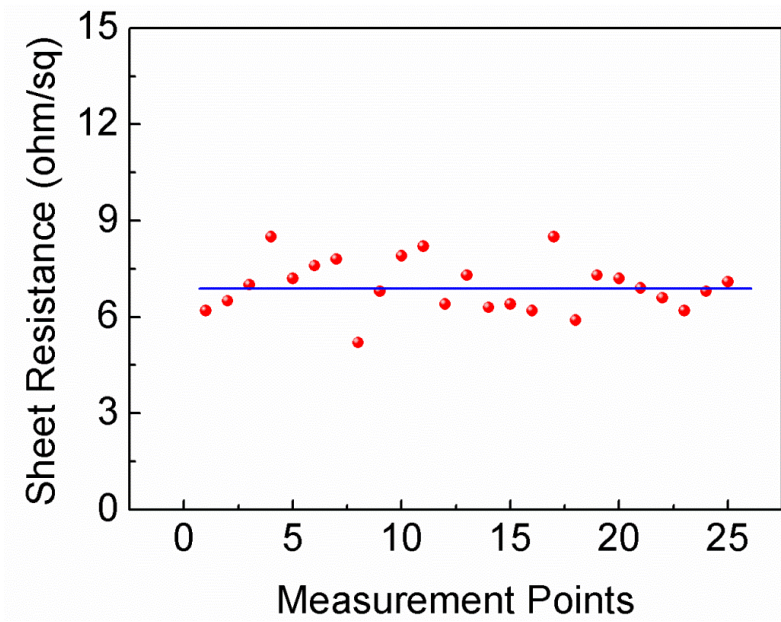


**Figure 3.40** SEM images of Ag NW networks annealed at 200°C with different durations of (a) 30, (b) 60, (c) 120, (d) 180, (e) 240 and (f) 300 minutes [76].



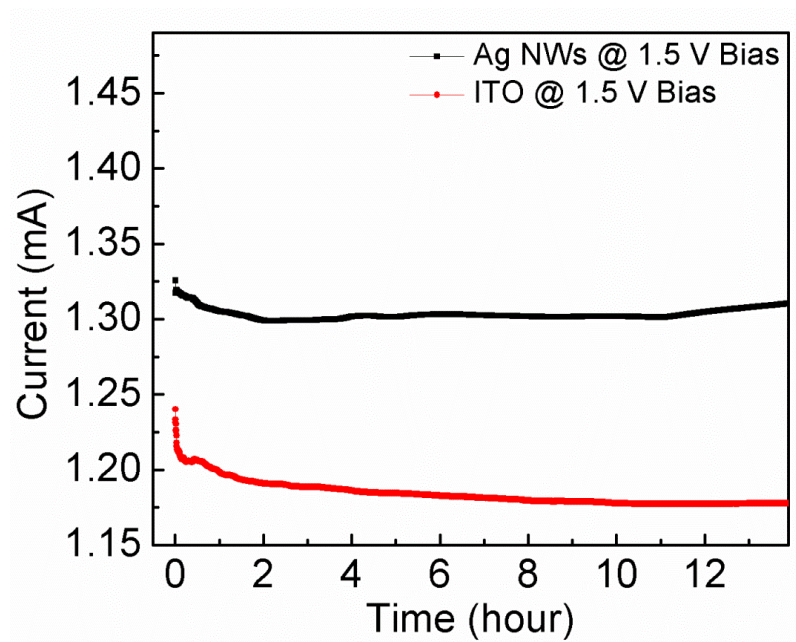
**Figure 3.41** Change in sheet resistance of Ag NW networks annealed at 200°C with time [76].

Figure 3.42 shows the variation in the sheet resistance values of the Ag NW networks fabricated in this work taken from various locations on a substrate. A mean sheet resistance of 6.8  $\Omega$ /sq has been obtained, were the maximum and minimum sheet resistance of 8 and 5  $\Omega$ /sq were measured, respectively, for that particular sample. This result reveals the uniformity of the Ag NW networks fabricated through spray coating. This clearly indicates that transparent and conducting Ag NW networks can be reproducibly produced via spray coating without any substrate size limit.



**Figure 3.42** Change in sheet resistance of an Ag NW network measured at 25 different spots on the sample [76].

Figure 3.43 shows the current carrying capacity, in other words, current versus time graph for the Ag NW networks fabricated in this work, in comparison to commercially available ITO (Delta technologies, Part No. CB – 40IN – S211  $R_{sh}$  : 4-8 ohms/square). For this purpose, a constant voltage (1.5 V) was applied to these samples for 14 hours. As it is seen from the graph, Ag NW networks are highly stable under constant voltage. In fact, Ag NW networks are found to be more stable than ITO.



**Figure 3.43** Current stability of ITO and Ag NW networks [76].



## CHAPTER 4

### UTILIZATION OF SILVER NANOWIRE NETWORKS AS ANODE IN ORGANIC LIGHT EMITTING DIODES

#### 4.1. Introduction

Lighting is one of the most important indications of the modern life. Approximately 5-10% of total energy consumption belongs to lighting. Traditional lighting devices are incandescent bulbs. However, these bulbs convert only less than 10% of the supplied electricity into light, whereas the remaining 90% is converted into heat. In 1980s, first fluorescent lamps were introduced. Today, they are five times more efficient than incandescent bulbs. Following the introduction of light emitting diodes (LEDs) which emit white light, their indoor and outdoor lighting applications have been investigated. Recently, LED based bulbs are introduced and it seems like they will be the major lighting sources of the modern world. They have many advantages over traditional lighting sources. Firstly, LED bulbs last 10 times longer compared to the compact fluorescents. Durability comes from the absence of any burning filament. Utilization of mercury in incandescent bulbs is a problem for environment. However, there is no mercury use in LEDs. They convert all supplied electricity into light without any loss. As a result, they are at least three times more efficient than fluorescent bulbs [78]. In inorganic LEDs, Ga-based light emitting materials are used. These materials are relatively expensive. So, researchers looked for the fabrication of LEDs with more abundant and cheaper materials. Demonstration of conducting polymers made this idea possible with organic materials. There are two types of OLEDs. In the first one, small organic molecules are used; whereas, in the second one solution processable polymers are used. The second type is called

polymer light emitting diodes (PLEDs). PLEDs have numerous advantages over OLEDs such as easy processing and cost. Figure 4.1 shows schematic of a typical PLED device. Poly [2-methoxy-5-(2-ethylhexyloxy)-phenylene vinylene] (MEH-PPV) is the electroluminescent layer of the device.

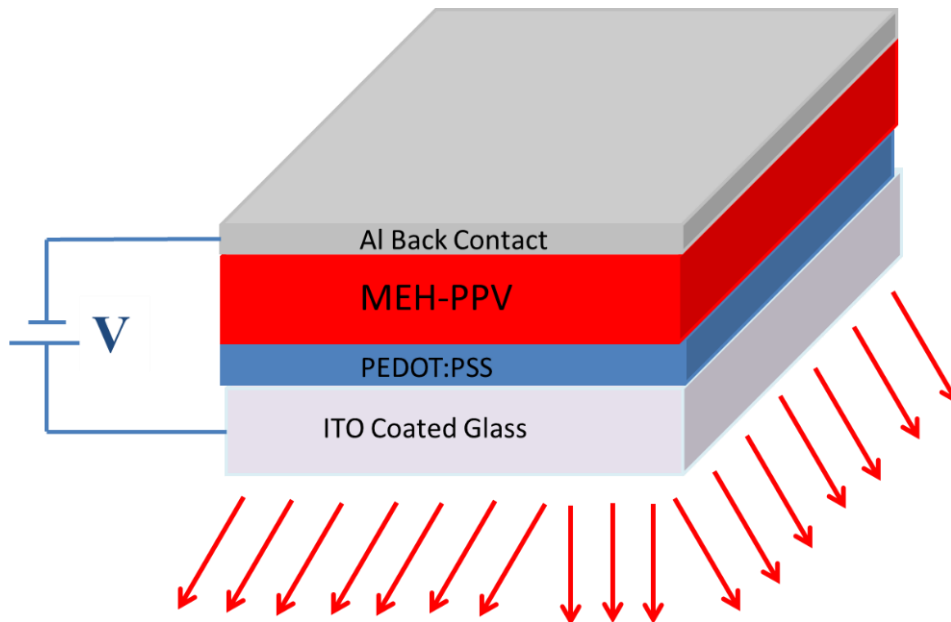


**Figure 4.1** Schematic of a typical MEH-PPV based PLED.

A typical PLED device composes of stacked layers. These layers include;

**Cathode:** When a voltage is applied to PLED, electrical current flows from cathode to anode through organic layers of the device. The cathode injects electrons to emissive layer. Aluminum thin film is used as cathode in this device, which is usually deposited as a thin film via evaporation.

**Anode:** It removes electrons when current flows; as a result, holes are formed. Anodes are chosen from transparent and conducting materials. In this structure vacuum deposited ITO is used as anode.

**Hole Injection Layer (HIL):** This layer is used for the transportation of holes from anode to the emissive layer. Poly(3,4-ethylenedioxythiophene)-poly(styrenesulfonate) (PEDOT:PPS) is HIL of this device deposited through spin coating.

**Emissive Layer (EL):** Under the influence of an applied electric field, the injected holes and electrons each migrate toward the oppositely charged electrode following a hopping transport regime which consists in a series of “jumps” of the charge from molecule to molecule. In the organic emissive layer (EML), when an electron and hole localize on the same molecule and are spatially close, a fraction of them recombine to form an exciton (a bound state of the electron and hole); which is a localized electron-hole pair having an excited energy state. Then some of these excitons relax via a photo-emissive mechanism and decay radiatively to the ground state by spontaneous emission. In some cases, the exciton may be localized on an excimer (excited dimer) or an exciplex (excited complex). Upon recombination, energy is released as light and at least one electrode must be semi-transparent to enable the light emission.

Following the successful demonstration of competitive transparency and conductivity values of Ag NW networks, their utilization in devices as alternative TCCs began to be investigated. Yu et al. [79] used Ag NW networks as anode layer in OLEDs. They used Ag NW/polyacrylate electrodes with 30  $\Omega$ /sq sheet resistance for the fabrication of solution-processed PLEDs. The device consisted of layers of polyacrylate substrate, Ag NW, poly(3,4-ethylenedioxythiophene) doped with polystyrene sulfonate (PEDOT:PSS, 40-nm-thick), an alkoxyphenyl substituted yellow emissive poly(1,4-phenylene vinylene) (SY-PPV, 60 nm), CsF (1 nm), and aluminum (100 nm) in the following sandwich configuration: polyacrylate/AgNW/PEDOT:PSS/SY-PPV/CsF/Al. ITO-based devices, for comparison, were also fabricated with a similar sandwich structure of glass/ITO/PEDOT:PSS/SY-PPV/CsF/Al.

Figure 4.2 shows the current density-voltage-luminance ( $I - V - L$ ) characteristics of fabricated PLEDs obtained by sweeping the applied voltage from 0 to 8 V in 100 mV increments. The PLEDs with Ag NW/polymer or ITO/glass electrodes exhibited quite similar  $I - V - L$  responses, except that the current and luminance of the Ag NW devices were lower than those of ITO based device driven at the same applied voltage values of the electrodes. This difference could be caused by the difference in the sheet resistance. Light emission from ITO based device started at 2.2 V (1  $\text{cd/m}^2$  brightness) and reached a luminance of 12 650  $\text{cd/m}^2$  at 8 V, while the devices

fabricated with Ag NWs turned on at 2.3 V and had a brightness of 8 470 cd/m<sup>2</sup> at 8 V. The luminous efficacy data of the devices are shown in Figure 4.2 (b). The control device with ITO anode had a maximum efficacy of 12.5 cd/A.

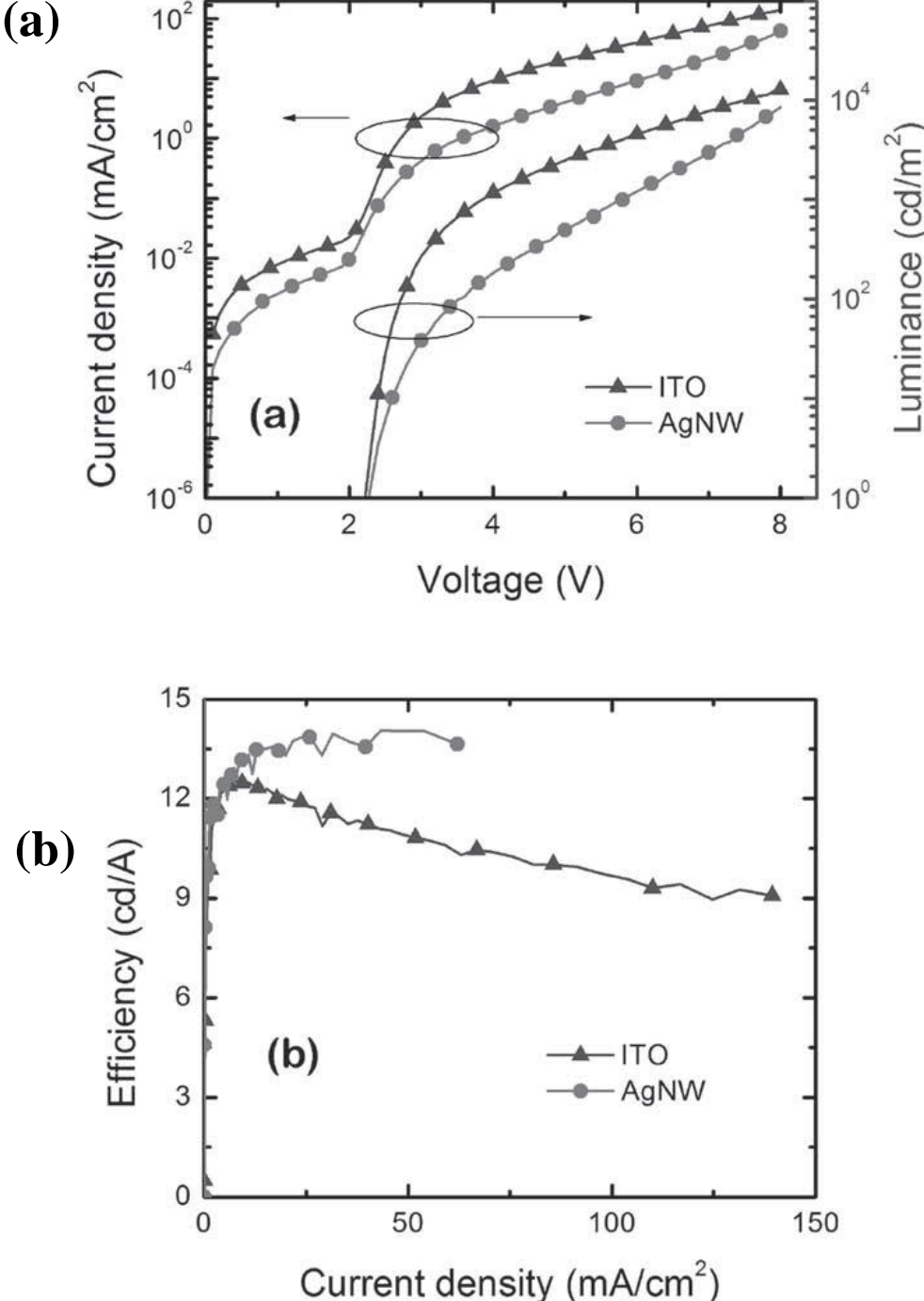


**Figure 4.2** *I* – *V* – *L* curves of PLEDs having a sandwich structure of AgNWs (or ITO) anode/PEDOT:PSS/SY-PPV/CsF/Al (a) and the luminous efficacy and current density graph of the fabricated devices (b) [79].

## **4.2 Characterization Methods**

### **4.2.1 Atomic Force Microscopy (AFM)**

Vecoo MultiMode V model AFM was used for the topographic analysis of Ag NW networks in tapping mode.

### **4.2.2 Current-Voltage Measurements**

Current-voltage (I-V) measurements were done using a Keithley 2400 sourcemeter. I-V characteristics of the fabricated PLEDs are measured between 0 and 6 V.

### **4.2.3 Electroluminescence Measurements**

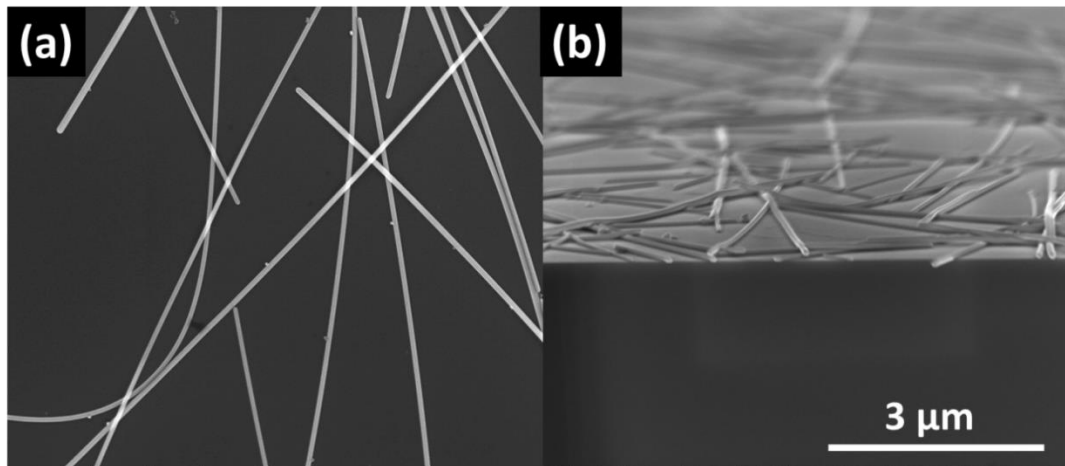
Newport 918-UV model integrated sphere and Maya 2000 model spectrometer were used for the electroluminescence measurements of the fabricated PLED devices.

## **4.3 Fabrication and Characterization of PLEDs**

Poly[2-methoxy-5-(2-ethylhexyloxy)-1,4-phenylenevinylene] (MEH-PPV) was purchased from Sigma Aldrich, chloroform and PEDOT: PSS was purchased from Merck. All chemicals were used without further purification. For the hole transport layer, PEDOT: PSS was either mixed with IPA in a volume ratio of 1:1 or used as purchased following filtering through a 200 nm pore size filter and spin coated on top of Ag NW networks at different spin coating speeds. Immediately after, the PEDOT: PSS coated Ag NW networks were dried using a vacuum oven set at 100°C. MEH-PPV was dissolved in chloroform (5 mg/ml) and served as the light emitting layer. MEH-PPV solution was spin coated on top of the dried PEDOT: PSS layer at 2500 rpm for 20 seconds. Again the polymer coated substrates were dried at 100°C using a vacuum oven for 30 minutes to ensure that all the solvent was evaporated. Device fabrication was finalized by the evaporation of 200 nm thick aluminum top contacts through evaporation using a shadow mask. For comparison purposes,

identical devices were fabricated on ITO coated glass substrates (Delta Technologies, Part No. CB – 40IN – S211 4-8  $\Omega$ /sq sheet resistance and 83% transmittance).

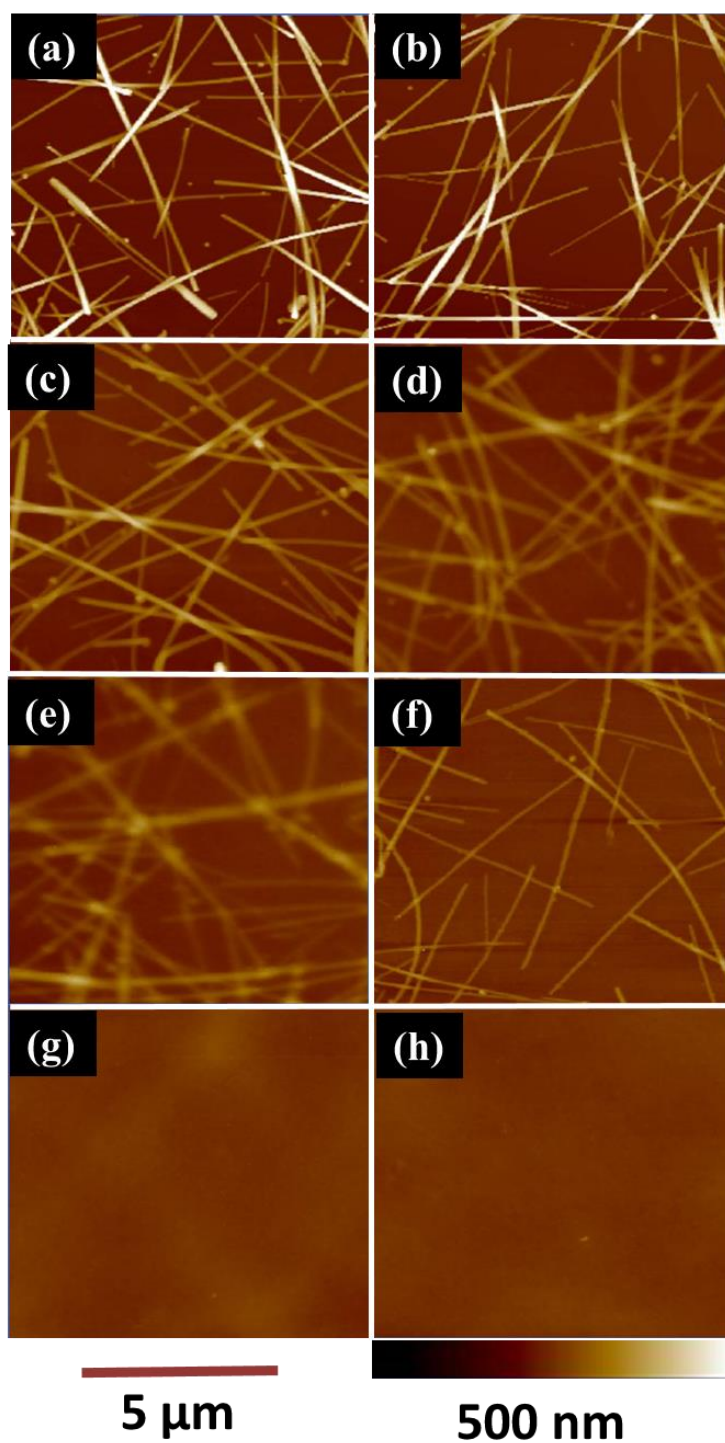
Since Ag NW networks are not forming a continuous film, they have relatively high roughness values. Figure 4.3 shows top and cross-sectional SEM images of Ag NW networks. Ag NWs cannot be deposited onto substrates as a monolayer, the roughness values of networks increase at the junction points.



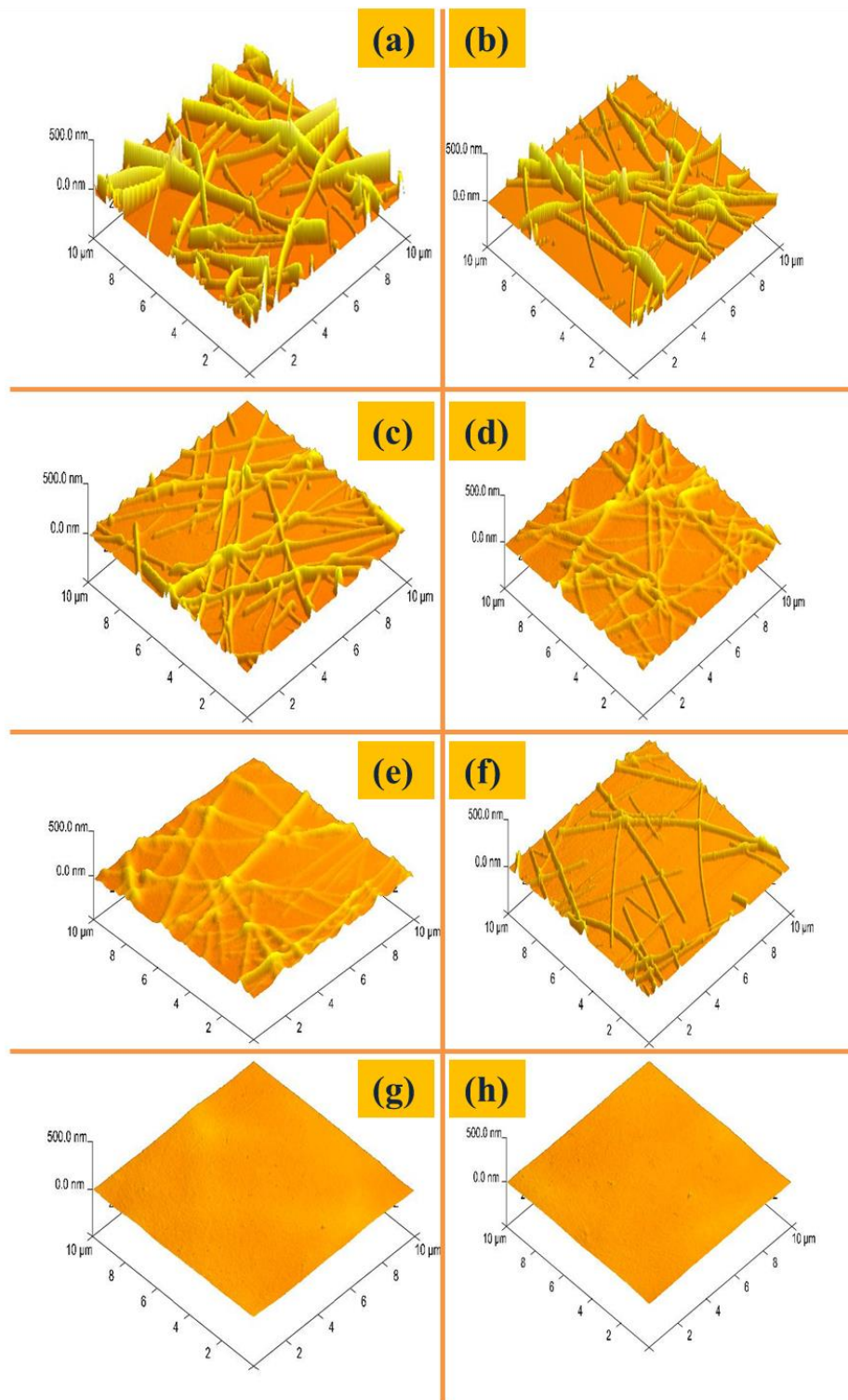
**Figure 4.3** Top and cross-sectional SEM images of Ag NW networks on Si wafer. Both scales are the same [76].

Especially in thin film devices, such as OLEDs and OPVs, this roughness may cause the device to short. So, the roughness of the nanowire networks must be somehow decreased. Coating a conducting polymer over the Ag NW networks not only will decrease roughness but also will serve as a hole injection layer (HIL) in PLEDs. A parametric study was conducted on PEDOT:PSS coating of Ag NW networks. In the first series of experiments, PEDOT:PSS were diluted with isopropyl alcohol at 1:1 volume ratio. In the second part, pure PEDOT:PSS solution was used. PEDOT:PSS solutions were deposited onto Ag NW networks via spin coating. Spin coating time set to 20 seconds. For roughness analysis, AFM was used in tapping mode. Figure 4.4 shows AFM phase images of Ag NW networks. With PEDOT:PSS layer, AFM 3D images provided better visualization of the roughness. Figure 4.5 show AFM 3D images of the Ag NW networks with PEDOT:PSS layer. Comparing both phase and 3D images it can be said that, covering ability of PEDOT:PSS increases with the

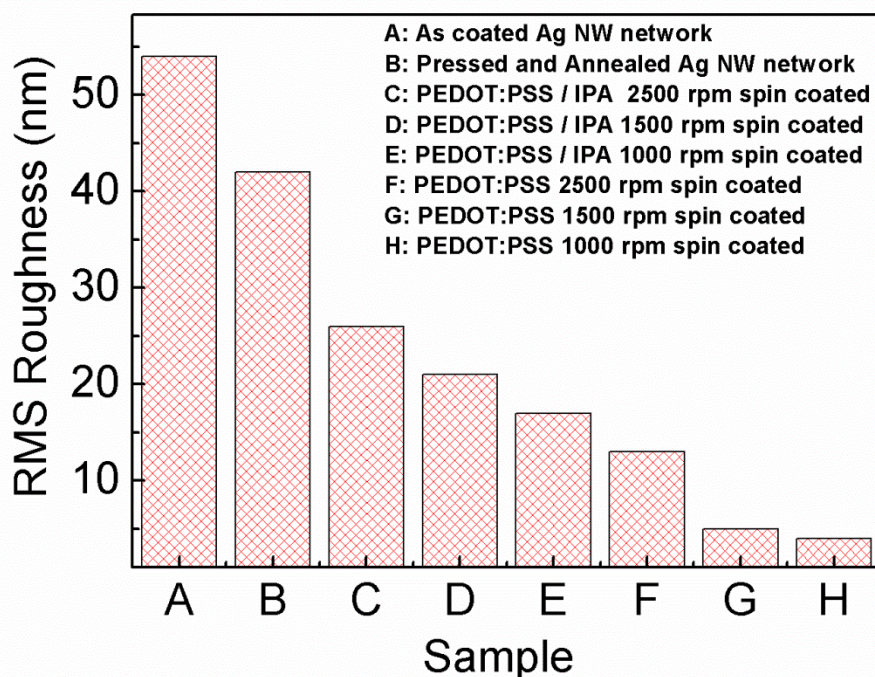
decrease in the spin coating speed. Moreover, since IPA evaporates quickly after spin coating, pure PEDOT:PSS forms thicker films than PEDOT:PSS / IPA mixture solution at the same spin coating speed. As it is seen from Figure 4.4 (g), (h) and Figure 4.5 (g), (h), when pure PEDOT:PSS was spin coated at 1500 and 1000 rpm, it totally covered the Ag NW network. Figure 3.6 shows how RMS roughness changed with the PEDOT:PSS coating processes. As coated Ag NWs had a RMS roughness of about 54 nm. Pressing during standard annealing process (@ 200°C for 30 minutes) decreased the RMS roughness value to 42 nm. For the sample that was pressed during annealing as spin coated with PEDOT:PSS / IPA solution at a spin coating speed 2500 rpm, the RMS roughness decreased to 25 nm. Experiments showed that this RMS roughness value was enough for fabrication of PLEDs. For different applications, spin coating parameters can be adjusted so that the desired RMS roughness values can be obtained.



**Figure 4.4** AFM phase images of Ag NW networks that are (a) as coated, (b) pressed during annealing, (c) PEDOT:PSS/IPA spin coated at 2500 rpm, (d) 1500 rpm (e) 1000 rpm, (f) PEDOT:PSS spin coated at 2500 rpm, (g) 1500 rpm, (h) 1000 rpm, respectively [76].

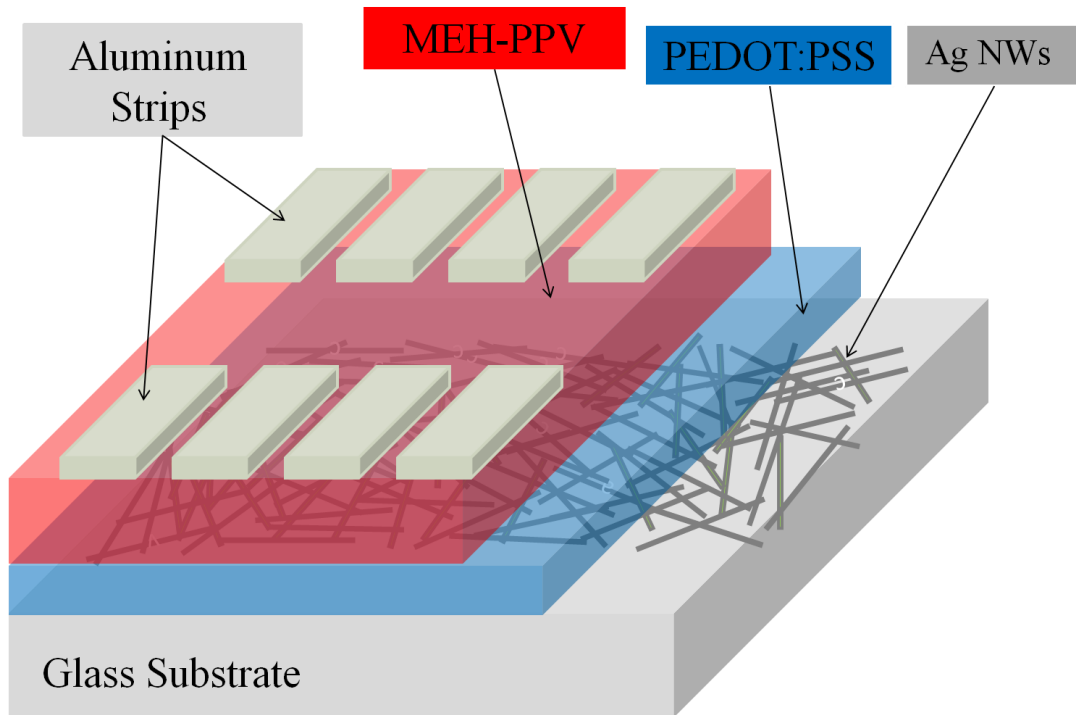


**Figure 4.5** AFM 3D images of Ag NW networks that are (a) as deposited, (b) pressed during annealing, (c) PEDOT:PSS/IPA spin coated at 2500 rpm, (d) 1500 rpm (e) 1000 rpm, (f) PEDOT:PSS spin coated at 2500 rpm, (g) 1500 rpm, (h) 1000 rpm, respectively [76].



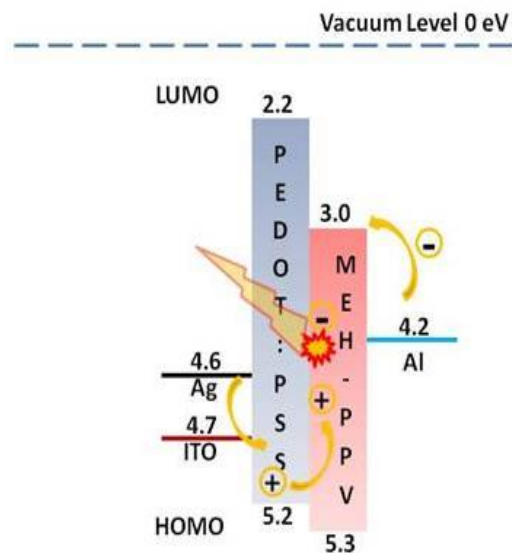
**Figure 4.6** RMS roughness change of different Ag NW network samples [76].

Roughness optimized Ag NW networks were then implemented as anodes in poly [2-methoxy-5-(2-ethyl-hexyloxy) -1,4-phenylene-vinylene] (MEH-PPV) PLED devices and their performance was compared to a device control fabricated with commercial ITO anode. Ag NW networks with PEDOT: PSS over layer were used as the anode and hole transport layer in PLED devices. In order to prevent the MEH-PPV from light and air, the solution was kept inside of an aluminum container and the container was kept inside of a glove box. Evaporation of 200 nm thick aluminum top contacts finalized the device fabrication. Figure 4.7 shows schematic structure of the fabricated PLED in this work [76].



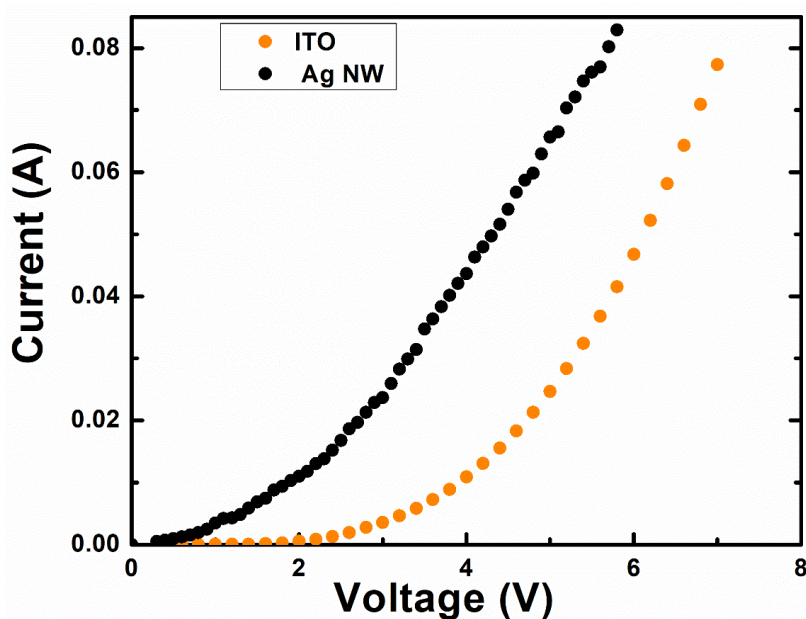
**Figure 4.7** Schematic structure of PLED in which Ag NW networks were used as anode.

Figure 4.8 shows corresponding band diagram for the fabricated PLED devices.



**Figure 4.8** Corresponding band diagram of the fabricated PLED devices with both ITO and Ag NW network anodes.

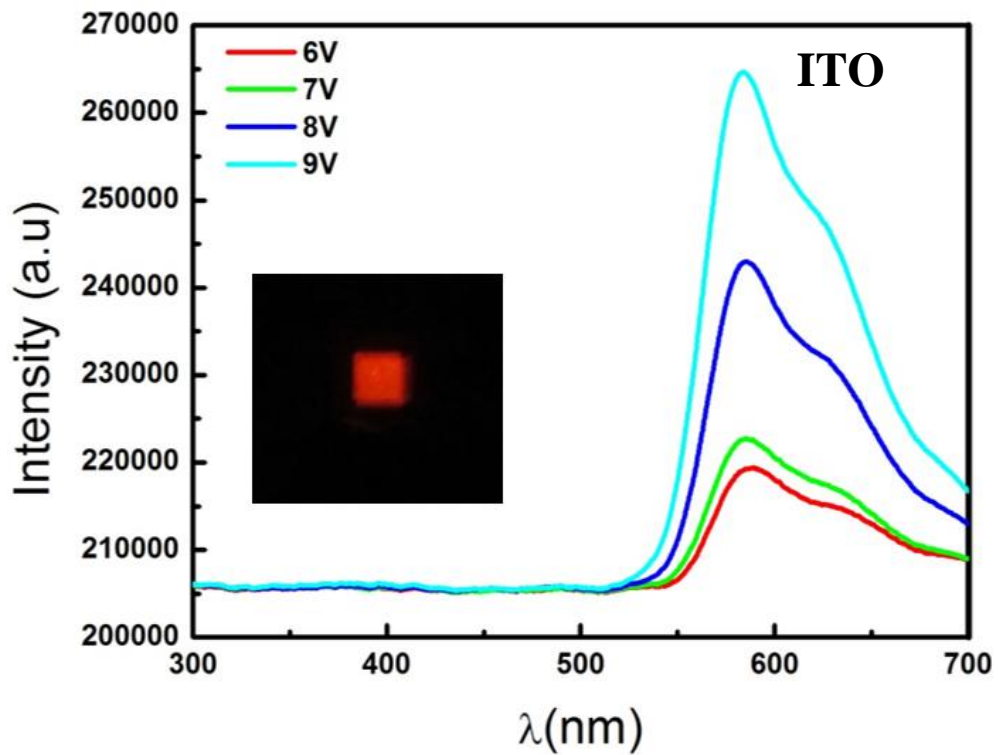
Devices were fabricated on glass substrates. Current-voltage (I-V) characteristics of the devices are provided in Figure 4.9. The threshold voltage of PLED with Ag NW network anode was 0.6V, much lower than that fabricated on ITO (2.4V). This fact can simply be explained by the oxide layer on the Ag NWs. A thin oxide layer was expected to form on the surface of the NW networks due to handling/storage in air following their deposition. Work function of silver oxide ( $\text{Ag}_2\text{O}$ ) is 5.1 eV [28], which is quite close to the highest occupied molecular orbital (HOMO) level of interpenetrated PEDOT: PSS (5.2 eV) and the HOMO level of MEH: PPV (5.3 eV), leading to a low threshold voltage. In contrast, the relatively high threshold voltage of the PLEDs with ITO anode was attributed to the large difference between the work function of ITO (4.7 eV) and HOMO level of MEH: PPV.



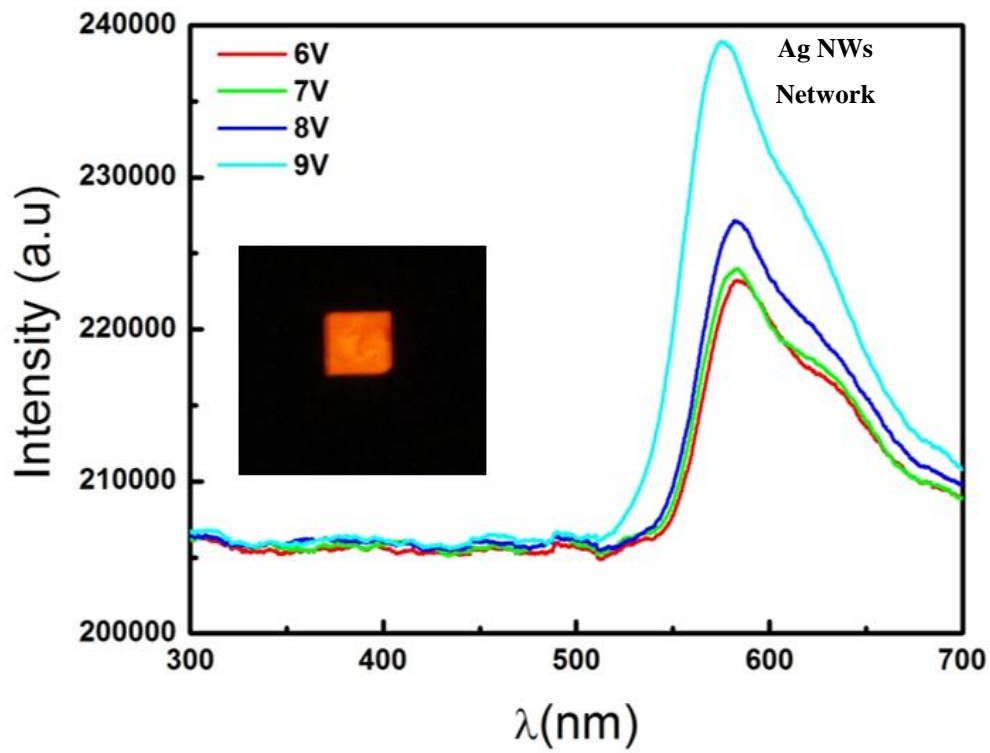
**Figure 4.9** Current-voltage (I-V) characteristics of the PLED devices fabricated in this work [76].

Figure 4.10 and 4.11 shows electroluminescence behavior of PLED devices fabricated using Ag NW network and ITO as anodes, respectively. The observed peaks (590 and 650 nm) are the characteristic emission peaks of MEH-PPV. Photos of PLEDs at bias that are sufficient for overcoming the lowest unoccupied molecular orbital (LUMO) and HOMO energy levels of the MEH-PPV were used to demonstrate the luminescence properties of the devices. One can see from Figure

4.10 and 4.11 that at applied bias of 6V, the intensity of the light emitted from the PLED with ITO anode is higher than the one with Ag NW network anode. At 7V and above, the intensity of the emitted light from the PLED with Ag NW network anode surpassed that of the ITO device. The enhancement in the intensity with applied voltage can be attributed to the scattering of emitted light by Ag NWs that increases the output light intensity [29].



**Figure 4.10** Electroluminescence characteristics of PLED device with ITO anode [76]. Inset shows a photo of emission.



**Figure 4.11** Electroluminescence characteristics of PLED device with Ag NWs networks anode [76]. Inset shows a photo of emission.

## CHAPTER 5

### STABILITY OF SILVER NANOWIRES

#### 5.1. Introduction

Besides very promising optoelectronic and mechanical properties of Ag NW networks, there are still a few points that need to be addressed prior to large-scale utilization of these materials and market entry. The first issue seemed to be high surface roughness of the Ag NW networks. As it was shown in the previous chapter, it is possible to decrease surface roughness of Ag NW networks via coating of over layers like a functional organic material and this would prevent the short circuit of the fabricated devices. The second and more challenging problem is the long-term stability of Ag NWs in ambient conditions and in devices that make use of Ag NW networks. Since the diameter of Ag NWs is less than 100 nm, very high surface to volume ratio make these nanomaterials highly vulnerable to corrosion. Failure of nanowires causes failure of the conductive network and as a result, the devices fail. When bulk Ag or Ag thin films were subjected to ambient conditions, the surface color of the metal turns into dark, which is known as “tarnishing”. Silver sulfide ( $\text{Ag}_2\text{S}$ ) layer forms on the surface of tarnished Ag. Although ambient stability and corrosion behavior of bulk Ag is a well-known subject, so far researchers conducted only very limited research on Ag NWs. Recently, Ag NWs were exposed to humidity [80], light [81], high temperatures [82] and high electrical currents [83] and all resulted in the enhanced degradation of Ag NWs. However, simple accelerated nanowire corrosion is unable to explain degradation mechanism of Ag NWs. Moreover, there is not consensus in the published literature on how long Ag NW networks can keep their initial sheet resistance values. For example, Mayousse et al. [84] reported that Ag NWs networks are stable under ambient conditions for two and half years. On the other hand, Jiu claimed that Ag NWs networks form open circuit

after six months [85]. Hence, corrosion of Ag NWs still needs further investigation, and thus; some versatile methods should be offered to increase their stability.

## 5.2 Corrosion of Bulk Silver

Since there are no comprehensive studies on the corrosion of Ag NWs, it can be helpful to review the corrosion of bulk Ag. Bulk Ag does not easily form an oxide layer on its surface unlike many other metals. When bulk Ag is exposed to reduced sulphur containing compounds such as carbonyl sulfide (OCS), sulphur dioxide (SO<sub>2</sub>) and hydrogen sulphide (H<sub>2</sub>S), a film of silver sulfide (Ag<sub>2</sub>S) is formed on its surface. Long exposure to ambient conditions causes formation of silver oxide (Ag<sub>2</sub>O). In addition, Franey et al. reported that, higher humidity and higher temperature resulted in corrosion of Ag at much higher rates [86]. Figure 5.1 shows how Ag<sub>2</sub>S formation rate depends on the sulphur gas source. OCS and H<sub>2</sub>S have the highest contribution for the formation of Ag<sub>2</sub>S.

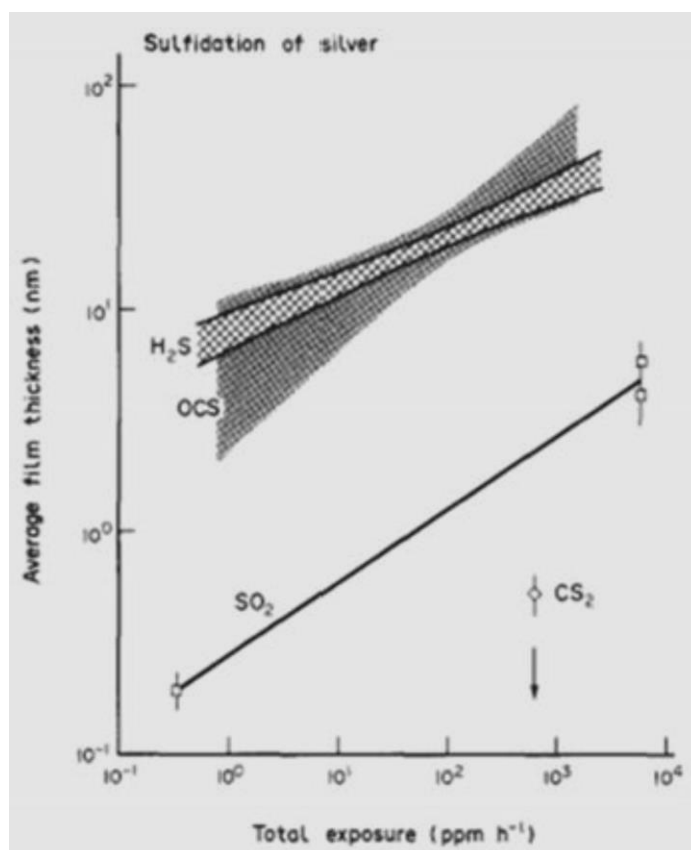


**Figure 5.1** Growth rates of Ag<sub>2</sub>S when exposed to various ambient sulfur-containing gases such as H<sub>2</sub>S, OCS, SO<sub>2</sub> and CS<sub>2</sub> [86].

Tsai et al. used terahertz spectrometry (THz) to investigate oxidation of Ag NW networks especially at the nanowire-to-nanowire (NW-to-NW) junctions [87]. They used scanning transmission electron microscopy (STEM) to make compositional analyses of oxidized Ag NWs. Figure 5.2 (a) and (d) show cross-sectional STEM images of individual and stacked silver nanowires. As it is clear from the images of contact surfaces between Ag NWs and Si substrate and two nanowires are darker than other nanowire regions. Those darker regions correspond to oxygen rich parts of the EDS (Energy Dispersive X-Ray Spectroscopy) mapping images provided in Figure 5.2 (b), (c), (e) and (f). Hence, it can be said that oxidation occurs at between nanowire – nanowire, nanowire – Si substrate and nanowire – air contact surfaces.

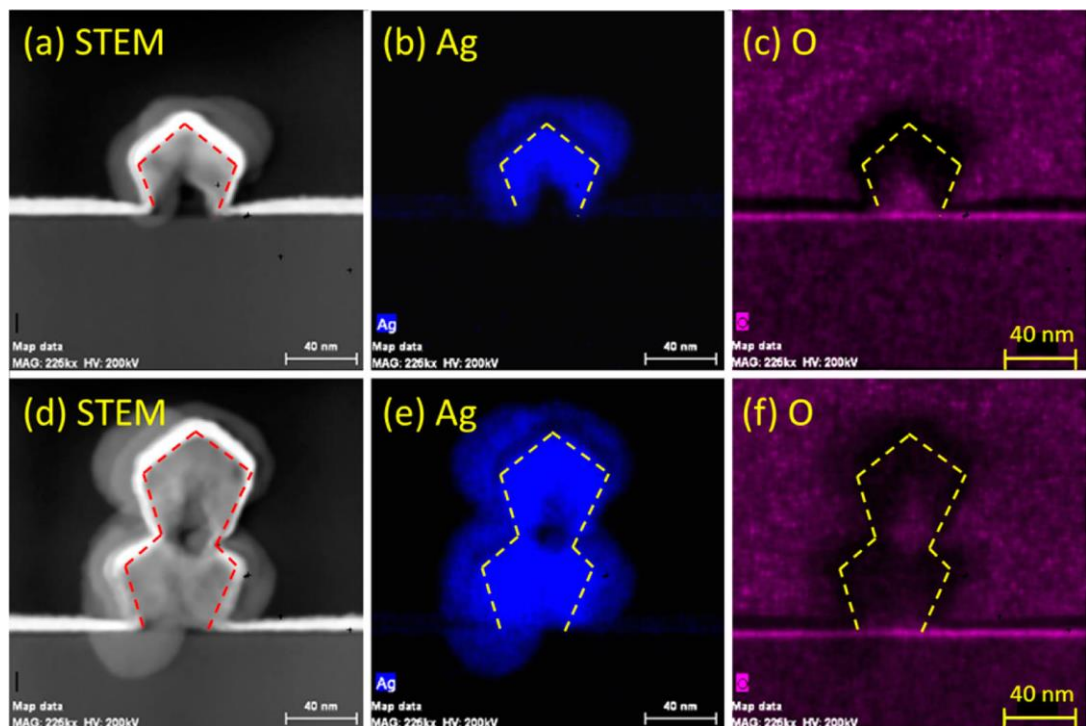


**Figure 5.2** Cross-sectional STEM and EDS mapping images of oxidized sample. (a–d) STEM images of a single Ag NW and stacked Ag NWs. EDS mapping images in (b) and (e) correspond to Ag atoms and those in (c) and (f) for O atoms. Dashed lines are guides for the eyes of pentagonal Ag NWs [87].

Ellechiguerra et al. [88] investigated atmospheric corrosion behaviors of Ag NWs and nanoparticles via spectroscopic techniques. Figure 5.3 shows TEM images of Ag NWs exposed to ambient conditions for different time intervals. In Figure 5.3 (a) as

synthesized Ag NWs are shown with smooth surfaces and twin boundaries. Upon the exposure of Ag NWs to ambient conditions for 3 weeks, lateral surfaces of the nanowires start to be rough and some nanoparticles are formed on the surface of the nanowires as it can be seen in Figure 5.3 (b). These nanoparticles have crystalline structure as it is seen in Figure 5.3 (c). As the exposure time to ambient conditions increases, the amount of formed nanoparticles increases. Ambient stability tests are applied to Ag NWs for up to 24 weeks. As nanoparticles around the nanowires grow, the core diameter of Ag NWs is found to decrease. However, Ag NWs are found to keep their 1D geometry.

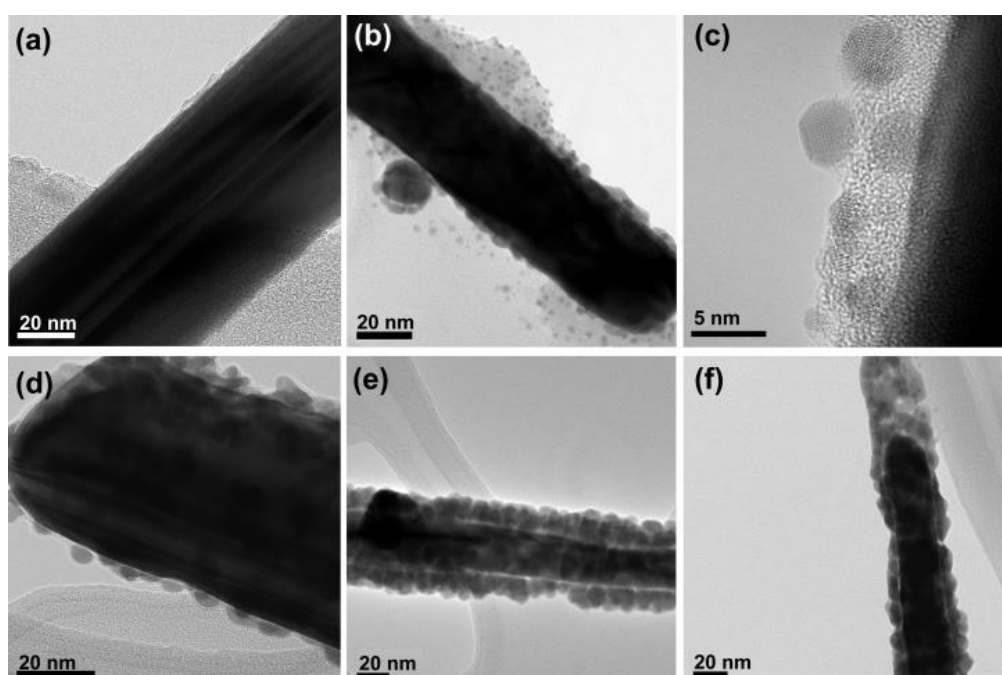


**Figure 5.3** TEM images of the same sample at different times after exposure to air under ambient conditions. (a) Sample just after synthesis. (b and c) TEM images of the sample after 3 weeks. TEM Images after (d) 4, (e) 5 (f) and 24 weeks [88].

XPS measurements have also been made to monitor the presence of residual PVP layer on lateral surfaces of Ag NWs, results of which are provided in Figure 5.4. The presence of carbon, nitrogen and oxygen on the surface of the sulfurized nanostructures is confirmed. The values for the binding energies of the three elements were similar to the values obtained for the original Ag NWs, confirming the presence of PVP on the surface of the sulfurized nanowires. These values are consistent with the reported data for Ag<sub>2</sub>S [88]. In addition, the XPS data confirmed

that no sulfites or sulfates are present. The formation of silver oxide (AgO) is not observed. The binding energy of the O 1s peak also confirms that no silver (I) oxide is formed, since the expected binding energy for the O 1s peak in silver (I) oxide should be 528.6 eV [32], which is significantly lower than the value obtained for the sulfurized nanowires.

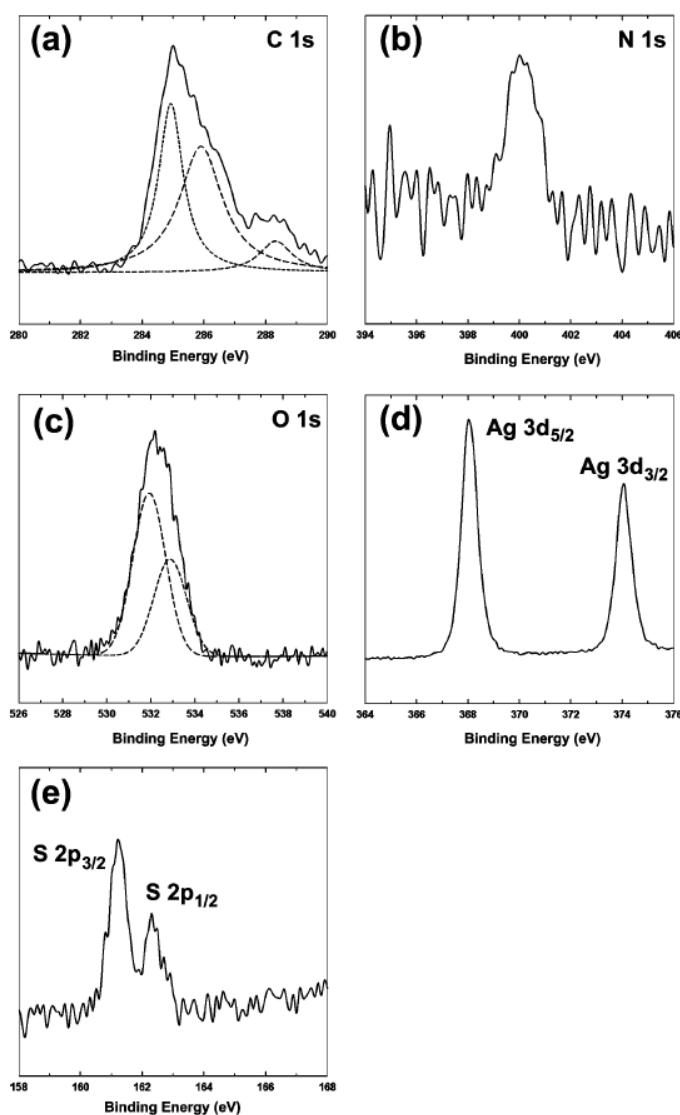


**Figure 5.4** XPS spectra of sulfurized Ag NWs, (a) C 1s spectrum, (b) N 1s spectrum, (c) O 1s spectrum, (d) Ag 3d<sub>5/2</sub> and Ag 3d<sub>3/2</sub> spectra and (e) S 2p<sub>3/2</sub> and S 2p<sub>1/2</sub> spectra [88].

Choo et al. investigated the degradation mechanism of Ag NWs under ultraviolet (UV) irradiation and heat treatment [89]. Figure 5.5 (a) and (b) shows the sheet resistance change with temperature and UV and ozone (O<sub>3</sub>) treatment time, respectively. Not considerable change in sheet resistance up to a temperature of 180 °C is observed. However, especially over 200 °C the sheet resistance of the samples increases dramatically. The sheet resistance of the Ag NW electrodes remained almost the same with the UV/O<sub>3</sub> treatment conducted at room temperature and heat treatment time for treatments up to 30 minutes. However, the sheet resistance of the Ag NW electrodes significantly increased with increasing UV/O<sub>3</sub> treatment time for treatment periods longer than 30 minutes. Longer periods also increased the standard deviation in sheet resistance measurements. For example, following a UV/ O<sub>3</sub> treatment of 180 minutes, the average sheet resistance and its standard deviation are measured as 1079 and 921 Ω/sq, respectively.

Figure 5.6 shows SEM images for the as-prepared Ag NWs, the UV/O<sub>3</sub>-treated Ag NWs and the annealed Ag NWs. While the pristine Ag NWs shown in Figure 5.6 (a) had smooth surfaces, very small nanoparticles are formed on the surfaces of the Ag NWs with increasing UV/O<sub>3</sub> treatment time, as shown in Figure 5.6 (b). As the UV light exposure time increases, Ag NWs start to rupture as it can be seen in Figure 5.6 (c). Figure 5.6 (d), (e) and (f) show SEM images of Ag NW networks exposed to heat treatments at different temperatures of 160, 190 and 210 °C, respectively. When the thermal treatment temperature was 160 °C, a few regions around the contact points of the Ag NWs melted due to the applied thermal energy. The number of the ruptured Ag NWs increases with the annealing temperature. However, when the thermal treatment temperature was raised to 210 °C, spherically shaped particles are generated. SEM image in Figure 5.6 (f) shows that even though many Ag NWs are separated by the thermal treatment, resulting in the formation of discrete nanoparticles, short and rod-shaped Ag NWs were still present in the networks [89].

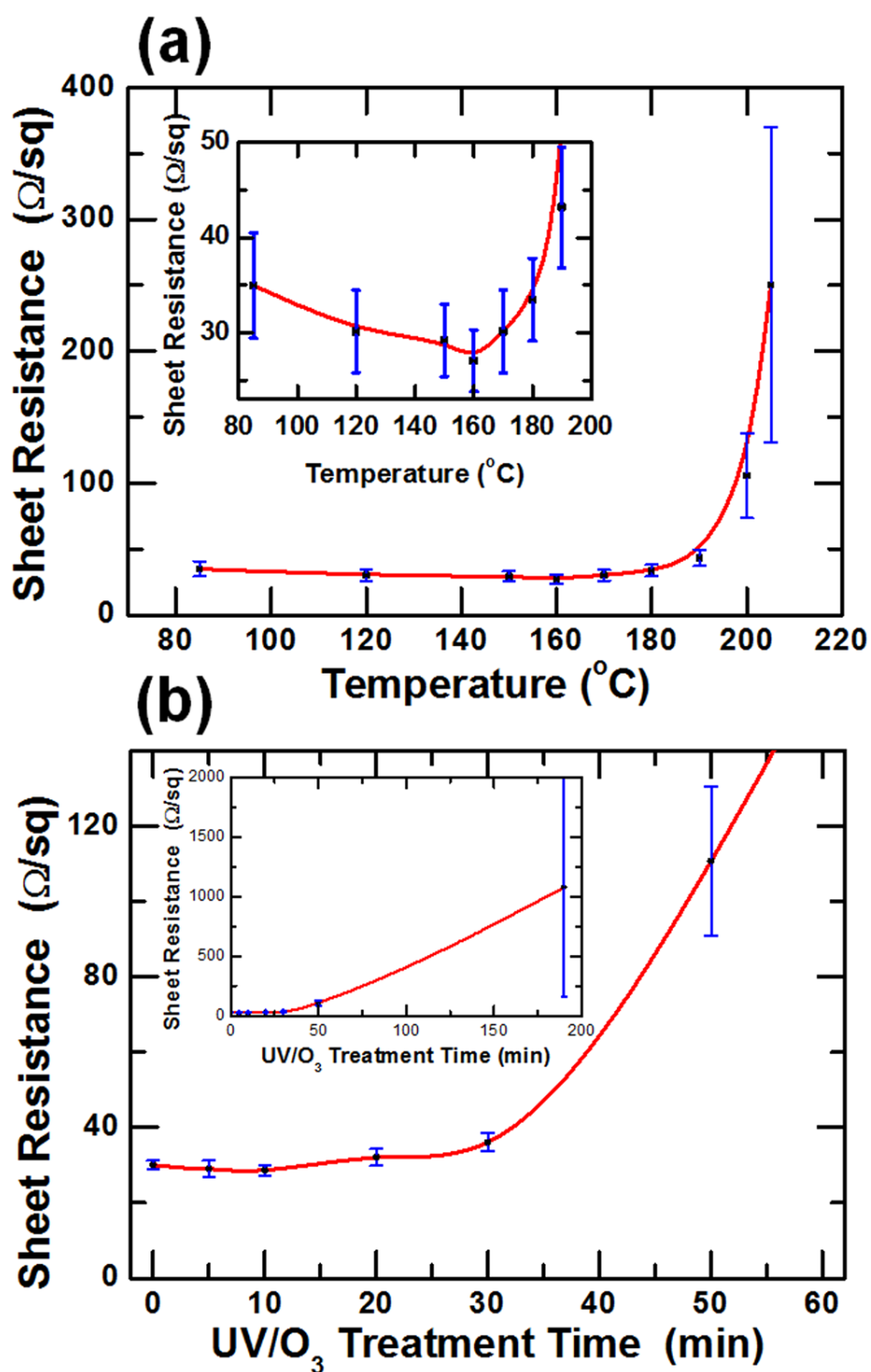


**Figure 5.5** Sheet resistance of the Ag NW electrodes as functions of the (a) thermal treatment temperature and (b) UV/O<sub>3</sub> treatment time [89].

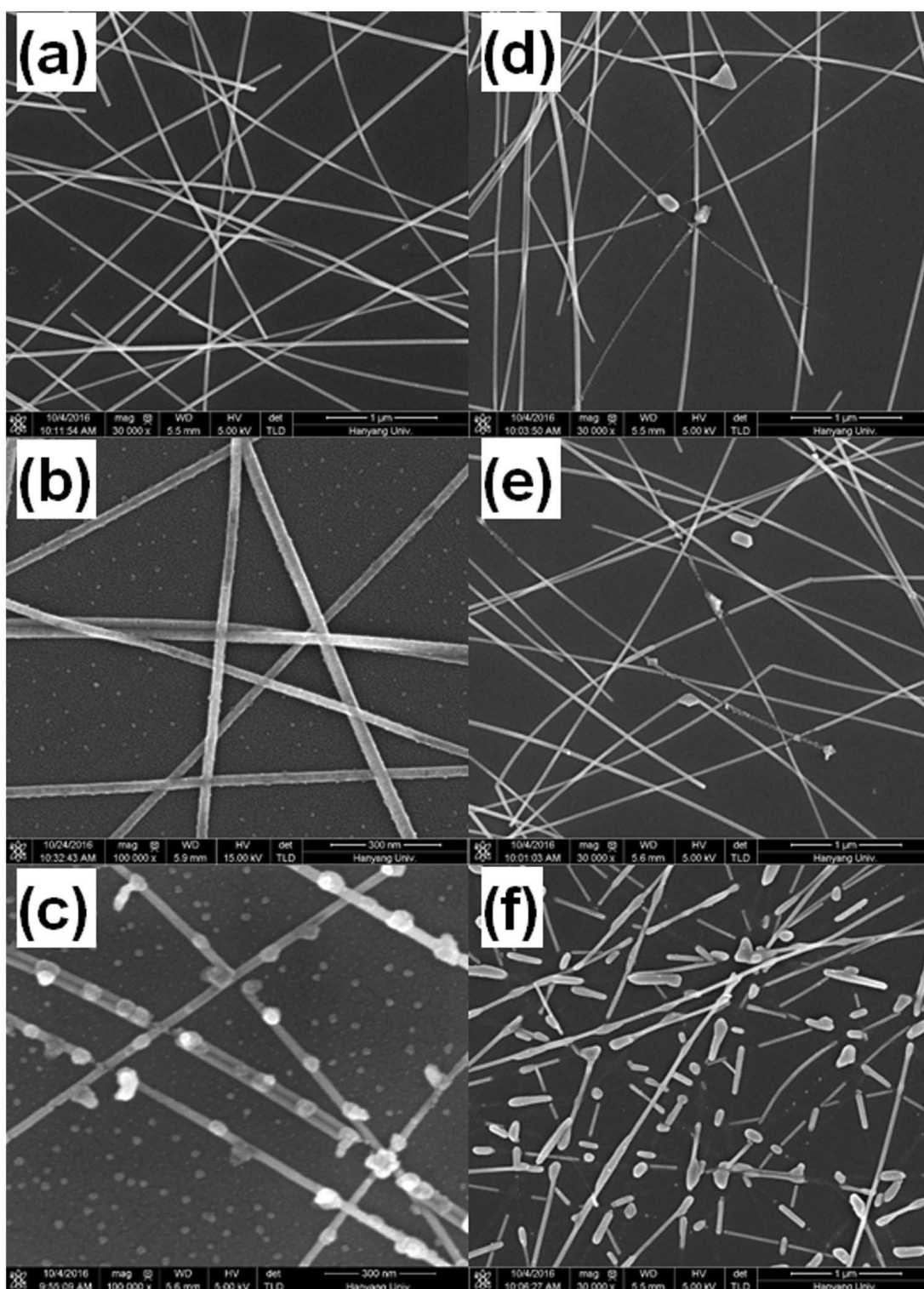


**Figure 5.6** SEM images of the (a) pristine Ag NWs, (b) 30 minutes UV/O<sub>3</sub>-treated Ag NWs, (c) 60 minutes UV/O<sub>3</sub>-treated Ag NWs, and the Ag NWs thermally treated at (d) 160, (e) 190, and (f) 210 °C for 10 minutes [89].

### **5.3 Characterization**

In order to investigate the morphology of Ag NW networks, SEM (FEI Nova Nano SEM 430, operated at 10 kV) was used. Ag NWs on Si substrates were directly placed onto the SEM sample holders. Furthermore, a detailed morphological and elemental analysis were conducted via transmission electron microscopy (TEM) performed on a JEOL FEG-TEM 2100F microscope, operated at 200 kV. Specimens for TEM analysis were prepared through the removal of Ag NWs from Si substrates using ultrasonication. Then, Ag NWs which diluted in ethanolic solutions were transferred onto holey carbon-coated copper grids. Energy dispersive X-Ray spectroscopy (EDS) attached to TEM was conducted for the compositional analysis. In addition, PHI 5000 VersaProbe spectrometer was used to collect XPS spectra. C (1s) line at 284.5 eV was used for reference and charge correction of the binding energies (BE). XRD measurements were performed on a Rigaku D/Max-2000 diffractometer at Bragg-Brentanno geometry at 40 kV.

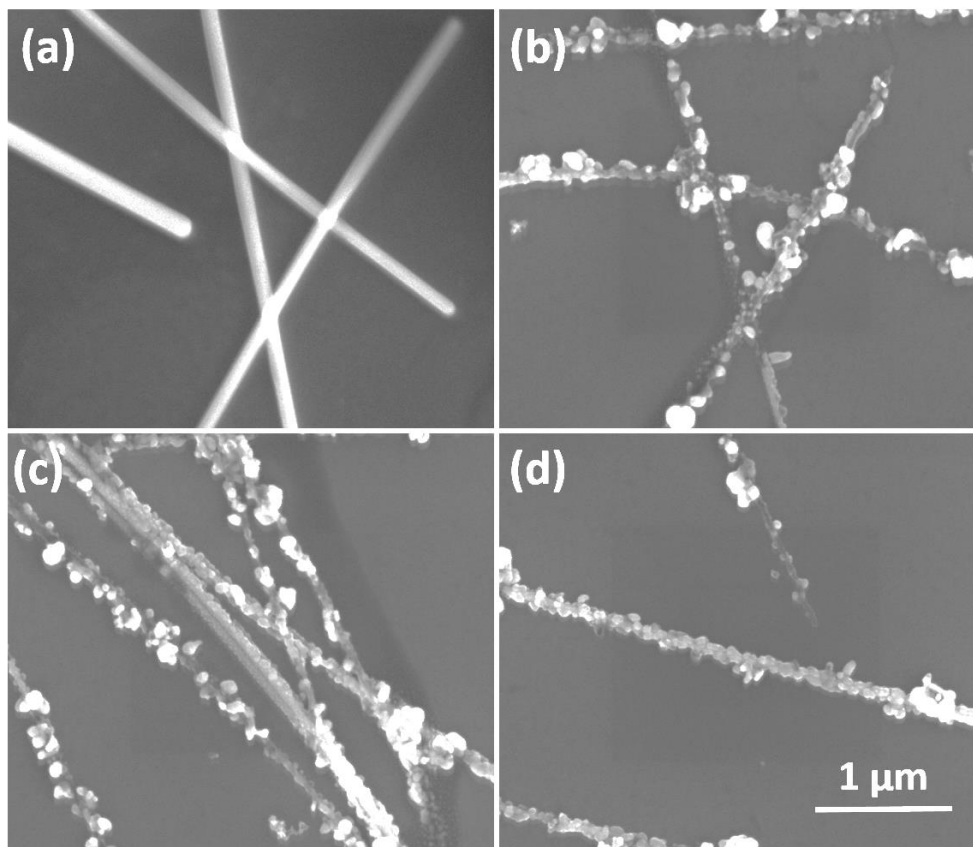
### **5.4 Sample Preparation**

Ethanolic solutions of Ag NWs were spray coated onto Si substrates. As prepared samples without any further treatment were kept at ambient conditions for stability tests up to 6 months. Ag NWs were redispersed in DI water, ethanol, 2-propanol (IPA) and chloroform after purification and kept at +4°C in a refrigerator the for solvent stability tests.

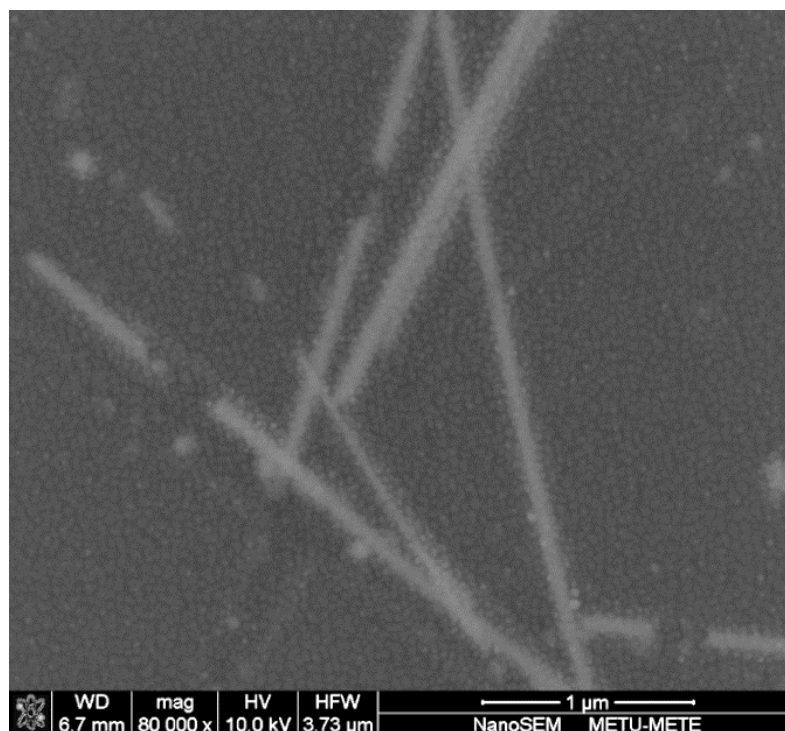
### **5.5 Results**

Figure 5.7 (a) shows SEM image of Ag NW networks in as prepared condition. As it can be seen from the figure, Ag NWs have smooth surfaces 1D morphology. However, some nanoparticle like structures are started to form on the lateral surfaces of Ag NWs kept in ambient conditions. Severe corrosion of Ag NWs causes rupture of the nanowires and so destruct the conductive network. In addition, Ag NWs are

not only vulnerable to the ambient atmosphere; but also, are sensitive to upcoming layers of the opto-electronic devices. For instance, Figure 5.8 shows an SEM image of Ag NW networks spin coated with PEDOT:PSS, and kept under protective atmosphere for one month. Due to the acidic nature of PEDOT:PSS (pH: ~2) Ag NWs started to dissolve in this polymeric media and lose its structural integrity.



**Figure 5.7** SEM images of Ag NW networks that are (a) as-prepared and kept in ambient conditions for 6 months (b), (c) and (d).



**Figure 5.8** SEM image of Ag NW networks spin coated with PEDOT:PSS and kept under protective atmosphere for 1 month.

Further investigation of as formed nanoparticles on lateral surfaces of Ag NWs were made via TEM. Figure 5.9 shows TEM images of corroded Ag NWs and nanoparticles on their surfaces. Nanoparticles are formed as residual PVP layer keeps its presence on lateral surfaces of the nanowires.

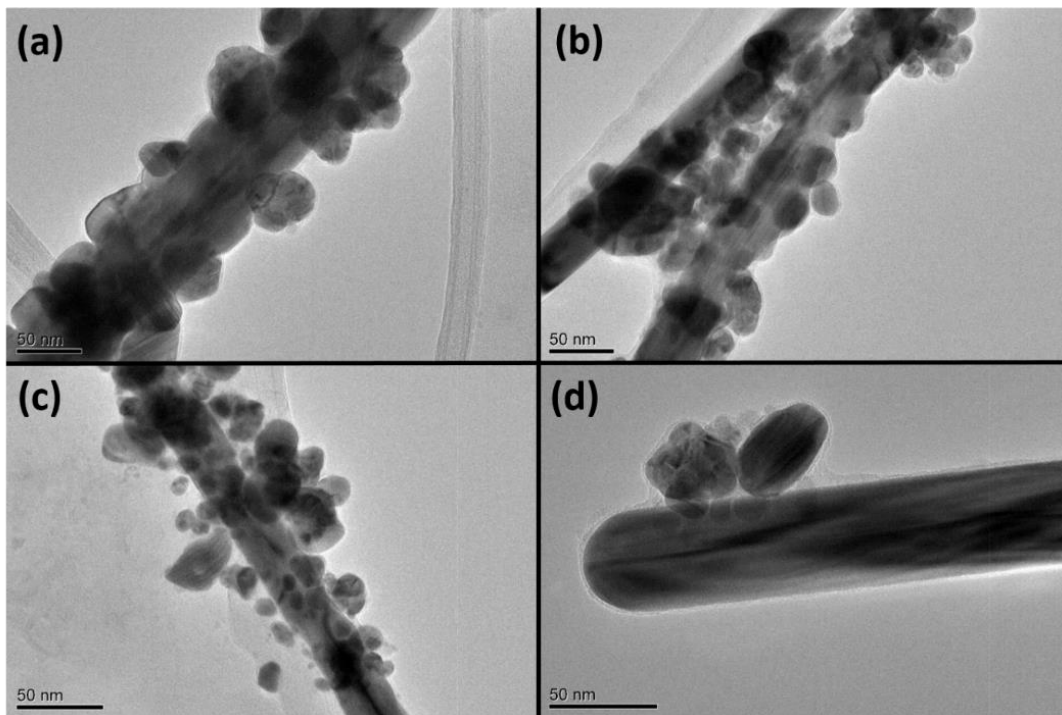


**Figure 5.9** TEM images of various corroded Ag NWs with as formed nanoparticles on their lateral surfaces (a), (b), (c) and (d).

Figure 5.10 shows HRTEM images of as prepared (a) and corroded Ag NWs (b), (c) and (d). As it can be seen from Figure 5.10 (a) as prepared Ag NWs have a smooth and defect free surfaces. In addition, residual PVP layer is still present on the lateral surfaces of the nanowires (~2-3 nm thick). Nanoparticles directly grow on the surface of the nanowires as shown in Figure 5.10 (b), (c) and (d). Moreover, as formed nanoparticles are also crystalline as shown in Figure 5.10 (c) and (d). Formed nanoparticles are polycrystalline, since at least two different growth directions are observed for these nanoparticles (Figure 5.10 (c) and (d)).

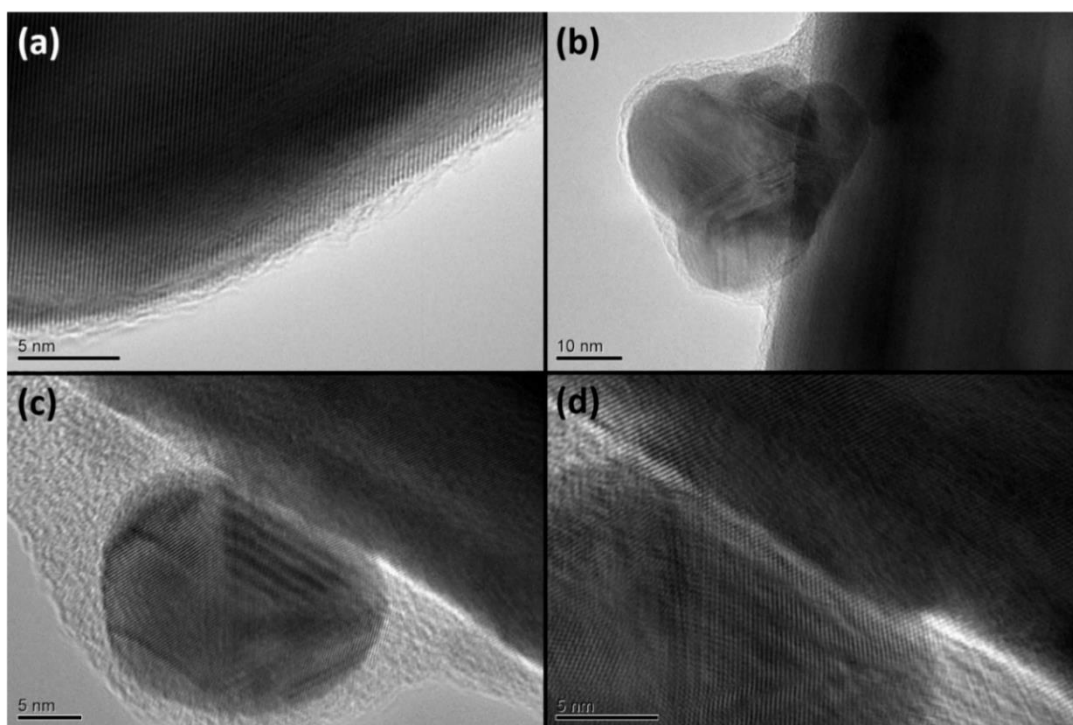


**Figure 5.10** HRTEM images of (a) as-prepared and (b), (c) and (d) various corroded Ag NWs with as formed nanoparticles on their lateral surfaces.

Figure 5.11 shows an EDS result for an individual Ag NW, obtained through S/TEM which is in as-prepared condition. Elemental compositions obtained during EDS analysis is tabulated and provided in Table 5.1, Ag is the only element present within the as-prepared nanowires. Since PVP contains O and N elements, they were intentionally excluded during the EDS measurement.

Figure 5.12 shows EDS result for a nanoparticle formed on lateral surface of a nanowire obtained through S/TEM. Elemental compositions obtained during EDS analysis is tabulated and provided in Table 5, besides Ag, S is also present in the structure. This result is quite coherent with the one reported by Elechiguerra et al. [88] and it can be said that these nanoparticles formed on the surfaces of nanowires are silver sulfide ( $\text{Ag}_2\text{S}$ ).

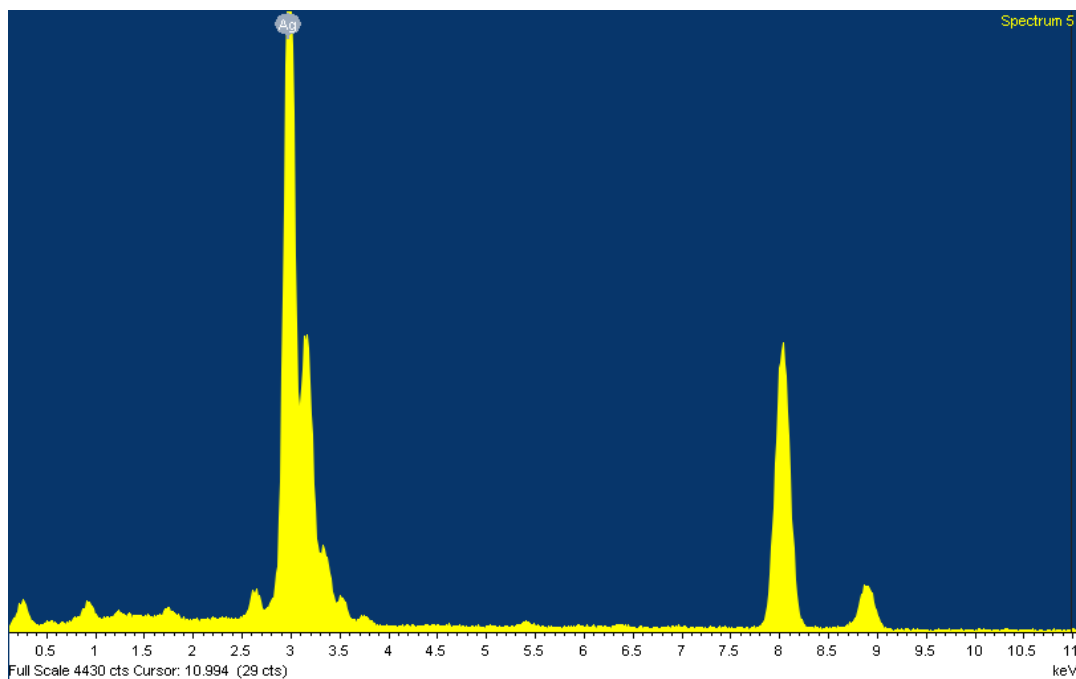


**Figure 5.11** EDS analysis of a Ag NW in as-prepared condition.

**Table 5.1** EDS result of an Ag NW in as-prepared condition.

Element	Peak	Area	k	Abs	Weight%	Weight%	Atomic%
	Area	Sigma	factor	Corn.		Sigma	
<b>Ag L</b>	105469	901	1.724	0.895	100.00	0.00	100.00
<b>Totals</b>					100.00		

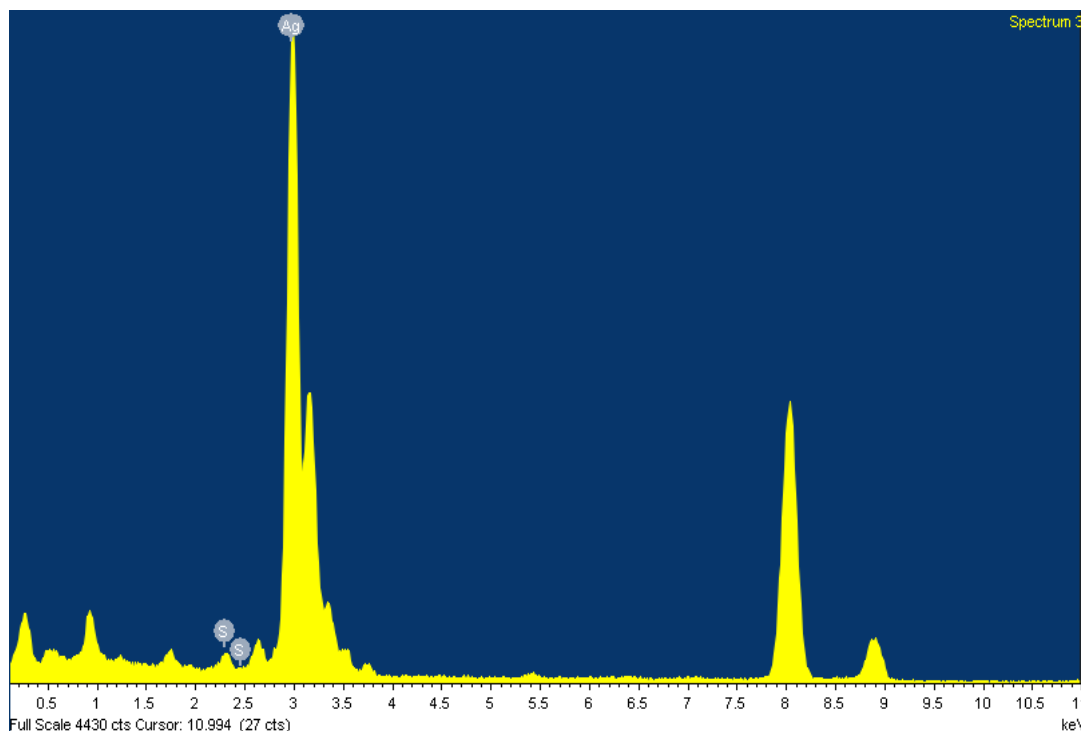
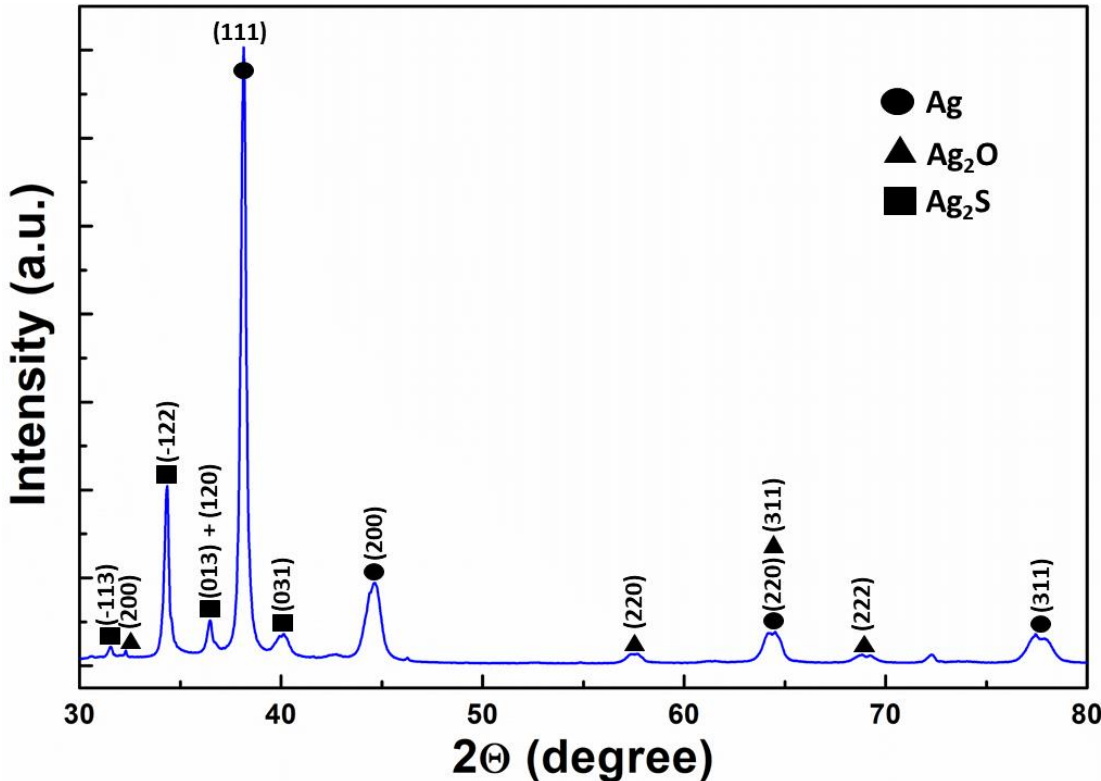


**Figure 5.12** EDS analysis of an Ag NW with nanoparticles on its lateral surfaces.

**Table 5.2** EDS results of a corroded Ag NW with nanoparticles on its lateral surfaces that was kept in ambient conditions for 6 months.

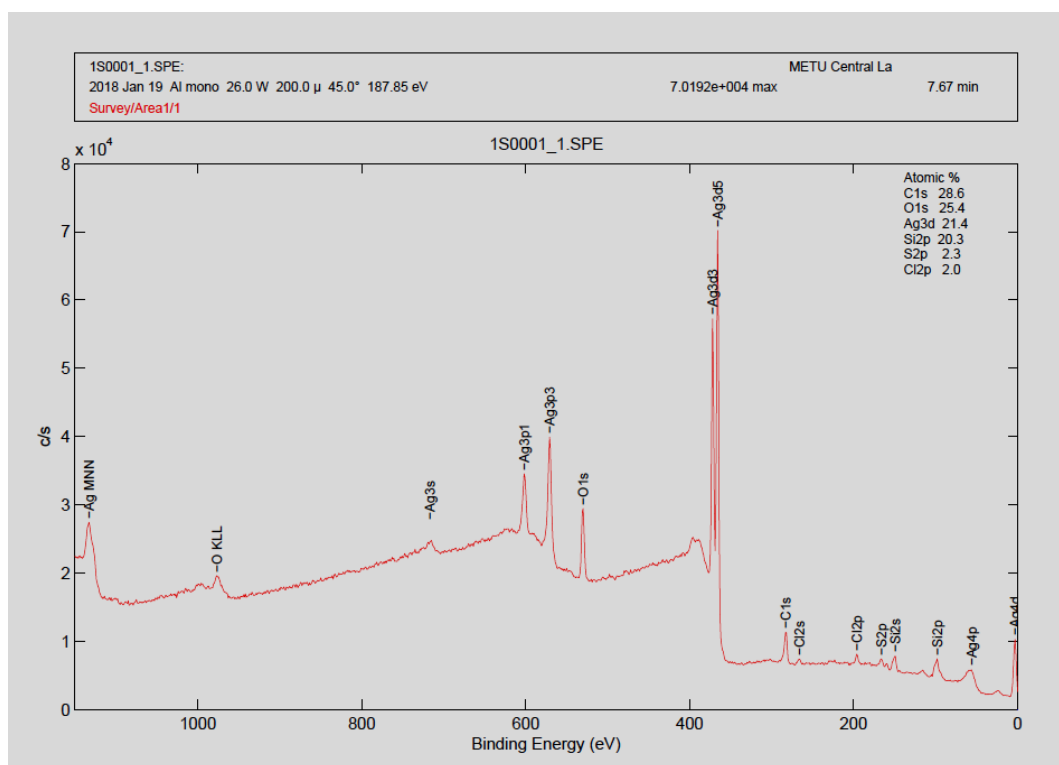
Element	Peak	Area	k	Abs	Weight%	Weight%	Atomic%
	Area	Sigma	factor	Corn.		Sigma	
<b>S K</b>	1476	141	0.940	0.928	0.89	0.09	2.94
<b>Ag L</b>	92682	845	1.724	0.896	99.11	0.09	97.06
<b>Totals</b>					100.00		

Figure 5.13 shows XRD spectrum of Ag NWs that were kept under ambient conditions for 6 months. Self-standing Ag NW foils fabricated via vacuum-filtration method was used for the XRD measurements. XRD analysis showed that Ag NWs within the foil gets both sulfurized and oxidized. Oxidation of bulk Ag generally necessitates more time than its sulfurization. However, since Ag NWs have much higher surface to volume ratio, their oxidation can readily take place under ambient conditions.



**Figure 5.13** XRD spectrum of corroded Ag NWs. (JCPDS card no 04-0783 for pure Ag, 76-1393 for Ag<sub>2</sub>O and 65-2356 for Ag<sub>2</sub>S)

XPS analysis was performed on an Ag NW network that was kept 6 months under ambient conditions for 6 months. Binding energies obtained in the XPS analysis calibrated against C 1s peak at 284.2 eV indicate the presence of C, Ag, O and S, as shown in Figure 5.14. Figure 5.15 shows the high resolution Ag 3d<sub>5/2</sub> and Ag 3d<sub>3/2</sub> peaks at 365.7 and 371.17, respectively with a spin-orbit separation of 5.47 eV. The presence of C, O, and S on the surface of the corroded Ag NWs was confirmed. The values for the binding energies of the three elements C 1s 282.3 and 283.2 eV as shown in Figure 5.16, O 1s peak can be deconvoluted into two peaks with binding energies of 531 and 531.9 eV as shown in Figure 5.17. The peaks observed in Figure 5.18 correspond to S 2p<sub>3/2</sub> and S 2p<sub>1/2</sub> have binding energies of 159.6 and 166.5 eV.



**Figure 5.14** XPS survey spectrum of corroded Ag NWs.

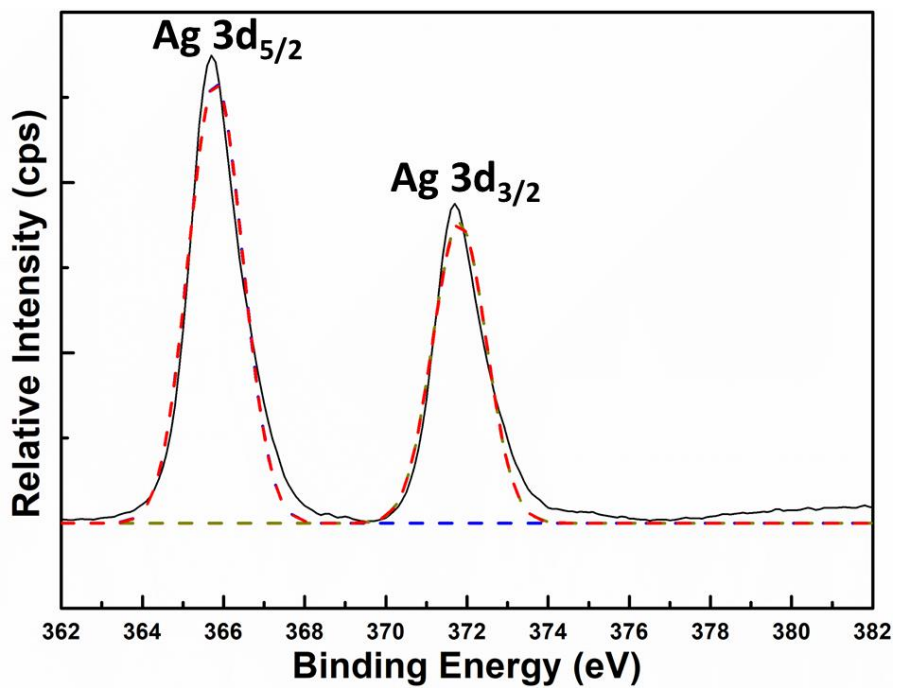


Figure 5.15 High-resolution XPS spectrum of Ag 3d.

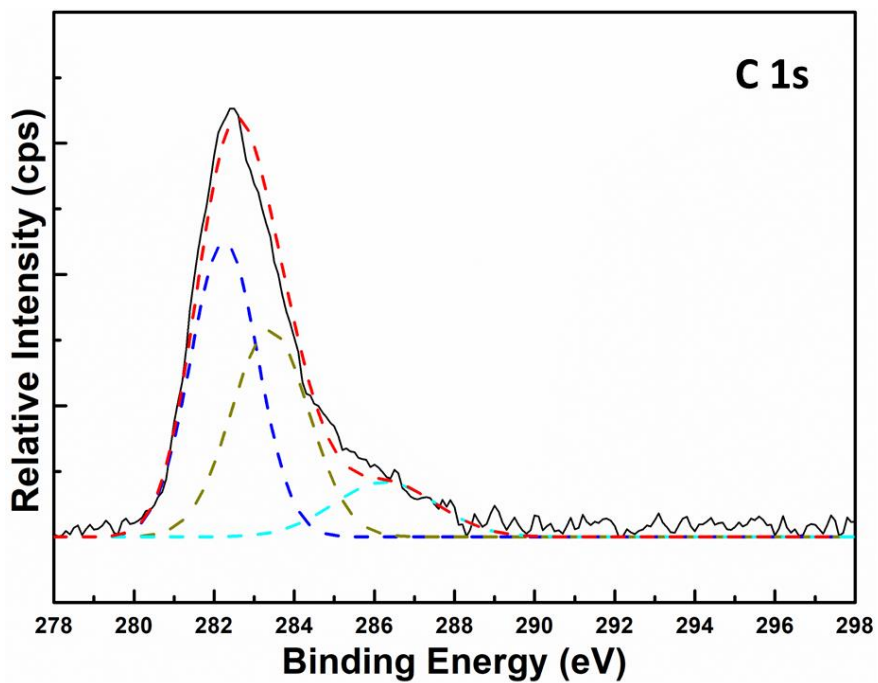
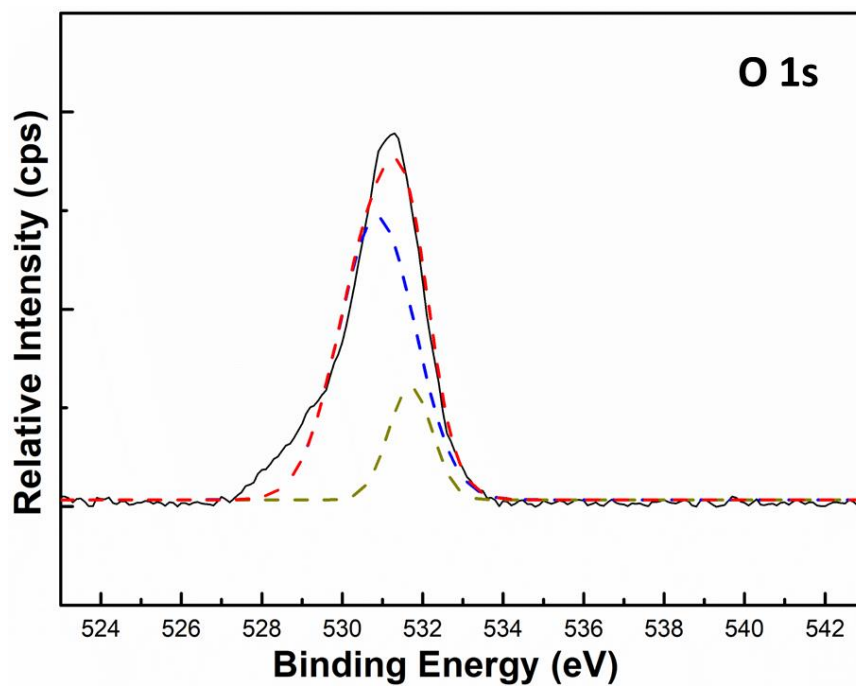
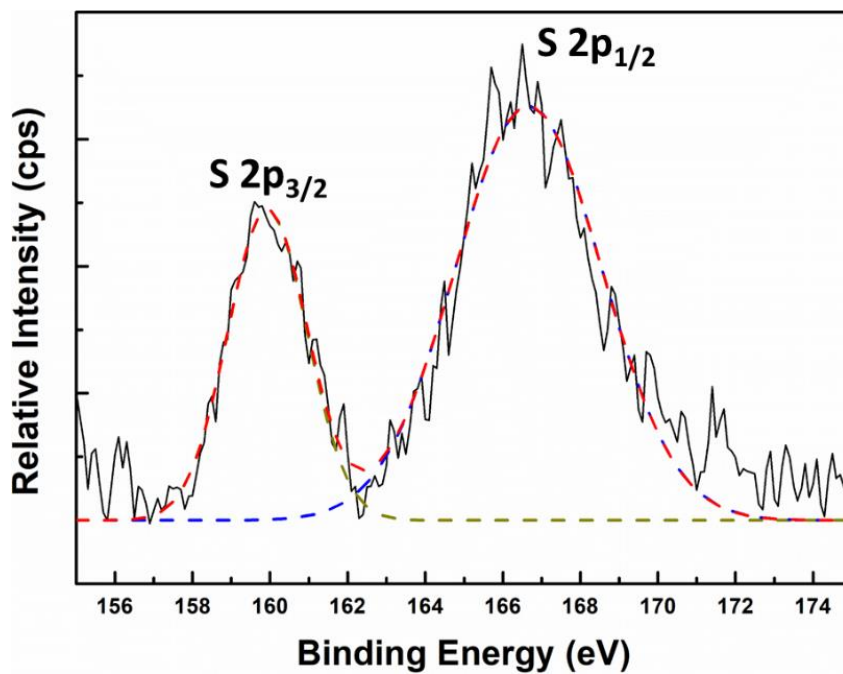


Figure 5.16 High-resolution XPS spectrum of C 1s.



**Figure 5.17** High resolution XPS spectrum of O 1s.



**Figure 5.18** High resolution XPS spectrum of S 2p.

As discussed in detail in the previous chapters, Ag NWs are synthesized via a solution process and then purified via multiple centrifuge processes. Then Ag NWs are dispersed in various solvents for further characterization and utilization. Hence, the solvent stability of Ag NWs is equally important to their network stability. As their solvent stability is explored, it will be possible to keep Ag NW in solution without degradation. For this purpose, Ag NWs were dispersed in various solvents such as DI water, ethanol, IPA and chloroform. These suspensions were kept at +4°C in a refrigerator. Figure 5.19 shows SEM images of Ag NWs dispersed in (a) DI water, (b) ethanol, (c) IPA and (d) chloroform for 2 years. As shown by SEM images, morphological change nor is degradation observed in silver nanowires. Ag NWs kept their pristine morphology and no degradation was observed.

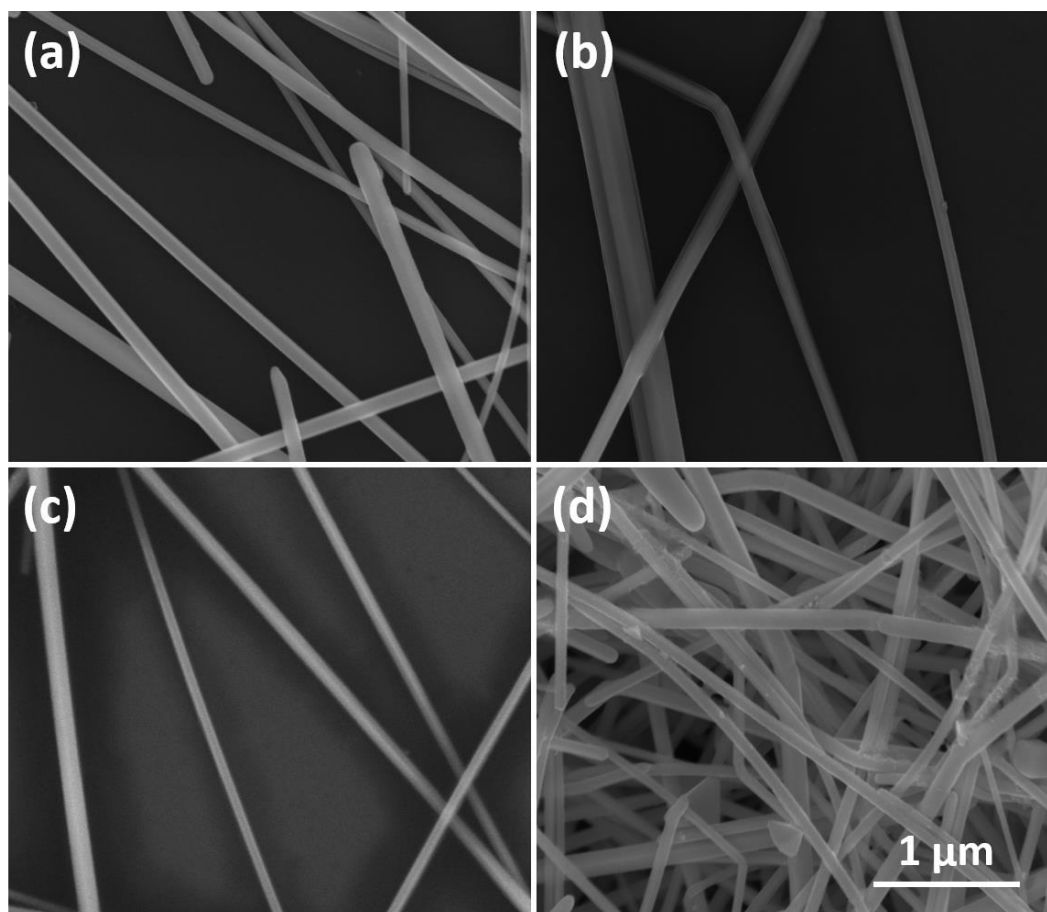


**Figure 5.19** SEM images of Ag NWs kept in (a) DI water, (b) ethanol, (c) IPA and (d) chloroform at 4°C for 2 years. All scales are the same.

Degradation of Ag NWs might also take place due to the service conditions of a device that utilizes them. Ag NWs networks generate heat via Joule heating mechanism when a direct current (DC) voltage is applied [90]. This heat may cause rupture of Ag NWs particularly targeting the ones with thinner diameters within the network. Figure 5.20 shows SEM images of Ag NW networks that were subjected to a high current flow. As shown by the SEM images, a discontinuity occurs in the network and although most nanowires remain intact, the ones in the channel gets destroyed.

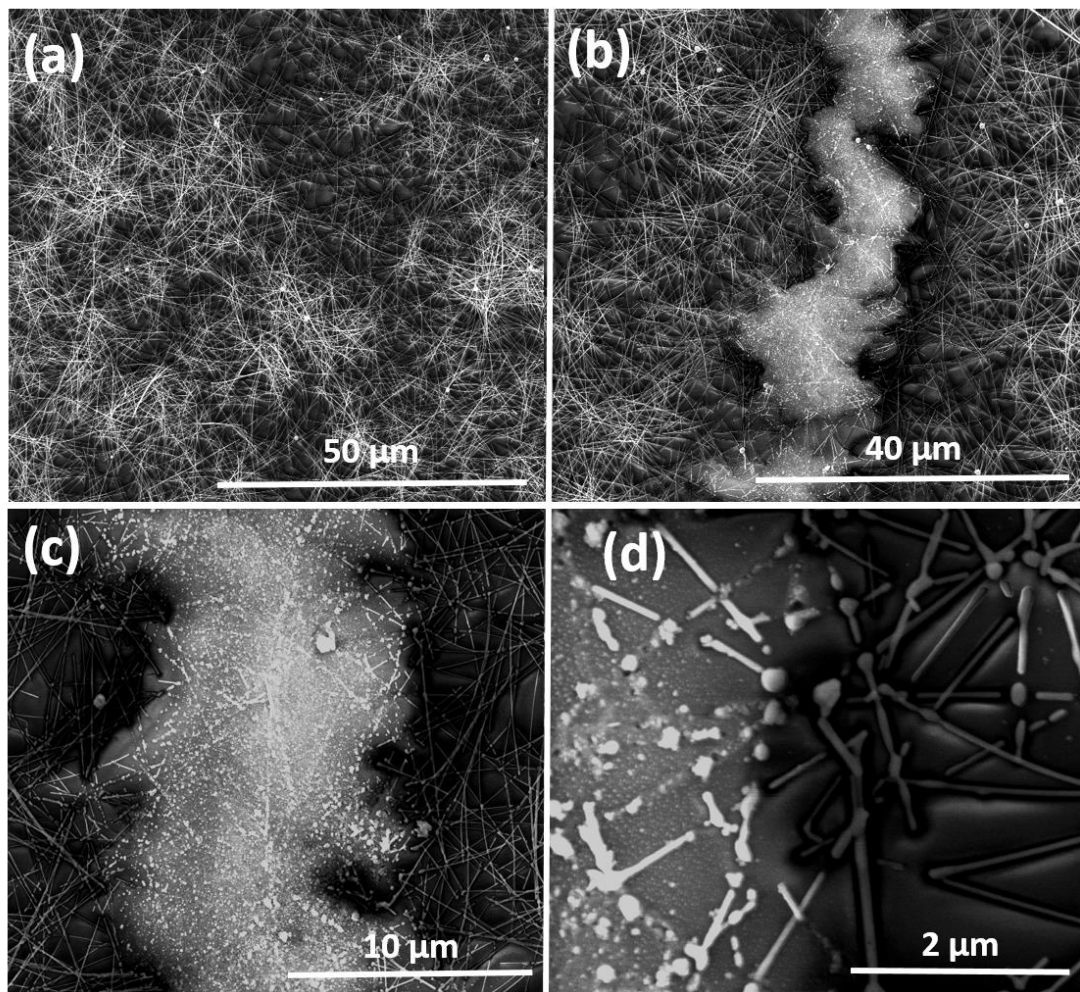


**Figure 5.20** SEM images of failed Ag NW networks under high current.

Figure 5.21 shows how the sheet resistance of Ag NW networks changes with temperature for the electrodes with two different resistance values. Heat treatment up to 250°C caused well integration of Ag NWs to each other at the junction points and decreased the resistance of the network. Depending on the initial resistance of the network, up to 7 orders of magnitude change in resistance can be obtained in the networks (Figure 5.21). However, temperature above 250°C irreversibly increased the resistance of the network. These results were found to be in reasonable agreement with the ones obtained in Chapter 3 Figure 3.41 where an annealing temperature of 200 °C was used for the Ag NW network following deposition in consecutive experiments. These measurements were made at LGMP, France. Samples were placed onto a heated stage and contacts were spring loaded during measurements. A photograph of the experimental setup is shown in Figure 5.21 as inset. A Keithley 2400 source meter was used for the measurements controlled through a LabVIEW programme. Samples were heated from 25 to 275 °C in air atmosphere at a heating rate of 10 °C/min while monitoring the change in resistance.

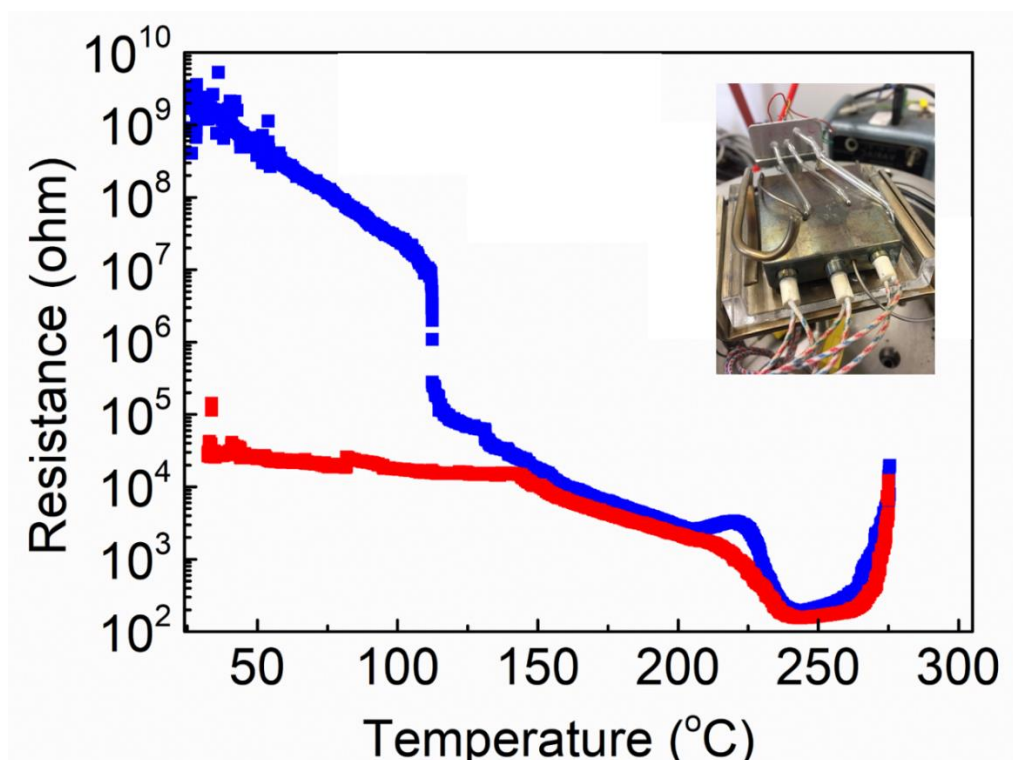


**Figure 5.21** Resistance change in Ag NW nanowire networks with increasing temperature. Inset show photograph of the measurement setup.

## CHAPTER 6

### SOL-GEL COATING OF NiO THIN FILMS ON SILVER NANOWIRE NETWORKS

#### 6.1. Introduction

Due to ambient vulnerability of Ag NWs, researchers seek for a protective layer to prevent oxidation of these 1D nanostructures. The upcoming layer to serve as a protector layer on Ag NW networks should also be transparent and should not decrease the network conductance. The use of Ag NWs as transparent conductors in opto-electronic device, such as organic photovoltaics (OPVs) or organic light emitting diodes (OLEDs) necessitate a hole transport layer (HTL), as discussed in Chapter 4. For this purpose, preferentially p-type semiconductors seem to be perfect candidates. They can serve as both protective and charge transport layers. So far, researchers have demonstrated the use of several semiconducting metal oxide layers in order to decrease the surface roughness and increase the stability of Ag NW networks. Ju et al. used indium doped zinc oxide (IZO) for this purpose [91]. Figure 6.1 shows how The IZO / Ag NW network nano composites were prepared through sputtering. It has been claimed that IZO buffer layer is critical in achieving a conductive nano composite with IZO buffer layer can achieve a highly conductive, excellent mechanical properties, stability and high transparency. In addition, the IZO layer entirely covers the Ag NWs, thereby filling empty spaces between nanowires, strongly binding the Ag NW network and reducing the sheet resistance of the network without a chemical treatment. IZO acted as an encapsulation layer protecting the Ag NWs from surface oxidation, thus improving the mechanical and chemical stability of the nano composite film [91].

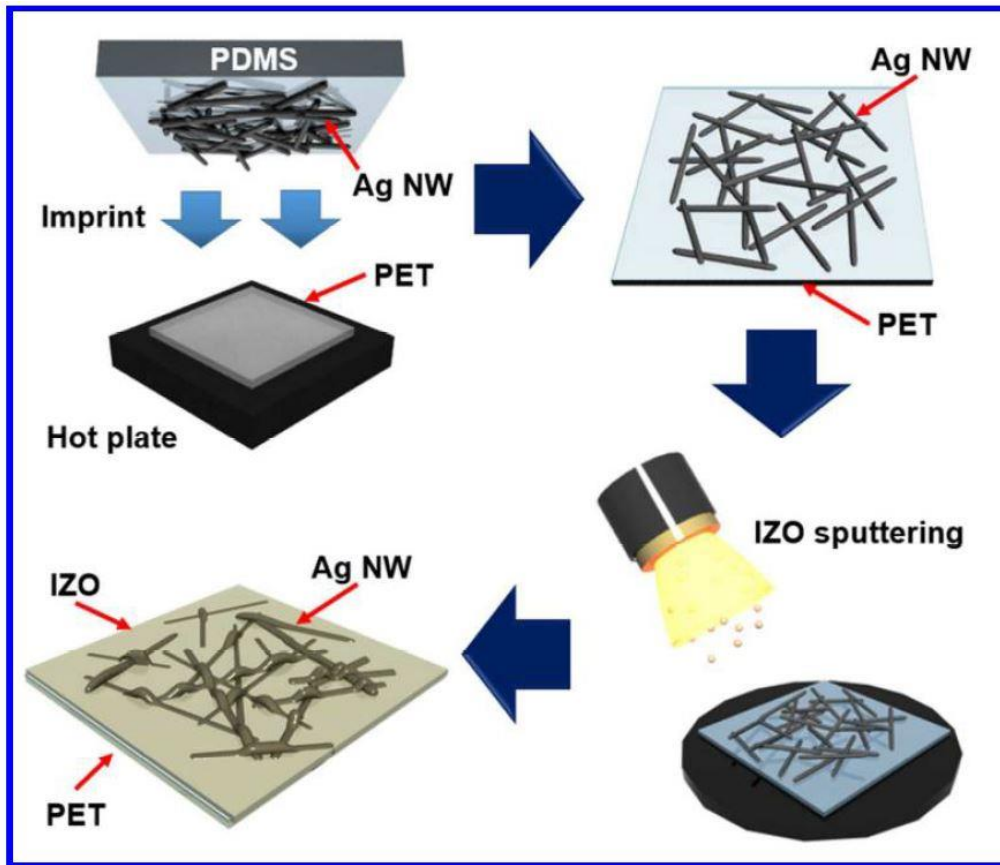


**Figure 6.1** Schematic representation of the preparation of IZO / Ag NW nano composites [91].

Figure 6.2 shows tilted SEM images of Ag NW networks following IZO deposition. Deposition of IZO decreased the surface roughness of the Ag NW networks.

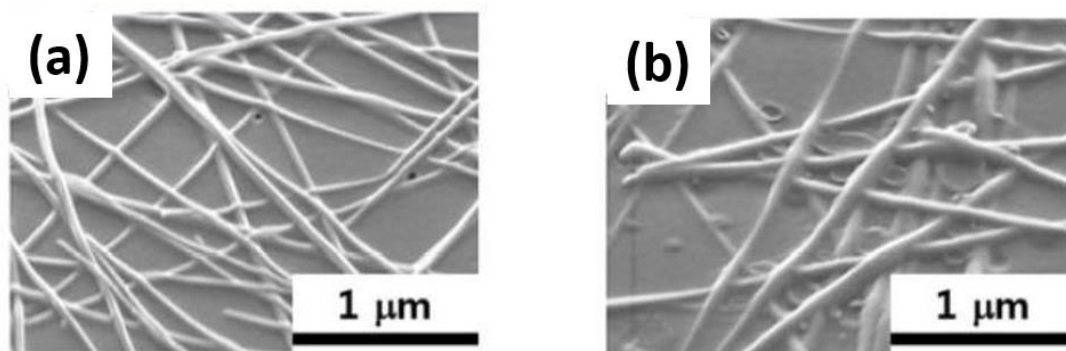


**Figure 6.2** Tilted cross-sectional SEM image of transferred Ag NWs (a), a composite Ag NW/IZO film (b) [91].

However, for a HIL or HTL a p-type semiconductor is desired rather than a hole deficient n-type semiconductor (such as ITO, IZO, ZnO). Therefore, the use of p-type semiconductors, such as NiO and MoO<sub>3</sub> on Ag NW networks is considered. Moreover, instead of vacuum based expensive methods such as sputtering and physical vapor deposition, solution-based routes are investigated.

Nickel oxide (NiO) is a well-known wide band gap (3.6-4.0 eV) semiconductor material possessing p-type conductivity. It has been widely used in gas sensing [92], catalysis [93], electrochromic [94] and optoelectronic applications. P-type electronic conductivity of NiO makes it a suitable candidate as a hole transport medium in LEDs and solar cells, where robustness and abundance of NiO is advantageous in comparison to expensive and unstable polymeric counterparts. Most of such electronic applications require thin, homogeneous and non-porous layers in order to exhibit low resistance and long carrier diffusion lengths. NiO thin films have been deposited on glass substrates using various techniques like magnetron sputtering [95], pulsed laser deposition [96], chemical vapor deposition [97] and sol-gel process [98]. Among these methods, sol-gel method is a promising and low cost method due to inexpensive equipment requirement, high purity, scalability and reproducibility. This method can be practiced by spray, dip or spin coating techniques for production of a film.

## **6.2 Characterization**

The resultant Ag NWs and thickness and the morphology of the NiO thin films were analyzed by FE-SEM (Nova NanoSEM) operated at 10 kV. X-Ray diffraction (XRD) measurements were carried out on a Rigaku D/Max-2000 pc diffractometer with Cu K<sub>α</sub> radiation operating at 40 kV.

## 6.3. Experimental

### 6.3.1. Fabrication of Silver Nanowire Network Transparent Electrodes

Then using purified silver nanowires, transparent and conducting contacts were fabricated using simple and cost effective procedures. Using spray coating, Ag NWs can be deposited onto various substrates without a size limitation. Figure 7 shows experimental setup for spray coating of silver nanowires. As it is seen, it is possible to coat enormous amount of substrates via spray coating simultaneously. As Ag NW density increases, transmittance and sheet resistance decreases. A good combination of 10  $\Omega$ /sq sheet resistance at % 85 transmittance is easily obtainable with as synthesized silver nanowires. Since there is a thin PVP layer on the lateral surfaces of Ag NWs, a simple annealing process is needed in order to decrease the contact resistance of Ag NWs. As a result, total sheet resistance of Ag NW networks decreases. Figure 6.4 shows SEM images of silver nanowire network at different magnifications.

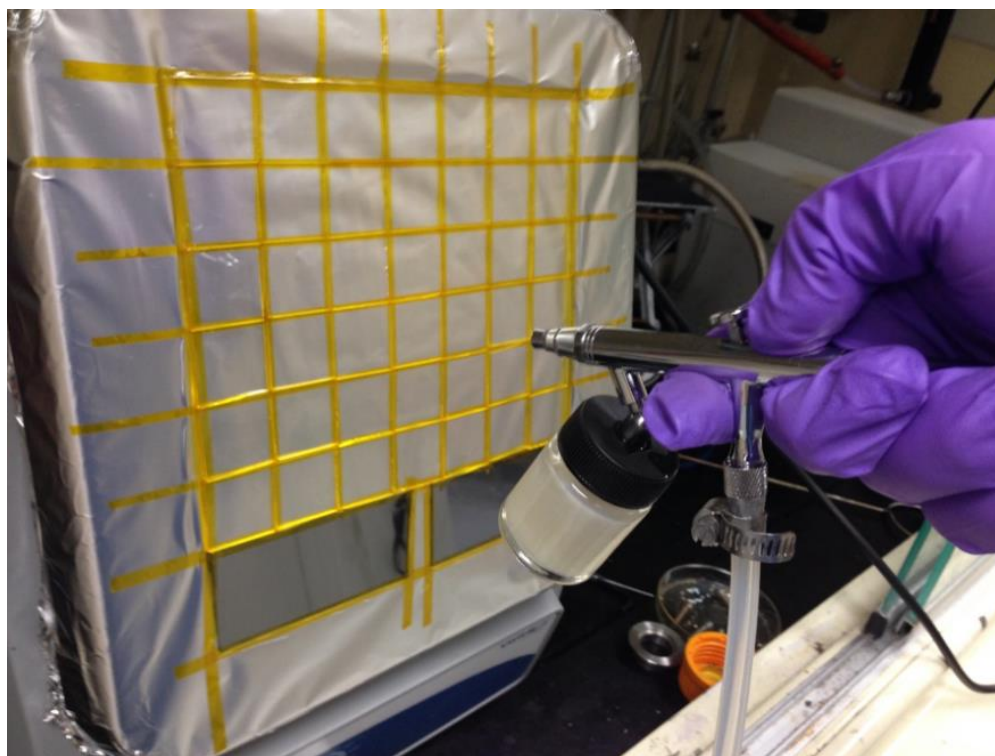


**Figure 6.3** Image of spray deposition set-up for silver nanowire coating.

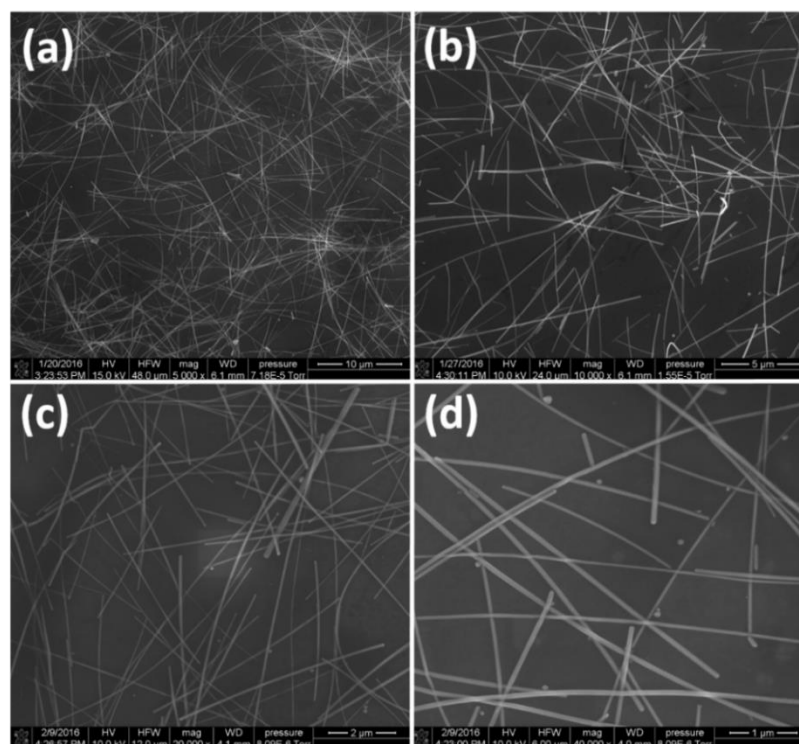


**Figure 6.4** (a) – (d) SEM images of silver nanowire based transparent conductors.

### 6.3.2. Synthesis of Nickel Oxide

NiO thin films have been prepared by sol-gel technique using nickel acetate ( $Ni(CH_3COO)_2 \cdot 4H_2O$ ) as the precursor, 2-methoxyethanol as the solvent and monoethanolamine (MEA) as the stabilizer. Following dissolution of 2 mM of precursor in 20 ml of solvent, 10  $\mu$ l of stabilizer was added to the mixture. The solution was then obtained by stirring at 60°C for 3h. After cooling down to room temperature, solution was ready for the coating process. Glass substrates were cleaned firstly by detergent, then in acetone, isopropanol and deionized water using ultrasonic cleaner and were dried with nitrogen. Solution was dropped onto the glass substrate and spray coated at 3000 rpm for 30 seconds. After each coating step, films were dried at 180°C for 15 min in a furnace to remove the extra solvent. In order to obtain homogeneous and dense layers, films have been grown on glass substrates by

consecutive spin coating of layers (5, 10 and 15) and annealed at different temperatures (400, 450 and 500°C) [99].

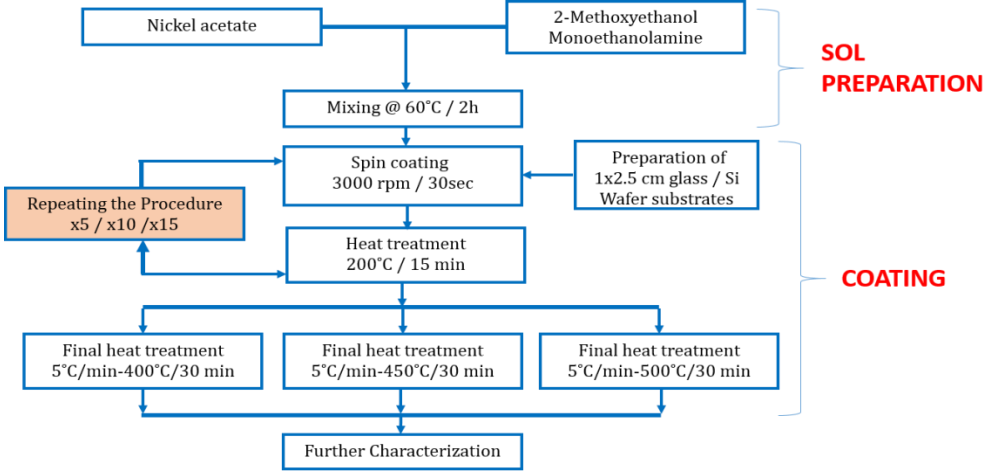


**Figure 6.5** Flowchart showing sol preparation and spin coating procedure of NiO thin films [99].

XRD pattern of a NiO thin film is provided in Figure 6.6. It is seen that films are composed of pure cubic structure of NiO and peaks observed at 37° (111), 43° (200), 63° (220) are assigned to bunsenite phase according to JCPDS card no 47-1049. No other secondary phases, such as Ni(OH)<sub>2</sub> or Ni<sub>2</sub>O<sub>3</sub> are observed. Ni(OH)<sub>2</sub> or Ni<sub>2</sub>O<sub>3</sub> are possible by products observed in literature for sol-gel derived NiO films. It was observed that peaks are not quite distinctive for films annealed at 500°C and intensity of the peaks increases with increasing annealing temperature, indicating that crystallinity of the films strongly depend on the annealing temperature. Films annealed above 500°C clearly shows crystalline structure [99].

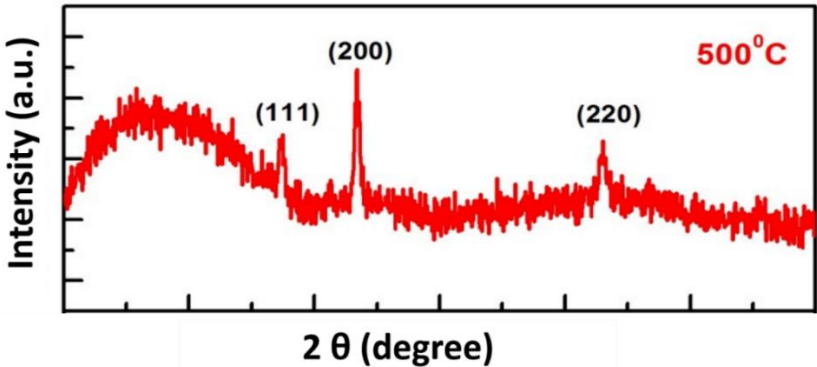


**Figure 6.6** XRD pattern of a NiO thin film annealed at 500° C (JCPDS card no 47-1049) [99].

Morphology of the film surfaces was also investigated and SEM micrographs of that are given in Figure 6.7. NiO thin films with three different thickness were annealed at 500 °C. Homogeneous films were found to be free of cracks and nanoparticles were extra fine and distributed uniformly on the glass substrate for all film thicknesses and annealing temperatures.

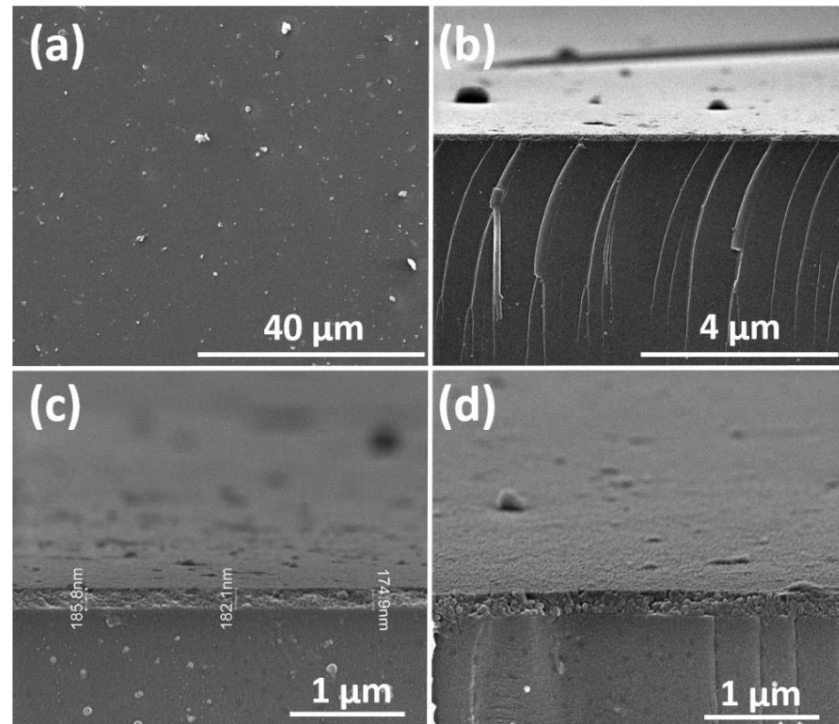


**Figure 6.7** (a) Top-view, (b) – (d) cross-sectional SEM images of NiO thin films on silicon substrates [99].

Following deposition of NiO solution, films were annealed at different temperatures in order to obtain crystalline films. Figure 6.8 shows SEM images of NiO thin films annealed at 400, 450 and 500 °C. SEM images showed that the average size of crystalline NiO particles consisting the thin films decrease with an increase in annealing temperature as the annealing temperature increases the average size of the crystalline NiO particles decreases.

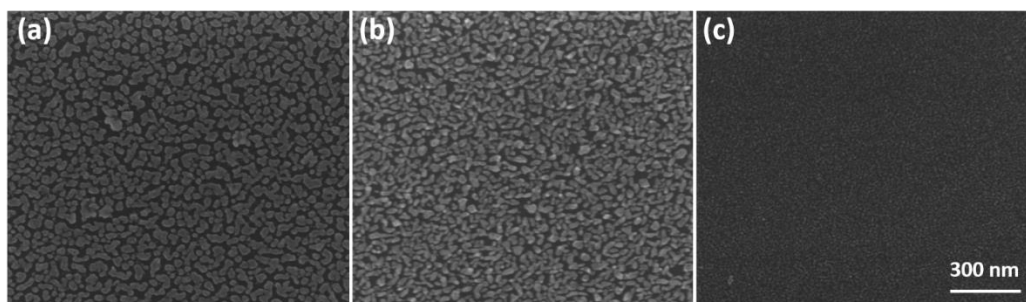


**Figure 6.8** SEM images of NiO thin films on silicon substrates annealed at different temperatures of (a) 400, (b) 450 and (c) 500 °C [99].

Following the successful formation of NiO thin films on Si substrates, the same procedure was applied for Ag NW coated glass and silicon substrates. Figure 6.9 shows SEM images of the samples that are as prepared, 5 times, 10 times and 15 times spin coated with NiO solution, respectively. SEM images showed that the Ag NWS become more and more invisible beneath to NiO thin film as the number of spin coating cycles increase.

Figure 6.9 shows cross-sectional SEM images of NiO thin film coated Ag NW based transparent conductors. It is clear that NiO thin film homogeneously covers the Ag NWs and decreases the surface roughness of the network. Homogeneous film formation is also crucial for the efficient protection of Ag NWs against oxidation. In addition, decreased roughness is also very important for device fabrication since higher surface roughness may cause device shorts in optoelectronic devices as discussed in Chapter 4.

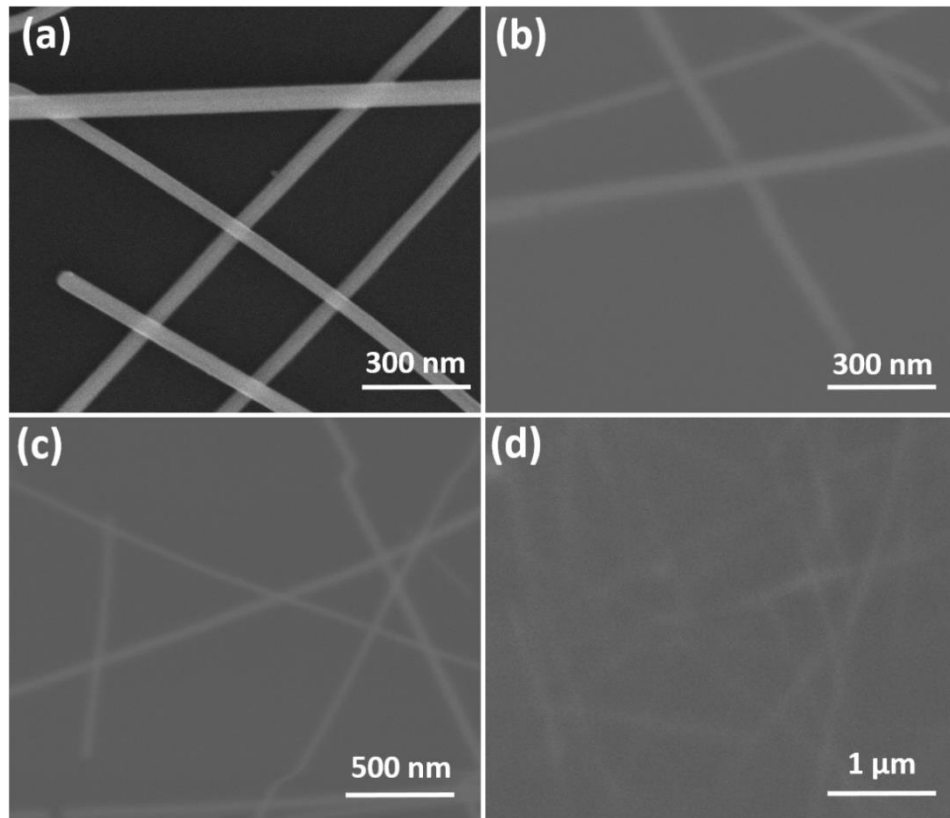


**Figure 6.9** Top-view SEM images of (a) bare Ag NWs networks, (b) 5, (c) 10 and (d) 15 times spin coated NiO thin films.

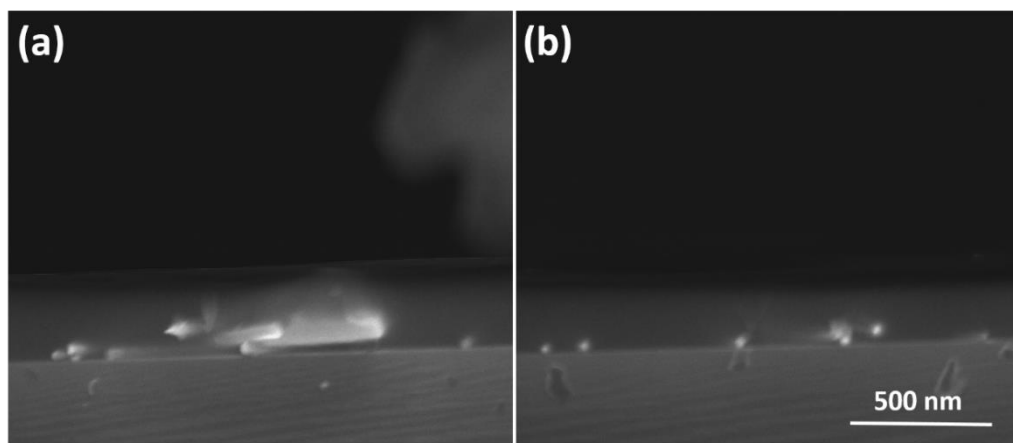


**Figure 6.10** Cross-sectional SEM images of NiO coated Ag NWs from 2 different spots.

Following spin coating, in order to obtain nanocrystalline NiO thin films, a post annealing procedure is needed. For this purpose, first of all, annealing at ambient conditions was investigated. Figure 6.11 shows SEM images of NiO / Ag NW nano composite thin films annealed at 500 °C under ambient conditions. Annealing under ambient conditions resulted in the destruction of Ag NWs, especially for 5 and 10 times spin coated samples. For the 15 times, spin coated sample, seemed to survive their nanowire morphology. This study clearly pointed out that the NiO / Ag NW nano composites should be annealed under the protective atmosphere to nanowire morphology.

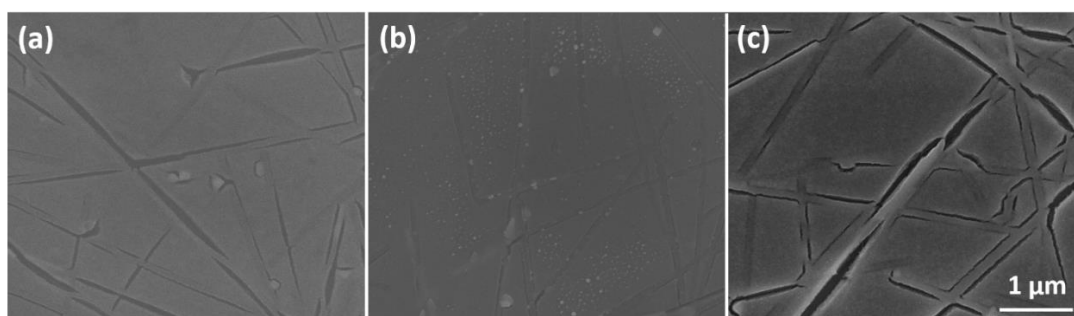
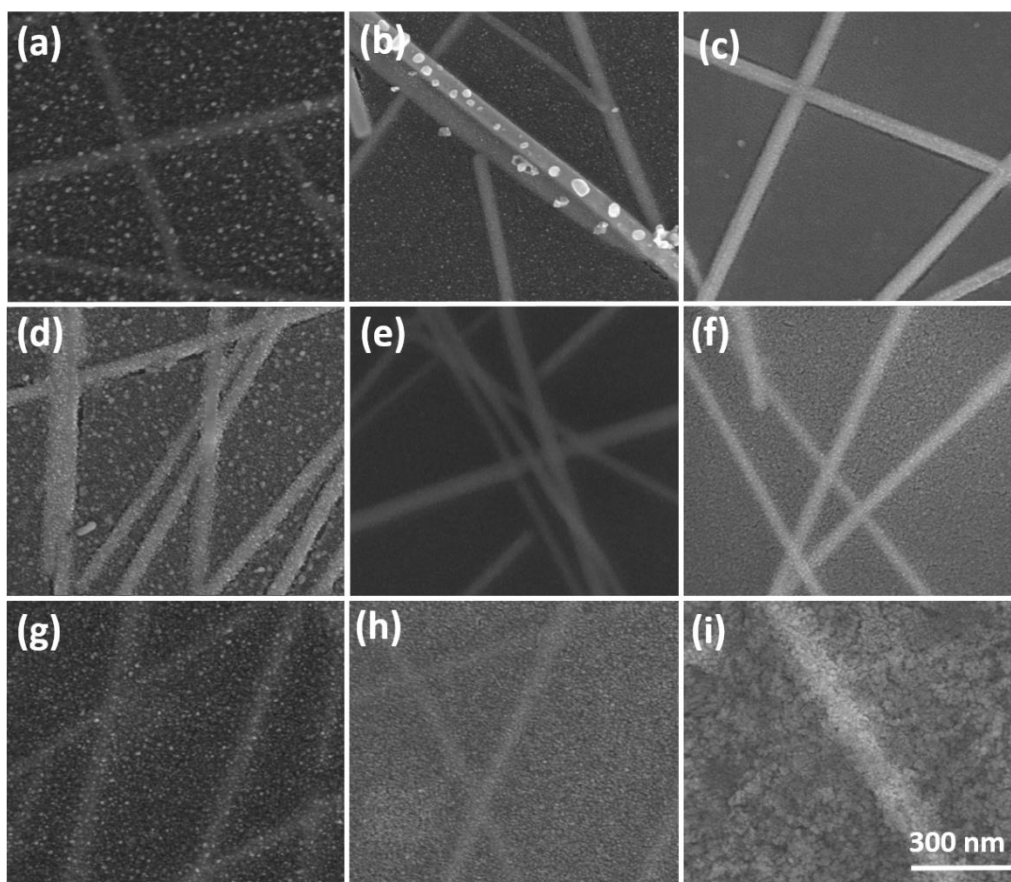


**Figure 6.11** SEM images of NiO / Ag NWs thin films on silicon substrates annealed at 500 °C in air atmosphere (a) 5x, (b) 10x and (c) 15x.

Figure 6.12 show set of SEM images of NiO / Ag NW nanocomposites with different NiO thicknesses (60, 110 and 150 nm) annealed at different temperatures. Annealing was conducted under argon atmosphere. SEM images showed that the particle size of NiO nanocrystals increase and the smoothness of the films gets improved with the increased number of coating cycles and annealing temperatures.

Figure 6.12 (a) shows SEM image of 5 times NiO deposited Ag NW networks annealed at 500°C under argon atmosphere. This sample was kept under ambient conditions until SEM characterization. As shown by the SEM image, NiO layer couldn't protect all Ag NWs. In Figure 6.12 (b) formation of silver oxide nanoparticles

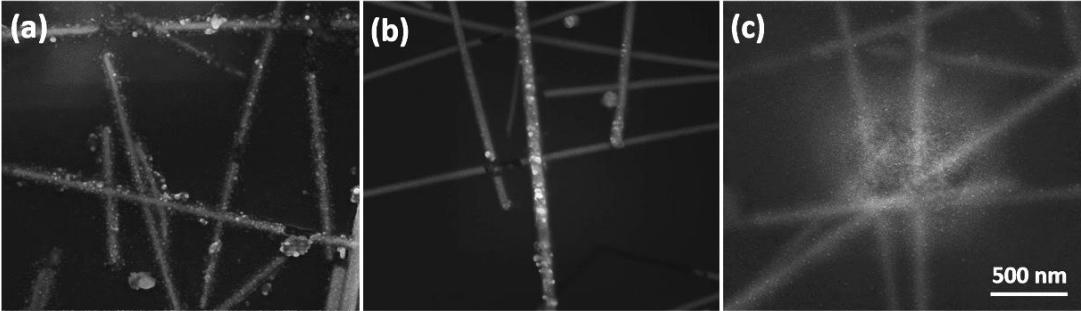
on Ag NWs is obtainable. That means that thicker NiO thin films should be deposited onto Ag NWs thus 10 or 15 deposition cycles should be preferred.



**Figure 6.12** SEM images of NiO/Ag NW nano composite films on Si substrates annealed at different temperatures with different coating cycles (a) 5 times, (b) 10 times, (c) 15 times at 400 °C , (d) 5 times, (e) 10 times, (f) 15 times 450 °C, (g) 5 times, (h) 10X times and (I) 15 times 500 °C under argon atmosphere.

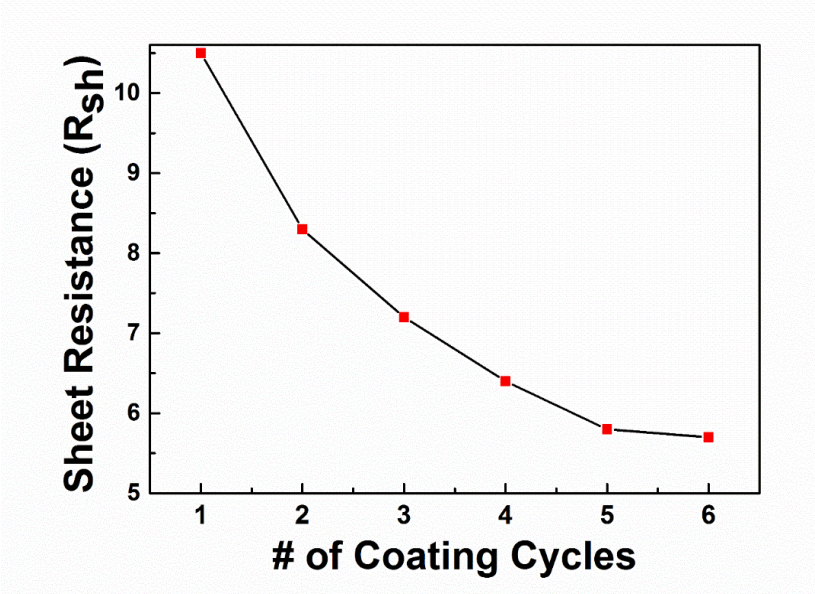
Figure 6.13 shows SEM images of NiO thin film deposited Ag NW network annealed at 500 °C which were kept under ambient conditions for 4 months. SEM images showed that the thickness of the protective NiO thin films has crucial effect on the oxidation behavior of silver nanowires. Five times NiO deposited Ag NWS are started to get oxidized after two months. In addition, the degree of oxidation increases with time. It was also observed that the ten times NiO deposited Ag NWs start to get oxidized after 4 months under ambient conditions. However, fifteen times NiO deposited Ag NWs remained unoxidized even when they were kept under ambient atmosphere for four months. As a result, NiO thickness as a protection layer

around Ag NWs is crucially important. It has been found that a NiO layer at a thickness of about 150 nm perform efficiently as a protection layer for Ag NW based transparent conductors.



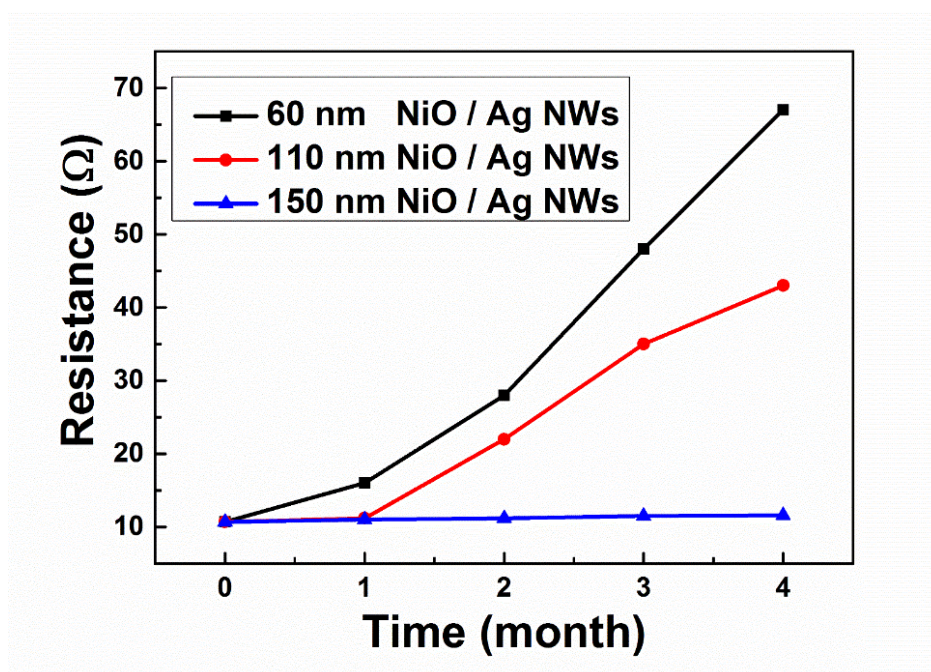
**Figure 6. 13** SEM images of (a) 5, (b) 10 and (c) 15 times NiO deposited Ag NW networks after 4 months. Under ambient conditions. All scales are the same.

Figure 6.14 shows how sheet resistance of Ag NW networks decrease with the number of NiO deposition cycles. This effect may arise from two simultaneous mechanisms. Firstly, annealing steps following each spin coating cycle can decrease the contact resistance between Ag NW junctions. Secondly, as deposited NiO nanoparticles at junction points improve the contacts in between the nanowires.



**Figure 6. 14** Change in sheet resistance for NiO / Ag NW nano composites with the number of NiO deposition cycles.

Figure 6.15 shows how sheet resistance values of NiO deposited Ag NW networks change with respect to time. Although 60 and 110 nm NiO coated networks cannot keep their initial sheet resistance, 150 nm NiO deposited network showed a quite stable sheet resistance behavior.



**Figure 6.15** Change in sheet resistance for NiO / Ag NW nano composites with time.

Figure 6.16 and 6.17 show percent transmittance and absorbance behavior of NiO deposited Ag NW networks, respectively. Absorbance and Transmittance spectra for bare glass and Ag NWs on glass is also provided for comparison. These measurements have shown that the increased NiO thickness decreased the transmittance of the networks while increasing their absorbance.

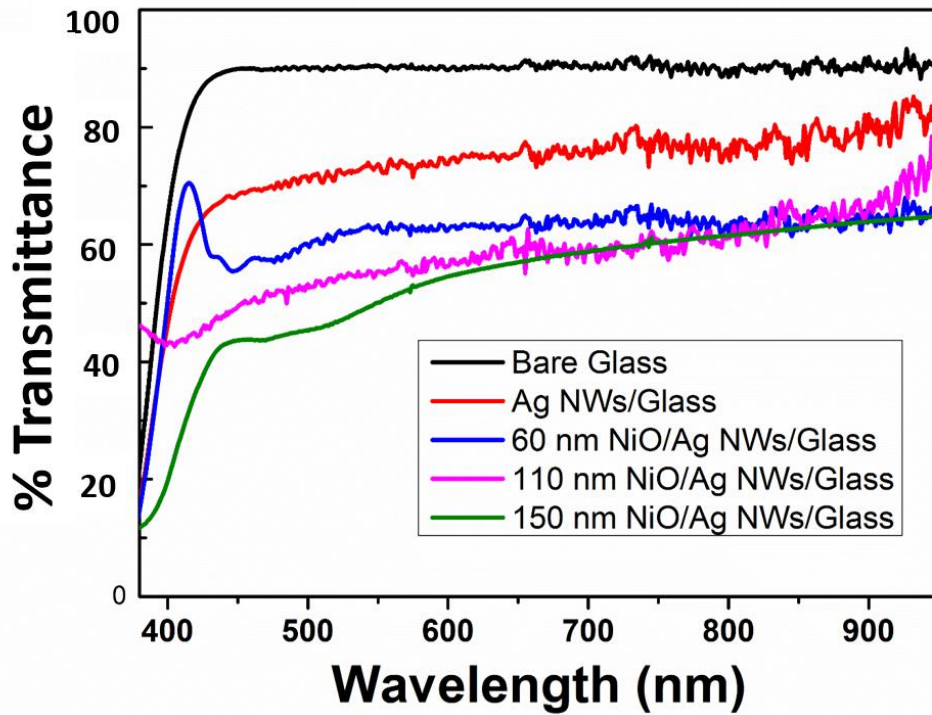


Figure 6.16 Percent transmittance of NiO / Ag NW nano composites.

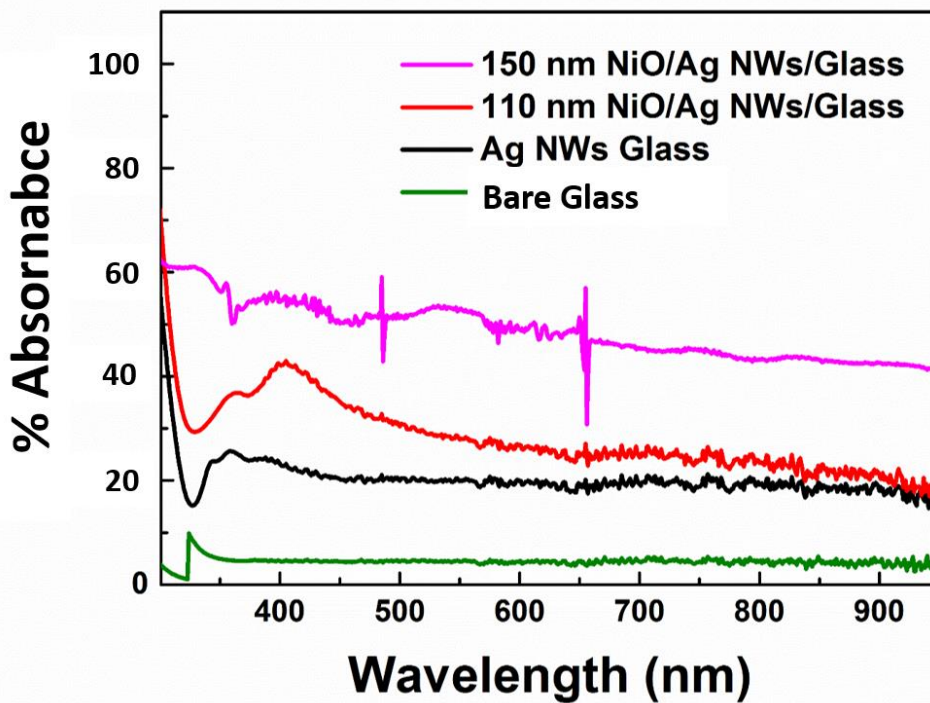
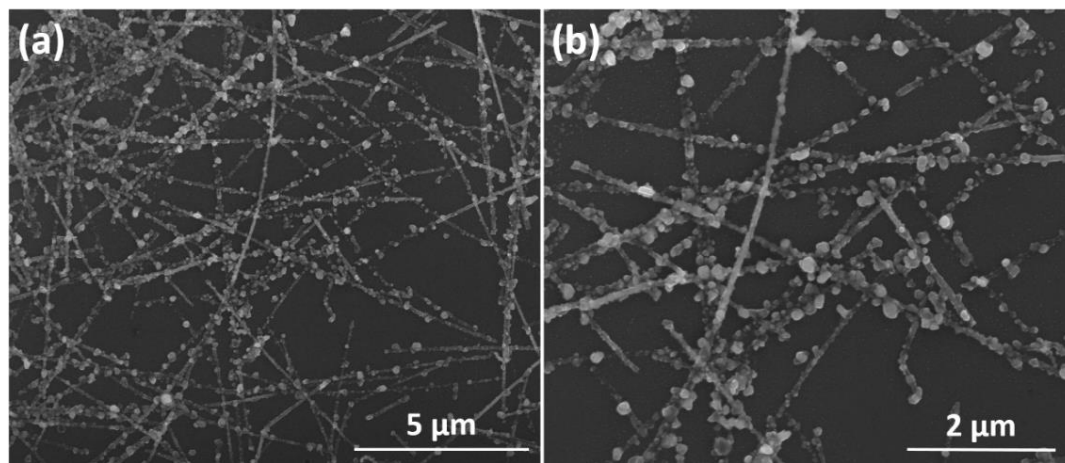


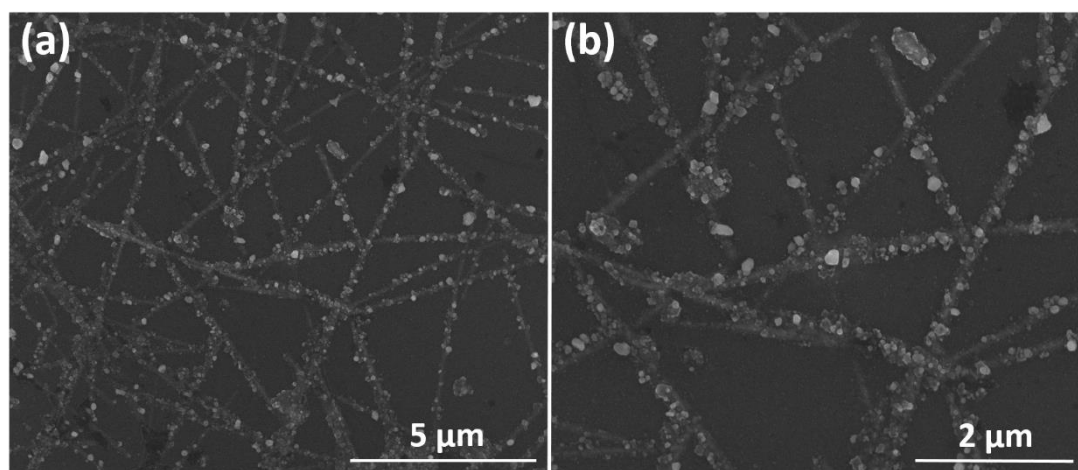
Figure 6.17 Percent absorbance of NiO / Ag NW nano composites.

Figure 6.18 shows SEM images of Ag NW networks deposited with 60 nm NiO thin films, which were kept under ambient conditions for 18 months. Upon the comparison of these SEM images with those taken after 4 months of storage (Figure 6.13) it becomes clear that the oxidation of Ag NWs increases gradually.



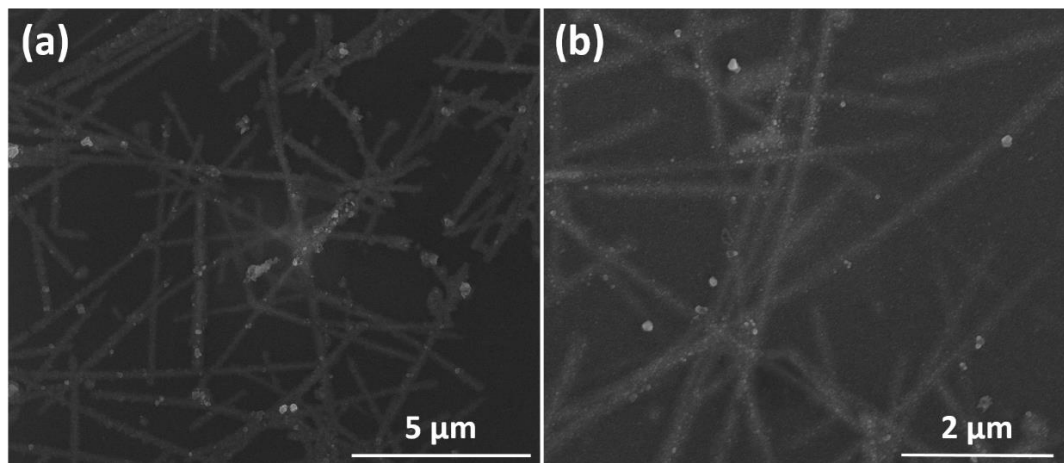
**Figure 6.18** SEM images of (a) and (b) 5X (60 m) NiO deposited Ag NW networks after 18 months storage under ambient conditions.

Figure 6.19 shows SEM images of Ag NW networks deposited with 110 nm thick NiO thin films, which were kept under ambient conditions for 18 months. As those SEM images compared with the one taken after 4 months it can be said that, oxidation of silver nanowires seem to increased gradually.



**Figure 6.19** SEM images of (a) (b) 10 times and NiO deposited Ag NW networks after 18 months under ambient conditions.

Figure 6.20 shows SEM images of Ag NW networks deposited with 110 nm thick NiO thin films, which were kept under ambient conditions for 18 months. Upon comparing these SEM images to those taken after 4 months of storage it becomes clear that the nanowires maintain their integrity. Only a few nanoparticles are observed to form on the surfaces of Ag NWs.



**Figure 6.20** SEM images of (a) and (b) 15 times NiO deposited Ag NW networks after 18 months under ambient conditions.

## CHAPTER 7

### CONCLUSIONS AND FUTURE RECOMMENDATIONS

#### 7.1. Conclusions

This thesis consists of a study on the synthesis of Ag NWs using modified polyol process and utilization of these Ag NWs for the fabrication of TCCs with the investigation of effective parameters. Such as, moreover, fabricated Ag NW networks were used as anodes in PLEDs. This was followed by the investigation of the stability of as-synthesized Ag NWs and Ag NW networks. Finally, NiO thin films were deposited on Ag NWs networks for the fabrication of NiO / Ag NW nano composites to increase the ambient stability of transparent conductors.

In the first part, the mechanism of the polyol process mechanism was investigated 400 mg in 2 hours and it was modified to synthesize large amount Ag NW in one pot.

In the second part, Ag NW based transparent and conducting contacts were fabricated using simple and cost effective procedures. Using spray coating, Ag NWs were deposited onto various substrates without a size limit. Ag NW density was controlled by the number of spray coating cycles and an increase in the Ag NW density resulted in a decrease in transmittance and sheet resistance of the networks. Since there is a thin PVP layer on the lateral surfaces of Ag NWs, a simple annealing process was needed to decrease the contact resistance between Ag NWs. As a result, the sheet resistance of Ag NW networks were found to decrease. Our results showed that, Ag NW networks can be annealed at 200°C up to three hours to improve nanowire-nanowire junctions and thus to decrease the sheet resistance of networks. Further annealing resulted in an increase in the sheet resistance of Ag NW networks.

Moreover, it has been found that temperatures over 200°C are not safe for Ag NW networks. Our best combination of figure of merit sheet resistance and optical transmittance was 11 ohm/sq and 87.6%, respectively. In order to utilize Ag NW networks as TCC, their

high roughness values should be decreased. As a simple solution, deposition of a conducting polymer layer was found to decrease the roughness of the networks.

In the third part, ambient and solvent stability of Ag NWs were investigated. Results showed that although Ag NWs are quite stable in solvents when kept in refrigerated, they form silver sulfide ( $\text{Ag}_2\text{S}$ ) and silver oxide ( $\text{Ag}_2\text{O}$ ) nanoparticles on lateral surfaces of silver nanowires under ambient conditions.

In the final part, sol-gel processed NiO thin films were deposited onto Ag NW networks in order to increase the ambient stability of transparent conductors. 150 nm thick NiO thin films could provide a suitable protective layer for Ag NWs networks.

## **7.2. Future Recommendations**

In this thesis, it is shown that Ag NWs can be synthesized in large quantities. A self-seeding polyol process was used for this purpose. Seeded version of this approach can be investigated. In addition, effect of different seed materials can be investigated as well. Stability results showed that, Ag NWs need a transparent and conductive protective layer. In addition, only some part of the nanowire paths are used when Ag NW networks were used as a contact material. Better coating methods or removal of some nanowires after contact fabrication can be investigated.

## REFERENCES

- [1] Cao, G., Liu, D., 2008, *Adv. Colloid Interface Sci.*, 136(1-2), 45–64.
- [2] Jorte, K. E., Skrabalak S.E., Xia Y., 2008, *Journal of Materials Chemistry*, 18, p.v437-441.
- [3] (a) Martin, B. R., Dermody, D. J., Reiss, B. D., Fang, M., Lyon, L. A., Natan, M. J., Mallouk, T. E., 1999, *Adv. Mater.*, 11, 1021. (b) Zhang, Z., Gekhtman, D., Dresselhaus, M. S., Ying, J. Y., 1999, *Chem. Mater.*, 11, 1659.
- [4] (a) Martin, C. R., Mitchell, D. T., 1999, *Electroanal. Chem.*, 21, 1. (b) Cepak, V. M.; Martin, C. R., 1999, *Chem. Mater.*, 11, 1363.
- [5] Edmondson, M. J., Zhou, W.; Sieber, S. A., Jones, I. P.; Gameson, I., Anderson, P. A., Edwards, P. P., 2001, *Adv. Mater.*, 13, 1608.
- [6] (a) Han, Y. J., Kim, J. M., Stucky, G. D., 2000, *Chem. Mater.* 12, 2068. (b) Huang, M. H.; Choudrey, A.; Yang, P., 2000, *Chem. Commun.*, 1063.
- [7] (a) Ajayan, P. M., Iijima, S., 1993, *Nature* 361, 333. (b) Ugarte, D., Chatelain, A., De Heer, W. A., 1996, *Science*, 274, 1897.
- [8] (a) Song, H. H., Jones, K. M., Baski, A. A., 1999, *J. Vac. Sci. Technol. A* 17, 1696. (b) Zach, M. P., Ng, K. H., Penner, R. M., 2000, *Science*, 290, 2120.
- [9] Bhattacharyya, S., Saha, S. K.; Chakravorty, D., 2000, *Appl. Phys. Lett.*, 76, 3896.
- [10] (a) Braun, E., Eichen, Y., Sivan, U., Ben-Yoseph, 1998, *G. Nature*, 391, 775. (b) Eichen, Y., Braun, E., Sivan, U., Ben-Yoseph, G., 1998, *Acta Polym.*, 49, 663.
- [11] (a) Zhang, D., Qi, L., Ma, J., Cheng, H., 2001, *Chem. Mater.*, 13, 2753. (b) Cornelissen, J. J. L. M., van Heerbeek, R., Kamer, P. C. J., Reek, J. N. H.; Sommerdijk, N. A. J. M., Nolte, R. J. M., 2002, *Adv. Mater.*, 14, 489.

- [12] (a) Jana, N. R., Gearheart, L., Murphy, C. J., 2001, *Chem. Commun.*, 617. (b) El-Sayed, M. A., 2001, *Acc. Chem. Res.*, 34, 257. (c) Murphy, C. J., Jana, N. R., 2002, *Adv. Mater.*, 14, 80.
- [13] Huang, L., Wang, H., Wang, Z., Mitra, A., Bozhilov, K. N., Yan, Y., 2002, *Adv. Mater.*, 14, 61.
- [14] Hong, B. H., Bae, S. C., Lee, C.-W., Jeong, S., Kim, K. S., 2001, *Science*, 294, 348.
- [15] Fievet, F., Lagier, J. P., Figlarz, 1989, *M. MRS Bull.* 14, 29.
- [16] Zhang, J. T., Li, X. L., Sun, X., Li, Y. D., 2005, *J. Phys. Chem. B* 109, 12544
- [17] Wiley, B., Sun, Y., Mayers, B., Xia, Y., 2005, *Chem.—Eur. J.* 11, 454
- [18] Chimentao, R. J., Kirm, I; Medina, F., Rodriguez, X.; Cesteros, Y., Salagre, P., Sueiras, 2004, *J. E. Chem. Commun.* 846.
- [19] Rycenga, M., Kim, M. H., Camargo, P. H. C., Cobley, C., Li, Z. Y., Xia, Y., 2009, *N. J. Phys. Chem. A*, 113, 3932.
- [20] Zhang, J. T., Li, X. L., Sun, X., Li, Y. D., 2005, *J. Phys. Chem. B*, 109, 12544.
- [21] Hu, X., Chan, C. T., 2004, *Appl. Phys. Lett.* 85, 1520
- [22] S. Z. Chu, S. Inoue, K. Wada, and K. Kurashima, *Electrochem. Acta.*, 51 820-26 (2005).
- [23] J. Xu, X. Zhang, F. Chen, T. Li, Y. Li, X. Tao, Y. Wang, and X. Wu, *Appl. Surf. Sci.*, 239 320-26 (2005).
- [24] C. Wu, F. Ko, and H. Hwang, *Microelectro. Eng.*, 83 1567-70 (2006).
- [25] X. Mei, M. Blumin, D. Kim, Z. Wu, and H. Ruda, *J. Cryst. Growth*, 251 253-57 (2003).
- [26] L. Malkinski, A. Chalastaras, A. Vovk, J. Jung, E. Kim, J. Jun, and C. Ventrice, Jr., *J. Magnetism and Magnetic Mater.*, 286 108-12 (2005).
- [27] A. Saedi and M. Ghorbani, *Mater. Chem. and Phys.*, 91 417-23 (2005).

- [28] O. Jessensky, F. Muller, and U. Gosele, *Appl. Phys. Lett.*, 72 1173-75 (1998).
- [29] S. Shingubara, Y. Murakami, K. Morimoto, and T. Takahagi, *Surf. Sci.*, 318 532-35 (2003).
- [30] B. Wu and J. Boland, *J. Colloid and Interface Sci.*, 303 611-16 (2006).
- [31] D. Choi, P. Lee, W. Hwang, K. Lee, and H. Park, *Appl. Phys.*, 6S1 e125-9 (2006).
- [32] X. Liu, J. Wang, J. Zhang, and S. Yang, *Mater. Sci. and Eng., A* 430 248-53 (2006).
- [33] Kim, Y.H., Han, Y.H., Lee, H.J., Lee, H.B., *Journal of the Korean Ceramic Society*, 45(4), 191-195 (2008).
- [34] Sun, Y.; Gates, B.; Mayers, B.; Xia, Y. *Nano Lett.* 2002, 2, 165.
- [35] Silvert P-Y, Herrera-Urbina R, Duvauchelle N, Vijayakrishnan V and Elhsissen K T 1996 *J. Mater. Chem.* 6 573-7
- [36] Fievet, F., Lagier, J. P., Figlarz, 1989, *M. MRS Bull.* 14, 29.
- [37] Zhang, J. T., Li, X. L., Sun, X., Li, Y. D., 2005, *J. Phys. Chem. B* 109, 12544.
- [38] Hu, X., Chan, C. T., 2004, *Appl. Phys. Lett.* 85, 1520
- [39] Wiley, B., Sun, Y., Mayers, B., Xia, Y., 2005, *Chem.—Eur. J.* 11, 454.
- [40] (a) Jana, N. R., Gearheart, L., Murphy, C. J., 2001, *Chem. Commun.*, 617. (b) El-Sayed, M. A., 2001, *Acc. Chem. Res.*, 34, 257. (c) Murphy, C. J., Jana, N. R., 2002, *Adv. Mater.*, 14, 80.
- [41] Hu, J. Q.; Chen, Q.; Xie, Z. X.; Han, G. B.; Wang, R. H.; Ren, B.; Zhang, Y.; Yang, Z. L. & Tian, Z. Q. (2004), *Vol. 14, No. 2*, 183-189, ISSN: 1616-301X.
- [42] Sun, Yugang & Mayers, Brian & Herricks, Thurston & Xia, Younan. (2003) *Nano Letters - NANO LETT.* 3. 10.1021/nl034312m.
- [43] (a) Xia, Y.; Xiong, Y.; Lim, B. & Skrabalak, S. E. (2009). *Angewandte Chemie – International Edition*, Vol. 48, No. 1, 60-103, ISSN: 1521-3773. (b) Wiley, B.; Sun, Y. G. & Xia, Y. N. (2007). *Accounts of Chemical Research*, Vol. 40, No. 10, 1067-

1076, ISSN: 0001- 4842. (c) Wiley, B.; Sun, Y. G.; Chen, J. Y.; Cang, H.; Li, Z.Y.; Li, X.D. & Xia, Y.N. (2005). MRS Bulletin, Vol. 30, No. 5, 356-361, ISSN: 0883-7694. (d) Chen, J. Y.; Wiley, B. J. & Xia, Y. N. (2007). Langmuir, Vol. 23, No. 8, 4120-4129, ISSN: 0743-7463. (e) Wiley, B.; Sun, Y. G.; Mayers, B. & Xia, Y. N. (2005). Chemistry-A European Journal, Vol. 11, No. 2, 454-463, ISSN: 0947-6539. (f) Sun, Y. G. & Xia, Y. N. (2002). Advanced Materials, Vol. 14, No. 11, 833-837, ISSN: 0935-9648.

[44] (a) Korte, K. E.; Skrabalak, S. E. & Xia, Y. (2008). Journal of Materials Chemistry, Vol. 18, No. 4, 437-441, ISSN: 0959-9428. (b)Wiley, B.; Sun, Y. G. & Xia, Y. N. (2005). Langmuir, Vol. 21, No. 8, 8077-8080, ISSN: 0743-7463.

[45] Wiley, B.; Herricks, T.; Sun, Y. G. & Xia, Y. N. 2004. Nano Letters, Vol. 4, No. 9, 1733-1739, ISSN: 1530-6984.

[46] Zhang W C, Wu X L, Chen H T, Gao Y J, Zhu J, Huang G S and Chu P K 2008 Acta Mater. 56 2508–13).

[47] Rycenga, M., Kim, M. H., Camargo, P. H. C., Cobley, C., Li, Z. Y., Xia, Y., 2009, N. J. Phys.Chem. A, 113, 3932.

[48] Coskun, S. Synthesis of Silver Nanowires Through Polyol Process, (Thesis, M.S.), Department of Metallurgical and Materials Engineering, Middle East Technical University, 2012.

[49] Ginley D.S., 2010, –Handbook of Transparent Conductors" Springer.

[50] <http://www.bp.com/statisticalreview> (2007).

[51] [https://upload.wikimedia.org/wikipedia/commons/9/9d/Bp\\_world\\_energy\\_consumption\\_2016.gif](https://upload.wikimedia.org/wikipedia/commons/9/9d/Bp_world_energy_consumption_2016.gif)

[52] [http://www.pion.cz/\\_sites/pion/upload/images/a14cf10a5583d19f7cfdebd63cf64382\\_electromagnetic-spectrum.png](http://www.pion.cz/_sites/pion/upload/images/a14cf10a5583d19f7cfdebd63cf64382_electromagnetic-spectrum.png).

[53] <http://rsl.eng.usf.edu/Documents/Tutorials/TutorialsWorkFunction.pdf>  
20.01.2012.

[54] Fan J. C. C., Bachner F. J., Foley G. H., 1976, Applied Physics Letters, 31, 773.

- [55] (a) Jana, N. R., Gearheart, L., Murphy, C. J., 2001, *Chem. Commun.*, 617. (b) El-Sayed, M. A., 2001, *Acc. Chem. Res.*, 34, 257. (c) Murphy, C. J., Jana, N. R., 2002, *Adv. Mater.*, 14, 80.
- [56] Li J., Hu L., Wang L., Zhou Y., Gruner G., Marks T.J., 2006, *Nano Lett.*, 6, 11.
- [57] Muthukumar, Anusha & Rey, Germain & Giusti, G & Consonni, Vincent & Appert, Estelle & Roussel, Hervé & Dakshanamoorthy, Arivuoli & Bellet, Daniel. (2013). *AIP Conference Proceedings*. 1512. 710-711. 10.1063/1.4791235.
- [58] Kim Y. H., Sachse C., Machala M. L., Müller-Meskamp L., Leo K., 2011, *Adv. Funct. Mater.*, 21, 1076–1081.
- [59] K.S. Novoselov, A.K. Geim, S.V. Morozov, D. Jiang, Y. Zhang, S.V. Dubonos, I.V. Grigorieva, A.A. Firsov, *Science* 306 (2004) 666—669.
- [60] X.S. Li, W.W. Cai, J.H. An, S. Kim, J. Nah, D.X. Yang, R. Piner, A. Velamakanni, I. Jung, E. Tutuc, S.K. Banerjee, L. Colombo, R.S. Ruoff, *Science* 324 (2009) 1312—1314.
- [61] Avrekh M., Thibadeau B. M., Monteiro O. R., Brown I. G., 1999, *Rev. Sci. Instrum.* 70, 4328.
- [62] Kang M.G. , Park H.J. , Ahn S.H. , Xu T. , Guo L.J., 2010, *IEEE J. Sel. Top. Quantum Electron*, 16, 1807.
- [63] Unalan, Husnu & Fanchini, Giovanni & Kanwal, Alokik & Pasquier, Aurelien & Chhowalla, Manish. (2006). *Nano letters*. 6. 677-82. 10.1021/nl052406l.
- [64] Li, D.; Xia, Y. N. *Adv. Mater.* 2004, 16 (14), 1151–1170.
- [65] Greiner, A.; Wendorff, J. H. *Angew. Chem., Int. Ed.* 2007, 46 (30), 5670–5703.
- [66] Bognitzki, M.; Becker, M.; Graeser, M.; Massa, W.; Wendorff, J. H.; Schaper, A.; Weber, D.; Beyer, A.; Golzhauser, A.; Greiner, A. *Adv. Mater.* 2006, 18 (18), 2384.
- [67] Li, D.; Xia, Y. N. *Nano Lett.* 2003, 3 (4), 555–560.
- [68] Wu, H.; Zhang, R.; Liu, X. X.; Lin, D. D.; Pan, W. *Chem. Mater.* 2007, 19 (14), 3506–3511.

- [69] Wu, Hui & Hu, Liangbing & W Rowell, Michael & Kong, Desheng & J Cha, Judy & McDonough, James & Zhu, Jia & Yang, Yuan & Mcgehee, Michael & Cui, Yi. (2010). *Nano letters*. 10. 4242-8. 10.1021/nl102725k.
- [70] Kim, Won-Kyung & Lee, Seunghun & Hee Lee, Duck & Hee Park, In & Seong Bae, Jong & Woo Lee, Tae & Kim, Ji-Young & Park, Ji Hun & Cho, Yong & Cho, Chaeryong & Jeong, Se-Young. (2015). *Scientific reports*. 5. 10715. 10.1038/srep10715.
- [71] Essam J.W., 1980, *Rep. Prog. Phys.*, 43.
- [72] White S.I., Mutiso R.M., Vora P.M., Jahnke D., Hsu S., Kikkawa J.M., Li J., J.E., Winey K.I., 2010, *Adv. Funct. Mater.*, 20, 2709–2716
- [73] Madaria A.R., Kumar A., Ishikawa F.N., Zhou C., 2010, *Nano Res.*, 3, 564–573
- [74] Pike G. E., Seager C., 1974, *I. Phys. Rev.B*, 10, 1421–1434.
- [75] Hu L., Kim H.S., Lee J.Y., Peumans P., Cui Y., 2010, *ACS Nano*, 4, 2955.
- [76] Coskun, Sahin & Selen Ates, Elif & Unalan, Husnu. (2013). *Nanotechnology*. 24. 125202. 10.1088/0957-4484/24/12/125202.
- [77] De S and Coleman J N, 2011, *MRS Bull.* 36 774–81
- [78] <https://www.energy.gov/articles/history-light-bulb>
- [79] Yu, Zhibin & Zhang, Qingwu & Li, Lu & Chen, Qi & Niu, Xiaofan & Liu, Jun & Pei, Qibing. (2011). *Advanced materials (Deerfield Beach, Fla.)*. 23. 664-8.
- [80] J. Jiu, J. Wang, T. Sugahara, S. Nagao, M. Nogi, H. Koga, K. Suganuma, M. Hara, E. Nakazawa and H. Uchida, *RSC Advances*, vol. 5, pp. 27657-27664, 2015.
- [81] P. Blake, P. D. Brimicombe, R. R. Nair, T. J. Booth, D. Jiang, F. Schedin, L. A. Ponomarenko, S. V. Morozov, H. F. Gleeson, E. W. Hill, A. K. Geim and K. S. Novoselov, *Nano Letters*, vol. 8, no. 6, pp. 1704-1708, 2008.
- [82] M. Lagrange, T. Sanniccolo, Munoz-Rojas, B. Guillo Lohan, A. Khan, M. Anikin, C. Jiménez, F. Bruckert, Y. Bréchet and D. Bellet, *Nanotechnology*, vol. 28, p. 055709, 2017.
- [83] H. H. Khaligh and I. A. Goldthorpe, *Nanoscale*, vol. 8, no. 1, p. 235, 2013.

- [84] C. Mayousse, C. Celle, A. Fraczkiewicz and J.-P. Simonato, *Nanoscale*, vol. 7, pp. 2107-2115, 2015.
- [85] J. Jiu, J. Wang, T. Sugahara, S. Nagao, M. Nogi, H. Koga, K. Suganuma, M. Hara, E. Nakazawa and H. Uchida, *RSC Advances*, vol. 5, pp. 27657-27664, 2015.
- [86] J. Franey, G. Kammlott and T. Graedel, *Corrosion Science*, vol. 25, no. 2, pp. 133-143, 1985.
- [87] Yao-Jiun Tsai, Chi-Ying Chang, Yi-Chun Lai, Pei-Chen Yu, and Hyeyoung Ahn *ACS Applied Materials & Interfaces* 2014 6 (1), 630-635
- [88] J. L. Elechiguerra, L. Larios-Lopez, C. Liu, D. Garcia-Gutierrez, A. Camacho-Bragado and M. J. Yacaman, *Chemistry of Materials*, vol. 17, no. 24, pp. 6042-6052, 2005.
- [89] Chul Choo, Dong & Whan Kim, Tae. (2017). *Scientific Reports*. 7. 10.1038/s41598-017-01843-9.
- [90] A. M. Prokhorov; et al., eds. (1972). *Great Soviet Encyclopedia* . 8. Moscow: Soviet Encyclopedia.
- [91] Hyun Jun Lee, Ju Hyun Hwang, Kyung Bok Choi, Sun-Gyu Jung, Kyu Nyun Kim, Yong Sub Shim, Cheol Hwee Park, Young Wook Park, and Byeong-Kwon Ju *ACS Applied Materials & Interfaces* 2013 5 (21), 10397-10403
- [92] A. M. Soleimanpour and A. H. Jayatissa, *Mater. Sci. Eng. C*, vol. 32, no. 8, pp. 2230–2234, 2012.
- [93] X. Wang, Y. Zhu, J. Yang, X. Lu and L. Wang, *Thermochim. Acta.*, vol. 437, pp. 106–109, 2005.
- [94] J. Lin, S. Chen and F. Kai, “Electrochromic Properties of Nano-Composite Nickel Oxide Film,” *Appl. Surf. Sci.*, vol. 254, pp. 3357–3363, 2008.
- [95] Y. M. Lu, W. S. Hwang, J. S. Yang and H. C. Chuang, *Thin Solid Films*, vol. 420–421, pp. 54–61, 2002.
- [96] M. D. Irwin, D. B. Buchholz, A. W. Hains, R. P. H. Chang and T. J. Marks, *Chem. Mater.*, vol. 23, no. 8, pp. 2218– 2226, 2011

[97] M. Z. Sialvi, R. J. Mortimer, G. D. Wilcox, A. M. Teridi, T. S. Varley, K. G. U. Wijayantha and C. A. Kirk, *ACS Appl. Mater. Interfaces*, vol. 5, no. 12, pp. 5675–5682, 2013.

[98] W. Guo, K. N. Hui, and K. S. Hui, *Mater. Lett.*, vol. 92, pp. 291–295, 2013.

[99] Sarac, B.E. (Thesis, M.S.), Department of Metallurgical and Materials Engineering, Middle East Technical University, 2017.

## APPENDIX A: PERMISSION LICENSES



**Copyright Clearance Center**

**Note:** Copyright.com supplies permissions but not the copyrighted content itself.

1  
PAYMENT

2  
REVIEW

**3  
CONFIRMATION**

### Step 3: Order Confirmation

**Thank you for your order!** A confirmation for your order will be sent to your account email address. If you have questions about your order, you can call us 24 hrs/day, M-F at +1.855.239.3415 Toll Free, or write to us at [info@copyright.com](mailto:info@copyright.com). This is not an invoice.

**Confirmation Number: 11694213**  
**Order Date: 01/20/2018**

**Payment Information**

HUSNU UNALAN  
unalan@metu.edu.tr  
+90 (312)2105939  
Payment Method: n/a

If you paid by credit card, your order will be finalized and your card will be charged within 24 hours. If you choose to be invoiced, you can change or cancel your order until the invoice is generated.

---

#### Order Details

**Nanotechnology**

**Order detail ID:** 70942280  
**Order License Id:** 4273000138852  
**ISSN:** 0957-4484  
**Publication Type:** Journal  
**Volume:**  
**Issue:**  
**Start page:**  
**Publisher:** IOP Publishing

**Permission Status:** ✔ **Granted**

**Permission type:** Republish or display content  
**Type of use:** Thesis/Dissertation

<b>Requestor type</b>	Author of requested content
<b>Format</b>	Print, Electronic
<b>Portion</b>	chart/graph/table/figure
<b>Number of charts/graphs/tables/figures</b>	10
<b>The requesting person/organization</b>	Sahin Coskun/Middle East Technical University
<b>Title or numeric reference of the portion(s)</b>	Figure 1, Figure 2, Figure 3, Figure 4, Figure 5, Figure 6, Figure S1, Figure S2, Figure S3, Figure S4.
<b>Title of the article or chapter the portion is from</b>	N/A
<b>Editor of portion(s)</b>	N/A
<b>Author of portion(s)</b>	Sahin Coskun
<b>Volume of serial or monograph</b>	N/A
<b>Page range of portion</b>	150 pages

<b>Publication date of portion</b>	January 2018
<b>Rights for</b>	Main product
<b>Duration of use</b>	Life of current edition
<b>Creation of copies for the disabled</b>	no
<b>With minor editing privileges</b>	no
<b>For distribution to</b>	Worldwide
<b>In the following language(s)</b>	Original language of publication
<b>With incidental promotional use</b>	no
<b>Lifetime unit quantity of new product</b>	Up to 499
<b>Title</b>	Applications of Silver Nanowire Networks in Opto-Electronic Devices
<b>Instructor name</b>	Husnu Emrah Unalan
<b>Instructor name</b>	Husnu Emrah Unalan
<b>Institution name</b>	Middle East Technical University
<b>Expected presentation date</b>	Jan 2018

**Note:** This item will be invoiced or charged separately through CCC's **RightsLink** service. [More info](#)

**\$ 0.00**

<b>Total order items: 1</b>	<b>This is not an invoice.</b>	<b>Order Total: 0.00 USD</b>
-----------------------------	--------------------------------	------------------------------

**Confirmation Number: 11694213**

**Special Rightsholder Terms & Conditions**

The following terms & conditions apply to the specific publication under which they are listed

**Nanotechnology**  
**Permission type:** Republish or display content  
**Type of use:** Thesis/Dissertation

**TERMS AND CONDITIONS**

**The following terms are individual to this publisher:**

These special terms and conditions are in addition to the standard terms and conditions for CCC's Republication Service and, together with those standard terms and conditions, govern the use of the Works.

As the "User" you will make all reasonable efforts to contact the author(s) of the article which the Work is to be reused from, to seek consent for your intended use. Contacting one author who is acting expressly as authorised agent for their co-author(s) is acceptable.

User will reproduce the following wording prominently alongside the Work:

- the source of the Work, including author, article title, title of journal, volume number, issue number (if relevant), page range (or first page if this is the only information available) and date of first publication. This information can be contained in a footnote or reference note; and
- a link back to the article (via DOI); and
- if practicable, and IN ALL CASES for new works published under any of the Creative Commons licences, the words "© IOP Publishing. Reproduced with permission. All rights reserved"

Without the express permission of the author(s) and the Rightsholder of the article from which the Work is to be reused, User shall not use it in any way which, in the opinion of the Rightsholder, could: (i) distort or alter the author(s)' original intention(s) and meaning; (ii) be prejudicial to the honour or reputation of the author(s); and/or (iii) imply endorsement by the author(s) and/or the Rightsholder.

This licence does not apply to any article which is credited to another source and which does not have the copyright line "© IOP Publishing Ltd". User must check the copyright line of the article from which the Work is to be reused to check that IOP Publishing Ltd has all the necessary rights to be able to grant permission. User is solely responsible for identifying and obtaining separate licences and permissions from the copyright owner for reuse of any such third party material/figures which the Rightsholder is not the copyright owner of. The Rightsholder shall not reimburse any fees which User pays for a republication license for such third party content.

This licence does not apply to any material/figure which is credited to another source in the Rightsholder's publication or has been obtained from a third party. User must check the Version of Record of the article from which the Work is to be reused, to check whether any of the material in the Work is third party material. Third party citations and/or copyright notices and/or permissions statements may not be included in any other version of the article from which the Work is to be reused and so cannot be relied upon by the User. User is solely responsible for identifying and obtaining separate licences and permissions from the copyright owner for reuse of any such third party material/figures where the Rightsholder is not the copyright owner. The Rightsholder shall not reimburse any fees which User pays for a republication license for such third party content.

User and CCC acknowledge that the Rightsholder may, from time to time, make changes or additions to these special terms and conditions without express notification, provided that these shall not apply to permissions already secured and paid for by User prior to such change or addition.

User acknowledges that the Rightsholder (which includes companies within its group and third parties for whom it publishes its titles) may make use of personal data collected through the service in the course of their business.

If User is the author of the Work, User may automatically have the right to reuse it under the rights granted back when User transferred the copyright in the article to the Rightsholder. User should check the copyright form and the relevant author rights policy to check whether permission is required. If User is the author of the Work and does require permission for proposed reuse of the Work, User should select 'Author of requested content' as the Requestor Type. The Rightsholder shall not reimburse any fees which User pays for a republication license.

If User is the author of the article which User wishes to reuse in User's thesis or dissertation, the republication licence covers the right to include the Accepted Manuscript version (not the Version of Record) of the article. User must include citation details and, for online use, a link to the Version of Record of the article on the Rightsholder's website. User may need to obtain separate permission for any third party content included within the article. User must check this with the copyright owner of such third party content. User may not include the article in a thesis or dissertation which is published by ProQuest. Any other commercial use of User's thesis or dissertation containing the article would also need to be expressly notified in writing to the Rightsholder at the time of request and would require separate written permission from the Rightsholder.

User does not need to request permission for Work which has been published under a CC BY licence. User must check the Version of Record of the CC BY article from which the Work is to be reused, to check whether any of the material in the Work is third party material and so not published under the CC BY licence. User is solely responsible for identifying and obtaining separate licences and permissions from the copyright owner for reuse of any such third party material/figures. The Rightsholder shall not reimburse any fees which User pays for such licences and permissions.

As well as CCC, the Rightsholder shall have the right to bring any legal action that it deems necessary to enforce its rights should it consider that the Work infringes those rights in any way.

For STM Signatories ONLY (as agreed as part of the STM Guidelines)

Any licence granted for a particular edition of a Work will apply also to subsequent editions of it and for editions in other languages, provided such editions are for the Work as a whole in situ and do not involve the separate exploitation of the

permitted illustrations or excerpts.

#### Other Terms and Conditions:

#### STANDARD TERMS AND CONDITIONS

1. Description of Service; Defined Terms. This Republication License enables the User to obtain licenses for republication of one or more copyrighted works as described in detail on the relevant Order Confirmation (the "Work(s)"). Copyright Clearance Center, Inc. ("CCC") grants licenses through the Service on behalf of the rightsholder identified on the Order Confirmation (the "Rightsholder"). "Republication", as used herein, generally means the inclusion of a Work, in whole or in part, in a new work or works, also as described on the Order Confirmation. "User", as used herein, means the person or entity making such republication.

2. The terms set forth in the relevant Order Confirmation, and any terms set by the Rightsholder with respect to a particular Work, govern the terms of use of Works in connection with the Service. By using the Service, the person transacting for a republication license on behalf of the User represents and warrants that he/she/it (a) has been duly authorized by the User to accept, and hereby does accept, all such terms and conditions on behalf of User, and (b) shall inform User of all such terms and conditions. In the event such person is a "freelancer" or other third party independent of User and CCC, such party shall be deemed jointly a "User" for purposes of these terms and conditions. In any event, User shall be deemed to have accepted and agreed to all such terms and conditions if User republishes the Work in any fashion.

#### 3. Scope of License; Limitations and Obligations.

3.1 All Works and all rights therein, including copyright rights, remain the sole and exclusive property of the Rightsholder. The license created by the exchange of an Order Confirmation (and/or any invoice) and payment by User of the full amount set forth on that document includes only those rights expressly set forth in the Order Confirmation and in these terms and conditions, and conveys no other rights in the Work(s) to User. All rights not expressly granted are hereby reserved.

3.2 General Payment Terms: You may pay by credit card or through an account with us payable at the end of the month. If you and we agree that you may establish a standing account with CCC, then the following terms apply: Remit Payment to: Copyright Clearance Center, 29118 Network Place, Chicago, IL 60673-1291. Payments Due: Invoices are payable upon their delivery to you (or upon our notice to you that they are available to you for downloading). After 30 days, outstanding amounts will be subject to a service charge of 1-1/2% per month or, if less, the maximum rate allowed by applicable law. Unless otherwise specifically set forth in the Order Confirmation or in a separate written agreement signed by CCC, invoices are due and payable on "net 30" terms. While User may exercise the rights licensed immediately upon issuance of the Order Confirmation, the license is automatically revoked and is null and void, as if it had never been issued, if complete payment for the license is not received on a timely basis either from User directly or through a payment agent, such as a credit card company.

3.3 Unless otherwise provided in the Order Confirmation, any grant of rights to User (i) is "one-time" (including the editions and product family specified in the license), (ii) is non-exclusive and non-transferable and (iii) is subject to any and all limitations and restrictions (such as, but not limited to, limitations on duration of use or circulation) included in the Order Confirmation or invoice and/or in these terms and conditions. Upon completion of the licensed use, User shall either secure a new permission for further use of the Work(s) or immediately cease any new use of the Work(s) and shall render inaccessible (such as by deleting or by removing or severing links or other locators) any further copies of the Work (except for copies printed on paper in accordance with this license and still in User's stock at the end of such period).

3.4 In the event that the material for which a republication license is sought includes third party materials (such as photographs, illustrations, graphs, inserts and similar materials) which are identified in such material as having been used by permission, User is responsible for identifying, and seeking separate licenses (under this Service or otherwise) for, any of such third party materials; without a separate license, such third party materials may not be used.

3.5 Use of proper copyright notice for a Work is required as a condition of any license granted under the Service. Unless otherwise provided in the Order Confirmation, a proper copyright notice will read substantially as follows: "Republished with permission of [Rightsholder's name], from [Work's title, author, volume, edition number and year of copyright]; permission conveyed through Copyright Clearance Center, Inc." Such notice must be provided in a reasonably legible font size and must be placed either immediately adjacent to the Work as used (for example, as part of a by-line or footnote but not as a separate electronic link) or in the place where substantially all other credits or notices for the new work containing the republished Work are located. Failure to include the required notice results in loss to the Rightsholder and CCC, and the User shall be liable to pay liquidated damages for each such failure equal to twice the use fee specified in the Order Confirmation, in addition to the use fee itself and any other fees and charges specified.

3.6 User may only make alterations to the Work if and as expressly set forth in the Order Confirmation. No Work may be used in any way that is defamatory, violates the rights of third parties (including such third parties' rights of copyright, privacy, publicity, or other tangible or intangible property), or is otherwise illegal, sexually explicit or obscene. In addition, User may not conjoin a Work with any other material that may result in damage to the reputation of the Rightsholder. User agrees to inform CCC if it becomes aware of any infringement of any rights in a Work and to cooperate with any reasonable request of CCC or the Rightsholder in connection therewith.

4. Indemnity. User hereby indemnifies and agrees to defend the Rightsholder and CCC, and their respective employees and directors, against all claims, liability, damages, costs and expenses, including legal fees and expenses, arising out of any use of a Work beyond the scope of the rights granted herein, or any use of a Work which has been altered in any unauthorized way by User, including claims of defamation or infringement of rights of copyright, publicity, privacy or other tangible or intangible property.

5. Limitation of Liability. UNDER NO CIRCUMSTANCES WILL CCC OR THE RIGHTSHOLDER BE LIABLE FOR ANY DIRECT, INDIRECT, CONSEQUENTIAL OR INCIDENTAL DAMAGES (INCLUDING WITHOUT LIMITATION DAMAGES FOR LOSS OF BUSINESS PROFITS OR INFORMATION, OR FOR BUSINESS INTERRUPTION) ARISING OUT OF THE USE OR INABILITY TO USE A WORK, EVEN IF ONE OF THEM HAS BEEN ADVISED OF THE POSSIBILITY OF SUCH DAMAGES. In any event, the total liability of the Rightsholder and CCC (including their respective employees and directors) shall not exceed the total amount actually paid by User for this license. User assumes full liability for the actions and omissions of its principals, employees, agents, affiliates, successors and assigns.

6. Limited Warranties. THE WORK(S) AND RIGHT(S) ARE PROVIDED "AS IS". CCC HAS THE RIGHT TO GRANT TO USER THE RIGHTS GRANTED IN THE ORDER CONFIRMATION DOCUMENT. CCC AND THE RIGHTSHOLDER DISCLAIM ALL OTHER WARRANTIES RELATING TO THE WORK(S) AND RIGHT(S), EITHER EXPRESS OR IMPLIED, INCLUDING WITHOUT LIMITATION IMPLIED WARRANTIES OF MERCHANTABILITY OR FITNESS FOR A PARTICULAR PURPOSE. ADDITIONAL RIGHTS MAY BE REQUIRED TO USE ILLUSTRATIONS, GRAPHS, PHOTOGRAPHS, ABSTRACTS, INSERTS OR OTHER

PORTIONS OF THE WORK (AS OPPOSED TO THE ENTIRE WORK) IN A MANNER CONTEMPLATED BY USER; USER UNDERSTANDS AND AGREES THAT NEITHER CCC NOR THE RIGHTSHOLDER MAY HAVE SUCH ADDITIONAL RIGHTS TO GRANT.

7. Effect of Breach. Any failure by User to pay any amount when due, or any use by User of a Work beyond the scope of the license set forth in the Order Confirmation and/or these terms and conditions, shall be a material breach of the license created by the Order Confirmation and these terms and conditions. Any breach not cured within 30 days of written notice thereof shall result in immediate termination of such license without further notice. Any unauthorized (but licensable) use of a Work that is terminated immediately upon notice thereof may be liquidated by payment of the Rightsholder's ordinary license price therefor; any unauthorized (and unlicensable) use that is not terminated immediately for any reason (including, for example, because materials containing the Work cannot reasonably be recalled) will be subject to all remedies available at law or in equity, but in no event to a payment of less than three times the Rightsholder's ordinary license price for the most closely analogous licensable use plus Rightsholder's and/or CCC's costs and expenses incurred in collecting such payment.

**8. Miscellaneous.**

8.1 User acknowledges that CCC may, from time to time, make changes or additions to the Service or to these terms and conditions, and CCC reserves the right to send notice to the User by electronic mail or otherwise for the purposes of notifying User of such changes or additions; provided that any such changes or additions shall not apply to permissions already secured and paid for.

8.2 Use of User-related information collected through the Service is governed by CCC's privacy policy, available online here: <http://www.copyright.com/content/cc3/en/tools/footer/privacypolicy.html>.

8.3 The licensing transaction described in the Order Confirmation is personal to User. Therefore, User may not assign or transfer to any other person (whether a natural person or an organization of any kind) the license created by the Order Confirmation and these terms and conditions or any rights granted hereunder; provided, however, that User may assign such license in its entirety on written notice to CCC in the event of a transfer of all or substantially all of User's rights in the new material which includes the Work(s) licensed under this Service.

8.4 No amendment or waiver of any terms is binding unless set forth in writing and signed by the parties. The Rightsholder and CCC hereby object to any terms contained in any writing prepared by the User or its principals, employees, agents or affiliates and purporting to govern or otherwise relate to the licensing transaction described in the Order Confirmation, which terms are in any way inconsistent with any terms set forth in the Order Confirmation and/or in these terms and conditions or CCC's standard operating procedures, whether such writing is prepared prior to, simultaneously with or subsequent to the Order Confirmation, and whether such writing appears on a copy of the Order Confirmation or in a separate instrument.

8.5 The licensing transaction described in the Order Confirmation document shall be governed by and construed under the law of the State of New York, USA, without regard to the principles thereof of conflicts of law. Any case, controversy, suit, action, or proceeding arising out of, in connection with, or related to such licensing transaction shall be brought, at CCC's sole discretion, in any federal or state court located in the County of New York, State of New York, USA, or in any federal or state court whose geographical jurisdiction covers the location of the Rightsholder set forth in the Order Confirmation. The parties expressly submit to the personal jurisdiction and venue of each such federal or state court. If you have any comments or questions about the Service or Copyright Clearance Center, please contact us at 978-750-8400 or send an e-mail to [info@copyright.com](mailto:info@copyright.com).

v 1.1

Close

**Confirmation Number: 11694213**

**Citation Information**

**Order Detail ID:** 70942280

**Nanotechnology by IOP Publishing. Reproduced with permission of IOP Publishing in the format Thesis/Dissertation via Copyright Clearance Center.**

Close



## CIRICULIM VITAE

### ŞAHİN COŞKUN

Department of Metallurgical and Materials Engineering

Middle East Technical University (METU)

06800, Ankara, TURKEY.

e-mail: [sacoskun@metu.edu.tr](mailto:sacoskun@metu.edu.tr)

[coskun@nanovatif.com](mailto:coskun@nanovatif.com)

[sahincoskun@gmail.com](mailto:sahincoskun@gmail.com)

phone: +90 (312) 210 78 90

fax: +90 (312) 210 25 18

gsm: +90 535 684 61 68

<https://scholar.google.com.tr/citations?user=FK8E-CcAAAAJ&hl=tr>

### FORMAL EDUCATION

- ***Doctor of Philosophy***, Metallurgical and Materials Engineering, (2018)  
Middle East Technical University, Ankara TURKEY.

Dissertation Title: –Applications of Silver Nanowire Networks in Opto-electronic Devices”

- ***Master of Science***, Metallurgical and Materials Engineering, (2012)  
Middle East Technical University, Ankara, TURKEY.

Dissertation Title: —Synthesis of Silver Nanowires through Polyol Process”

- *Bachelor of Science*, Department of Metallurgy, (2007)  
Gazi University, Ankara, TURKEY.

#### **AWARDS AND ACHIEVEMENTS**

- Winner Award, New Ideas & New Business 2016 (YFYİ), METU  
TEKNOKENT,
- Winner Award, –Nano Picture Contest” Nanoday Event 26.05.2014 UNAM,  
Bilkent University, Ankara, Turkey.
- Young Researcher Award, 16<sup>th</sup> International Metallurgy & Materials Congress  
(IMMC) 2012.
- Thesis of the Year Award, METU Graduate School of Natural and Applied  
Sciences 2012.
- Graduate Course Performance Award, METU Graduate School of Natural and  
Applied Sciences 2012.
- Ranked first in the bachelor degree among 43 students in 2007.

#### **ACADEMIC RESEARCH EXPERIENCE**

- Research Assistant (2009 - 2018)  
Nanomaterials and Devices Laboratory, Metallurgical and Materials Engineering,  
Middle East Technical University.
- Visiting Scholar (August 2015 – August 2016)  
Department of Materials Science and Engineering, Northwestern University,  
USA  
Supervisor: Assoc. Prof. Dr. Jiaying Huang

## **TEACHING EXPERIENCE**

- MetE 307 Metallography
- MetE 329 Materials Science and Engineering
- MetE 225 Engineering Materials
- MetE 433 Materials for Organic Electronics
- MetE 550 Solar Cells

## **JOB EXPERIENCE**

- Co-Founder and Financial Manager of NANO VATİF Materials Technologies, METU Teknokent, Ankara.

## **RESEARCH INTERESTS**

Synthesis of 1-D nanomaterials (nanowires), large area and flexible/organic, transparent and textile integrated electronics, semiconducting devices, solar cells, light emitting diodes, photodetectors and heaters.

## **PATENTS (4)**

- TPE: Enerji Gereksinimi Azaltılan Bir Küçük Ev Aleti (2015/05461)
- PCT: A Household Appliance Provided With a Heating Element Comprising Metallic Nanowire Material (PCT/EP2016/056730)
- TPE: Metal Nanotel Kaplamalı Isıtılabilir Kumaş (2015/10587)
- PCT: Metal Nanowire Decorated Heatable Fabrics (PCT/TR2016/050302)

## **PUBLICATIONS (22)**

- Polyol Synthesis of Silver Nanowires: An Extensive Parametric Study, **S. Coskun**, B. Aksoy, H.E. Unalan, Crystal Growth & Design 11 (2011) 4963.
- Transparent, Highly Flexible, All Nanowire Network Photodetectors, B. Aksoy, **S. Coskun**, S. Kucukyildiz, H.E. Unalan, Nanotechnology 23 (2012) 325202.

- Gold nanowires with aspect ratio and morphological purity: Synthesis, characterization, and evaluation of parameters, E. Dertli, **S. Coskun**, E. N. Esenturk, J. Mater. Res., 28, 2013, 250.
- All Solution Processed, Nanowire Enhanced UV Photodetectors, A. Afal, **S. Coskun**, H.E. Unalan, Appl. Phys. Lett. 102 (2013) 043503.
- Optimization of Silver Nanowire Networks for Polymer Light Emitting Diode Electrodes, **S. Coskun**, E.S. Ates, H.E. Unalan, Nanotechnology 24 (2013) 125202.
- Silicon Nanowire Network Metal-Semiconductor-Metal Photodetectors, E. Mulazimoglu, **S. Coskun**, M. Gunoven, B. Butun, E. Ozbay, R. Turan, H.E. Unalan, Appl. Phys. Lett. 103 (2013) 083114.
- Metal-Enhanced Fluorescence from Silver Nanowires with High Aspect Ratio on Glass Slides for Biosensing Applications, B. Abel, **S. Coskun**, M. Mohammed, R. Williams, H. E. Unalan, K. Aslan, J. Phys. Chem. C 119 (2015) 675.
- Enhanced Second Harmonic Generation from Coupled Asymmetric Plasmonic Metal Nanostructures, B. C. Yildiz, M. E. Tasgin, M. K. Abak, **S. Coskun**, H. E. Unalan, A. Bek, J. Optics 17 (2015) 125005.
- Growth of Branched Gold Nanoparticles on Solid Surfaces and Their Use as Surface-Enhanced Raman Scattering Substrates, N. I. Evcimen, **S. Coskun**, D. Kozanoglu, G. Ertas, H. E. Unalan, E. Nalbant Esenturk, RSC Advances 5 (2015) 101656.
- An Effective Surface Design Based On A Conjugated Polymer And Silver Nanowires For the Detection Of Paraoxon In Tap Water And Milk, J. Turan, M. Kesik, S. Soylemez, S. Goker, **S. Coskun**, H. E. Unalan, L. Toppare, Sens. Act. B. 228 (2016) 278-286.
- Coaxial Silver Nanowire Network Core Molybdenum Oxide Shell Electrodes, R. Yuksel, **S. Coskun**, H. E. Unalan, Electrochim. Acta 193 (2016) 39-44.
- Electrical, Mechanical and Thermal Properties of Aligned Silver Nanowire/Polylactide Nanocomposite Films, D. Doganay, **S. Coskun**, C. Kaynak, H. E. Unalan, Composites Part B 99 (2016) 288-296.
- Silver Nanowire Decorated Heatable Textiles, D. Doganay, **S. Coskun**, S. Polat, H. E. Unalan, Nanotechnology 27 (2016) 435201.

- Flexible, Silver Nanowire Network Nickel Hydroxide Core-Shell Electrodes for Supercapacitors, R. Yuksel, **S. Coskun**, Y. E. Kalay, H. E. Unalan, J. Power Sources 328 (2016) 167-173
- High Performance, Bare Silver Nanowire Network Transparent Heaters, O. Ergun, **S. Coskun**, Y. Yusufoglu, H. E. Unalan, Nanotechnology 27 (2016) 445708.
- M. T. Cole, **S. Coskun**, R. J. Parmee, P. Hiralal, C. Cepek, A. W. Robertson, C. Li, Q. Dai, J. H. Warner, W. I. Milne, H. E. Unalan, Suppressed Hysteretic Field Emission from Polymer Encapsulated Silver Nanowires, IEEE Trans. Nanotechnol. 16 (2017) 11.
- M. Charehsaz, **S. Coskun**, H. E. Unalan, R. Reis, S. Helvacioğlu, A. K. Giri, A. Aydin, Genotoxicity Study of High Aspect Ratio Silver Nanowires, Toxicol Environ Chem. 99 (2017) 837.
- R. Yuksel, **S. Coskun**, G. Gunbas, A. Cirpan, L. Toppare, H. E. Unalan, Silver Nanowire / Conducting Polymer Nanocomposite Electrochromic Supercapacitor Electrodes, J. Electrochem. Soc. 164 (2017) A721.
- E. Bonyi, Z. Kukoyi, O. Daodu, Z. Boone-Kukoyi, **S. Coskun**, H. E. Unalan, K. Aslan, Metal Oxide Surfaces for Enhanced Colorimetric Response in Bioassays, Colloids Surf B Biointerfaces 154 (2017) 331.
- Onur Turel, Serife Ozdemir Hacioglu, **Sahin Coskun**, Levent Toppare, Husnu Emrah Unalan, Sequential Deposition of Electrochromic MoO<sub>3</sub> Thin films with High Coloration Efficiency and Stability, Accepted for Journal of The Electrochemical Society, 2017.
- Eylül Şimşek, **Sahin Coskun**, Tuba Okutucu-Ozyurt, Husnu Emrah Unalan, Heat transfer enhancement by silver nanowire suspensions in microchannel heat sinks, International Journal of Thermal Sciences 123 (2018) 1-13.
- L. Lin, M. Wang, X. Peng, E. Lissek, Z. Mao, L. Scarabelli, E. Adkins, **S. Coskun**, H. Unalan, B. Korgel, L. Liz-Marzán, E. Florin, Y. Zheng, Opto-thermoelectric nanotweezers, Nature Photonics (2018).

## PRESENTATIONS (43)

- Silver Nanowires for Supercapacitor Electrodes, R. Yuksel, **S. Coskun**, H. E.Unalan, MRS Fall' 2017 USA.
- Silver Nanowire Decorated Antibacterial Fabrics, D. Doganay, A. Kanicioglu, **S. Coskun**, G. Akca, H. E. Unalan, MRS Fall' 2017 USA.
- Copper Nanowire Based Transparent Electrodes with Improved Oxidation Stability, S. Polat Genlik, D. Tigan, **S. Coskun**, H. E. Unalan, MRS Fall' 2017 USA.
- 3D Printed Antibacterial Ag NW/PLA Nanocomposites, I. Bayraktar, D. Doganay, **S. Coskun**, A. Kanicioglu, G. Akca, H. E. Unalan, MRS Fall' 2017 USA.
- Antibacterial Silver Nanowire-Chitosan Nanocomposite Films, D. Doganay, S.K. Somek, D. Aydin, A.Kanicioglu, **S. Coskun**, S. Senel, G. Akca, H. E. Unalan, MRS Fall' 2017 USA.
- Heatable Textiles With Silver Nanowires, D. Doganay, **S. Coskun**, S. Polat, H. E. Unalan, EMRS Spring' 2017 France.
- Utilization of Silver Nanowires in Supercapacitors, R. Yuksel, **S. Coskun**, H.E. Unalan, TMS Meeting' 2017 USA.
- Silver Nanowire Heaters on Glass and Textiles, **S. Coskun**, O. Ergun, D. Doganay, S. Polat, Y. Yusufoglu, H.E. Unalan, TMS Meeting' 2017 USA.
- Flexible Silver Nanowire Networks for High Frequency Shielding, E. Alpugan, **S. Coskun**, A. Dericioglu, H. E. Unalan, MRS Fall' 2016 USA
- Stability and Opto-Electronic Properties of Nickel Oxide-Silver Nanowire Nanocomposite Electrodes, **S. Coskun**, H. E. Unalan, J. Huang, MRS Fall' 2016 USA.
- Toxicological Evaluation of High Aspect Ratio Silver Nanowires, Muhammed Hamitoglu, **Sahin Coskun**, Rengin Reis, Sinem Helvacioglu, Ahmet Aydin, H. E. Unalan, NANOTR 12'2016 Turkey.
- Silver nanowire/polylactide Nanocomposite conducting films, D. Doğanay, **S. Coskun**, C. Kaynak, H. E. Unalan, TMS Meeting' 2016 USA.
- Silver nanowire networks for flexible electromagnetic interface shields, E. Alpugan, **S. Coskun**, A. Dericioğlu, H. E. Unalan, TMS Meeting' 2016 USA.

- Metal-enhanced fluorescence from silver nanowires with high aspect ratio on plana surfaces for biosensing applications, K. Aslan, B. Abel, E. Bonyi, H. E. Unalan, **S. Coskun**, PASIFICHEM' 2015 USA.
- Electrical Properties of Silver Nanowire/Poly lactide Nanocomposite Films, D. Doganay, **S. Coskun**, C. Kaynak, H. E. Unalan, MRS Fall' 2015 USA.
- Electromagnetic Interface Shielding Behavior of Silver Nanowire Networks, E. Alpugan, **S. Coskun**, A. F. Dericioğlu, H. E. Unalan, MRS Fall' 2015 USA.
- Optoelectronic Properties of Nickel Oxide Thin Films Elaborated by Sol-Gel, E. B. Sarac, **S. Coskun**, H. E. Unalan, C. Durucan, MRS Fall' 2015 USA.
- Silver Nanowire - Molybdenum Oxide Nanocomposite Electrodes for Flexible Supercapacitors, R. Yuksel, **S. Coskun**, C. Durucan, H. E. Unalan, MRS Fall' 2015 USA.
- A Comparative Analysis of Silver Nanowire Network, Indium Tin Oxide and Traditional Metal Contacts for Nitride Light Emitting Diodes, M. B. Acan, D. Doganay, **S. Coskun**, H. E. Unalan, B. Imer, MRS Fall' 2015 USA.
- Silver Nanowire - Molybdenum Oxide Nanocomposite Electrodes for Organic Light Emitting Diodes, **S. Coskun**, G. Kocak, A. Cirpan, H.E. Unalan, TMS Meeting' 2015 USA.
- Effects of Silver Nanowires on the Behavior of Poly lactide Nanocomposite Films, D. Doganay, **S. Coskun**, H.E. Unalan, C. Kaynak, TMS Meeting' 2015 USA.
- Silver Nanowire - Molybdenum Oxide Nanocomposite Electrodes for Optoelectronic Applications, **S. Coskun**, G. Kocak, A. Cirpan, H. E. Unalan, MRS Fall' 2014 USA.
- Silver Nanowire Network Transparent Heaters, **S. Coskun**, O. Ergun, H. E. Unalan, MRS Fall' 2014 USA
- Silver Nanowire Network Transparent Heaters, **S Coskun**, O Ergun, H.E. Unalan, NANOTR 10, Yeditepe University, 2014, Turkey.
- Silver Nanowire Networks for Polymer Light Emitting Diode Electrodes, **S. Coskun**, E.S. Ates, H.E. Unalan, MRS Fall' 2013 USA.

- Transparent and Flexible Photodetectors with Zinnoxide Nanowires Nanowire Networks for Polymer Light Emitting Diode Electrodes, A. Afal, **S. Coskun**, E.S. Ates, S. Kucukyildiz, C. Durucan, H.E. Unalan, MRS Fall' 2013 USA.
- Silicon Nanowire Network Metal-Semiconductor-Metal Photodetectors, E. Mulazimoglu, **S. Coskun**, M. Gunoven, B. Butun, E. Ozbay, R. Turan, H.E. Unalan, NanoTR' 9 2013 Erzurum, Turkey.
- Silver Nanowire Anodes in PLEDs, **S. Coskun**, E.S. Ates, H.E. Unalan, NanoTR' 9 2013 Erzurum, Turkey.
- Transparent and Flexible Photodetectors with Zinc Oxide Nanowires Aysegul Afal, **Sahin Coskun**, Elif Selen Ates, Seyda Kucukyildiz, Husnu Emrah Unalan, NanoTR' 9 2013 Erzurum, Turkey.
- Ultraviolet Photodetectors with Zinc Oxide and Silver Nanowires, A. Afal, **S. Coskun**, H. E. Unalan, ICMAT' 2013 Singapore.
- Silver Nanowire Network Electrodes for Polymeric Light Emitting Diodes, **S. Coskun**, E.S. Ates, H.E. Unalan, ICMAT' 2013 Singapore.
- Surface Plasmon Enhanced Silicon Nanowire Based Photodetectors, E. Mulazimoglu, **S. Coskun**, R. Turan, H. E. Unalan, MRS Fall' 2012 USA.
- Fabrication of Transparent and Conducting Silver Nanowire Networks and Their Utilization in PLEDS, **S. Coskun**, E.S. Ates, H. E. Unalan, MRS Fall' 2012 USA.
- Germanium Nanowire Enhanced Photodetectors, B. Aksoy, **S. Coskun**, S. Kucukyildiz, H. E. Unalan, MRS Fall' 2012 USA.
- Zinc Oxide Nanowire Based UV Photodetectors, **S. Coskun**, E. Mulazimoglu, A. Afal, H. E. Unalan, MRS Fall' 2012 USA.
- All Nanowire Network Photodetectors with Germanium and Silver Nanowires, B. Aksoy, **S. Coskun**, S. Kucukyildiz, H.E. Unalan, IMRC' 2012 Mexico.
- Zinc Oxide Nanowire Based Ultraviolet Photodetectors, **S. Coskun**, A. Afal, H. E. Unalan, NanoTR' 8 2012 Ankara Turkey.
- Production of Very High Aspect Ratio Gold NWs in High Yield and Morphological Purity, E. Dertli, **Ş. Coşkun**, H. E. Ünalın, E. Nalbant Esentürk, NanoTR' 8 2012 Ankara Turkey.
- Silver Nanowire Networks, **Sahin Coskun**, H. E. Unalan, MRS Fall' 2011 USA.

- Polyol Synthesis of Silver Nanowires, **S. Coskun**, B. Aksoy, H. E. Unalan, NanoTR' 7 2011 İstanbul, Turkey
- Transparent and Conducting Silver Nanowire Thin Films, **S. Coskun**, H. E. Unalan, EMRS Spring' 2011 France.
- Synthesis of Silver Nanowires and Determination of the Process Parameters, **S. Coskun**, H. E. Unalan, IMMC' 2010 İstanbul Turkey
- The Influence of Cooling at Various Cooling Rates from Intercritical Austenizing Temperatures on Microstructure and Mechanical Properties of Ductile Cast Iron, **S. Coskun**, V. Kılıçlı, M. Erdoğan, IMMC' 2008 İstanbul, Turkey.